

**Unraveling the Potential Role of DHHCs-mediated  
Protein *S*-palmitoylation in Cancer Biology  
through Untargeted Metabolomics and *In Silico*  
Approaches**

**Ph.D. Thesis  
by  
SUCHI CHATURVEDI**



**DEPARTMENT OF BIOSCIENCES & BIOMEDICAL  
ENGINEERING  
INDIAN INSTITUTE OF TECHNOLOGY INDORE  
June, 2025**



# **Unraveling the Potential Role of DHHCs-mediated Protein S-palmitoylation in Cancer Biology through Untargeted Metabolomics and *In Silico* Approaches**

**A THESIS**

*Submitted in partial fulfillment of the  
requirements for the award of the degree  
of*

**DOCTOR OF PHILOSOPHY**

*by*

**SUCHI CHATURVEDI**



**DEPARTMENT OF BIOSCIENCES &  
BIOMEDICAL ENGINEERING**

**INDIAN INSTITUTE OF TECHNOLOGY  
INDORE**

**June, 2025**







# INDIAN INSTITUTE OF TECHNOLOGY INDORE

I hereby certify that the work which is being presented in the thesis entitled **Unraveling the Potential Role of DHHCs-mediated Protein S-Palmitoylation in Cancer Biology through Untargeted Metabolomics and In Silico Approaches** in the partial fulfillment of the requirements for the award of the degree of **DOCTOR OF PHILOSOPHY** and submitted in the **Department of Biosciences & Biomedical Engineering, Indian Institute of Technology Indore**, is an authentic record of my own work carried out during the time period from July, 2018 to June, 2025 under the supervision of Dr. Avinash Sonawane, Professor, Department of BSBE, IIT Indore, and Dr. Sushabhan Sadhukhan, Associate professor, Department of Chemistry, IIT Palakkad.

The matter presented in this thesis has not been submitted by me for the award of any other degree of this or any other institute.

*Suchi*  
*30-06-25*

Signature of the student with date  
Suchi Chaturvedi

This is to certify that the above statement made by the candidate is correct to the best of my/our knowledge.

*Avinash*  
*30.06.2025*

Signature of Thesis Supervisor #1 with date

Prof. Avinash Sonawane

*Sushabhan*  
*30-06-25*

Signature of Thesis Supervisor #2 with date

Dr. Sushabhan Sadhukhan

Suchi Chaturvedi has successfully given his/her Ph.D. Oral Examination held on 30<sup>th</sup> June 2025.

*Avinash*  
*30.06.2025*

Signature of Thesis Supervisor #1 with date

Prof. Avinash Sonawane

*Sushabhan*  
*30-06-25*

Signature of Thesis Supervisor #2 with date

Dr. Sushabhan Sadhukhan



## Acknowledgments

First and foremost, I would like to express my heartfelt gratitude to the Almighty God for providing me with the opportunity to grow and evolve. God represents “faith,” which gives me the strength and support to achieve the unexpected. Those who seek this faith will find it. I am profoundly thankful to God for choosing, trusting, and guiding me through every phase of my learning journey. I pray for his continued guidance as I navigate the journey of life ahead.

When I began my PhD program, I was like shapeless clay, but with the help of many people, I have been molded into a vessel of wisdom. Today, I am grateful for the chance to formally acknowledge their contributions.

I owe a deep debt of gratitude to my mentors, **Prof. Avinash Sonawane** and **Dr. Sushabhan Sadhukhan**, for granting me the opportunity to explore and realize my potential in research. **Dr. Sonawane** is an exceptionally talented and admirable, and I feel fortunate to have been mentored by him. He is not only an intellectual scientist but also a wise and action-oriented individual. His extraordinary dedication and commitment to his work have been a constant source of inspiration. Working with him has been a valuable experience that has helped me become a better version of myself.

At the beginning of this journey, **Dr. Sadhukhan** told me that pursuing a PhD is like a roller coaster ride, and not all days would be the same. Over time, these words of wisdom have become increasingly meaningful to me. I am deeply thankful to him for his steadfast guidance, faith, and invaluable insights, which have played a pivotal role in transforming my research career and developing my

skills. His method of explaining science and engaging in scientific discussions has always inspired me. I would also like to express my deepest appreciation to my PSPC members, **Prof. Suman Mukhopadhyay** and **Dr. Mirza Saquib Baig**, for their insightful suggestions and evaluations throughout my Ph.D. journey.

My heartfelt gratitude extends to the Head and DPGC convener of the Department of Bioscience and Biomedical Engineering at IIT Indore for their encouragement and support during my Ph.D. I am also extremely thankful to all the faculty members of the BSBE department for their valuable contributions to my research through the various courses taught during my coursework. I am grateful to IISc Bangalore for providing access to the LC-MS/MS metabolomics facility. Additionally, I would like to thank Professor **Hening Lin** from the Department of Chemistry and Chemical Biology at Cornell University, Ithaca, New York, for his generous assistance with the plasmids.

This journey would not have been possible without the supportive environment provided by my colleagues at IITI. I extend my gratitude to my lab members—**Sibi Karthik, Kishan, Barsa, Satyam, Bhagyshree, and Priya**—for fostering a conducive atmosphere for research. I also deeply appreciate my senior lab members—**Ananya Shree, Mainak, and Dr. Jhasketan Badhai**—for their moral support and for sharing their valuable knowledge of techniques, scientific writing, and discussions. Additionally, I am thankful to my friends **Dr. Nirali Pandya**, and **Krishna Singh** for their unwavering support and for providing a healthy environment. I am also grateful for the steadfast support from **Dr. Anupama Binoy, Revathy, Sai Kumari, and Shalini**. It has been a pleasure to receive their relentless support.

I would like to extend my heartfelt thanks to **Mr. Gaurav**

**Singh, Mr. Amit Kumar**, and **Mr. Arif Patel** for their invaluable assistance and support in ensuring the smooth operation of lab instruments and other academic tasks. I also express my gratitude to **Mr. Tapesb Parihar**, Manager of Academics, for his timely help in various aspects. I take this opportunity to thank the library staff and technical staff of IIT Indore for their support during my research work. Special thanks go to **Mr. Sunny Singh** for his assistance with DST-INSPIRE financial matters. I would also like to acknowledge the Sophisticated Instrumentation Center (SIC) at the Indian Institute of Technology Indore (IITI) for their facilities. Lastly, I would like to acknowledge the Department of Science and Technology, INSPIRE, India, for the financial assistance provided during my Ph.D.

Family is the sanctuary where one can rejuvenate, create cherished memories, and find resilience. It is my immense privilege and deep honor to express my gratitude to my father, **Mr. Satish Chandra Chaturvedi**, and my mother, **Mrs. Kiran Chaturvedi**, for granting me the freedom to pursue my path. Your belief in my abilities and your constant encouragement have been the pillars that sustained me during the challenging times. Mom, your endless prayers and comforting words always gave me strength and reassurance. Dad, your wise advice and steady guidance helped me navigate through the complexities of academic life. Together, you provided the loving support and understanding that I needed to persevere. I am deeply grateful for your sacrifices to ensure my success. From the countless late-night calls to the care and the unwavering faith you placed in me, I am forever indebted to you both. I am fortunate to have a younger brother, **Mr. Somu Chaturvedi**, and a sister-in-law, **Mrs. Prachi Chaturvedi**, who have supported me in every possible way throughout my journey. The trust and faith my family has in me continuously motivate me

to strive for excellence. Their immense support in every aspect has been instrumental in the completion of this journey. Their presence and belief in me remind me of my goals and give me the energy to keep moving forward. This achievement is as much yours as it is mine. Thank you for everything.

I would like to extend my deepest gratitude to my beloved fiancé, **Mr. Anand Kumar Shukla**, whose unwavering support and understanding have been the cornerstone of my Ph.D. journey. His patience, encouragement, and endless love have been my anchors through the challenging and rewarding moments of this experience. Thank you for standing by me, celebrating the highs, and comforting me during the lows. Your presence has made this journey not only possible but also meaningful. I am profoundly grateful for your companionship and unwavering faith in me. This accomplishment is as much yours as it is mine.

**Suchi Chaturvedi**

**This thesis is dedicated  
to my Parents and Family**





## Synopsis

---

### **Introduction: Protein *S*-palmitoylation in cancer:**

Protein *S*-palmitoylation is a reversible protein lipidation in which a thioester bond is formed between a cysteine (Cys) residue of a protein and a 16-carbon fatty acid chain. This modification is catalyzed by palmitoyl acyl transferases, also known as the DHHCs, because of their Asp-His-His-Cys (DHHC) catalytic motif [1]. Deregulation of DHHC enzymes has been linked to various diseases, including cancer and various infections [2, 3]. Cancer, a major cause of global mortality, is characterized by features like uncontrolled cell growth, resistance to cell death, angiogenesis, invasion, and metastasis [4]. Several of these processes are controlled by DHHC-mediated *S*-palmitoylation of oncogenes or tumor suppressors, including growth factor receptors (e.g., epidermal growth factor receptor; EGFR), kinases (e.g., protein kinase B; AKT), and transcription factors (e.g.,  $\beta$ -catenin) [5, 6]. Given the critical role of *S*-palmitoylation in cancer, targeting the enzymes involved in this modification and the palmitoylated proteins themselves represents a promising therapeutic strategy. However, significant challenges remain, including the lack of effective inhibitors and the impact of DHHCs on cancer cell metabolism. Addressing these challenges is essential for advancing cancer therapy through the modulation of *S*-palmitoylation. Given the information above, the primary goals of this study are as follows:

- To identify phytochemicals that can potentially act as DHHC inhibitors.
- Untargeted metabolomics using LC-MS/MS to understand the role of individual DHHC isoforms in knock-down and over-expressed cancer conditions.
- Revealing the interaction between extracellular domain (ECD)-EGFR and DHHC isoforms to address the challenges of cancer burden associated with EGFR.

**The Ph.D. thesis work has been reported in the form of five chapters:**

**Chapter 1** deals with introducing the subject, reviewing the literature, and the scope of the thesis.

**Chapter 2:** This chapter focused on identifying the key phytochemicals that can potentially act as DHHCs targeting inhibitors.

Protein *S*-palmitoylation, mediated by DHHC enzymes, is associated with various health disorders, including cancer, neurodegenerative diseases, and autoimmune conditions [3, 7]. Notably, the identification of DHHC inhibitors, are classified into lipid-based and non-lipid-based types, remains limited. Among the lipid-based inhibitors, 2-bromopalmitic acid (2-BP), tunicamycin, and cerulenin analogs have been identified, with 2-BP being the most widely used [8]. However, the pharmacological properties of existing pan-DHHC inhibitors, such as their off-target effects and toxicity, have restricted their further clinical trials [9].

As therapeutic research advances, there is a growing interest in natural products valued for their diverse structures, chemical stability, and lower toxicity [10]. Recent studies suggest that these natural products could be effective *S*-acylation inhibitors. For instance, research by X. Chen et al. (2020) demonstrated that disrupting the DHHC17-mitogen-activated protein kinase kinase 4 (MAP2K4) complex with genistein inhibited glioblastoma (GBM) cell proliferation and glioma stem cell (GSC) self-renewal capacity [11]. Another study by Binoy et al. (2024) showed that the 4"-alkyl ether lipophilic derivatives of epigallocatechin gallate (EGCG) can inhibit *S*-acylation. They found that 4"-EGCG significantly reduced protein *S*-palmitoylation *in vitro*, particularly in cells overexpressing DHHC3 [12]. Therefore favourable therapeutic properties of natural compounds prompted us to investigate them as DHHC inhibitors through computational approaches.

**Chapter 3:** The focus of this chapter was to elucidate the direct role of DHHCs on cancer metabolism, which remains significantly underexplored.

The increased hydrophobicity resulting from palmitoylation is a crucial biochemical trait that affects protein functions by adding variations to the role of DHHCs in diseases [13]. For example, DHHC2-mediated *S*-palmitoylation of acylglycerol kinase (AGK) facilitates its translocation to the plasma

membrane, activating the phosphatidylinositol 3-kinase-protein kinase B-mammalian target of rapamycin (PI3K-AKT-mTOR) signaling pathway in clear cell renal cell carcinoma (ccRCC) and influencing sensitivity to sunitinib [14]. Conversely, another study showed diminished DHHC2 expression in gastric tumor tissues through qRT-PCR and immunostaining. Low DHHC2 expression correlated significantly with lymph node metastasis and histological grade in gastric adenocarcinoma patients [15].

Apart from this, the deregulation of cellular metabolism supports uncontrolled proliferation, which leads to distinct metabolite profiling that can serve as cancer diagnostic markers. The role of several key regulators in cancer metabolism, such as EGFR, AKT, and p53, has been extensively studied [5, 16, 17]. In addition, the impact of palmitoylated protein substrates on cellular metabolic changes, such as palmitoylated- prolactin-releasing peptide 31 analog (palm11-PrRP31), which demonstrated improved biochemical parameters, including lowered body weight and glucose tolerance *via* a significant decrease of 1-methyl nicotinamide and formate in spontaneously hypertensive rats (SHR) and alanine, dimethylamine, N-butyryl glycine and, allantoin in normotensive Wistar Kyoto (WKY) rats, have been studied [18].

Despite these insights, there remains a gap in understanding the direct influence of DHHCs on cancer cell metabolism, an area currently underexplored in scientific literature. As highlighted above, DHHC2 exhibits various properties in cancer, necessitating thorough investigation to validate its significance in cancer progression or prevention. Hence, the second objective aimed to delve into the influence of DHHC2 on cancer biology by quantitatively identifying associated metabolites and metabolic pathways through LC-MS/MS-based untargeted metabolomics.

**Chapter 4:** The key objective of this chapter was to unveil the interaction of DHHCs and the ECD-EGFR to mitigate the oncogenic effect on cancer progression.

DHHCs are crucial in modifying various proteins, including EGFR, programmed death-ligand 1(PD-L1), and AKT, contributing to cancer progression. It has been reported that deregulation of EGFR, either through

overexpression of its wild-type form (WT-EGFR) or mutant variants, is common in cancer [6, 19, 20]. Concerning the *S*-palmitoylation and EGFR, two studies have reported that the palmitoylation of the intracellular domain of EGFR by DHHCs is associated with its abnormal expression in cancer. The first study showed that DHHC20-mediated reversible *S*-palmitoylation of EGFR enhances its activation in non-small cell lung cancer (NSCLC). This process involves attaching the palmitate chain to the intracellular domain of EGFR, effectively "pins" its unstructured C-terminal tail to the plasma membrane, thereby boosting EGFR activation [21, 22].

The second study revealed that fatty acid synthase (FASN)-mediated palmitoylation of the intracellular domain of EGFR promotes its ligand-independent activation in cancer cells [6]. From these two studies, we concluded that much attention had been given to targeting the intracellular domain of EGFR, which drives its signaling post-ligand binding at the ECD. However, the role of *S*-palmitoylation in ECD-EGFR has been relatively overlooked. To investigate this hypothesis, we utilized computational approaches to identify critical DHHCs interacting with ECD-EGFR. Our research aimed to bridge the gap in understanding the role of *S*-palmitoylation in ECD-EGFR activity, which can mimic a ligand-bound state or stabilize an active conformation of the ECD, thereby facilitating receptor dimerization and activation independently of ligand binding in malignant cells.

**Chapter 5** focuses on the conclusion of the work done in the thesis and the future perspective of the study.

## **List of Publications**

### **From the thesis:**

- ❖ **Chaturvedi S.**, Biswas M., Sadhukhan S., and Sonawane A., (2023). Role of EGFR and FASN in breast cancer progression. *J Cell Commun Signal*, 17(4),1249-1282. <https://doi.org/10.1007/s12079-023-00771-w>
- ❖ **Chaturvedi S.**, Pandya N., Sadhukhan S., & Sonawane A., (2024). Identification of selective plant-derived natural carotenoid and flavonoids as

the potential inhibitors of DHHC-mediated protein S-palmitoylation: an *in silico* study. *J Bio Struct Dyn*, 1-14.

- ❖ **Chaturvedi S., & Sonawane A.,** (2025). Recapitulating the potential contribution of protein S-palmitoylation in cancer. *Cancer Metastasis Rev*, 44(1), 1-26. <https://doi.org/10.1007/s10555-024-10217>
- ❖ **Chaturvedi S., Karthik S., Sadhukhan S., & Sonawane A.,** (2025). Unraveling the potential contribution of DHHC2 in cancer biology via untargeted metabolomics. *BBA-Mol Cell Biol Lipids*, 1870(2), 159593. <https://doi.org/10.1016/j.bbalip.2025.159593>.
- ❖ **Chaturvedi S., et al.,** (2025). Exploring the potential cross-talk between DHHCs and EGFR through *in silico* studies, (Under Submission)

## List of Publications

- ❖ **Chaturvedi S.**, Biswas M., Sadhukhan S., and Sonawane A., (2023). Role of EGFR and FASN in breast cancer progression. *J Cell Commun Signal*, 17(4),1249-1282. <https://doi.org/10.1007/s12079-023-00771-w>
- ❖ **Chaturvedi S.**, Pandya N., Sadhukhan S., & Sonawane A., (2024). Identification of selective plant-derived natural carotenoid and flavonoids as the potential inhibitors of DHHC-mediated protein S-palmitoylation: an in-silico study. *J Bio Struct Dyn*, 1-14.
- ❖ **Chaturvedi S.**, & Sonawane A., (2025). Recapitulating the potential contribution of protein S-palmitoylation in cancer. *Cancer Metastasis Rev*, 44(1), 1-26. <https://doi.org/10.1007/s10555-024-10217>
- ❖ **Chaturvedi S.**, Karthik S., Sadhukhan S., & Sonawane A., (2025). Unraveling the potential contribution of DHHC2 in cancer biology via untargeted metabolomics. *BBA-Mol Cell Biol Lipids*, 1870(2), 159593. <https://doi.org/10.1016/j.bbalip.2025.159593>.
- ❖ **Chaturvedi S.**, et al., (2025). Exploring the potential cross-talk between DHHCs and EGFR through *in silico* studies, (Under Submission)

## Table of contents

<b>List of abbreviations .....</b>	<b>xv</b>
<b>Nomenclatures .....</b>	<b>xvii</b>
<b>List of figures.....</b>	<b>xvii</b>
<b>List of tables.....</b>	<b>xxiii</b>
<b>Chapter 1: Introduction and literature review .....</b>	<b>2</b>
1.1 Introduction: Protein S-palmitoylation:.....	2
1.1.1 Discovery and mechanism of DHHCs: .....	5
1.1.2 Palmitoylation and depalmitoylation cycling required for cellular physiology: .....	6
1.1.2.1 Crosstalk between protein S-palmitoylation and other post-translational modifications .....	9
1.1.3 DHHC isoforms and their association with cancer: .....	11

1.1.4 <i>S</i> -palmitoylation and depalmitoylation targeting inhibitors: .....	25
1.1.5 Methods to detect and characterize <i>S</i> -palmitoylation: .....	32
1.2 Introduction: EGFR and breast cancer: .....	36
1.2.1 Recapitulation of EGFR family: .....	37
1.2.2 Cross talk between EGFR and palmitoylation:.....	42
1.3 Conclusion: .....	44
1.4 Aim of the thesis:.....	45
1.4.1 Organization of the thesis: .....	46
<b>Chapter 2: Identification of selective plant-derived natural carotenoid and flavonoids as the potential inhibitors of DHHC-mediated protein <i>S</i>-palmitoylation: an <i>in silico</i> study .....</b>	<b>49</b>
2.1 Introduction: .....	49
2.2 Methods: .....	51
2.2.1 Retrieval of protein crystal structure and ligands: .....	51
2.2.2 Preparation and docking parameters for protein and ligands: .....	52
2.2.3 Analysis of protein-ligand complexes: .....	52
2.2.4 Parameters for MD simulation:.....	52
2.2.5 The absorption, distribution, metabolism, excretion, and toxicity (ADMET) and physicochemical characteristics of ligands: .....	54
2.2.6 Prediction of molecular targets: .....	54
2.2.7 PASS evaluation: Predictions of biological activity:.....	54
2.3 Results and Discussions: .....	55
2.3.1 Analysis of the three best ligand molecules that bind to DHHC20 (PDB ID: 6BML): .....	55
2.3.2 MD simulation and binding free energy calculation: .....	60
2.3.3 The physiochemical and ADMET properties of the selected molecules: .....	68
2.3.4 Identification of molecular targets: .....	73
.....	74
2.3.5 PASS analysis: Predictions of biological activity:.....	74
2.4 Conclusion: .....	76
<b>Chapter 3: Unraveling the potential contribution of DHHC2 in cancer biology <i>via</i> untargeted metabolomics .....</b>	<b>79</b>
3.1 Introduction: .....	79
3.2. Material and methods: .....	81
3.2.1 Cell culture and reagents:.....	81
3.2.2 Cell culture, transfection, and RNA extraction:.....	82
3.2.3 Parameters for qRT-PCR: .....	82

3.2.4. Western blot analysis:.....	83
3.2.5 Metabolites extraction: .....	84
3.2.6 Metabolomics data analysis:.....	84
3.2.7 Identification of the metabolites through MS-DIAL:.....	85
3.2.8 Statistical analysis: .....	86
3.3 Results:.....	86
3.3.1 Silencing of <i>DHHC2</i> gene post-esiRNA mediated knockdown in HEK-293T cell line: .....	86
3.3.2 Identification of metabolites:.....	87
3.3.3 Classification of differentially expressed metabolites <i>via</i> multivariate and univariate analysis: .....	91
3.3.4 Pathway enrichment analysis: Investigating the impact of metabolites on the biological pathways: .....	98
3.3.5 p53 can be a potential marker behind DHHC2-mediated tumor suppressive activity: .....	105
3.4 Discussion and conclusion: .....	107
<b>Chapter 4: Exploring the potential cross-talk between EGFR and DHHCs through <i>in silico</i> methodologies .....</b>	<b>113</b>
4.1 Introduction:.....	113
4.2. Methods:.....	114
4.2.1 Retrieval of protein structures: .....	114
4.2.2 Prediction of palmitoylation sites and point mutation residue: .....	115
4.2.3 Mutant generation:.....	115
4.2.4 Validation of the mutant EGFR C7S 3D model:.....	115
4.2.5 Parameters for molecular docking:.....	116
4.2.6 Parameters for MD simulation: .....	116
4.3 Results and discussion: .....	118
4.3.1. Identification of the best DHHCs that are potentially interacting with Cys7 residue of EGFR:.....	118
4.3.2 Validation of EGFR C7S mutant followed by molecular docking with the identified crucial isoforms: .....	121
4.3.3 MD simulation and binding free energy calculation: .....	125
4.4 Conclusion:.....	129
<b>Chapter 5: Conclusion and future perspective.....</b>	<b>131</b>
5.1 Summary of the thesis:.....	131
5.2 Future perspective: .....	134
<b>Appendix.....</b>	<b>137</b>
<b>References.....</b>	<b>215</b>



## List of abbreviations

<b>2-BP</b>	2-Bromopalmitic acid
<b>APT1 and APT2</b>	Acyl protein thioesterases-1 and 2
<b>AGK</b>	Acylglycerol kinase
<b>ARF6</b>	ADP-ribosylation factor 6
<b>AMPK<math>\alpha</math>1</b>	AMP-activated protein kinase
<b>AR</b>	Androgen receptor
<b>APF</b>	Anti-proliferative factor
<b>D-H-H-C</b>	Asp-His-His-Cys
<b>BL-BC</b>	Basal-like breast cancer
<b>BSA</b>	Bovine serum albumin
<b>BL</b>	Burkitt lymphoma
<b>CRC</b>	Critical colorectal cancer
<b>cDNA</b>	complementary DNA
<b>CMA</b>	Cyanomethyl-N-myrcylamide
<b>CRD</b>	Cys rich domain
<b>CKAP4</b>	Cytoskeleton-associated protein 4
<b>DNA</b>	Deoxyribonucleic acid
<b>DMEM</b>	Dulbecco's Modified Eagle's Medium
<b>esiRNA</b>	Endoribonuclease-prepared siRNA
<b>ER</b>	Endoplasmic reticulum
<b>ECs</b>	Endothelial cells
<b>EZH2</b>	Enhancer of zeste homolog 2-
<b>EGFR</b>	Epidermal growth factor receptors
<b>EMT</b>	Epithelial-mesenchymal transition
<b>ECD</b>	Extracellular domain
<b>ERK</b>	Extracellular signal-regulated kinase
<b>FASN</b>	Fatty acid synthase
<b>FBS</b>	Fetal bovine serum
<b>FLOT-1</b>	Flotillin-1
<b>GO</b>	Gene Ontology
<b>GTE<sub>x</sub></b>	Genotype-Tissue Expression
<b>GBM</b>	Glioblastoma
<b>GSCs</b>	Glioblastoma stem cells
<b>GAPDH</b>	Glyceraldehyde 3-phosphate dehydrogenase
<b>H-Ras</b>	Harvey Ras viral homolog
<b>HCC</b>	Hepatocellular carcinoma
<b>HEK-293T</b>	Human embryonic kidney cell line-293 T
<b>HILIC</b>	Hydrophilic interaction chromatography
<b>HIF</b>	Hypoxia-inducible transcription factor
<b>IFITM3</b>	Interferon-induced transmembrane protein 3
<b>IL</b>	Interleukin
<b>ICGC</b>	International Cancer Genome Consortium
<b>JAK</b>	Janus kinase
<b>K-Ras</b>	Kirsten rat sarcoma viral oncogene homolog

<b>KEGG</b>	Kyoto Encyclopedia of Genes and Genomes
<b>LDHA</b>	Lactate dehydrogenase A
<b>LC-MS/MS</b>	Liquid chromatography-mass spectrometry/mass spectrometry
<b>LUAD</b>	Lung adenocarcinoma
<b>mTOR</b>	Mammalian target of rapamycin
<b>MMP</b>	Matrix metalloproteinase
<b>MC1R</b>	Melanocortin 1 receptor
<b>mRNA</b>	Messenger RNA
<b>MAPK</b>	Mitogen-activated protein kinase
<b>MEK kinase</b>	Mitogen-activated protein kinase kinase
<b>MD simulations</b>	Molecular dynamics simulations
<b>MM-GBSA</b>	Molecular Mechanics with Generalized Born and Surface Area solvation
<b>MDM2</b>	Mouse double minute 2 homolog
<b>MYC</b>	Myelocytomatosis oncogene
<b>NCCS</b>	National Center for Cell Science
<b>N-Ras</b>	Neuroblastoma-Ras viral oncogene homolog
<b>NSCLC</b>	Non-small cell lung cancer
<b>WKY</b>	Normotensive Wistar Kyoto
<b>OSCC</b>	Oral squamous cell carcinoma
<b>OXPHOS</b>	Oxidative phosphorylation
<b>PAT</b>	Palmitoyl acyl transferase
<b>PPT1 and PPT2</b>	Palmitoyl protein thioesterases -1 and 2
<b>Palm11-prrp31</b>	Palmitoylated- prolactin-releasing peptide 31 analog
<b>PMS</b>	Palmitoylation metabolism-related signature
<b>PLS-DA</b>	Partial least squares-discriminant
<b>PTEN</b>	Phosphatase and Tensin Homolog
<b>PBS</b>	Phosphate buffer saline
<b>PI3K</b>	Phosphatidylinositol 3-kinase
<b>PTMs</b>	Post-translational modifications
<b>PCA</b>	Principle component analysis
<b>PR</b>	Progesterone receptor
<b>PD-L1</b>	Programmed death-ligand 1
<b>AKT</b>	Protein kinase B
<b>qRT-PCR</b>	Quantitative real-time reverse-transcription PCR
<b>Rg</b>	Radius of gyration
<b>RNA</b>	Ribonucleic acid
<b>RMSD</b>	Root mean square deviation
<b>ROS</b>	Reactive oxygen species
<b>RMSF</b>	Root mean square fluctuations
<b>SARS-CoV-2</b>	Severe acute respiratory syndrome virus 2
<b>STAT</b>	Signal transducer and activator of transcription
<b>siRNA</b>	Small interfering RNA
<b>SDS-PAGE</b>	Sodium dodecyl sulfate–polyacrylamide gel electrophoresis
<b>SASA</b>	Solvent-accessible surface area
<b>SHR</b>	Spontaneously hypertensive rats

**SREBP1c**  
**TMZ**

Sterol regulatory element-binding protein 1c  
Temozolomide

## Nomenclatures

<b>g</b>	Gram
<b>kDa</b>	Kilo Dalton
<b>mg</b>	Milligram
<b>ml</b>	Millilitre
<b>mM</b>	Millimolar
<b>ng</b>	Nanogram
<b>µg</b>	Microgram
<b>nM</b>	Nanomolar
<b>ns</b>	Nanosecond
<b>ps</b>	Picosecond
<b>U</b>	Unit
<b>µl</b>	Microlitre
<b>µM</b>	Micromolar
<b>µs</b>	Microsecond
<b>°C</b>	Degree centigrade
<b>Å</b>	Angstrom
<b>α</b>	Alpha
<b>β</b>	Beta
<b>γ</b>	Gamma
<b>K</b>	Kelvin
<b>ΔG<sub>bind</sub> Covalent</b>	Covalent binding energy
	van der Waals
<b>ΔG<sub>bind</sub>vdW</b>	interactions
<b>ΔG<sub>bind</sub>Lipo</b>	Lipophilic energy
<b>ΔG<sub>bind</sub>Hbond</b>	Hydrogen-bonding
<b>ΔG<sub>bind</sub></b>	Binding free energy
<b>KD</b>	Dissociation constant

## List of figures

### ❖ Chapter 1

- Figure 1.1 The above figure illustrates the mechanism of action of DHHC enzymes. Step 1: Autoacylation - Palmitoyl-CoA provides a palmitate group, which is transferred to the active cysteine site of palmitoyl *S*-acyltransferase (PATs) or DHHCs, leading to their auto-*S*-palmitoylation. Step 2: Palmitoyl Group Transfer- The palmitoyl group is then transferred from the palmitoyl-PAT intermediate to the cysteine residue of the substrate protein, forming a thioester bond and thereby

modifying the substrate protein (This figure was created using www.biorender.com). .....	11
➤ Figure 1.2 DHHC enzymes play a multifaceted role in cancer progression by influencing various crucial activities that support cancer growth. For example, DHHC3-mediated palmitoylation of PD-L1 prevents its degradation, aiding immune escape. DHHC12 influences protein stability, such as CLDN3 in ovarian cancer. DHHC2 promotes the localization of proteins like AGK in clear cell carcinoma. DHHC15 activates cancer-related signaling pathways, like IL-6-STAT3, through GP130 palmitoylation. DHHC9 enhances the Warburg effect by increasing lactate production and reducing ROS <i>via</i> LDHA palmitoylation, and it also exacerbates cancer symptoms by upregulating APLN. DHHC21 activates oxidative phosphorylation in leukemia, and DHHC4 contributes to TMZ resistance by facilitating GSK3β palmitoylation in GBM cells.....	24
➤ Figure 1.3 Chemical structure of DHHC-targeting inhibitors (These figures were drawn using ChemDraw Pro 12.0.2).....	29
➤ Figure 1.4 Chemical structure of depalmitoylation -targeting inhibitors (These figures were drawn using ChemDraw Pro 12.0.2).....	32
➤ Figure 1.5 Analytical techniques for the identification and characterization of protein S-palmitoylation. (This figure was drawn using ChemDraw Pro 12.0.2).....	35
➤ Figure 1.6 Structural depiction of EGFR: A) (I) The Extracellular domain (ECD): domain I/L1, domain II/ CR1, domain III/L2, domain IV/CR2. (II) Transmembrane domains (TMD). (III) The intracellular domains (ICD): (i) The tyrosine kinase domain (TKD), site for the mutations associated with resistance and sensitivity to TKIs; ii) The auto-phosphorylation site at the regulatory domain (Y953-Y1186). B) A canonical model representing the various sites for EGFR-specific inhibitors. Monoclonal antibodies target the ECD of EGFR and prevent the binding of ligand molecules to ECD, while TK-inhibitors compete with ATP for binding to the intracellular tyrosine kinase domain of EGFR (This figure was created using www.BioRender.com).....	39

- Figure 1.7 The schematic representation illustrates the various signaling pathways activated by EGFR in a cell. Step 1-2: Transition of inactive monomer to active dimeric EGFR complex upon ligand binding. Step 3: Dimeric EGFR activate intracellular adaptor adaptor proteins, such as the Ras-RAF-MEK-MAPK, PI3K-AKT, and JAK-STATs etc. Step4: The regulation of FASN via SERBP1c and EGFR signaling. Step 5: EGFR mediated signaling cascades promote activation of anti-apoptotic proteins such as, BCL-2, BCL-XL, and FASN and control diverse cellular responses such as, cell proliferation, protein synthesis, angiogenesis etc. (This figure was created using [www.BioRender.com](http://www.BioRender.com)).  
.....42

## ❖ Chapter 2

- Figure 2.1 Schematic representation of the workflow. This figure was created using [www.biorender.com](http://www.biorender.com).....51
- Figure 2.2 3D models of DHHC20 in complex with ligands: A) 2-BP acid, B) lutein, C) 5-hydroxyflavone, and D) 6-hydroxyflavone. All values are in kcal/mol.....56
- Figure 2.3 2D models of DHHC20 in complex with ligands: A) 2-BP, B) lutein, C) 5-hydroxyflavone, and D) 6-hydroxyflavone. ....57
- Figure 2.4 Analysis of RMSD trajectories A) DHHC20 protein trajectories in complex with ligands. B) ligand trajectories in complex with DHHC20 protein throughout 100 ns MD simulation run. ....61
- Figure 2.5 Analysis of A) Rg and B) SASA trajectories of DHHC20 in complex with ligands (lutein, 5-hydroxyflavone, and 6-hydroxyflavone) throughout the 100 ns MD simulation run. ....62
- Figure 2.6 Graphical representation of RMSF plot of DHHC20 in complex with ligands (lutein, 5-hydroxyflavone, and 6-hydroxyflavone) throughout the 100 ns MD simulation run. ....63
- Figure 2.7 Binding free energies and the corresponding energy components (lipophilic, covalent, and generalized Born electrostatic solvation, and van der Waals) obtained *via* MM-GBSA analysis of DHHC20 in complex with ligands (lutein, 5-hydroxyflavone, and 6-

hydroxyflavone) throughout the 100 ns MD simulation run. All values are in kcal/mol.....	64
➤ Figure 2.8 Protein-ligand contact maps were generated between DHHC20 and ligands (lutein, 5-hydroxyflavone, and 6-hydroxyflavone) throughout 100 ns MD simulation run.....	66
➤ Figure 2.9 Protein-ligand interactions were monitored between DHHC20 and ligands (lutein, 5-hydroxyflavone, and 6-hydroxyflavone) throughout 100 ns MD simulation run. These interactions are classified into four types: Hydrophobic, H-bonds, Ionic, and Water bridges.....	67
➤ Figure 2.10 The pie chart depicting the molecular targets of the selected compounds: A) lutein, B) 5-hydroxyflavone, and C) 6-hydroxyflavone. ....	74

### ❖ Chapter 3

➤ Figure 3.1 Schematic representation of the workflow (The figure was drawn using <a href="http://www.biorender.com">www.biorender.com</a> ).....	81
➤ Figure 3.2 A) Western blot analysis of DHHC2 and Ctrl post-transfection. B) Relative fold change of mRNA expression post-DHHC2 overexpression and knockdown compared to the control conditions. Samples were normalized with the endogenous control GAPDH (n=3).....	87
➤ Figure 3.3 A) The heatmap depicting the correlation of identified 73 metabolites with their respective conditions (DHHC2-OE, DHHC2-KD and Ctrl). B) The pie chart representing the classification of metabolites into the 6 super compound classes.....	90
➤ Figure 3.4 A) PCA score plot: The X and Y axes were labeled with the first and second principal components, accounting for 25.1% and 19.7% of the total variation, respectively. B) PLS-DA score plot: The X and Y axes were labeled with the first and second components, accounting for 24 % and 15.1 % of the total variation, respectively. Colors in PCA and PLS-DA score plots indicated three different groups. C) The top 10 features responsible for the segregation of OE, KD, and Ctrl groups having VIP > 1. ....	92

- Figure 3.5 A) Volcano plots of differentially expressed metabolites. The graph was plotted in the  $[\log_2(FC)]$  vs. t-test  $P$  values  $[-\log_{10}(P \text{ value})]$ . In this figure, down refers to the FC: DHHC2-KD > DHHC2-OE, while up refers to FC:DHHC2-OE > DHHC2-KD. B) The bar graph representing significantly altered 22 metabolites in DHHC2-KD and DHHC2-OE groups post comparison with Ctrl in the HEK-293T cell line.....94
- Figure 3.6 The graphs representing the pathways obtained through MetaboAnalyst 5.0. A) DHHC2-KD and B) DHHC2-OE. The pathways were identified based on the enrichment ratio of the metabolites in the particular pathway vs. the t-test based  $P$  value  $[-\log_{10}(P \text{ value})]$ . C) Relative CAD-mRNA fold change expression post-DHHC2 overexpression and knockdown compared with Ctrl in HEK-293T cell line. Samples were normalized with the endogenous control GAPDH (n=3)..... 101
- Figure 3.7 Relative p53-mRNA fold change expression post-DHHC2 overexpression and knockdown compared with Ctrl in HEK-293T cell line. Samples were normalized with the endogenous control GAPDH (n=3)..... 107
- Figure 3.8 The above figure depicts how DHHC2 negatively regulates the pyrimidine pathway through CAD..... 108
- Figure 3.9 The schematic representation of the identified metabolites and their associated pathways. The metabolites and pathways highlighted in green are significantly expressed in the DHHC2-OE condition and considered upregulated (glycine and serine metabolism, betaine metabolism, and methionine metabolism). Conversely, the blue color indicates the presence of the metabolites and pathways in DHHC2-KD that were considered downregulated (pyrimidine metabolism, urea cycle, and aspartate metabolism). KG: ketoglutarate, OAA: oxaloacetate, DMG: dimethylglycine, SAM: *S*-adenosyl methionine, UMP: uridine-monophosphate, dSAM: decarboxylated *S*-adenosyl methionine. This figure was created using [www.BioRender.com](http://www.BioRender.com)..... 111

## ❖ Chapter 4

- Figure 4.1 Schematic representation of the workflow. The above figure denotes the cysteine and serine as C and S (This figure was created using [www.biorender.com](http://www.biorender.com)). ..... 114
- Figure 4.2 Identification of the significant *S*-palmitoylation site in the ECD domain of EGFR (PDBID: 7SYD) through CSS palm..... 118
- Figure 4.3 3D models of protein-protein complexes where Chain A of DHHCs is considered receptor (brown) and Chain B of EGFR as ligand (green) during molecular docking. A) DHHC1-EGFR and B) DHHC4-EGFR. The docking scores are represented in kcal/mol..... 119
- Figure 4.4 Details of the individual residue-residue interactions that occurred across the protein-protein complexes are obtained through PDBsum A) DHHC1-EGFR and B) DHHC4-EGFR. Chain A of DHHCs and Chain B of EGFR were utilized. .... 120
- Figure 4.5 The Ramachandran plot of EGFR C7S mutant protein obtained through PROCHECK server. .... 122
- Figure 4.6 3D models of protein-protein complexes where Chain A of DHHCs is considered receptor (brown) and Chain B of EGFR C7S as ligand (green) during molecular docking. A) DHHC1-EGFR C7S and B) DHHC4-EGFR C7S. The docking scores are represented in kcal/mol. .... 123
- Figure 4.7 Details of the individual residue-residue interactions that occurred across the protein-protein complexes are obtained through PDBsum A) DHHC1-EGFR C7S and B) DHHC4-EGFR.C7S Chain A of DHHCs and Chain B of EGFR were utilized. .... 124
- Figure 4.8 Analysis of RMSD trajectories of EGFR and EGFR C7S in complex with DHHC1 and DHHC4 throughout 100 ns MD simulation run. .... 125
- Figure 4.9 Analysis of Rg trajectories of EGFR and EGFR C7S in complex with DHHC1 and DHHC4 throughout 100 ns MD simulation run. .... 126
- Figure 4.10 Analysis of SASA trajectories of EGFR and EGFR C7S in complex with DHHC1 and DHHC4 throughout 100 ns MD simulation run. .... 127



- Figure 4.11 Binding free energies and the corresponding energy components (covalent, lipophilic, Hbond, and van der Waal) obtained from MM-GBSA analysis for EGFR and EGFR C7S in complex with DHHC1 and DHHC4 throughout 100 ns MD simulation run..... 128

## ❖ Appendix

- Figure A1 Metabolites characterization using *in silico* spectral libraries. The MS/MS spectra for the 22 significantly ( $P$  value < 0.05) altered metabolites are showcased. The upper spectra represents the experimental (blue) peaks of selected metabolite, and the lower spectra shows the reference (red) peaks from the *in silico* spectral libraries, respectively. .... 139
- Figure A2 A) Western blot analysis of p53 protein post-DHHC2 transfection compared with a Ctrl in HEK-293T cell line. B) Statistical representation of relative fold change expression of p53 protein post-DHHC2 transfection compared to Ctrl. C) Relative MDM2-mRNA fold change expression post-DHHC2 overexpression compared with Ctrl in HEK-293T cell line. Samples were normalized with the endogenous control GAPDH (n=3)..... 140
- Figure A3 Verify 3D plot: The plot predicts 72.69% of the residues in mutant EGFR C7S have an averaged 3D-1D score > 0.1. .... 141
- Figure A4 ERRAT server analysis. Graphics show the overall quality factor of the mutant EGFR C7S protein..... 141

## List of tables

### ❖ Chapter 2

- Table 2.1 The best 24 natural molecules interacting with Cys 156\*\_DHHC20 with binding energy higher than 2-BP (-7.0 kcal/mol) obtained *via* molecular docking. .... 58
- Table 2.2 Lists the mean RMSD, Rg, and SASA scores of DHHC20 protein in complex with ligands. .... 64
- Table 2.3 Lists the energy components obtained for protein-ligand complexes..... 65

- Table 2.4 Lists the physicochemical characteristics of lutein, 5-hydroxyflavone, ..... 70
- Table 2.5 Lists the ADMET characteristics of lutein, 5-hydroxyflavone, and 6-hydroxyflavone. .... 71
- Table 2.6 Lists the biological activities associated with lutein, 5-hydroxyflavone, and 6-hydroxyflavone. .... 74

### ❖ Chapter 3

- Table 3.1 List of primers used in mRNA expression analysis using qRT-PCR. .... 83
- Table 3.2 Lists the classification of metabolites into the 6 super-compound classes through MetaboAnalyst 5.0. .... 90
- Table 3.3 List of 45 metabolites having VIP score > 0.7 identified through VIP-multivariate analysis. .... 94
- Table 3.4 List of the significantly altered pathway in DHHC2-KD group identified *via* MetaboAnalyst 5.0. .... 101
- Table 3.5 List of the significantly altered pathway in DHHC2-OE group identified *via* MetaboAnalyst 5.0. .... 105

### ❖ Chapter 4

- Table 4.1 The 6 DHHC isoforms interacting with Cys7-EGFR identified through H-Dock-based molecular docking. .... 119
- Table 4.2 Lists the average RMSD, Rg, and SASA scores obtained for EGFR and EGFR C7S in complex with DHHC isoforms. .... 127
- Table 4.3 Lists the energy components obtained for DHHC isoforms in complex with EGFR and EGFR C7S. .... 128

### ❖ Appendix

- Table A1 Summarizing the role of 23 DHHC isoforms in cancer progression and prevention. .... 143
- Table A2 Binding energy of natural molecules docked with DHHC20 (6BML) generated *via* PyRx based molecular docking. .... 146

➤ Table A3 (A) Predicated molecular targets of Lutein <i>via</i> Swiss Target Prediction.	173
➤ Table A3 (B) Predicated molecular targets of 5-hydroxyflavone <i>via</i> Swiss Target Prediction.....	184
➤ Table A3 (C) Predicated molecular targets of 6-hydroxyflavone <i>via</i> Swiss Target Prediction.....	195
➤ Table A4 List of total 73 metabolites identified across DHHC2 overexpression, knockdown and Ctrl conditions <i>via</i> MS-DIAL based spectral matching from the reference libraries .....	208





# Chapter 1: Introduction and literature review

---

## **1.1 Introduction: Protein *S*-palmitoylation:**

Post-translational modifications (PTMs) encompass alterations in the amino acids side chain of proteins after their synthesis. Till now, more than 400 types of PTMs that play a crucial role in regulating various cellular processes have been identified [23, 24]. These modifications significantly impact protein structure and function. However, disruptions in PTMs, including methylation, ubiquitination, and protein lipidation, can lead to dysfunction in essential biological processes and contribute to the progression of multiple diseases [3, 25].

One of the well-reported PTM is protein lipidation, which involves the utilization of lipids, one of the four major biomolecules, as a critical substrate [26]. In the cellular system, lipids are fundamental components in forming cellular boundaries (membranes), essential for cell survival and proliferation [27-29]. The organization of cellular materials within these membrane structures necessitates efficient communication with the extracellular environment and among membrane organelles facilitated by cell signaling and membrane trafficking [29-31]. Nature facilitates the efficient coordination of these processes by lipid-mediated regulation of membrane-protein interactions through two mechanisms [29, 32]. The first strategy is in which a few specific proteins have evolved to bind to particular lipid molecules selectively. Examples include pleckstrin homology domains recognizing specific phosphoinositides and blood clotting factors recognizing phosphatidylserine, present exclusively in the inner leaflet of the plasma membrane. [29, 33-36]. The second prevalent interaction strategy involves the covalent modification of proteins through lipid molecules [29, 37]. Adding a lipid molecule to proteins imparts distinct characteristics, including hydrophobicity and structural stability [1, 38, 39]. The three most common protein-lipid modifications are palmitoylation, prenylation, and myristoylation. Over the past decade, intensive research has been done on the enzymes responsible for prenylation, myristoylation, and identifying target sequences for these modifications [40-42]. However, compared to prenylation and myristoylation, palmitoylation has been relatively understudied [43]. *S*-

palmitoylation, also referred to as *S*-acylation, involves the formation of a thioester bond between a cysteine (Cys) thiol side chain of protein and the saturated and unsaturated long-chain fatty acids with different carbon contents, including myristic acid (C14:0), arachidonic acid (C20:4), palmitoleic acid (C16:1), stearic acid (C18:0), palmitic acid (C16:0), oleic acid (C18:1), and eicosapentaenoic acid (C20:5) [44]. Notably, the prevalence of palmitic acid over other fatty acids contributes to protein *S*-acylation, commonly known as protein *S*-palmitoylation [45].

Biochemically *S*-palmitoylation catalyzed by palmitoyl acyl transferase (PAT), also known as DHHCs, due to the highly conserved Asp-His-His-Cys (D-H-H-C) tetrapeptide motif essential for catalysis, has garnered significant attention in the last two decades [13, 46-48]. This heightened interest is attributed to the instability of the thioester bond, making it the only reversible lipidation process. Additionally, DHHCs exhibit a diverse distribution within cells and play various roles in cellular functions, including protein trafficking, localization, cellular signaling, meiosis, massive endocytosis, and interactions with pathogens [49]. However, the participation of DHHCs in several cellular processes has led to the progression of various diseases, including cancer, autoimmune disorders, and infections. Also, it has been implicated in a variety of neurodegenerative and neurodevelopmental disorders, including Schizophrenia, Alzheimer's disease, Huntington's disease, and cranial nerve diseases, with several notable studies shedding light on its role [7, 50, 51]. For example, a study disclosed that the DHHC21<sup>T209S</sup> variant exacerbates synaptic dysfunction and cognitive impairment in Alzheimer's disease by increasing the palmitoylation of protein kinase FYN and A $\beta$  precursor protein (APP) [52]. Additionally, DHHC2 has been linked to an increased risk of Schizophrenia [53]. Recently, DHHC15 has emerged as a candidate gene for autism spectrum disorder [54]. In addition to neurological disorders, DHHC enzymes play crucial roles in facilitating pathogenic infections by modifying various proteins. Since the discovery of palmitoylated glycoproteins of Vesicular stomatitis virus and Sindbis virus in 1979, many other palmitoylated viral proteins have been identified [55]. These include the spike protein of SARS-CoV-2, where research has shown inhibition of cell-cell syncytia formation and decrease in the SARS-CoV-2 infectivity by

blocking DHHC-mediated *S*-palmitoylation of the Spike protein [56, 57]. Other examples encompass hemagglutinin of influenza virus, the protein G of Vesicular Stomatitis virus, nonstructural protein 2 of Hepatitis C virus, and the fusion protein of the measles virus [57-63]. Apart from mammalian viruses, palmitoylation of proteins is critical in viruses infecting aquatic animals and plants, affecting viral replication, protein localization, and other related functions. Research has shown that exogenous palmitic acid promotes red-spotted grouper nervous necrosis virus (RGNNV) infection; consequently, disrupting palmitoylation inhibits RGNNV replication [64]. Also, *S*-palmitoylation plays a crucial role in bacterial infections, where pathogenic bacteria exploit the host cell's palmitoylation machinery to enhance their entry, survival, and replication within cells [57, 65]. Despite identifying over 5000 palmitoylation substrates and ongoing research revealing various disease implications [66], *S*-palmitoylation remains relatively mysterious compared to other lipidation processes. This is primarily due to factors such as the limited sensitivity of current analytical methods and the absence of a clear crystal structure for every DHHC.

Apart from the above-delineated diseases, the connection between DHHC enzymes and cancer is an area of growing research interest. Cancer, which is a predominant contributor to global mortality, resulted in nearly 10 million deaths in 2020, with projections estimating an increase to 16.3 million by 2040 [67]. This disease is marked by continual cell proliferation, sustained angiogenesis, resistance to apoptosis, and increased cellular invasion [4, 68, 69]. These characteristics are often accompanied by alterations in cellular metabolism, genome instability, replicative immortality, sustained inflammation, and immune suppression [69, 70]. Many of these processes are regulated by various tumor suppressors and oncogenes, a significant number of which undergo modification through *S*-palmitoylation, such as epidermal growth factor receptors (EGFR), protein kinase B (AKT), and transcription factors (e.g.,  $\beta$ -catenin) thereby promoting tumor growth and progression [5, 71, 72]. Consequently, enzymes involved in palmitoylation or palmitoylated proteins are promising targets for cancer therapy. Therefore, in the subsequent sections will briefly discussed the enzymes involved in *S*-palmitoylation and



depalmitoylation, followed by their catalytic mechanisms and involvement in cancer advancement. Lastly, we discussed the difficulties associated with DHHC-targeting inhibitors and briefly described current research efforts to overcome these challenges.

### **1.1.1 Discovery and mechanism of DHHCs:**

The recognition of *S*-palmitoylation dates back to the early 1970s, with uncertainty prevailing about whether it occurred spontaneously or through enzymatic processes. A significant breakthrough in 2002 unveiled the first PAT in *Saccharomyces cerevisiae*, Erf2p/Erf4p, which played a crucial role in Ras function [73]. Simultaneously, another yeast PAT, Akr1p, was identified through phenotypic analysis. Akr1p catalyzed the palmitoylation of Yck2p, both *in vitro* and *in vivo* [74-76]. Akr1p and Erf2p were integral membrane proteins with multiple transmembrane domains (TMDs) and shared a common DHH/YC-CRD (Asp-His-His/Tyr-Cys-Cys rich domain) between two TMDs [77]. Mutations in the DHH/YC motif of both proteins resulted in the loss of *S*-acylation activity and emphasized the criticality of this motif in the palmitoylation process. Further exploration of the yeast genome led to the identification of five other potential PATs, namely Akr2p, Pfa4p, Swf1p, Pfa3p, and Pfa5p [78-81]. Examination of translated genome databases revealed the presence of 7 DHHC proteins in *Saccharomyces cerevisiae*, 22 in *Drosophila melanogaster*, 5 in *Schizosaccharomyces pombe*, 24 in *Arabidopsis thaliana*, 15 in *Caenorhabditis elegans* and 23 in *Homo sapiens* [82, 83]. DHHC genes are denoted as zDHHC1 to zDHHC24 in mammalian genomes, except for zDHHC10. The prefix "Z" signifies the presence of two zinc ions associated with the DHHC-CRD in the CCHC zinc-finger domains. These zinc ions play a crucial structural role by aligning the active-site cysteine nucleophile, which is vital for catalytic function [84].

In 2018, the first crystal structures of two DHHCs, a catalytically inactive mutant of zebrafish DHHC15 (zfDHHS15), and human DHHC20 (hDHHC20) were discovered [85]. The structural analysis of DHHC20 in complex with 2-Bromopalmitic acid (2-BP) revealed a tepee-like arrangement of four TM helices, with the CRD and the C-terminus extending into the cytosol. These structures displayed significant interactions between the C-terminal domain,

CRD, and four TM [85]. However, according to structural topology algorithms, some DHHC members might deviate from the conventional four TM helices architecture. For example, DHHC13 and 17 are anticipated to have six TMDs based on the experimentally determined topology of Akr1 [86]. Nevertheless, the TM topologies of other DHHC members are yet to be experimentally established, posing an intriguing and open question. Notably, the DHHC-CRD consistently positions itself on the cytosolic side, thereby confining DHHC PAT-mediated *S*-acylation to the cytosolic environment. Additionally, the structure highlights significant hydrophobic residues on the TM helices and within the DHHC domain that are likely crucial for acyl chain recognition and determining chain-length selectivity [86, 87].

Rana et al. (2018) elucidated the catalytic triad mechanism utilized by DHHC20 in two steps. The first step is auto-acylation, where Asp153 plays a role in polarizing His154 and acts as a base to extract a proton from Cys156. This process converts Cys156 into a thiolate nucleophile [85]. The thiolate form of Cys156 then attacks the carbonyl carbon in the fatty acyl-CoA thioester, forming an auto-acylated DHHC, an intermediate in the catalytic cycle. In the second step, the fatty acyl chain is transferred to a protein substrate, effectively regenerating the DHHC enzyme for another catalytic cycle (**Figure 1.1**) [85]. This pivotal discovery uncovered the catalytic mechanism of DHHC20 and suggested a crucial avenue for targeting DHHCs by identifying inhibitors that disrupt this triad mechanism. However, the crystal structure of the remaining DHHCs remains a captivating and unanswered question in this scientific field.

### **1.1.2 Palmitoylation and depalmitoylation cycling required for cellular physiology:**

One of the most fascinating aspects of *S*-palmitoylation is its reversibility, a process known as protein depalmitoylation involving the removal of thioester-linked long-chain fatty acids from Cys residue in a protein. Despite the numerous known DHHCs, the enzymes identified for depalmitoylation are limited to three classes. These include palmitoyl protein thioesterases -1 and 2 (PPT1 and PPT2), acyl protein thioesterases-1 and 2 (APT1 and APT2),  $\alpha/\beta$  hydrolase domain-containing 17 proteins (ABHD17s) [88-90]. The first

discovered depalmitoylase enzyme is PPT1, which is primarily located in lysosomes and operates through the mannose 6-phosphate receptor pathway [89]. Another enzyme of the PPT family is PPT2, shares 26% resemblance with PPT1. However, their ability to bind substrates differs considerably. Both enzymes required substrates to fit between their  $\beta 3$ - $\alpha A$  and  $\beta 8$ - $\alpha F$  loops, which are located just above their lipid binding sites. Notably, PPT1 has more space between these loops than PPT2, facilitating the binding of fatty acids with bulky or branched head groups in PPT1. In contrast, the confined region between the loops of PPT2 allows it to bind either short ( $<14$  carbons) or long ( $\geq 18$  carbons) fatty acids [91]. APT1, identified as the second significant depalmitoylase enzyme, was initially believed to be confined to the cytosol. However, subsequent studies revealed its presence in various cellular compartments, including the plasma membrane Golgi apparatus, endoplasmic reticulum (ER), mitochondria, and nuclear membrane [92, 93]. Initially noted for its ability to remove radiolabelled palmitate from the  $\alpha$ -subunit of G-proteins [94]. In the wake of this finding, APT2, sharing a 64% structural identity with APT1, was identified, with its primary substrate being growth-associated protein 43 (GAP-43) [95]. Mechanistically, APT2 modifies the lipid bilayer to extract the acyl chain from its substrate and captures it in a hydrophobic pocket for subsequent hydrolysis. This molecular understanding elucidates the complexities of APT2-mediated deacylation across the endomembrane system [96]. The most recent addition to the depalmitoylating enzymes family is the ABHD17s family, discovered through activity-based profiling of palmostatin B (APT1/2 inhibitor) targets, which depalmitoylated and localizes the Neuroblastoma-Ras viral oncogene homolog (N-Ras) to inner cellular membranes [97]. ABHD17 enzymes undergo self-palmitoylation, typically at the N-terminal CRD, essential for their association with the plasma membrane and interaction with substrates. Increasing the expression of ABHD17A-C in primary neurons results in the decreased *S*-palmitoylation of microtubule-associated protein 6 (MAP6), leading to the retention of MAP6 in axons and controlling the microtubule stability [98]. Nevertheless, additional efforts are necessary to investigate the substrate preferences and physiological functions associated with individual isoforms of ABHD17.

In a cellular system, enzymatic depalmitoylation help in maintaining effective membrane targeting by regulating the palmitoylation cycle and has several implications for signaling, and cellular organization. For instance, APT1 catalyzed the depalmitoylation of flotillin-1 (Flot-1), while DHHC19-mediated repalmitoylation of the depalmitoylated Flot-1 prevents insulin-like growth factor-1 receptor (IGF-1R) desensitization due to endocytosis and lysosomal degradation, resulting in sustained and excessive activation of IGF-1R in cervical cancer cells and their proliferation [99]. Another notable example involves the N-Ras protein, which relies on a palmitoylation/depalmitoylation cycle to regulate its subcellular trafficking and oncogenicity. The inhibitor ABD957, targeting the ABHD17 family of depalmitoylases, impairs depalmitoylation of N-Ras and inhibits the growth of N-Ras-mutant acute myeloid leukemia (AML) cells synergistically with mitogen-activated protein kinase kinase (MEK kinase) [100]. In the case of  $\beta$ -catenin, DHHC9-mediated palmitoylation promotes its ubiquitination and degradation, while APT1-induced depalmitoylation increases its abundance and nuclear translocation. Targeting APT1 or inhibiting it with ML348 demonstrated protective effects against kidney fibrosis induced by unilateral ureter obstruction (UUO) or ischemia/reperfusion injury (IRI) in male mice [101]. DHHC7-mediated palmitoylation of Cys108- signal transducer and activator of transcription 3 (STAT3) enhances its membrane recruitment and phosphorylation. However, the APT2-mediated depalmitoylation of p-STAT3 enables it to translocate to the nucleus. Disrupting either process negatively influences T-helper 17 (T<sub>H</sub>17) cell differentiation and alleviates the symptoms of inflammatory bowel disease (IBD), presenting a potential therapeutic strategy [102]. Lastly, a study has shown that nucleotide-binding domain (NBD), leucine-rich repeat (LRR), and pyrin domain (PYD)-containing protein 3 (NLRP3) is palmitoylated by DHHC5 at the LRR domain. This modification facilitates the assembly and activation of the NLRP3 inflammasome. Silencing of DHHC5 disrupts NLRP3 oligomerization and the formation of large intracellular ASC aggregates. Consequently, this leads to the inhibition of caspase-1 activation and Gasdermin D cleavage in both human cells and mice. Furthermore, ABHD17A mediated the depalmitoylation of NLRP3, and mutation in NLRP3 is associated with defective ABHD17A binding and increased palmitoylation. Therefore, targeting

NLRP3 palmitoylation can be a potential therapeutic option for NLRP3 inflammasome-driven diseases [103]. These examples underscore that enzymes involved in adding and removing palmitate contribute to a complex regulatory network that governs the protein function and transport in response to intracellular and extracellular signals and controlling crucial aspects of a cellular system.

#### **1.1.2.1 Crosstalk between protein *S*-palmitoylation and other post-translational modifications:**

Increasing evidence emphasizes that numerous PTMs regulate a protein to influence its biological effects. Notably, along with the depalmitoylation, *S*-palmitoylation harmonized with other PTMs, such as phosphorylation, glycosylation, nitrosylation, etc., to modulate protein dynamics, either facilitating healthy physiological functions or contributing to disease states. For example, a study by Shetty et al. (2023) analysed how these *S*-palmitoylation and phosphorylation harmonize to maintain the mobility of the dopamine transporter (DAT), essential for dopamine reuptake in the brain. Using fluorescence recovery after photobleaching, it was shown that DAT membrane mobility is bidirectionally regulated: conditions that promote phosphorylation or inhibit palmitoylation [e.g., protein kinase C (PKC) activation, or amphetamine treatment] improve mobility while elevating palmitoylation or decreasing phosphorylation (e.g., DHHC2 overexpression or specific mutations) declines mobility. This study highlights how PTMs controls DAT behaviour in brain [104]. Another instance is the activity-regulated cytoskeleton-associated protein (Arc), which is involved in synaptic functions like long-term depression and potentiation (LTD and LTP). Various PTMs, such as phosphorylation by PKC at Ser84 and 90, modulate Arc's function. The phosphomimetic mutations of these sites with glutamic acid prevent Arc-palmitoylation on nearby Cys residues, leading to synaptic weakening. These mutations also disrupt Arc's ability to bind nucleic acids and destabilize its higher-order oligomers. Hence, phosphorylation of Arc potentially limits full LTD expression and mRNA transport between neurons [105].

In obesity, palmitoylation and nitrosation crosstalk play a crucial role. A study demonstrates that obesity reduces caveolin-1 (Cav1) expression in endothelial

cells (ECs), resulting in hyperlipidemia in Cav1 knockout mice while maintaining endothelial function through elevated nitric oxide (NO) levels. Endogenous NO nitrosates the fatty acid translocase CD36 at Cys residues typically palmitoylated, preventing its membrane trafficking and lipid uptake, thus protecting ECs from lipotoxicity and preserving their function [106].

Palmitoylation and nitrosylation also display substantial crosstalk in anxiety disorders of rats. It is reported that high-anxiety rats exhibit low palmitoylation and high nitrosylation in the basolateral amygdala (BLA). Inhibition of palmitoylation using 2-BP induces anxiety-like behaviours in the BLA. Conversely, inhibiting nitric oxide synthase with 7-nitroindazole (7-NI) provides anxiolytic effects. This interplay between palmitoylation and nitrosylation may offer new avenues for anxiety treatments [107].

The ability of S protein to function in SARS-CoV-2 infections depends on glycosylation and palmitoylation. Tien et al. (2022) showed that mutation of the <sup>611</sup>LY<sup>612</sup> motif alters glycosylation and reduces infectivity in SARS-CoV-2 S pseudoviruses produced using a VSV vector. Also, mutations in Cys-rich clusters I and II, vital palmitoylation sites, reduce pseudovirus generation and membrane fusion activity. These findings highlight the significance of glycosylation and palmitoylation in S protein maturation and viral infectivity [108].

Lastly, palmitoylation and myristoylation crosstalk are vital in psychiatric disorders, mainly through proteins like Cyclin Y (CCNY). CCNY, which inhibits LTP in hippocampal neurons, requires myristoylation for its localization to the trans-Golgi network (TGN) and its subsequent palmitoylation required to move from TGN to the synaptic cell surface. These modifications are essential for the inhibitory role of CCNY in synaptic transmission, learning, and LTP [109]. The examples above underline the critical role of PTM crosstalk in regulating protein function, cellular dynamics, and disease mechanisms, demonstrating the need for integrated therapeutic options to reduce the disease burden.

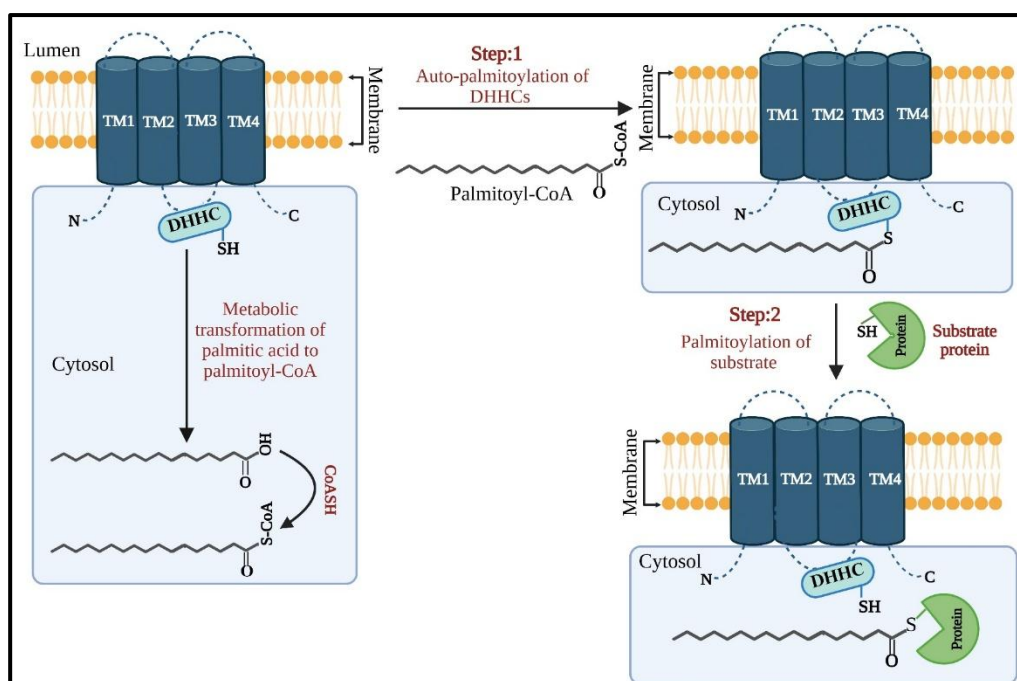


**Figure 1.1** The above figure illustrates the mechanism of action of DHH enzymes. Step 1: Autoacylation - Palmitoyl-CoA provides a palmitate group, which is transferred to the active cysteine site of palmitoyl *S*-acyltransferase (PATs) or DHHs, leading to their auto-*S*-palmitoylation. Step 2: Palmitoyl Group Transfer- The palmitoyl group is then transferred from the palmitoyl-PAT intermediate to the cysteine residue of the substrate protein, forming a thioester bond and thereby modifying the substrate protein (This figure was created using [www.biorender.com](http://www.biorender.com)).

### 1.1.3 DHH isoforms and their association with cancer:

Growing evidence from genetic studies and animal models consistently suggests the participation of palmitoylation in a diverse range of pathological conditions, including neurological, neuropsychiatric disorders, and cancer. Furthermore, extensive data analysis from nearly 150 cancer studies has revealed genomic alterations in various DHHs, potentially contributing to their role in cancer pathology [110]. Notably, the 23 isoforms of DHHs are reported to be associated with cancer, showcasing their involvement in either facilitating anti-carcinogenic effects or promoting oncogenic influences (**Appendix Table A1**). Consequently, the subsequent sections will provide an in-depth discussion of key studies conducted thus far on DHHs, elucidating their associations with cancer.

#### DHHC1

DHHC1 has emerged as a potential tumor suppressor, as evidenced by a study revealing frequent silencing of DHHC1 expression in various tumor cells and specimens due to promoter methylation. The restoration of DHHC1 expression has demonstrated the ability to impede cancer cell progression by promoting

apoptosis and cell cycle arrest, suppressing metastasis, reversing epithelial-mesenchymal transition (EMT), increasing oxidative and ER stress to facilitate pyroptosis for anti-cancer purposes [111]. A recent study showed a correlation between reduced DHHC1 levels in uterine corpus endometrial carcinoma (UCEC), poorer prognosis, and higher cancer cell proliferation [112]. Besides, DHHC1 expression is negatively associated with colorectal cancer progression *in vivo* and *in vitro*. This underlying effect is explained by DHHC1's role in modifying lipase G (LIPG) mRNA stability *via* palmitoylating insulin-like growth factor 2 mRNA binding protein 1 (IGF2BP1) in an m6A-dependent way, hindering lipid storage in cancer cells [113].

## **DHHC2**

DHHC2 was initially identified as REAM (reduced expression in metastasis) due to its association with reduced metastatic potential in various cancers, such as colorectal, ovarian, liver, and lymph node metastasis [114]. One of its critical substrates is cytoskeleton-associated protein 4 (CKAP4), which undergoes palmitoylation required for translocation from the ER to the cell membrane. Palmitoylated CKAP4 acts as a receptor for anti-proliferative factor (APF), triggering a signaling cascade that inhibits the mitogen-activated protein kinase-extracellular signal-regulated kinase (MAPK-ERK) and phosphatidylinositol 3-kinase (PI3K)-AKT pathways vital for cancer cell survival and proliferation [115-117]. Another interacting ligand of CKAP4 is Dickkopf-1 (DKK1), known as a Wnt signaling antagonist, which induces depalmitoylation of CKAP4 and low-density lipoprotein receptor-related proteins 6 (LRP6), leading to their translocation to the non-detergent-resistant membrane (non-DRM) region of the plasma membrane. Ultimately, activation of the PI3K-AKT pathway in cancer cells [118]. Subsequently, two other vital substrates of DHHC2 include transmembrane family members CD9 and CD151. The process of palmitoylation enhances their interaction with  $\alpha 3$ -integrin and various other proteins, leading to the inhibition of EMT and the regulation of cell migration [119]. On the other hand, two recent findings have uncovered the tumor-promoting role of DHHC2 in cancer. The first one indicated that knocking down DHHC2 or inhibiting with 2-BP has been associated with suppression of nuclear factor erythroid 2-related factor 2 (Nrf2) palmitoylation, enhancing anti-cancer immunity *in vitro* and mice-bearing xenograft [120]. Furthermore, the second



study reported that DHHC2-mediated *S*-palmitoylation of acylglycerol kinase (AGK) promotes its translocation to the plasma membrane, activating the PI3K-AKT- mammalian targets of rapamycin (mTOR) signaling pathway in clear cell renal cell carcinoma (ccRCC) (**Figure 1.2**). Also, it influences sensitivity to sunitinib, a multitargeted tyrosine kinase inhibitor [14, 121]. In conclusion, DHHC2 emerges as a promising target for enhancing the effectiveness of sunitinib in treating ccRCC.

### **DHHC3**

DHHC3 has been identified as a critical regulator in cancer, particularly in oxidative stress hindrance and its role as a tumor promoter. To understand how DHHC3 regulates oxidative stress, a comprehensive palmitoyl-proteomic methodology called PalmPISC was employed. Combining global palmitoyl-proteomic techniques with mass spectrometric identification and stable isotope labeling by amino acids in cell culture (SILAC) provided the identification of DHHC3 substrates in prostate and breast cancer cell lines. Notably, 22-28 antioxidant and redox-regulatory proteins, including key proteins such as thioredoxin-related transmembrane protein 3 (TMX3), glutathione peroxidase 8 (GPX8), and peroxiredoxins 1, 4, and 5 (PRDX1, PRDX4, PRDX5) were identified among the substrates. Additionally, the ablation of DHHC3 in combination with chemotherapeutic drug treatment led to a marked increase in oxidative stress and enhanced anti-proliferative activity in breast cancer cell MDA-MB-231 [122, 123]. Another crucial substrate of DHHC3 is programmed death-ligand 1 (PD-L1), which is responsible for immune escape and significantly impacts cancer progression. Inhibiting *S*-palmitoylation of PD-L1 or silencing DHHC3 activated the anti-tumor immunity in mice bearing MC38 tumor cells and *in vitro* [124, 125].

### **DHHC4**

DHHC4 has garnered attention for its relevance in glioblastoma (GBM) and lung adenocarcinoma (LUAD). A recent study unveiled significant insights into the functional interactions between glioblastoma stem cells (GSCs), a highly aggressive subset within GBM, and the glycogen synthase kinase 3- $\beta$  (GSK3 $\beta$ ) in promoting malignant traits. The research revealed that the palmitoylation of Cys14-GSK3 $\beta$  facilitated by DHHC4 enhances the stemness of GBM cells resistant to temozolomide (TMZ) by activating the enhancer of zeste homolog

2- signal transducer and activator of transcription (EZH2-STAT3) signaling pathway (**Figure 1.2**) [126]. This breakthrough provides a novel theoretical framework for understanding the mechanisms driving TMZ resistance and recurrence in GBM treatment. Another investigation used qRT-PCR to establish DHHC4's involvement in LUAD. The results showcased elevated expression levels of DHHC4/12/18/24 in LUAD compared to healthy lung tissues, suggesting its potential connection with the tumor microenvironment in LUAD [127]. However, identifying additional targets of DHHC4 is imperative for a more comprehensive understanding of its role in cancer.

### **DHHC5**

DHHC5, like its counterpart DHHC4, has been extensively studied in the context of LUAD and GBM cancers. In LUAD, DHHC5 showed elevated expression at both the mRNA and protein levels, correlating with an unfavorable prognosis. The research described inner centromere protein (INCENP), a nuclear protein, as a pivotal link connecting the LUAD stem gene network with DHHC5. Furthermore, immunofluorescence validation substantiated the nuclear localization of DHHC5 in the A549 cell line. This finding elucidates the functional role of *S*-palmitoylation on INCENP and advocates for DHHC5 inhibition as a potential strategy against cancer stem cells in LUAD [128].

Regarding GBM, DHHC5's significance is underscored by two crucial findings. Firstly, DHHC5 was identified as a mediator of palmitoylation at Cys456-focal adhesion kinase (FAK), a protein critical for cell proliferation, invasion, and EMT [129]. The second discovery revolves around the interaction between mutant p53 and DHHC5. The investigations uncovered that mutant p53 transcriptionally upregulates DHHC5 and the nuclear transcription factor-Y (NF-Y), which contribute to the alterations in the phosphorylation and palmitoylation status of the tumor suppressor EZH2 and glioma development [130]. This research positions DHHC5 as a potential therapeutic target for managing p53-mutated cancers.

### **DHHC6**

Concerning DHHC6 and cancer, a study by Shan et al. (2024) showed that DHHC6 promotes *S*-palmitoylation of peroxisome proliferator-activated receptor gamma (PPAR $\gamma$ ) within its DNA binding domain, thus enhancing

PPAR $\gamma$ 's stability and diminishing its vulnerability to destabilization. This modification protects PPAR $\gamma$  from degradation mediated by lysosomes and facilitates its transport to the nucleus. Also, the study revealed that DHHC6 enhances fatty acid biosynthesis and facilitates colorectal cancer development, suggesting a mechanism in which DHHC6 supports tumor growth by palmitoylating and stabilizing PPAR $\gamma$ , hence promoting fatty acid synthesis in colon cancer [131]. This research outlines a possible therapeutic approach aimed at fatty acid synthesis, potentially advantageous for individuals exhibiting heightened DHHC6 expression in colorectal carcinoma.

### **DHHC7**

DHHC7, like other DHHC enzymes, play crucial roles in the progression and prevention of various cancer types due to its diverse range of substrates. For instance, in the MCF-7 cell line (breast cancer), DHHC7 and DHHC21 were responsible for localizing progesterone receptor (PR), estrogen receptor and androgen receptor (AR) at the plasma membrane. Knocking down DHHC7 or DHHC21 hindered the membrane trafficking of AR, PR, estrogen receptor and rapid signaling in cancer cells [132]. In HepG2 cells, DHHC7-mediated palmitoylation boosts the expression of STAT3 targeting gene *hypoxia-inducible transcription factor A (HIF1A)*, encoded HIF1 $\alpha$ . On top of that, the stabilization of HIF1 $\alpha$  by cyclin-dependent kinase 5 (CDK5) creates a positive feedback loop between DHHC7, STAT3, and HIF1 $\alpha$ , enhancing the growth of hepatocellular carcinoma (HCC) cells *in vivo* [133]. Kong et al. (2023) explored the landscape of protein palmitoylation in human cancers. They revealed that abnormal DNA methylation and myelocytomatosis oncogene (MYC)-driven transcription contribute to the deregulation of palmitoylation-related genes, affecting key cancer pathways and tumorigenesis. The study identified DHHC7 and DHHC23 as crucial regulators of mTOR signaling, DNA repair, and immune responses, emphasizing their roles in tumor development. Additionally, BI-2531, etoposide, and piperlongumine were identified as potential modulators of palmitoylation, suggesting new therapeutic strategies [134].

In contrast to the above finding, a research study has reported that DHHC7 hindered cancer progression. The study shown that depleting DHHC7 increases the oncogenic properties of prostate cancer (PCa) cells *via* upregulating the AR

protein level. Conversely, restoring DHHC7 was sufficient to suppress the proliferation and invasion of PCa cells *in vitro* and mitigate xenograft tumor growth *in vivo*. However, due to the constantly evolving list of DHHC substrates, determining their precise role in cancer pathophysiology is challenging [135].

### **DHHC8**

The function of DHHC8 in cancer was unknown prior to 2024. However, in 2024, a critical study found that ferroptosis resistance during GBM is dependent on DHHC8-mediated *S*-palmitoylation of solute carrier family 7 member 11 (SLC7A11), which protects SLC7A11 from ubiquitination. Mechanistically, AMP-activated protein kinase (AMPK $\alpha$ 1) directly phosphorylates DHHC8 at the Ser299 site to support the interaction between DHHC8 and SLC7A11. This interaction promotes SLC7A11 *S*-palmitoylation and subsequent deubiquitination, contributing to the resistance mechanism [136].

### **DHHC9**

In the context of DHHC9 and its involvement in cancer, numerous studies have detailed its role as a tumor promoter through various mechanisms, some of which are outlined below. For instance, one study revealed that DHHC9 contributed to the elevation of PD-L1 by impacting the interferon- $\gamma$  (IFN- $\gamma$ )-induced Janus kinase (JAK)-STAT1 signaling pathway and suppressing cluster of differentiation 8 (CD8<sup>+</sup>) T mediated cell-toxicity in colon cancer [137, 138].

In bladder cancer, specific protein 1 (SP1) was shown to activate DHHC9 transcriptionally. Subsequently, DHHC9 palmitoylated the binding immunoglobulin protein (Bip) protein at Cys420, inhibiting the unfolded protein response (UPR). This palmitoylation enhances Bip's stability and maintains its localization in the ER and supports tumor proliferation [139]. Ras genes are mutated in approximately 20% of human cancers [140], and the mechanisms of Ras-mediated signaling are still being explored. Concerning this, it has been discovered that DHHC9-mediated palmitoylation of Cys residues in the C-terminal hypervariable regions of Harvey Ras viral homolog (H-Ras) and N-Ras is crucial for Ras signaling in complex with its accessory Golgi complex-associated protein of 16 kDa (GCP16) protein. The cryo-electron microscopy structures of DHHC9-GPC16 complex revealed that phospholipid binding to an arginine-rich region of DHHC9

and palmitoylation at three residues (Cys 24, Cys 25, and Cys 288) is essential for the catalytic activity of the DHHC9-GCP16 complex. Additionally, GCP16 forms complexes with DHHC14 and DHHC18 to facilitate Ras palmitoylation [141]. Apart from the above-findings, DHHC9 is a crucial regulator of the Warburg effect by activating lactate dehydrogenase A (LDHA). This study proved that DHHC9-mediated palmitoylation of Cys163-LDHA is increased in cancer. Palmitoylation of LDHA enhances lactate production while decreasing reactive oxygen species (ROS) generation. Substituting endogenous LDHA with palmitoylation-deficient mutant results in reduced proliferation of pancreatic cancer cells, increased T-cell infiltration, and restricted tumor growth (**Figure 1.2**) [142]. Moreover, aside from exacerbating cancer, DHHC9 has been associated with neuropathic cancer pain (NCP), a significant symptom in cancer patients. It was reported that DHHC9 is upregulated in NCP through palmitoylation of apelin receptor (APLNR). Subsequently, palmitoylated APLNR protects DHHC9 from lysosomal degradation, maintaining its stability and promoting enhanced morphine tolerance in mouse models (**Figure 1.2**) [143]. Consequently, targeting APLNR palmitoylation, combined with morphine, emerges as a potent approach for treating cancer-related pain.

### **DHHC11**

Burkitt lymphoma (BL) is a highly curable form of non-Hodgkin lymphoma primarily diagnosed in young children. DHHC11 has been identified as a critical BL progression marker by forming a novel network with MYC, micro-RNA-150 (miR-150), DHHC11B, and v-MYB avian myeloblastosis viral oncogene homolog (MYB). The research revealed that MYC plays a vital role in maintaining elevated levels of MYB, which is crucial for the rapid proliferation of BL cells. It occurs through two mechanisms: the first one is the downregulation of miR-150 through MYC and the releasing of MYB from miR-150-mediated repression. The second mechanism involves induction of DHHC11 and DHHC11B through MYB, to maintain its high level [144, 145]. Apart from BL, DHHC11 has also been identified as a critical colorectal cancer (CRC) promoter through transcriptome analysis and immunoprecipitation. The study shows that heterogeneous nuclear ribonucleoprotein (hnRNP) G-T stabilizes 174 mRNAs, including DHHC11 mRNA. Transfection of DHHC11 siRNA leads to suppressed cell growth, and hnRNP G-T siRNA decreases both

mRNA and protein expression of DHHC11 [146]. These results suggest that hnRNP G-T promotes CRC cell growth by regulating DHHC11 mRNA, making it a promising therapeutic target in CRC therapy. In contrast to the above-described studies, a research reported that DHHC11B inhibits proliferation, migration, and invasion of LUAD cells and induces apoptosis. In addition, western blot analysis revealed the inhibition of molecular markers of EMT under DHHC11B overexpressed conditions [147].

## **DHHC12**

GBM stands out as one of the most aggressive brain tumors, and although various investigations have explored the involvement of multiple DHHCs in GBM progression. Nevertheless, the understanding of its pathogenesis remains limited. Notably, DHHC12 has emerged as one of those PATs linked to GBM progression, supported by two key findings. Firstly, analysis of Genotype-Tissue Expression (GTEx) and The Cancer Genome Atlas (TCGA) databases revealed significantly elevated DHHC12 expression in GBM compared to normal brain tissue ( $P$  value  $< 0.01$ ). Knockdown of DHHC12 in GBM cell lines (U87 and U251) led to decreased yes-associated protein 1 (YAP1) level and alterations in EMT-related markers. Restoring YAP1 reversed the changes induced by DHHC12 knockdown, and tissue analysis further confirmed a positive correlation between DHHC12 and YAP1 expression, emphasizing the relevance of the DHHC12/YAP1 axis in GBM progression [148]. Secondly, mechanistic insights demonstrated that DNA hypomethylation increased DHHC12 mRNA expression and correlated with poor prognoses in GBM [149]. These findings underscore the association of DHHC12 with GBM-promoting characteristics and its poor prognosis. Besides, the TCGA ovarian cancer data indicated that among DHHCs, the DHHC12 expression was markedly high and strongly correlated with ROS pathways. Further transcriptomics analyses of the SNU119 cell and ovarian cancer data set linked DHHC12 to mitochondrial oxidative metabolism and ROS regulation pathways. Markedly, DHHC12 inhibition improved cisplatin anti-tumor effectiveness in ascites-derived organoid line of platinum-resistant ovarian cancer and an ovarian cancer xenograft model [150]. DHHC12 also contribute to ovarian cancer through its interaction with a membrane protein claudin-3 (CLDN3), crucial for tight junction formation. In ovarian cancer, DHHC12-mediated *S*-palmitoylation of

CLDN3 was found to regulate its stability and localization, ultimately promoting tumorigenesis (**Figure 1.2**) [151].

### **DHHC13**

In the context of DHHC13, it is reported that phosphorylation of DHHC13 by AMPK at Ser208 was identified as a mechanism that promotes melanocortin 1 receptor (MC1R) activation and suppresses melanocyte transformation. This study suggested that activating AMPK could prevent melanoma, particularly in individuals with red hair [152].

### **DHHC14**

It is reported that prostate cancer and testicular germ cell tumor samples have decreased protein and RNA levels of DHHC14. Intriguingly, experiments involving inducible overexpression of DHHC14 demonstrated increased apoptosis through the classic caspase-dependent apoptotic pathway. Additionally, heterozygous knockout of DHHC14 resulted in an enhanced ability for cell colony formation [153]. However, in contrast, the qRT-PCR analysis showed overexpression of DHHC14 mRNA in 27% of the gastric cancer tissue samples compared to normal non-neoplastic gastric mucosa. Knockdown of DHHC14 in gastric cancer cells led to decreased invasiveness and downregulation of matrix metalloproteinase (MMP-17) mRNA. The forced expression of DHHC14 activated the invasion and migration of gastric cancer cells *in vitro* [154]. These findings collectively indicate that DHHC14 plays a complex role, acting as a tumor suppressor in some cancers, such as prostate cancer and testicular germ cell tumors, while functioning as a promoter in gastric cancer.

### **DHHC15**

Discussing the diverse glioma-associated datasets, a study delved into the expression patterns and potential biological functions of DHHC15 in glioma. The investigation uncovered a notable upregulation of DHHC15 expression in glioma, showing a positive correlation with malignant phenotypes. Analyses of Gene Ontology (GO) and the Kyoto Encyclopedia of Genes and Genomes (KEGG) highlighted DHHC15's involvement in regulating cell cycle and migration. The study demonstrated that the knockdown of DHHC15 hindered glioma cell proliferation and migration. Additionally, the result from the GESA

analysis indicated the association between DHHC15 and STAT3 signaling [155].

In previous preclinical studies, local anesthetics were observed to inhibit tumor activities directly, though the underlying mechanism remained unclear. Fan et al. (2021) uncovered a novel mechanism by which local anesthetics impact the malignant phenotype of glioma. The finding suggested local anesthetics could diminish DHHC15 transcripts, reducing glycoprotein 130 (GP130) palmitoylation and its membrane localization. This inhibition, in turn, suppresses the interleukin-6 (IL6)-STAT3 signaling in glioma progression [156]. This discovery is a valuable reference for further exploring the connection between palmitoylation and commercially available local anesthetics in cancer research.

### **DHHC16**

DHHC16 plays a significant role in HCC. It is reported that DHHC16-mediated palmitoylation at Cys600- proprotein convertase subtilisin/kexin type 9 (PCSK9) leads to lysosome-mediated tensin homolog (PTEN) degradation and subsequent AKT activation. The research team has also developed a biologically active peptide derived from PCSK9 that competitively inhibits PCSK9 palmitoylation. This inhibition suppresses phosphorylation of AKT and enhances anti-tumor effects in HCC [157].

### **DHHC17**

Phosphorylation, a widely recognized PTM, is known for its role in the abnormal activation of the MAPK pathway in cancer [158]. Despite attempts to target phosphorylation to control MAPK activation, success has been limited. Therefore, exploring other PTMs associated with MAPK activation is a prominent strategy for combating cancer. In this context, a research study has uncovered that DHHC17 interactions with MAP2K4 and p38- c-Jun N-terminal kinases (JNKs) establish a crucial signaling module for MAPK activation and glioma progression [11]. In cerebral cancer, the DHHC17 mediated S-palmitoylation of octamer-binding transcription factor 4A (Oct4A, transcription factor required for proliferation, and differentiation of stem cells) is essential for maintaining the stability by protecting it from lysosomal degradation. Furthermore, the palmitoylation of Oct4A promotes the interaction between



Oct4A and sex determining region Y-box 4 (SOX4) in the sex determining region Y-box 2 (SOX2) enhancer region, supporting the ability of GSCs to self-renew and their potential to cause tumors [159]. Also, DHHC17 and DHHC24 have been identified as contributors to the palmitoylation of AKT, exerting oncogenic effects in liver tumorigenesis [160]. Hence, these studies offer insights into potential strategies for regulating the diverse forms of PTMs and their associated pathways in the context of cancer.

### **DHHC18**

The precise role of DHHC18 in cancer remains incompletely understood; recent research has proposed a potential involvement where DHHC18, along with DHHC23, targets GSCs within GBM to regulate cellular plasticity. Furthermore, in-depth mechanistic investigations have unveiled that DHHC18 and DHHC23 interact with B cell-specific Moloney murine leukemia virus integration site-1 (BMI1), E3 ligase, and ring finger protein144A (RNF144A) protein. This interaction regulates the polyubiquitination and accumulation of BMI1, thereby influencing the transition of GSCs in GBM and promoting cell survival under challenging tumor microenvironment conditions [161]. This study shed light on a potential mechanism through which DHHC18 and DHHC23 regulate cancer plasticity and worsen cancer prognosis.

### **DHHC19**

Osteosarcoma (OS) stands out as the most common malignant primary bone tumor affecting children and young adults. In the context of OS and DHHCs, a study conducted by Liang et al. (2022) revealed that DHHC19 is a direct target of miR-940. The overexpression of DHHC19 was shown to partially counteract the suppression of migration, proliferation, and invasion induced by miR-940. Bioinformatics analysis and rescue experiments confirmed that the pro-oncogenic effect of miR-940/DHHC19 axis is regulated through the Wnt- $\beta$ -catenin pathway. This finding highlighted the miR-940/DHHC19 axis as a novel target for OS treatment [162].

Another study indicated that DHHC19 is associated with a poor prognosis and immune infiltration in patients with kidney renal clear cell carcinoma (KIRC) [163]. However, further in-depth investigation into the role of DHHC19 in KIRC is warranted to design successful therapeutic strategies.

## **DHHC20**

DHHC20 has been linked to poor prognosis in various cancer types, including breast, ovarian, lung, and prostate cancers. The mRNA and clinical data from liver hepatocellular carcinoma (LIHC) patients in the TCGA and International Cancer Genome Consortium (ICGC) databases disclosed that those with high palmitoylation metabolism-related signature (PMS) had a poorer prognosis and elevated expression of immune checkpoints. In SMCC-7721 and HepG-2, si-DHHC20 improved apoptosis and reduced proliferation compared to si-NC, emphasizing a tumor-promoting role of DHHC20 in LIHC [164]. Recently, Tomic et al. (2024) showed that DHHC20 deletion significantly reduces the metastatic capacity of pancreatic ductal adenocarcinoma (PDAC) cells, especially in the liver and lungs, while not affecting initial tumor growth. In addition, the study showed that in mice with impaired immune systems, DHHC20 knockout (KO) cells can still develop tumors. However, tumorigenicity is decreased in immunocompetent mice, probably due to interactions with natural killer (NK) cells. As an outcome, researchers discovered putative DHHC20 protein substrates that might interact with NK cells and other immune system components and could be accountable for this decline. This study indicates that an alternative strategy to prevent PDAC metastasis includes focusing on DHHC20 or its substrates [165]. Furthermore, it has been shown Kirsten rat sarcoma viral oncogene homolog (K-Ras) mutations can activate DHHC20-mediated *S*-palmitoylation of YTH domain-containing family protein 3 (YTHDF3). This modification accumulates MYC and promotes the development of PDAC by restricting YTHDF3 from localizing to lysosomes and degrading [166].

## **DHHC21**

Previously, it was reported that increased fatty acid synthase (FASN) expression promotes the synthesis of endogenous palmitate, potentially elevating palmitoylation. Conversely, inhibitors of FASN have been shown to reduce the palmitoylation of specific proteins in various cancer types [167, 168]. Notably, a reverse loop of palmitoylation and FASN has been identified, where DHHC21-mediated palmitoylation of Cys317-FASN impedes its stability and fatty acid synthesis. Remarkably, the FDA-approved compound lanatoside C interacts with DHHC21, enhancing DHHC21 protein stability and reducing

FASN expression, ultimately suppressing diffuse large B-cell lymphoma (DLBCL) growth *in vitro* and *in vivo* [169]. This discovery suggests that targeting the DHHC21/FASN axis could be a promising therapeutic strategy against DLBCL.

In contrast to the study highlighting DHHC21 as a tumor suppressor, an investigation revealed its role as a tumor promoter in AML cells through the palmitoylation of mitochondrial adenylate kinase 2 (AK2). This palmitoylation led to the activation of oxidative phosphorylation (OXPHOS) in leukemic blasts. Interestingly, targeting DHHC21 suppressed OXPHOS, eradicating AML blasts and enhancing the efficacy of chemotherapy in relapsed/refractory leukemia (**Figure 1.2**) [170]. These findings underscore the dynamic nature of DHHC21 in different cancers, providing new insights into the biological function of DHHC21 in cancer regulation.

### **DHHC22**

Before 2022, there was no available information regarding the involvement of DHHC22 in cancer. However, for the first time, J. Huang et al. (2022) unveiled that DHHC22 functions as a tumor suppressor in breast cancer by influencing the stability of mTOR. The proposed mechanism involves DHHC22-mediated palmitoylation of mTOR, which impedes its stability and reduces the activation of the AKT signaling pathway. Introducing DHHC22 through ectopic expression restored sensitivity to tamoxifen therapy in MCF-7R cells [171].

### **DHHC23**

The three studies below collectively support the role of DHHC23 as a tumor promoter. The first report identified intricate interactions between miRNAs and mRNAs within a regulatory network in esophageal cancer, drawing from TCGA and the Gene Expression Omnibus (GEO) database. The study highlighted that miR-132-3p/cullin-associated and neddylation-dissociated 1(CAND1)/DHHC23 and miR-576-5p/aryl hydrocarbon receptor (AHR) constitute critical molecular pathways associated with the radiosensitivity of esophageal cancer [172].

In the second study, through TCGA, Rembrandt databases and validation through cell-based experiments reveal aberrant expression of five DHHCs (DHHC11, DHHC12, DHHC15, DHHC22, and DHHC23) in glioma. These

DHHCs are suggested to exert their effects through the PI3K-AKT signaling pathway [173]. Furthermore, inhibition of DHHCs with 2-BP suppresses glioma cell viability while promoting apoptosis. Significantly, targeting DHHCs also enhances the sensitivity of glioma cells to TMZ chemotherapy [173]. This study proposed that targeting tumor-promoting DHHCs could be a crucial strategy in overcoming the challenges of drug resistance and potentially contributing to treating various cancers, particularly glioma.

Lastly, DHHC23 is responsible for palmitoylating plant homeodomain finger protein 2 (PHF2), promoting the ubiquitin-dependent degradation of PHF2. This research elucidated the role of PHF2 as a tumor suppressor, where it acts as an E3 ubiquitin ligase targeting sterol regulatory element-binding protein 1c (SREBP1c), a key transcription factor in regulating lipogenesis. Therefore, further exploration of the SREBP1c/PHF2 axis holds promise for mitigating the progression of HCC [174].

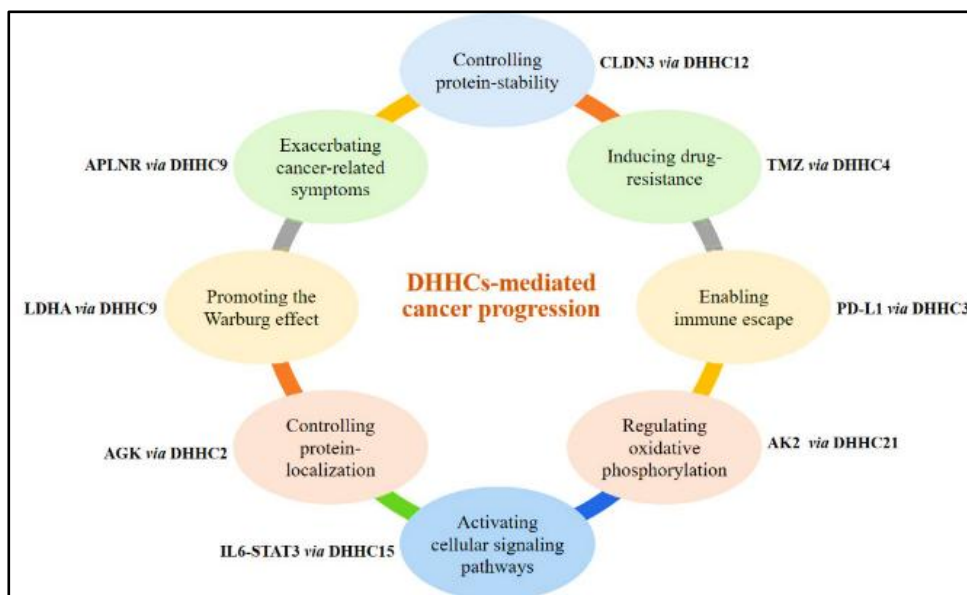


**Figure 1.2** DHHC enzymes play a multifaceted role in cancer progression by influencing various crucial activities that support cancer growth. For example, DHHC3-mediated palmitoylation of PD-L1 prevents its degradation, aiding immune escape. DHHC12 influences protein stability, such as CLDN3 in ovarian cancer. DHHC2 promotes the localization of proteins like AGK in clear cell carcinoma. DHHC15 activates cancer-related signaling pathways, like IL-6-STAT3, through GP130 palmitoylation. DHHC9 enhances the Warburg effect by increasing lactate production and reducing ROS via LDHA palmitoylation, and it also exacerbates cancer symptoms by upregulating APLNR. DHHC21 activates oxidative phosphorylation in leukemia, and DHHC4 contributes to TMZ resistance by facilitating GSK3 $\beta$  palmitoylation in GBM cells.

#### **1.1.4 S-palmitoylation and depalmitoylation targeting inhibitors:**

The literature discussed above highlights that the enzymes responsible for adding and removing palmitate play crucial roles in a complex regulatory network that governs protein function and its role in disease progression and prevention. Numerous researchers have made significant efforts to develop chemical modulators targeting DHHCs and protein depalmitoylase to maintain the delicate balance of S-palmitoylation and depalmitoylation cycling. The key findings from these efforts are summarized in this section.

##### **1.1.4.1 S-palmitoylation targeting inhibitors:**

The aforementioned investigations indicated the promising potential of DHHC-mediated S-palmitoylation as targets for anti-tumor therapies. The discovery of DHHC inhibitors is categorized into lipid and non-lipid-based types. Lipid-based inhibitors included 2-BP (**Figure 1.3A**), tunicamycin (**Figure 1.3E**), and cerulenin (**Figure 1.3C**) analogs, 2-BP being the most frequently utilized [175]. Biochemically, 2-BP is an electrophilic  $\alpha$ -brominated fatty acid that blocks DHHC-mediated S-palmitoylation by directly and irreversibly obstructing the formation of acyl intermediates [176]. However, 2-BP has multiple off-target, e.g., APT1, APT2, fatty acid-CoA ligase, carnitine acyl transferase, and enzymes involved in triacylglycerol biosynthesis in cells [177, 178]. Furthermore, 2-BP is commonly administered at micromolar concentrations (10–100  $\mu$ M), which surpass its toxicity threshold [9].

Another inhibitor, cerulenin, is a natural antibiotic having an  $\alpha$ -keto-epoxy group with an octadienyl chain [179]. Lawrence et al. (1999) elucidated that the  $\alpha$ -keto-epoxy carboxamide moiety is crucial for palmitoylation inhibition, and analogs with extended aliphatic chains (15-17 carbon chains) exhibit heightened efficacy in inhibiting palmitoylation of N-Ras, and H-Ras proteins without compromising fatty acid synthesis [180]. Unfortunately, due to the reactive nature and highly lipophilic properties of the epoxy carboxamide moiety, further drug development of cerulenin was unsuccessful [8].

Finally, the nucleoside antibiotic tunicamycin, primarily used to inhibit protein N-glycosylation and lipid palmitoylation, has been found to directly interfere with palmitate transfer to proteins *in vitro* [181]. Notably, both cerulenin and

tunicamycin exhibit non-specific effects on other cellular processes, such as fatty acid biosynthesis and N-glycosylation.

The limitations associated with lipid-based non-selective inhibitors prompted the investigation of selective non-lipid-based inhibitors. Ducker et al. (2006) identified five compounds through a cell-based screening assay, having selectivity for DHHC [182]. Four of these compounds exhibited specificity for type 1 PAT (farnesylation-dependent palmitoylation), while the fifth (compound IV) showed selectivity for type 2 PAT (myristoylation-dependent palmitoylation) [182]. However, subsequent validation by Jennings et al. (2009) revealed that only compound IV effectively inhibited the auto-palmitoylation of DHHC isoforms. Notably, both 2-BP and compound IV hindered the auto-palmitoylation of DHHC enzymes with a time-dependent inhibition, but IV's inhibition proved to be reversible, in contrast to the irreversible inhibition by 2-BP [183].

Additionally, curcumin (**Figure 1.3D**) emerged as another non-lipid-based inhibitor. Researchers found that curcumin blocked DHHC3 autoacylation, which is responsible for integrin (ITG $\beta$ 4) palmitoylation [184]. The lack of specificity in these inhibitors limits their therapeutic applications and makes them unsuitable as chemical tools for investigating the biological functions of PATs-mediated *S*-palmitoylation. Consequently, ongoing research is focused on identifying new selective DHHC inhibitors.

To address the limitations associated with DHHC-mediated *S*-palmitoylation inhibitors, various research groups are actively identifying effective inhibitors. One such group developed two novel protein *S*-palmitoylation inhibitors based on a bis-piperazine backbone. These inhibitors selectively blocked SARS-CoV-2 *S*-protein palmitoylation and inhibited viral infection [56]. Following this, another group of Yu et al. (2023) has designed a series of innovative covalent *S*-acylation inhibitors. From which compounds 8d, 8i, 8j, and 10e notably demonstrated significant inhibition of MCF-7 cells, with half maximal inhibitory concentration (IC<sub>50</sub>) values below 20  $\mu$ M. Among them, 8i exhibited the highest efficacy, achieving an 89.3% inhibitory rate at a concentration of 20  $\mu$ M. Moreover, 8i hindered the migration of MCF-7 cells, inducing cell cycle arrest in the G0/G1 phase and promoting apoptosis [185]. The most recent

advancement involves cyanomethyl-*N*-myracrylamide (CMA) (**Figure 1.3B**), a lipid-based covalent inhibitor with an acrylamide-based structure. This inhibitor has a warhead known for faster reactivity with Cys thiol than serine hydroxyl groups, reducing the likelihood of forming reactive acyl CoA intermediates observed with the  $\alpha$ -halo carboxylate of 2-BP. CMA demonstrated reduced cytotoxicity, enhanced potency relative to 2-BP, and avoided off-target inhibition of other enzymes such as APT1 and APT2 [186]. The CMA hindered the DHHC-associated cellular functions such as CD36-mediated lipid uptake, droplet formation, and EGFR-mediated cell signaling [187]. Emerging chemical inhibitors have shown promising results in inhibiting *S*-palmitoylation with reduced toxicity, and addressing the challenge of off-target effects. However, the main issue remained the lack of isoform-specific inhibition for DHHC enzymes. To tackle this, two key strategies were devised. The first strategy employed a high-throughput FRET-based assay to identify compounds that disrupt the autoacylation of DHHC2. Through screening over 350,000 compounds, two structurally related tetrazole-containing compounds, TTZ-1 and TTZ-2, were identified. These compounds demonstrated isoform selectivity in HEK-293T cells, where they effectively inhibited the *S*-acylation of substrates synaptosomal-associated protein 25 kDa (SNAP25) and postsynaptic density protein 95 (PSD95), each mediated by different DHHC enzymes. This assay provided a new approach to discovering DHHC inhibitors. It helped narrow down a more specific set of compounds for studying the biological roles of DHHC enzymes in *S*-acylation [188]. In the second strategy, researchers utilized Halo-PROTACs to explore their effects in cell lines engineered to express Halo-tagged DHHC5 and DHHC20. In the HaloTag-PROTACs, a HaloTag protein (a modified bacterial dehalogenase that covalently binds to a specific 6-carbon chloroalkane), is combined with an E3 ligase ligand. In HEK-derived FT-293 cells, degradation of Halo-DHHC5 resulted in a significant decrease in the palmitoylation of its substrate, phospholemman. Similarly, the degradation of Halo-DHHC20 substantially reduced the palmitoylation of its substrate, interferon-induced transmembrane protein 3 (IFITM3). However, no such effect was observed on the palmitoylation of the SARS-CoV-2 spike protein. In contrast, in the Vero E6 kidney-derived cell line, degradation of DHHC20 did not affect the palmitoylation of IFITM3 or the SARS-CoV-2 spike

protein. These results suggest that PROTAC-mediated targeting of specific DHHC enzymes can effectively reduce substrate palmitoylation [189].

Overall, these chemical tools and the emerging targeting methodologies demonstrated effective and precise inhibition of a broad range of DHHCs mediated *S*-palmitoylation, overcoming the limitations of existing inhibitors. This advancement offers a more reliable approach to studying the biological effects of disrupting DHHC-mediated *S*-palmitoylation.

In addition, as therapeutic advancements continue to progress, researchers are increasingly focusing on natural remedies highly esteemed for their chemical stability, varied structures, and lower toxicity. Within this framework, recent studies suggest that these natural products have the potential to serve as potent *S*-palmitoylation inhibitors. For example, a study by X. Chen et al. (2020) illustrated that disrupting the DHHC17-MAP2K4 complex through genistein led to the inhibition of GBM cell proliferation and GSC self-renewal capacity [11]. Another study by Binoy et al. (2024) highlighted the significance of 4"-alkyl ether lipophilic derivatives of epigallocatechin gallate (EGCG) in inhibiting *S*-palmitoylation. The group found that 4"-EGCG effectively reduced protein *S*-palmitoylation *in vitro*, particularly attenuating cells overexpressing DHHC3 [12]. Apart from this, it has been documented that artemisinin (ART) covalently inhibited DHHC6. Consequently, it reduced the palmitoylation of the oncogenic protein N-Ras and its subcellular localization and mitigated downstream pro-proliferative signaling cascades [190]. In continuation, an *in silico* investigation revealed that lutein, 6-hydroxyflavone, and 5-hydroxyflavone could be validated as *S*-palmitoylation inhibitors through computational docking and molecular dynamics simulation analysis [191]. Conjugated linoleic acid (CLA) is a diet supplement mainly obtained from milk and dairy products from ruminants. It has been proven safe and helpful for treating obesity. Research by F. Zhang et al. (2024) showed that CLA inhibits the palmitoylation of CD36 by DHHC7 and the subsequent ERK signaling pathways in high fat diet (HFD)-mice, leading to decreased intestinal fatty acid uptake and chylomicron development [192]. Finally, a recent study revealed that benzoscaptopin C, a natural marine compound, can hinder the palmitoylation process of PD-L1 by blocking the enzymatic activity of DHHC3. As a result,



PD-L1 is relocated from the cell membrane to the cytoplasm and cannot be recycled back to the membrane *via* endosomes. This leads to the degradation of PD-L1 through lysosome-mediated pathways [193].

Significant advancements have been achieved in identifying pharmacological palmitoylation inhibitors, as evidenced by various studies. It is worth noting that incorporating additional characteristics could enhance the specificity of a DHHC-targeting inhibitor. For instance, directing attention towards individual PATs or identifying crucial isoforms or combinations thereof that play pivotal roles in the targeted disease would be advantageous. Designing inhibitors tailored to these specific targets holds the potential for increased effectiveness. Additionally, DHHCs are distributed in various organelles; therefore, optimizing the delivery system for the inhibitor is paramount. This can be accomplished by generating cell-penetrating peptides or utilizing nanoparticle-based systems, ensuring the precise delivery of the inhibitor to the designated target site [194-196]. In this context, a recent notable advancement involves the design of the first disulfide-bridged cyclic peptide PROTAC. This compound has demonstrated substantial downregulation of DHHC3 and PD-L1 expressions in human cervical cancer. The efficacy of this targeted degradation effect is augmented with increased doses and prolonged treatment durations,

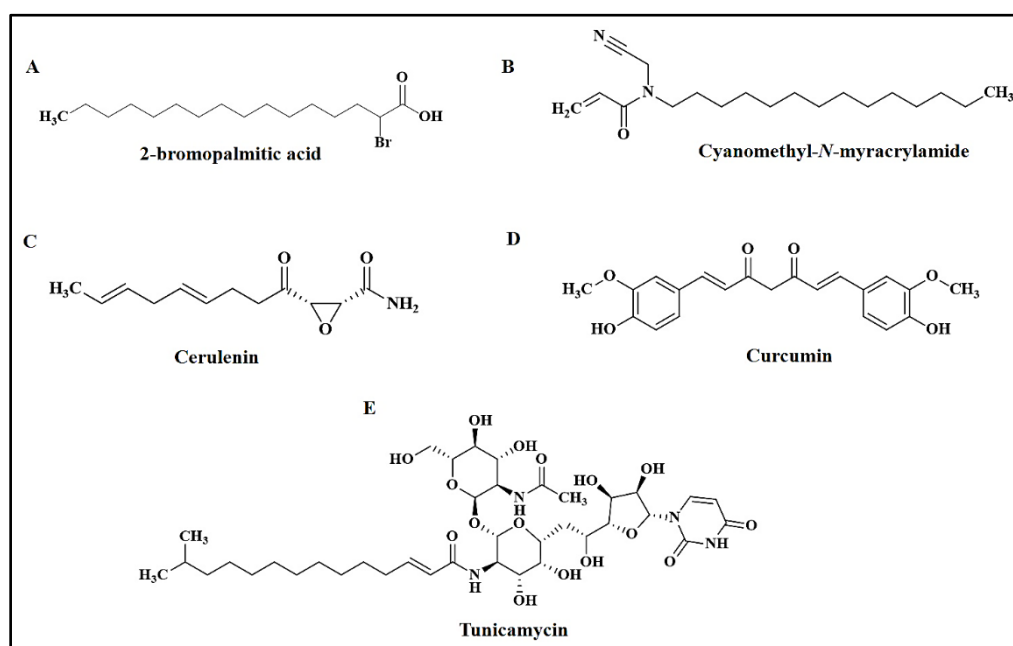


**Figure 1.3** Chemical structure of DHHC-targeting inhibitors (These figures were drawn using ChemDraw Pro 12.0.2).

with a half-maximal degradation concentration ( $DC_{50}$ ) value significantly lower than that for previously discovered linear peptides *via* the same group [19, 197]. Lastly, it is recommended to conduct comprehensive off-target profiling before designing inhibitors to address challenges associated with off-target inhibition [198-200]. This approach ensures that inhibitors are devised with minimal impact on unrelated cellular pathways. Implementing these strategies has the potential to design more specific inhibitors and alleviate the burdens of the disease associated with DHHCs.

#### 1.1.4.2 Depalmitoylation targeting inhibitors:

The cycles of depalmitoylation and repalmitoylation are essential to preserving the steady-state localization and functionality of several protein including EGFR. The chemical restriction of these cycles provides a mechanism to change cellular localization and function of proteins, which can control signaling pathways and the disease burden. Therefore, this section offers a brief overview of the deacylation process-targeting inhibitors, emphasizing their mechanisms, selectivity, and possible uses.

Palmostatin B (**Figure 1.4A**) is the first APT1 inhibitor proven to inhibit Ras depalmitoylation within cells, unlike previous compounds that were ineffective in cellular assays. Additionally, palmostatin B partially reverses the changed phenotype of H-Ras<sup>G12V</sup>-transformed MDCK-F3 cells and does not affect cell viability at the concentrations used, ensuring that basal signaling required for cell survival remains intact. Palmostatin B is highly selective for APT1 over other lipid esterases, such as PLA1, PLA2, PLD, and PLC $\beta$ , with an  $IC_{50}$  of 670 nM [201]. Later on, the same group revealed that APT2 is a target of palmostatin B [202, 203]. However, its high reactivity in serum limits its use, requiring repeated doses to maintain efficacy [204].

In addition to Palmostatin B, a fluorescence polarization-based competitive activity-based protein profiling (fluoro-ABPP) high-throughput screening campaign identified triazole urea micromolar inhibitors, including ML211 (**Figure 1.4B**), a dual APT1/APT2 inhibitor, and ML348 (**Figure 1.4C**) and ML349 (**Figure 1.4D**), which selectively inhibit APT1 and APT2, respectively [205]. Structural analysis of human APT1 in complex with ML348 (1.55 Å) and

APT2 with ML349 (1.64 Å) revealed that while their peptide backbones are similar, the inhibitors adopt different conformations within each active site. In APT1, the trifluoromethyl group of ML348 is positioned above the catalytic triad. In contrast, in APT2, the sulfonyl group of ML349 forms hydrogen bonds with active site waters, indirectly engaging the oxyanion hole and catalytic triad. These structural insights provide a basis for isoform-specific inhibition and guide future probe development [206]. The transcription factor Snail induces the displacement of Scribble (Scrib) from the plasma membrane in benign epithelial cells, a pattern also seen in aggressive cancers. Snail disrupts the palmitoylation cycle by downregulating PATs and upregulating APT2, leading to Scrib mislocalization. Treatment with the APT2 inhibitor ML349 restores Scrib's membrane localization in malignant cells, increases Scrib S-palmitoylation, and suppresses MAPK signaling independent of Ras. These findings underscore the critical role of S-palmitoylation in maintaining cell polarity and tumor suppression [207]. Additional depalmitoylase inhibitors include hexadecylfluorophosphonate (HDFP), a broad-spectrum serine hydrolase inhibiting PPT1, ABHD10, ABHD17, and APT1/2 [208, 209]. Zuhl et al. (2010) developed Aza-β-Lactams (ABLs), which exhibit enhanced inhibitory activity against ABHD10, with ML257 (**Figure 1.4E**) demonstrating exceptionally high potency, *in vitro* (IC<sub>50</sub> = 17 nM) [210]. Remsberg et al. (2021) performed a gel-based activity-based protein profiling (ABPP) screening using a native mouse brain proteome and a library of serine hydrolase-targeted compounds developed at Lundbeck La Jolla Research Center, Inc. Through chemical optimization, they identified ABD957 (**Figure 1.4F**) as a more selective pan-ABHD17 inhibitor. This compound effectively inhibits the depalmitoylation of N-Ras in human AML cells [211].

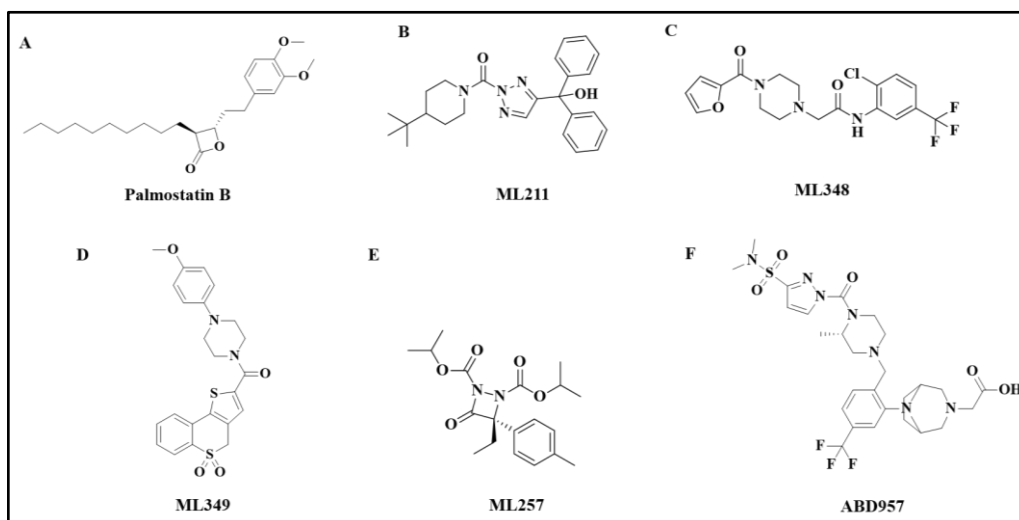


**Figure 1.4** Chemical structure of depalmitoylation -targeting inhibitors (These figures were drawn using ChemDraw Pro 12.0.2).

### 1.1.5 Methods to detect and characterize *S*-palmitoylation:

Detecting and characterizing protein *S*-palmitoylation has proven to be more challenging than other types of lipid modifications. The proteomic analysis of *S*-palmitoylated proteins has consistently presented difficulties. Although no specific antibody is available for *S*-palmitoylation, researchers have developed various methods to detect this modification, outlined below.

#### 1.1.5.1 Radiolabeled palmitic acid as probe:

The most traditional technique for identifying protein *S*-palmitoylation was discovered in 1979 through the use of radioisotope-labeled palmitic acids, wherein the natural  $^1\text{H}$  and  $^{12}\text{C}$  in palmitic acid were replaced with radioactive  $^3\text{H}$  and  $^{14}\text{C}$ , respectively (**Figure 1.5A**) [212, 213]. By preserving the structural integrity of natural palmitic acid, this substitution permitted the precise *S*-palmitoylation mimicking. Experimentally, radiolabeled palmitic acid is introduced into cells, converted to acyl-CoA, and then integrated into target proteins *via* DHHC enzymes. Subsequently, the radiolabeled *S*-palmitoylation is captured through SDS-PAGE and fluorography [214, 215]. Despite its widespread use, this conventional method has several limitations. These include variability in the palmitoylation turnover rate for specific proteins and challenges with the cellular penetration of radiolabeled palmitic acid, significantly impacting labeling efficiency [216]. Additionally, the fluorography exposure time can range from a few days to several months, depending on the protein's abundance, labeling efficiency, and immunoprecipitation [217].

### 1.1.5.2 Bio-orthogonal labeling *via* Click reaction, acyl-biotin exchange (ABE), and acyl resin-assisted capture (Acyl-RAC):

As a result of the shortcomings of conventional method, three novel techniques were developed to recover all palmitoylated proteins from extracts such as tissue homogenates and cell lysates: the bio-orthogonal Click reaction, ABE, and Acyl-RAC assay. The first technique is bio-orthogonal labeling Click reaction in which metabolic labeling with 17-octadecenoic acid (17-ODYA), a commercial alkynyl fatty acid analog can occur (**Figure 1.5B**). Within the natural cellular atmosphere, 17-ODYA is incorporated into endogenous palmitoylation sites by the cellular palmitoylation machinery. After sufficient labeling, the cells are lysed, and Cu (I)-catalyzed Click chemistry is applied to link the alkynyl groups to azide-linked reporter tags. After rhodamine/ biotin-azide conjugation, palmitoylated proteins can be readily identified by fluorescence microscopy or gel-based analysis [209, 218, 219]. This technique recognized protein palmitoylation in Jurkat T cell, identifying 125 predicted *S*-palmitoylated proteins, including the fluorophosphonate (FP)-reactive serine hydrolase (FAM108) protein [220]. This bio-orthogonal method offers several advantages, including the fact that it does not require thiol reduction and alkylation, and one can analyze small sample sizes without requiring several months to weeks [221]. Nonetheless, a noteworthy drawback is that, during cell lysates, the integrity of native subcellular structures becomes compromised, resulting in limited information regarding the subcellular location of palmitoylated proteins [222].

The second technique ABE, introduced in 2004, has significantly propelled the field forward, surpassing the earlier use of radiolabeled palmitate. This method blocks free thiols, followed by hydroxylamine (NH<sub>2</sub>OH)-mediated cleavage of thioester bonds at Cys residues. After cleavage, the newly exposed thiols react with biotin disulfide, allowing for biotin-avidin enrichment of *S*-palmitoylated proteins (**Figure 1.5C**) [223, 224]. Identifying 12 of the 15 previously known palmitoylated proteins and 35 new candidates in *Saccharomyces cerevisiae* marked the first successful application of the ABE technique [81]. Subsequently, with the introduction of the third technique Acyl-RAC in 2011, the method improved further by substituting avidin enrichment and Cys-

biotinylation with a single "resin-assisted capture" stage using Sepharose-immobilized reactive disulfide, thereby making it more straightforward to detect and quantify *S*-acyl sites (**Figure 1.5D**) [224, 225]. The first example of this technique was the identification of the bovine brain membrane proteins, which included *S*-palmitoylated proteins growth-associated protein of 43 kDa (GAP43; neuromodulin) and Gαz [225, 226].

A major challenge in ABE experiments was the high background noise caused by the capture of non-*S*-palmitoylated proteins. Zhou et al. (2019) addressed this issue by developing a low-background ABE (LB-ABE) technique, which involves the addition of 2,2'-dithiodipyridine to block any remaining free Cys residues before the biotin-HPDP reaction, thereby enabling the identification of thousands of potential palmitoylated proteins [227]. Moreover, it was demonstrated that ABE and Acyl-RAC do not always have the same efficiency in detecting all *S*-acylated proteins [228].

#### **1.1.5.3 Acyl-PEGyl exchange gel-shift (APEGS) and acylation-coupled lipophilic induction of polarization methods:**

The techniques mentioned above have enhanced the detection of *S*-acylated proteins and proteomic analysis. However, the quantitative levels and understanding of how specific sites of this PTM influence cellular pathways remain a significant challenge. A novel method called Acyl-PEGyl exchange gel-shift (APEGS) has been developed to address this (**Figure 1.5E**). This technique involves labeling palmitoylated proteins with fixed mass labels (e.g., 2 kDa, 5 kDa, or 10 kDa methoxy polyethylene glycol maleimide, mPEG-mal) and detecting them *via* western blotting [229]. For instance, endogenous IFITM3 has been identified as *S*-acylated on three Cys residues. The site-specific modification of these highly conserved Cys residues plays a critical role in the antiviral activity of this IFN-stimulated immune effector [229].

Another major concern was the time consumption, excessive background noise, and higher cost. To circumvent this Hong et al. (2021), developed a simple mix-and-measure method known as the acylation-coupled lipophilic induction of polarization (Acyl-cLIP) assay. In this method, a fluorescent label is added to the DHHC peptide substrate, and acylation induces the binding of the labeled peptide to detergent micelles, thereby increasing fluorescent polarization.

Therefore, the DHHC enzyme activity can be directly determined by measuring the extent of fluorescence polarization. The main advantage of using this assay is that background noise and expense can be minimized while conducting this experiment in a standardized manner. This investigation effectively evaluated DHHC3, 7, and 20 activity using the Acyl-cLIP method and screened a number of 2-BP analogs for possible DHHC inhibitors [230].

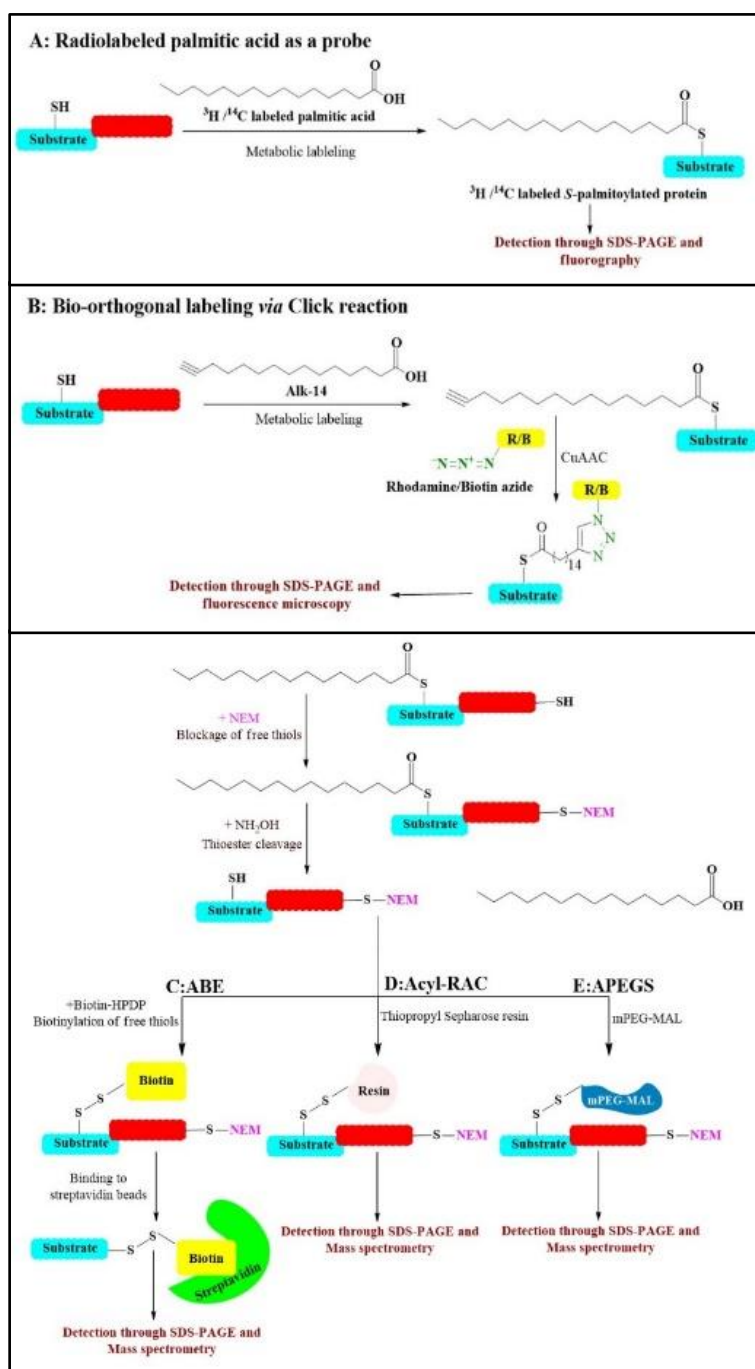


**Figure 1.5** Analytical techniques for the identification and characterization of protein S-palmitoylation. (This figure was drawn using ChemDraw Pro 12.0.2).

## **1.2 Introduction: EGFR and breast cancer:**

Breast cancer is the most predominant cause of cancer death, with a higher incidence in women under 50 years. It represents approximately 29% of cancer diagnosed in women [231]. According to GLOBOCAN 2020 statistics, over 2.3 million new cases (accounting for 11.4% of all cases) and 684,996 million deaths (overall 6.9%) occurred due to breast cancer without appropriate diagnostic measures [232]. The global incidence of female breast cancer is predicted to reach 3.2 million cases per year by 2050 [233]. Multiple endogenous and exogenous factors are connected to the growth of breast cancer; exogenous factors include a sedentary lifestyle, increasing pollution, delayed sex, oral contraceptives, smoking, consumption of alcohol, and unhealthy foods etc. [234]. In addition, various endogenous biomarkers have been identified as a new therapeutic tool for breast cancer patients, including mutations in the breast cancer gene 1 and 2 (*BRCA1* and *BRCA2*), which account for 20-25% of inherited breast cancer and 5-10% of all the breast cancer [235]. Similarly, EGFR is another highly expressed crucial biomarker in breast cancer. Previous studies have suggested that approximately 60% of basal-like breast cancer (BL-BC) and 30-52% of triple-negative breast cancer (TNBC) cells overexpress EGFR [236]. It participates in oncogenic processes by activating several signaling pathways and phosphorylating associated adapter proteins [48]. These pathways include the PI3K-AKT, Ras-RAF, and JAK-STAT [237-239]. These pathways regulate gene expression, apoptosis, angiogenesis, cell motility, and adhesion. Clinical studies have shown that disruptions in EGFR function, due to either copy number amplification or oncogenic mutations, lead to the uncontrolled activation of downstream signaling cascades, transforming normal cells into cancerous cells [240-242]. However, even after several EGFR targeting inhibitors, the chances of EGFR-associated cancer relapse are not diminishing concerning Cruz et al. (2020) through a genome-wide CRISPR-Cas9 genetic knockout reported that the elongator protein complex (ELP) promotes the synthesis of the anti-apoptotic protein myeloid cell leukemia-1 (MCL-1), which contributes to the insensitivity of TNBC cells to erlotinib, a first-generation EGFR inhibitor [243]. However, the precise mechanism underlying EGFR amplification remains unclear. In this regard, Bolu et al.



(2015) identified that ligand-independent activation of EGFR occurs in certain cancer cells [6]. They proposed that FASN-dependent palmitoylation of EGFR is necessary for its dimerization and kinase activation. Inhibition of FASN or PATs reduced EGFR activity and sensitized cancer cells to EGFR tyrosine kinase inhibitors. This mechanism suggests a new target for enhancing EGFR-based cancer therapy, potentially explaining the resistance to EGFR inhibitors and the unwanted amplification of EGFR in cancer [6]. Therefore, in the second section, we explored the ligand-dependent signaling cascade of EGFR in the context of breast cancer. Following this, we discussed the ligand-independent activation of EGFR, explicitly emphasizing the role of palmitoylation in activating EGFR in cancer cells.

### **1.2.1 Recapitulation of EGFR family:**

The ErbB family, also known as the erythroblastic leukemia viral oncogene family, consists of four structurally similar receptors: ErbB1/HER1/EGFR, ErbB2/HER2/Neu, ErbB3/HER3, and ErbB4/HER4. Each ErbB1 receptor comprises three main domains: the extracellular domain (ECD), the TMD, and the intracellular domain (ICD). The ECD of EGFR has 622 amino acids and is responsible for ligand binding [244]. The TMD spans the membrane and consists of 23 amino acids, while the ICD, which has 540 amino acids, regulates the receptor's intrinsic tyrosine kinase (TK) activity (**Figure 1.6**) [245].

The ECD is further divided into four sub-domains: I/L1, II/CR1, III/L2, and IV/CR2, with sub-domains I/L1 and III/L2 being leucine-rich and sub-domains II/CR1 and IV/CR2 being cysteine-rich [246]. The ICD is present in both the monomeric (unstimulated) and dimeric (stimulated) states of the receptor. Based on their receptor specificity, various ligands have been identified for ErbB family members. For instance, transforming growth factor- $\alpha$  (TGF $\alpha$ ), amphiregulin (AR), and EGF are specific to ErbB1, while heparin-binding EGF-like growth factor (HGF), epiregulin (EPR), and betacellulin (BTC) can bind to both ErbB1 and ErbB4 [247]. The neuregulin family members (NRG-1, NRG-2) are specific for ErbB3 and ErbB4 [247]. Signaling machinery is activated by binding ligands onto the ECD of their monomeric receptors, thereby forming homo or heterodimer complexes of receptors. Later, it induces dimerization and consequent trans-auto-phosphorylation of tyrosine residues in the C-terminal

region of the receptor and the activation of the downstream signaling cascade [248]. These signalling pathways regulate gene expression, apoptosis, angiogenesis, cell motility, adhesion, etc. According to clinical studies, disturbances in the function of EGFR, either due to copy number amplification or oncogenic mutation, leads to the uncontrolled activation of downstream signalling cascades and transform a healthy cell into a cancerous cell [249].

#### **1.2.1.1 PI3K-AKT signaling pathway:**

The PI3K-AKT pathway is hyper-activated in an estimated 70% of breast cancer patients [250]. PI3K proteins are classified into three main classes: PI3KI, PI3KII, and PI3KIII, based on sequence homology, substrate specificity, and cellular functions. Class I PI3Ks primarily promote oncogenic properties, while Class II PI3Ks are involved in clathrin-mediated endocytosis, mitosis, vesicular trafficking, cortical remodeling, and glucose transport [251]. Class III PI3Ks mainly regulate endosome-lysosome maturation, endosomal protein sorting, autophagosome formation, autophagy flux, and cytokinesis [251]. Class I PI3Ks are further divided into two subclasses: Class IA PI3Ks, activated by G-protein-coupled receptors (GPCRs) or receptor tyrosine kinases (RTKs), and Class IB PI3Ks, regulated mainly by GPCRs [251]. Among these, Class IA PI3Ks are directly involved in tumor progression. Class IA PI3Ks consist of a p110 catalytic subunit [p110 $\alpha$  (*PI3KCA* gene), p110 $\beta$  (*PI3KCB* gene), and p110 $\delta$  (*PI3KCD* gene)] and a regulatory subunit p85, along with its splice variants p55 $\alpha$ , p50 $\alpha$  (*PIK3R1* gene), p85 $\beta$  (*PIK3R2* gene), and p55 $\gamma$  (*PIK3R3* gene) [251]. Mutations in the p110 $\alpha$  subunit of the *PI3KCA* gene have been reported in approximately 30% of BC cases, with p110 $\alpha$ His<sup>1047</sup>Arg and Glu<sup>545</sup>Lys being the two prominent mutations [252, 253]. Inositol polyphosphate-4-phosphatase type II B (INPP4B) is a negative regulator of PI3K, and its suppression is associated with an aggressive form of TNBC (**Figure 1.7**) [254]. Ferroptosis, a form of iron-dependent cell death resulting from the accumulation of phospholipid peroxides and their metabolic by-products, is inhibited by mutations in the *PI3K* gene or loss of PTEN. This protection is mediated *via* SERBP-1-dependent lipogenesis [255, 256]. Besides PI3K, its downstream

protein AKT has also been identified as a promising target in breast cancer progression.

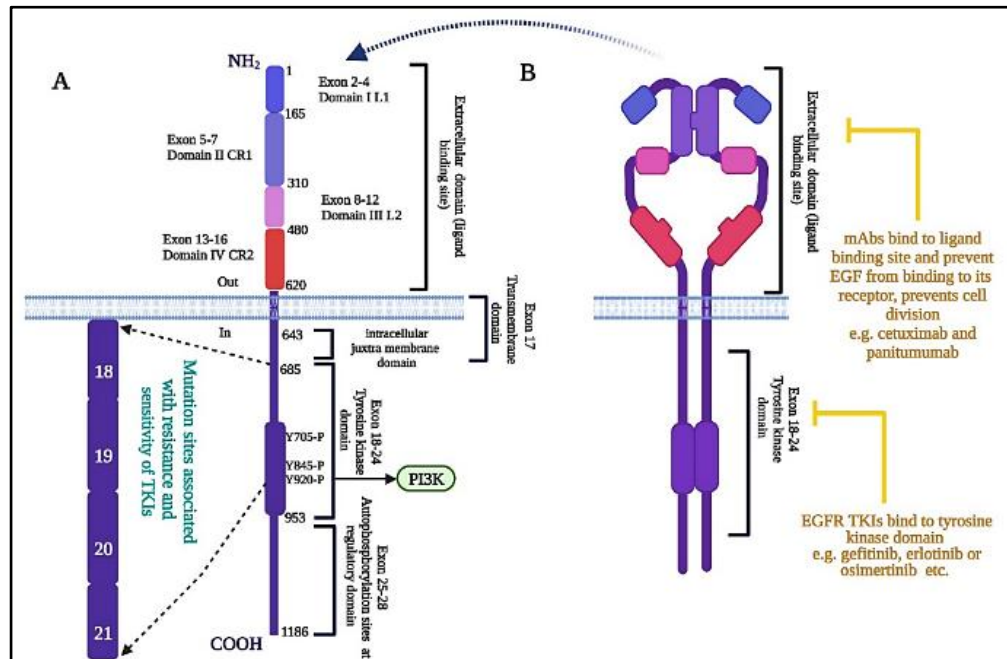


**Figure 1.6** Structural depiction of EGFR: A) (I) The Extracellular domain (ECD): domain I/L1, domain II/ CR1, domain III/L2, domain IV/CR2. (II) Transmembrane domains (TMD). (III) The intracellular domains (ICD): (i) The tyrosine kinase domain (TKD), site for the mutations associated with resistance and sensitivity to TKIs; (ii) The auto-phosphorylation site at the regulatory domain (Y953-Y1186). B) A canonical model representing the various sites for EGFR-specific inhibitors. Monoclonal antibodies target the ECD of EGFR and prevent the binding of ligand molecules to ECD, while TK-inhibitors compete with ATP for binding to the intracellular tyrosine kinase domain of EGFR (This figure was created using [www.BioRender.com](http://www.BioRender.com))

#### 1.2.1.1.1 Intracellular functioning of PI3K-AKT mediated signaling in breast cancer:

AKT is a crucial serine/threonine kinase involved in the PI3K signaling pathway, essential for regulating cell growth and survival in breast cancer. Its activation is tightly regulated by PI3K activity and signaling from EGF and EGFR [257]. Upon PI3K phosphorylation, AKT translocates to the plasma membrane *via* its pleckstrin homology domain, where it undergoes phosphorylation. Specifically, phosphoinositides-dependent kinase 1 (PDK1) phosphorylates the Thr308 residue in the activation loop, and the mTOR2 phosphorylates the Ser473 residue in the C-terminal tail's hydrophobic motif of AKT [258]. Phosphorylation of AKT leads to activation of downstream adaptor proteins such as tuberous sclerosis protein 2 (TSC2), proline-rich Akt substrate of 40 kDa (PRAS40), and mTORC1 [259]. Activated mTORC1 further phosphorylates ribosomal S6 kinases (S6K1, S6K2) and 4E-BPs (eIF4E-binding

proteins), promoting protein synthesis crucial for cell survival by releasing the inhibition on translation initiation [260]. In healthy cells, AKT remains inactive due to low EGF-EGFR activity and the presence of functional PTEN [261]. PTEN negatively regulates AKT expression by dephosphorylating phosphatidylinositol (3, 4, 5)-triphosphate (PIP3) to phosphatidylinositol (4, 5)-bisphosphate (PIP2) (**Figure 1.7**). However, in breast cancer, frequent loss of PTEN results in hyper-activation of AKT, contributing to cellular transformation [262]. AKT inhibits forkhead box O (FOXO), a tumour suppressor [263], and promotes tumourigenic properties of the cell. AKT also regulates nuclear factor kappa-light-chain-enhancer of activated B cells (NF- $\kappa$ B)- dependent transcription of anti-apoptotic proteins like B-cell lymphoma-extra-large (BCL-xL), X-linked inhibitor of apoptosis protein (XIAP), and B-cell lymphoma-2 (BCL-2) [264], and expression of tumour promoter matrix metalloproteinase (MMP2 and MMP9) [265]. In summary, targeting EGFR-mediated PI3K-AKT pathways represents a promising therapeutic strategy to mitigate cancer progression.

#### **1.2.1.2 Summarizing Ras-RAF signaling in breast cancer progression:**

RAS proteins are pivotal downstream effectors in the EGF-EGFR signaling cascade. Belonging to the superfamily of small GTPases, Ras includes three main isoforms: H-Ras, N-Ras, and K-Ras, with K-Ras further divided into splice variants K-Ras4A and K-Ras4B [266]. Despite their structural similarity (85% amino acid identity), these isoforms exhibit distinct functions [267]. The RAS/RAF signaling pathway is initiated by binding growth factors such as EGF, TGF, and IGF to the monomeric form of EGFR, leading to EGFR dimerization and the trans-phosphorylation of a tyrosine residue at the cytoplasmic tail. This creates a binding site for the SH2 domain of growth factor receptor-bound protein 2 (GRB2), which, along with its SH3 domain, recruits Son of Sevenless (SOS) proteins to activate Ras through guanine nucleotide exchange factors (GEFs) activity (**Figure 1.7**) [268]. Once activated, Ras-GTP (the active form) translocates to the plasma membrane due to farnesylation, where it stimulates downstream effector proteins such as RAF, MEK1, and MEK2 *via* phosphorylation. This cascade ultimately regulates cellular proliferation and survival [269].

In breast cancer, up to 71% of tumors have shown elevated Ras protein expression compared to normal breast tissue [266]. Hu et al. (2017) communicated that the mutants K-RAS<sup>Gly12Val</sup> and H-RAS<sup>Gly12Val</sup> suppress the expression of  $\Delta$ Np63 $\alpha$  (isoform of p63 protein, a homolog of the tumour-suppressive transcription factor p53) and augment carcinogenic properties of cells, including migration, invasion, and tumour metastasis *via* AKT-FOXO3a pathway [270]. RAS also provides resistance to anti-neoplasm therapies in breast cancer [271]. For instance, RAS induces resistance to lapatinib (a dual EGFR/HER2 inhibitor) [272], cetuximab and panitumumab (EGFR targeting mAbs) [273]. It also protects cells against Cis-platinum-based chemotherapies by increasing GST-pi expression [274]. H-RAS upregulates excision repair cross-complementation group 1 (ERCC1) protein expression (promotes DNA repair capacity of cells) to protect cells from platinum-based anti-cancerous therapies [274]. Additionally, K-Ras stimulates *de novo* lipid synthesis by activating mTORC1 and SREBP, facilitating cell growth [275]. Conclusively, these diverse roles of Ras in breast cancer progression and therapy resistance underscore its potential as a therapeutic target for combating this disease.

### 1.2.1.3 JAK-STAT signaling pathway:

STATs are intracellular transcription factors [276, 277]. Structurally, STAT isoforms share similar homology; they consist of three domains, including (1) an oligomerization domain, (2) a DNA binding domain, and (3) a SH2 domain [278]. In a cellular system, activation of STATs depends on the binding of non-cytokine (EGF, IGF, and HGF, etc.) or cytokines [(Interleukins (IL-6, and IL-27), interferons (IFN $\gamma$ , and IFN $\beta$ ), etc.)] (**Figure 1.7**) ligands to their corresponding transmembrane receptor. Thus, ligand binding drives the phosphorylation of JAKs. Subsequently, activated JAKs phosphorylate the monomeric form of STATs, leading to their dimerization, tyrosine phosphorylation, and translocation from cytoplasm to nucleus (nSTATs) [279, 280]. Later, nSTATs regulate the expression of specific genes by binding to their consensus DNA elements. In healthy cells, STAT1 is required to induce p21<sup>Cip1/WAF1</sup> [281]. Contradictory, non-phosphorylated nSTAT3, both independently or in association with other transcription factors e.g., c-JUN, can boost the expression of many oncogenic proteins such as MCL-1, BCL-2, BCL-

xL, and c-Myc (**Figure 1.7**) [282]. STAT3 also downregulates apoptotic proteins like p53, BAX, and IFN- $\beta$ , promoting cell survival and tumor progression [283]. Additionally, cytokines such as IL-6 secreted from adipocytes activate STAT3, inducing EMT, a critical step in tumor metastasis [284]. This pathway enhances breast cancer progression by promoting cell proliferation and altering gene expression involved in EMT. Conclusively, various signalling cascades and proteins stimulated by EGFR aggravate cancer and barricade the route for anti-carcinogenic medication. Thus, an in-depth investigation and revelation of all the aspects of EGFR will help to find a more promising anti-carcinogenic treatment.

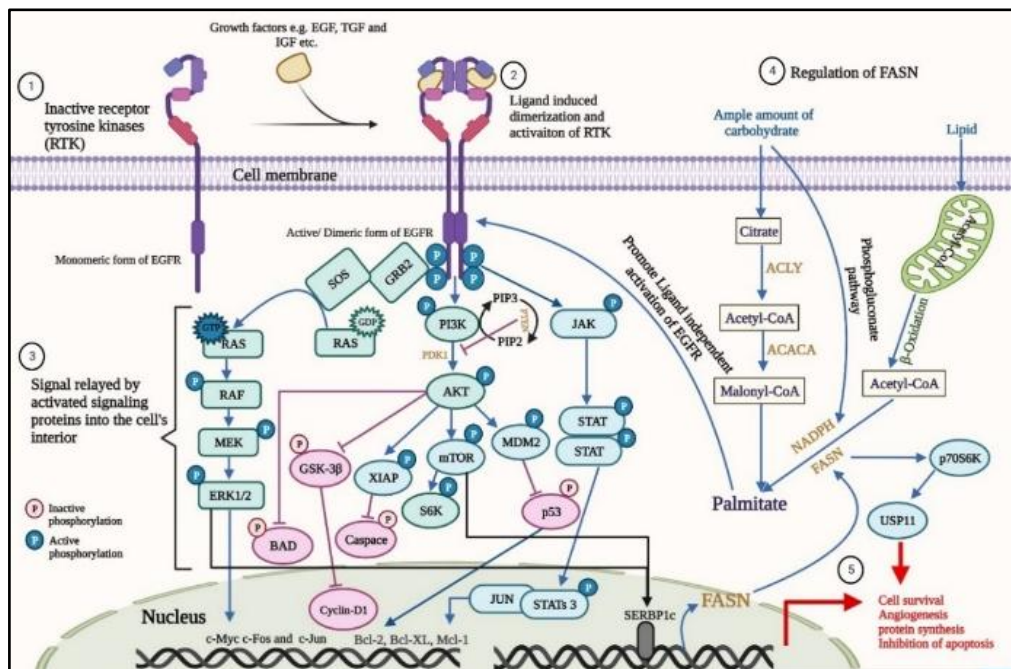


**Figure 1.7** The schematic representation illustrates the various signaling pathways activated by EGFR in a cell. Step 1-2: Transition of inactive monomer to active dimeric EGFR complex upon ligand binding. Step 3: Dimeric EGFR activate intracellular adaptor adaptor proteins, such as the Ras-RAF-MEK-MAPK, PI3K-AKT, and JAK-STATs etc. Step4: The regulation of FASN via SERBP1c and EGFR signaling. Step 5: EGFR mediated signaling cascades promote activation of anti-apoptotic proteins such as, BCL-2, BCL-XL, and FASN and control diverse cellular responses such as, cell proliferation, protein synthesis, angiogenesis etc. (This figure was created using [www.BioRender.com](http://www.BioRender.com)).

### 1.2.2 Cross talk between EGFR and palmitoylation:

EGFR activation generally occurs upon ligand binding, such as with EGF, to its ECD, triggering receptor dimerization and autophosphorylation of its intracellular domain [285]. Beyond phosphorylation, EGFR can also undergo activation through S-palmitoylation, which may occur in both ligand-dependent



and independent manners and is crucial in specific cancers. Supporting this, several studies have highlighted the importance of DHHC-mediated palmitoylation at the intracellular domain for EGFR's abnormal activation in cancer cell. One of them has reported that DHHC20 promotes cancer by supporting the aberrant activation of EGFR. The mechanism involves the reversible palmitoylation of EGFR, where palmitate modification "pins" the unstructured C-terminal tail to the plasma membrane, enhancing EGFR activation in non-small cell lung cancer (NSCLC) [194]. In K-Ras-mutant lung cancer cells, inhibiting the palmitoylation of EGFR by DHHC20 has increased their sensitivity to PI3K inhibitors. This occurs because, in K-Ras-mutant patients, K-Ras is locked in its GTP-bound state. Therefore, when EGFR is not palmitoylated, it preferentially binds to the MAPK adaptor protein Grb2 rather than PI3K regulatory subunit p85. Therefore, due to the impaired PI3K-AKT pathway, the cancer cells are more vulnerable to PI3K inhibitors. Consequently, targeting EGFR-PI3K signaling through the inhibition of DHHC20 could provide therapeutic advantages for patients with K-Ras-mutant tumors by improving the efficacy of PI3K inhibitors [195]. The second study emphasized that DHHC13-mediated palmitoylation of EGFR is essential for its localization to the plasma membrane, with ADP-ribosylation factor 6 (ARF6) identified as a critical player in this process. N-myristoylated ARF6 recognizes palmitoylated EGFR, forming a lipid-lipid interaction that recruits the exocyst complex, facilitating EGFR budding from the Golgi and its transportation to the plasma membrane in a GTP-bound form. Hence, disrupting this sorting system is a potent strategy for treating EGFR-dependent tumors [52]. The third discovery revealed that Ras-related protein (RAB27A)-mediated regulation of EGFR palmitoylation by DHHC13 contributes to oral squamous cell carcinoma progression [286]. Finally a study by the Bollu et al. (2015) group showed that FASN-mediated palmitoylation of EGFR leads to its ligand-independent activation in cancer cells [6]. However, in addition to the intracellular palmitoylation of the cysteine residue, several critical mutations in the ECD-EGFR also contribute to ligand-independent activation. For example, the Thr<sup>263</sup>Pro mutation, located in Subdomain II just before the "β-hairpin" that interacts with Subdomain IV in the inactive "tethered" conformation, can induce conformational changes in the ECD of EGFR. Disrupting the tether between

Subdomains II and IV causes the "β-hairpin" of Subdomain II to interact with other regions, leading to basal phosphorylation of the mutant EGFR in the absence of ligand [287]. Similarly, the Gly<sup>33</sup>Ser and Asn<sup>56</sup>Lys mutations prevent the EGFR from adopting the fully closed (tethered) and inactive conformation, thus hindering the receptor's ability to bind EGF or cetuximab. Binding studies have shown that these untethered mutants display a reduced affinity for both EGF and cetuximab while maintaining sustained activation, staying at the cell surface, and exhibiting impaired internalization and sorting for endosomal degradation, which results in prolonged AKT signaling [288]. Conclusively, the findings above suggest that addressing ligand-independent activation or identifying additional key mutations within the ECD of EGFR in cancer cells could be valuable strategies to mitigate challenges associated with cancer relapse.

### **1.3 Conclusion:**

The role of palmitoylation in cancer progression has been well-studied. However, answering a few crucial questions can advance the therapeutic benefits. Firstly, no *S*-palmitoylation inhibitors have advanced to clinical trials despite the critical role of DHHC-mediated *S*-palmitoylation in disease. While 2-BP is the most commonly used DHHC inhibitor, its limitations, such as a lack of selectivity for individual DHHC enzymes and unintended inhibition of other intracellular proteins, make it unsuitable as a drug lead or therapeutic candidate [289]. Therefore, it is essential to validate emerging inhibitors like CMA, 4"-EGCG, and others in disease models and conduct clinical studies to mitigate the disease burden linked to DHHC-mediated *S*-palmitoylation.

Secondly, advancements in tumor immunotherapy have shown promise, but challenges like low response rates and immune-related severe side effects persist. The tumor immune microenvironment heavily influences the effectiveness of these therapies. Understanding the role of *S*-palmitoylation in regulating this environment could provide new strategies to enhance immunotherapy efficacy [290], making it a crucial area of research with significant clinical implications.

Thirdly, several research studies have elucidated the role of intracellular domain palmitoylation in EGFR-related cancer. However, no research has addressed the



role of ECD-EGFR palmitoylation, which could mimic a ligand-bound state or stabilize an active ECD conformation. This stabilization can result in receptor dimerization and activation without ligand binding, promoting continuous cancer signaling. Investigating this crucial aspect will help to overcome the challenges posed by EGFR in cancer treatment. Subsequently, nano-particle-based co-delivering of protein inhibitors like 2-BP and EGFR inhibitor gefitinib can further enhance cancer treatment. Since EGFR is *S*-palmitoylated by DHHC20, this combination can simultaneously block the tyrosine phosphorylation and the *S*-palmitoylation site of EGFR in cancer cells to prevent its aberrant expression [21]. This co-targeting technique can address challenges related to cancer relapse often seen with EGFR-targeting therapies. Lastly, identifying palmitoylated proteins at the proteome level, facilitated by genetic screens such as CRISPR [291], offers exciting prospects for future research in understanding the systemic roles of palmitoylation and its potential as a target for cancer treatment.

#### **1.4 Aim of the thesis:**

The objective of this thesis is to tackle the shortcomings of existing *S*-palmitoylation inhibitors and investigate its role in cancer progression. Current DHHC-targeting inhibitors, such as 2-BP, cerulenin, tunicamycin, and compound V, are known to have significant toxic effects, poor selectivity, and insufficient characterization in cellular models, highlighting the need for more specific and less harmful alternatives [183]. Natural molecules derived from plants and other organisms are ideal due to their chemical stability, structural diversity, and broad therapeutic activity against various disorders [190]. Despite this, limited studies have investigated the interaction between DHHCs and natural drug targets. In this thesis, a virtual screening of 115 selected natural compounds was conducted using *in silico* methods to evaluate their fit within the DHHC20 binding pocket. The results were then validated through MD simulations.

Another underexplored area is the direct impact of DHHCs on cancer metabolism. Cancer cells undergo metabolic reprogramming, which alters their metabolic pathways to provide energy and substrates necessary for rapid proliferation and survival. Understanding the influence of tumour suppressor or

promoter proteins on these metabolic changes can uncover potential therapeutic targets[292, 293]. Concerning this, the impact of several key oncogenes and tumour suppressors including, EGFR, p53 and AKT on the cancer cell metabolome has been studied [294, 295]. However, the role of DHHCs in cancer metabolism remains unclear. To address this gap, we employed LC-MS/MS-based untargeted metabolomics. The identification of critical metabolites and disrupted pathways was carried out using MS-DIAL and MetaboAnalyst 5.0 tools under DHHC2-knockdown, overexpression, and empty vector control conditions. This study aims to elucidate the specific contributions of DHHC2 to cancer metabolism and identify novel therapeutic targets.

It has been well-documented that EGFR overexpression is associated with survival in cancer patients. However, the underlying reasons for its over-amplification still need to be better understood. Previous studies have highlighted the role of intracellular palmitoylated cysteine residues of EGFR in cancer[6, 22]. Nonetheless, the impact of palmitoylation on the cysteine residues of the ECD-EGFR has not been investigated. The palmitoylation of ECD-EGFR could mimic a ligand-bound state or stabilize an active EGFR conformation, leading to receptor dimerization and activation without ligand binding, thereby promoting continuous cancer signaling. Thus, in this study we employed computational methodologies, including molecular docking and MD simulations, to identify key cysteine residues of ECD-EGFR interacting with the DHHCs. Subsequently, we generated cysteine ECD-EGFR mutants and evaluated their interaction with the selected DHHCs. This study aims to elucidate the role of palmitoylation in ECD-EGFR-mediated cancer signaling and identify potential therapeutic targets through *in silico* approaches.

In summary, this study proposed that natural molecules can act as promising DHHC inhibitors and overcome the limitations of currently available inhibitors. It also provides detailed information on the potential role of DHHCs in cancer biology by impacting its metabolism and supporting the activation of critical oncogenes such as EGFR.

#### **1.4.1 Organization of the thesis:**

**Chapter 1** is structured into two sections. The first section thoroughly explores protein S-palmitoylation and depalmitoylation and its implications in cancer,

highlighting the constraints of existing inhibitors. The second section covers pivotal studies on the role of EGFR in breast cancer progression, alongside discussions on the interplay between *S*-palmitoylation and EGFR. This chapter extensively reviews existing literature, outlining the thesis's scope and objectives.

**Chapter 2** included the identification of several natural compounds that can act as DHHC inhibitors. Among these, lutein emerged as a selective molecule for the binding groove of DHHC20. This specificity is due to the formation of H-bonds and hydrophobic interactions between lutein and the DHHC20 receptor.

**Chapter 3** delves deeper into the effects of DHHC2 on HEK-293T-cell biology using untargeted metabolomics. The findings showed that silencing DHHC2 resulted in higher expression of onco-metabolites, including glutamine, uridine, and glutamic acid. Contrarily, overexpression of DHHC2 is linked to increased expression of metabolites known for their anti-cancer properties, such as betaine and 5-methylthioadenosine.

**Chapter 4** unravels the interaction between DHHCs and ECD-EGFR using computational methods. The results suggested that DHHC1 and DHHC4 can be suitable Cys7-ECD-EGFR targeting isoforms. Nonetheless, *in vitro* experiments are needed to validate these findings, and to address the challenges related to resistance to monoclonal antibodies, and mitigate EGFR-mediated cancer progression.

**Chapter 5** deals with the conclusion of the thesis and the future perspective of the work.



## **Chapter 2: Identification of selective plant-derived natural carotenoid and flavonoids as the potential inhibitors of DHHC-mediated protein *S*-palmitoylation: an *in silico* study**

---

### **2.1 Introduction:**

The diverse substrate recognition abilities of DHHCs enable them to partake in various cellular functions, including ion channel activation, protein trafficking, and cellular signaling, associating them with several disorders, such as cancer, neurodegenerative diseases, and pathogenic infections [290]. For e.g., a recent study has shown that DHHC9-mediated palmitoylation of PD-L1 supports lung cancer growth [296, 297]. Another notable example is the reduction in SARS-CoV-2 infectivity and inhibition of cell-cell syncytia formation achieved by blocking DHHC-mediated *S*-palmitoylation of the S-protein [56, 298]. Until 2017, the lack of DHHC crystal structures posed a significant obstacle in studying *S*-palmitoylation. To overcome the limitation, Rana et al. (2018) discovered the first crystal structures of hDHHC20 and zfDHHC15, revealing that the DHHC binding cavity is a prolonged tunnel composed of four transmembrane helices and a hydrophobic acyl chain-binding groove. The specificity for recognizing acyl chains and determining their length within this groove is primarily governed by the DHHC motif. The Cys residue of DHHC, located at the onset of the acyl-binding groove within the active site, facilitates the nucleophilic interaction with the acyl-CoA donor substrate[299].

As mentioned, the aberrant palmitoylation activity can have several pathological implications. Hence, it has drawn more attention as a therapeutic marker[1, 300]. However, the need for appropriate inhibitors is the primary roadblock to investigating DHHCs. Though 2-BP is utilized as a pan-DHHC inhibitor, its frequent use is limited by its poor selectivity and cellular toxicity [87, 301]. At least two *S*-acylation erasers, APT1 and APT2, are inhibited by 2-BP in living organisms. Moreover, 2-BP is frequently utilized in micromolar doses (10-100  $\mu$ M) at or above its toxicity threshold [302]. Global analysis of cellular targets

revealed that 2-BP also targets other protein forms, including chaperones, transporter channels, and enzymes [303], which indicates that 2-BP is opportunistic. Apart from 2-BP, several other *S*-acylation inhibitors that have been studied, like cerulenin, tunicamycin, and compound V, have considerable harmful effects, poor selectivity, and are not well characterized in cellular models [87]. Hence, to overcome challenges posed by the DHHCs targeting inhibitors, a more specific, less toxic molecule is required.

Historically, natural compounds derived from plants and other organisms have been highly valued for their chemical stability and diverse structures. These natural molecules offer effective and comprehensive therapeutic benefits against various disorders by targeting multiple disease-associated proteins, such as EGFR, FASN, and PI3K, without causing significant side effects [304]. Therefore, to circumvent the limitations of the current inhibitors, we selected a total of 115 natural compounds. Our selection criteria focused on molecules that could fit into the tunnel-shaped hydrophobic binding groove of DHHC20, having long-chain, flat, or planar structures such as lutein or calystatin A (which share structural similarities with palmitic acid). We also evaluated natural drug candidates that effectively hindered disorders directly or indirectly linked to DHHCs. For example, compounds like resveratrol, curcumin, EGCG, and quercetin are used to treat various neurological disorders, including Alzheimer's disease and Schizophrenia. It is worth noting that certain DHHC isoforms, such as 2, 5, 18, 9, and 21, are implicated in neurological conditions [305]. Furthermore, flavonoids have been associated with apoptosis by suppressing the carcinogenic activity of oncogenic proteins like Ras, EGFR, and PD-L1. Conversely, DHHC-mediated palmitoylation activates these oncogenes to promote cancer [306]. Notably, to date, there is a lack of scientific evidence elucidating whether natural drug candidates, such as carotenoids and flavonoids, impede the DHHCs-mediated protein-*S*-palmitoylation in humans. To address this gap, we performed *in silico* virtual screening of the 115 selected natural compounds within the DHHC20 binding pocket and compared them with the pan-DHHC inhibitor 2-BP. As a result, we discovered that lutein, 5-hydroxyflavone, and 6-hydroxyflavone showed remarkably high occupancy in the DHHC20 binding pocket, with binding energies (B.E.) of -9.2, -8.5, and -

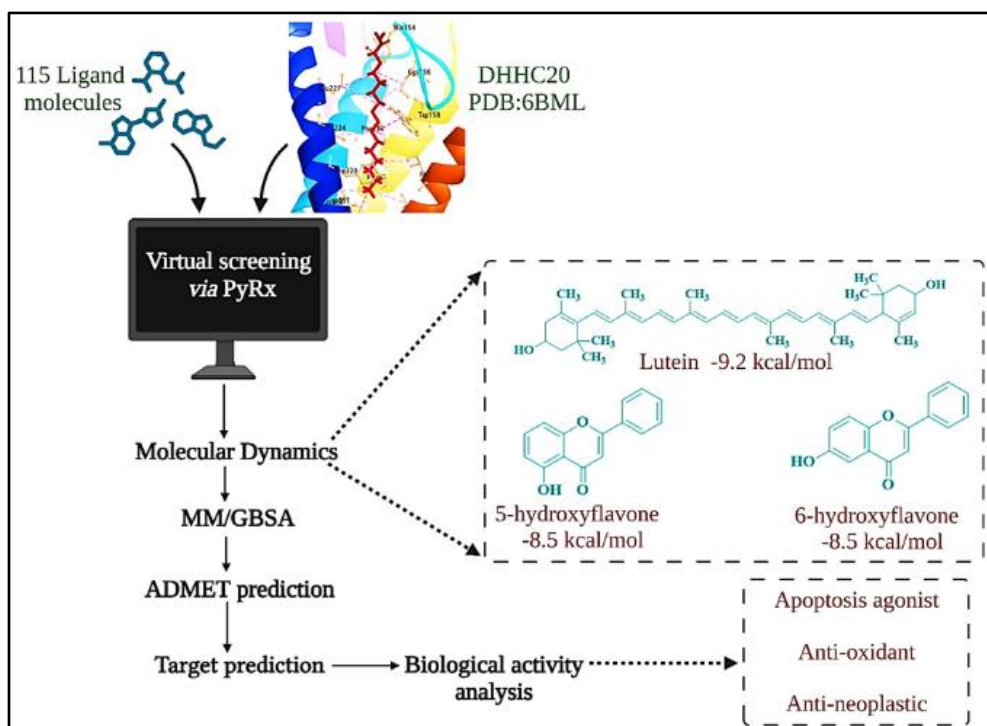


**Figure 2.1** Schematic representation of the workflow. This figure was created using [www.biorender.com](http://www.biorender.com)

8.5 kcal/mol, respectively, compared to 2-BP (-7.0 kcal/mol). We conducted a 100-nanosecond (ns) MD simulation with these three complexes, to eliminate inaccurate predictions, ligand-binding free energy was analyzed using the molecular mechanics generalized Born surface area (MM-GBSA) approach. The binding free energy ( $\Delta G_{\text{bind}}$ ) calculation supported our docking results. In conclusion, this study revealed that lutein retains a higher affinity for the DHHC20 groove, stabilized through hydrogen and hydrophobic interactions (**Figure 2.1**). However, to advance the search for a specific DHHC inhibitor, this study requires *in vitro* validation.

## 2.2 Methods:

### 2.2.1 Retrieval of protein crystal structure and ligands:

The DHHC20-2-Bromopalmitoyl CoA complex was obtained from the RCSB Protein Data Bank with the PDB ID: 6BML [www.rcsb.org](http://www.rcsb.org) [307]. The Simplified Molecular Input Line Entry System (SMILES), as well as the three-dimensional (3D) and two-dimensional (2D) SDF structures of the ligands, were sourced from the PubChem database [PubChem \(nih.gov\)](http://PubChem.nih.gov) [308]. The chemical

structures of these molecules were drawn using ChemDraw Ultra 12.0, available at [Free Download ChemDraw Ultra 12.0 - ChemistryDocs.Com](http://FreeDownloadChemDrawUltra12.0-ChemistryDocs.Com).

### 2.2.2 Preparation and docking parameters for protein and ligands:

In this study, Chain A of DHHC20 was utilized. The crystal structure preparation involved removing the typical 2-BP molecule, adding hydrogen atoms, and applying Gasteiger charges using AutoDock Vina 1.1.2 [Downloads – AutoDock Vina \(scripps.edu\)](http://Downloads-AutoDockVina.scripps.edu). The file was then saved in PDBQT format [309]. Energy minimization and the transformation of ligand molecules to PDBQT format, followed by protein-ligand docking, were conducted using PyRx software <https://sourceforge.net/projects/pyrx> at an exhaustiveness (E) level of 8, which indicates the depth of search in AutoDock Vina 1.1.2 [309]. For the specified active site residues, namely Asp153, His154, His155, and Cys156, a grid box was established with coordinates of 21.27, -47.85, and -49.90 (x, y, z) and dimensions of 16.60, 21.80, and 25.335 (x, y, z) on the receptor's surface.

### 2.2.3 Analysis of protein-ligand complexes:

The interactions, including hydrogen bonds (H-bonds), hydrophobic interactions (amide- $\pi$  stacking,  $\pi$ - $\pi$  stacking, and  $\pi$ -sigma), electrostatic interactions, van der Waals forces, unfavourable donor-donor, and acceptor-acceptor interactions between protein-ligand complexes were visualized. Their 3D and 2D plots were produced using Discovery Studio Client 2021 <https://discover.3ds.com/discovery-studio-visualizer-download> and LigPlot<sup>+</sup> v.2.2 <https://www.ebi.ac.uk/thornton-srv/software/LigPlus> [310, 311].

### 2.2.4 Parameters for MD simulation:

The protein-ligand docking offer a specific viewpoint on how a ligand binds to a protein's active site; in addition, computational MD simulations attempt to determine atom movements over a period using Newton's classical equations of motion [308, 312]. In this study, 100 ns MD simulations were conducted to examine ligand binding under physiological conditions using the Desmond package from Schrödinger ([Desmond | Schrödinger \(Schrodinger. com\)](http://Desmond|Schrödinger(Schrodinger.com))) [313]. The results obtained from the molecular docking were considered as the basis for the MD simulation. The initial configurations for protein-ligand interactions



were set up using the Protein Preparation Wizard within the Maestro Schrodinger Suite 2017, ensuring optimization and simplification of the complexes <https://www.schrodinger.com/protein-preparation-wizard> [314]. For simulation setup, the System Builder tool facilitated the model system preparation. The molecular characteristics, such as coordinates and topology, were defined based on the optimized potentials for liquid simulations\_2005 (OPLS) force field. Subsequently, each complex was immersed in a solvation environment using the transferable intermolecular interaction potential 3 points (TIP3P) water model. To ensure sufficient space for the simulation, these solvated complexes were enclosed within an orthorhombic box, maintaining a 10 Å distance from the protein atoms to the box edges. Energy minimization of the system was achieved using a hybrid approach combining the steepest descent method (with a minimum of 10 steps) and the limited-memory Broyden–Fletcher–Goldfarb–Shanno (LBFGS) algorithm (with an LBFGS vector size of 3). Counter ions were added as necessary to maintain a neutral charge in the system. A 0.15 M sodium chloride (NaCl) salt solution was integrated to generate physiological conditions, and simulations were executed under the isothermal-isobaric ensemble (NPT) at 1 atm pressure and 300 K temperature. A relaxation phase for the models was ensured before the actual simulation. Throughout the 100 ns production run, trajectory data was saved at 10-picosecond (ps) intervals. The stability of the simulations was gauged using root mean square fluctuations (RMSF) and root mean square deviation (RMSD) metrics over time, with RMSD plots constructed based on the protein backbone of the equilibrated complex as a reference structure.

#### **Free energy calculation through MM-GBSA method:**

The molecular mechanical energies paired with MM-GBSA or Poisson-Boltzmann methodologies (MM-PBSA) are essential for determining the binding free energy ( $\Delta G_{\text{bind}}$ ) of small compounds binding to biological macromolecules [315]. The binding free energies were predicted *via* the Prime MM-GBSA approach, using the OPLS\_2005 force field and the variable dielectric surface generalized Born 2.0 (VSGB) solvation model. The docking positions of these compounds were determined using the Glide algorithm available through Schrödinger's platform ([www.schrodinger.com](http://www.schrodinger.com)).

The following equation is the formula for the  $\Delta G_{\text{bind}}$ :

$$\Delta G_{\text{bind}} = \Delta G (\text{solv}) + \Delta E (\text{MM}) + \Delta G (\text{SA})$$

Here,  $\Delta G (\text{solv})$  signifies the variation in solvation energies, encompassing the unbound protein, ligand, and their complex, assessed *via* the GBSA methodology.  $\Delta E (\text{MM})$  represents the disparity in energies between the unbound states of the protein and ligand versus (vs.) the minimized energy of their bound complex. Lastly,  $\Delta G (\text{SA})$  describes the difference in surface area energies between the unbound protein and ligand and their complex counterpart [315, 316]. For a comprehensive analysis, data from various trajectories, including RMSD, RMSF, radius of gyration (Rg), solvent-accessible surface area (SASA), B.E., and H-bond interactions, were interpreted using GraphPad Prism version 5.0 [GraphPad Prism 5.0 Download - prism.exe \(informer.com\)](http://www.graphpad.com/prism/prism.exe) [317, 318].

### **2.2.5 The absorption, distribution, metabolism, excretion, and toxicity (ADMET) and physicochemical characteristics of ligands:**

The physicochemical attributes of the selected molecules, such as molar refractivity, topological surface areas (TPSA), H-bond donors, acceptors, and lipophilicity ( $\log P_{\text{o/w}}$ ), were determined using the SWISS-ADME server <http://www.swissadme.ch> [311, 319].

Following this, the pkCSM server <http://structure.bioc.cam.ac.uk/pkcsml> was employed to assess ADMET properties, including blood-brain barrier (BBB) permeability, human intestinal absorption (HIA), skin permeability, interactions with Cytochrome-P (CYP) enzymes, potential toxicity, and modes of excretion [311, 320].

### **2.2.6 Prediction of molecular targets:**

The three selected natural compounds impact a range of proteins, enzymes, lipids, and their associated molecular processes. Therefore, we utilized the Swiss Target Prediction tool <http://www.swisstargetprediction.ch/index.php> to identify new molecular targets linked to these molecules [321].

### **2.2.7 PASS evaluation: Predictions of biological activity:**

To understand the potential biological characteristics of the selected compounds, the PASS web server

<https://www.way2drug.com/PassOnline/predict.php> was employed. This server uses the chemical formulas and SMILES notation of the compounds to predict biological activities, highlighting that the molecular structure influences biological activity. It provides a prediction score for biological properties, determined by the ratio of "probability to be active (Pa)" to "probability to be inactive (Pi)." A higher Pa value indicates a greater likelihood that the chemical exhibits a specific biological attribute [322, 323].

## **2.3 Results and Discussions:**

### **2.3.1 Analysis of the three best ligand molecules that bind to DHHC20 (PDB ID: 6BML):**

The significant therapeutic potential of natural compounds has captured our interest in evaluating them as potential inhibitors targeting DHHCs, aiming to address the challenges associated with the pan-DHHCs targeting inhibitor 2-BP. We screened 115 natural phytochemicals targeting the DHHC20 active site to foster therapeutic advancements ( **Appendix Table A2**). As reported by Rana et al. (2018), the Cys156 residue at the start of the acyl-binding groove in DHHC20 is crucial for facilitating nucleophilic attacks on the acyl-CoA donor substrate [299]. Based on this concept, we identified 24 compounds that interact with the Cys156 residue and exhibit higher B.E. than 2-BP, following site-specific molecular docking (**Table 2.1**). Among these, we selected three promising molecules [lutein (**Figure 2.2B** and **Figure 2.3B**), 5-hydroxyflavone (**Figure 2.2C** and **Figure 2.3C**), and 6-hydroxyflavone (**Figure 2.2D** and **Figure 2.3D**)] based on their favorable B.E. The standard ligand 2-BP had a B.E. of  $-7.0$  kcal/mol (**Figure 2.2A** and **2.3A**). In comparison to 2-BP, lutein showed the highest B.E. of  $-9.2$  kcal/mol, surrounded by Val224, Phe174, Leu175, His155, His154, Thr241, Ile242, Met152, Pro157, Leu227, Cys156, Ser178, Cys182, and Val26 (**Figure 2.3B**). Additionally, 5-hydroxyflavone and 6-hydroxyflavone were stabilized in the DHHC20 groove through H-bonds with Cys156, Asp153, His154, and Ser178 (**Figures 2.3C** and **2.3D**). In summary, our findings indicate that these natural compounds have the potential to

overcome the limitations of 2-BP (-7.0 kcal/mol) by effectively blocking the DHHC20 active site.

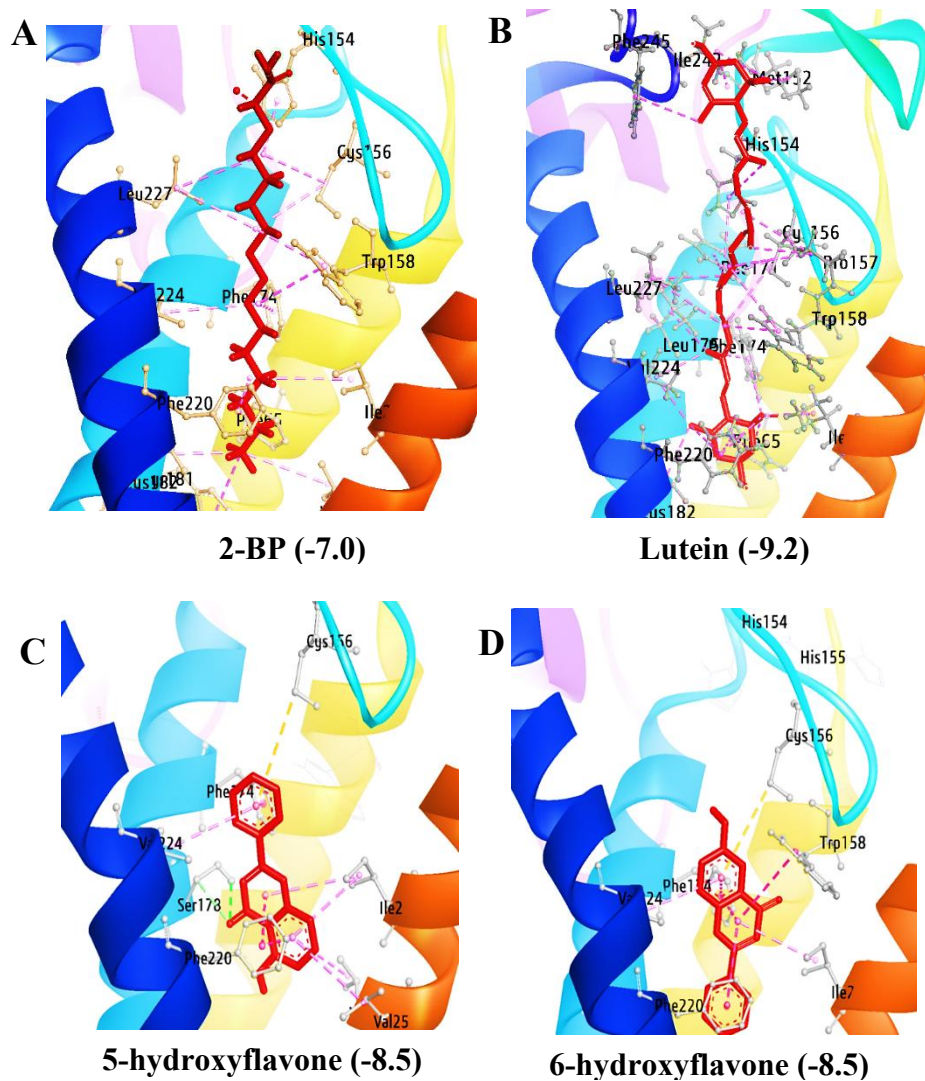


**Figure 2.2** 3D models of DHHC20 in complex with ligands: A) 2-BP acid, B) lutein, C) 5-hydroxyflavone, and D) 6-hydroxyflavone. All values are in kcal/mol.

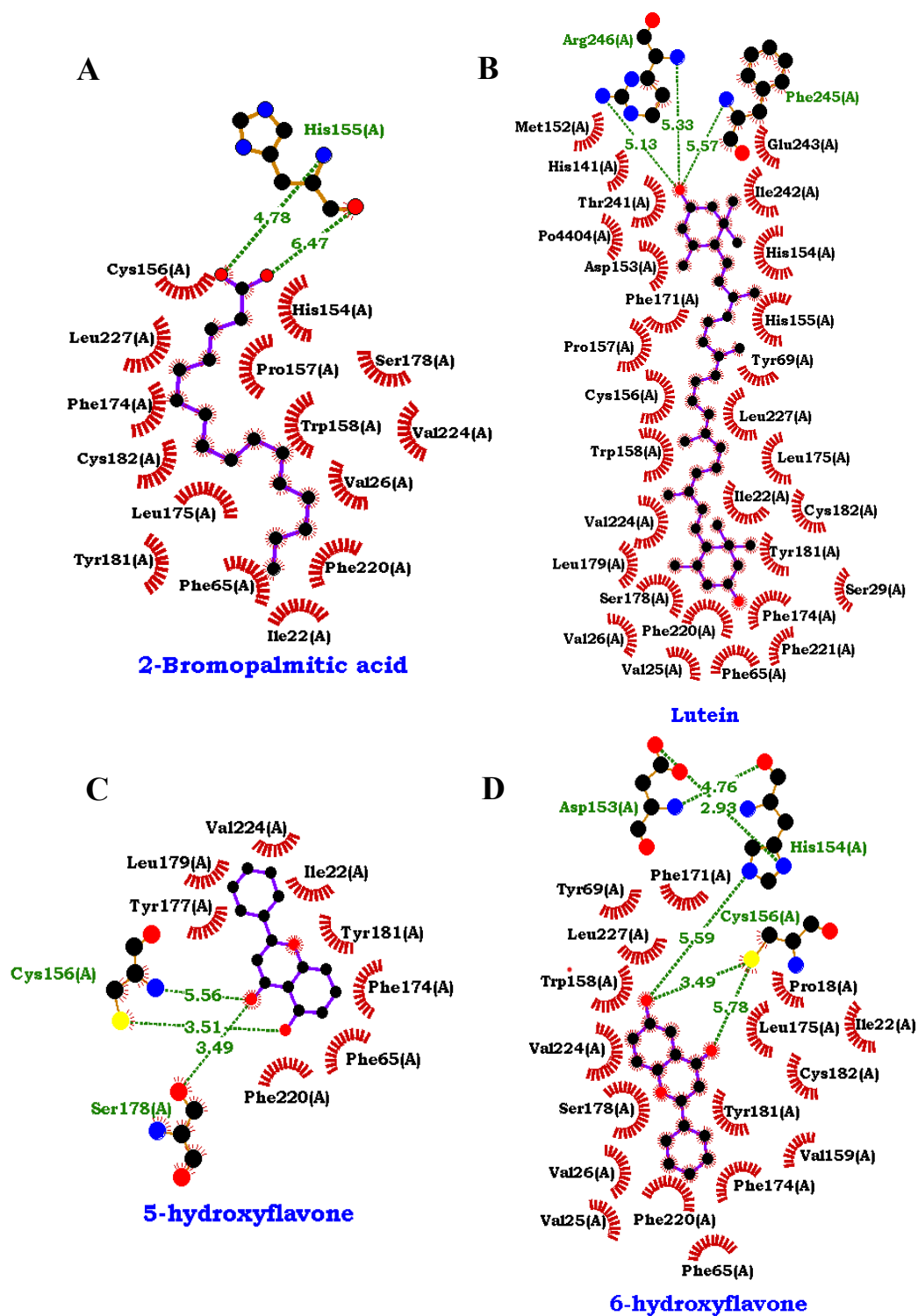


**Figure 2.3** 2D models of DHHC20 in complex with ligands: A) 2-BP, B) lutein, C) 5-hydroxyflavone, and D) 6-hydroxyflavone.

**Table 2.1** The best 24 natural molecules interacting with Cys 156\*<sub>DHHC20</sub> with binding energy higher than 2-BP (-7.0 kcal/mol) obtained via molecular docking.

S.no.	Molecules	Binding energy (kcal/mol)	Interacting amino acids
1	Lutein	-9.2	Val224, Phe174, Leu175, His155, His154, Thr241 Phe245, Arg246, Met152, Pro157, Leu227, <b>Cys156*</b> , Ser178, Cys182, Val26
2	5-hydroxyflavone	-8.5	<b>Cys156</b> , Phe174, Phe65, Val224, Ile22, Val25, Ser178, Phe220
3	6-hydroxyflavone	-8.5	Trp158, <b>Cys156*</b> , Val224, Phe220, Ile22, Phe174
4	(R)-equol	-8.2	<b>Cys156*</b> , Trp158, Val224, Phe174, Ile22, Phe220
5	Formononetin	-8	Leu227, <b>Cys156*</b> , Trp158, Phe174, Val224, Phe220, Phe65, Ile22
6	Resveratrol	-7.9	<b>Cys156*</b> , Phe174, Val224, Val26, Phe65, Phe220, Cys182, Ile22
7	Pinosylvin	-7.9	Ile22, <b>Cys156*</b> , Trp158, Val224, Phe174, Val26, Phe65, Cys182, Phe220
8	Daidzein	-7.8	<b>Cys156*</b> , Phe174, Trp158, Phe220, Ile22
9	Baicalein	-7.7	Phe220, Phe174, Ile22, Val224, Trp158, Cys182, <b>Cys156*</b>
10	Chrysin	-7.7	Trp158, <b>Cys156*</b> , Phe174, Val224, Phe220, Cys182, Phe174, Ile22
11	Glycitein	-7.7	Trp158, Val224, Phe220, Phe65, Val25, Ile22, Val26, <b>Cys156*</b>

S.no.	Molecules	Binding energy (kcal/mol)	Interacting amino acids
12	Pinocembrin	-7.7	<b>Cys156*</b> , Phe65, Val224, Ile22, Cys182, Phe220
13	Urolithin A i	-7.6	Phe174, Val224, ILE22, Cys182, Phe220, <b>Cys156*</b> , Trp158,
14	Liquiritigenin	-7.5	<b>Cys156*</b> , Phe174, Val224, Ile22, Val26, Cys182, Phe220, Ser178
15	Rhapontigenin	-7.4	Leu227, <b>Cys156*</b> , Trp158, His154, Cys182, Val224, Phe220, Phe65, Ser178
16	Pinostrobin	-7.4	Leu227, <b>Cys156*</b> , Trp158, Cys182, Val224, Phe220, Phe65, Ile22
17	Biochanin A	-7.3	Leu227, <b>Cys156*</b> , Trp158, Cys182, Val224, Phe220, Phe65, Ile22
18	Luteolin	-7.3	Leu227, <b>Cys156*</b> , Trp158, Phe174, Val224, Ser223, Ile22
19	Irilone	-7.3	Leu227, <b>Cys156*</b> , Trp158, Cys182, Phe220, Phe65, Ile22
20	Phloretin	-7.2	Leu227, <b>Cys156*</b> , Trp158, Cys182, Val224, Phe220, Ile22
21	Alpinetin	-7.2	Phe174, Val224, Ile22, Leu227, <b>Cys156*</b> , Trp158
22	Prunetin	-7.2	Leu227, <b>Cys156*</b> , Trp158, His154, Cys182, Val224, Phe220, Phe65, Ser178
23	Genistein	-7.1	Val224, <b>Cys156*</b> , Ile22, Leu227

S.no.	Molecules	Binding energy (kcal/mol)	Interacting amino acids
24	Mesuxanthone A	-7.1	Cys156*, Trp158, Val224, Val26, Phe220, Ile22

**Cys156\***: The rationale for selecting Cys156 lies in its location at the beginning of the acyl-binding groove in DHHC20, enabling it to facilitate the nucleophilic attack on the acyl-CoA donor substrate. Concerning this concept, we identified the above-mentioned 24 molecules targeting Cys156 post-molecular docking.

### 2.3.2 MD simulation and binding free energy calculation:

The affinity and selectivity of the identified candidates for DHHC20 were computationally predicted and rationalized through MD simulation. Molecular docking indicated that the three ligands (lutein, 5-hydroxyflavone, and 6-hydroxyflavone) exhibited stronger binding affinities for the DHHC20 receptor. Consequently, a 100 ns standard MD simulation was conducted to examine the stability of the protein-ligand complexes. The RMSD plot was utilized to predict the conformational changes in the protein backbone from its initial to final structure throughout the simulation. Prior studies have shown that RMSD fluctuations for each protein, relative to its alpha carbon (C $\alpha$ ), typically exhibit a stable pattern during simulations[324]. Notably, after the initial 30 ns of MD simulations, the RMSD pattern for DHHC20 remained consistent for the subsequent simulation period (>20 ns). These specific frames of trajectory were noted until the end of the MD simulation. The average RMSD values for DHHC20 in complex with lutein, 5-hydroxyflavone, and 6-hydroxyflavone were 3.60Å, 4.28Å, and 3.59Å, respectively (**Figure 2.4A** and **Table 2.2**). Additionally, the average ligand-RMSD values for lutein, 5-hydroxyflavone, and 6-hydroxyflavone were 2.39Å, 0.59Å, and 0.65Å, respectively, indicating



that these ligands contributed to the stability of the protein throughout the 100 ns production run (**Figure 2.4B**).

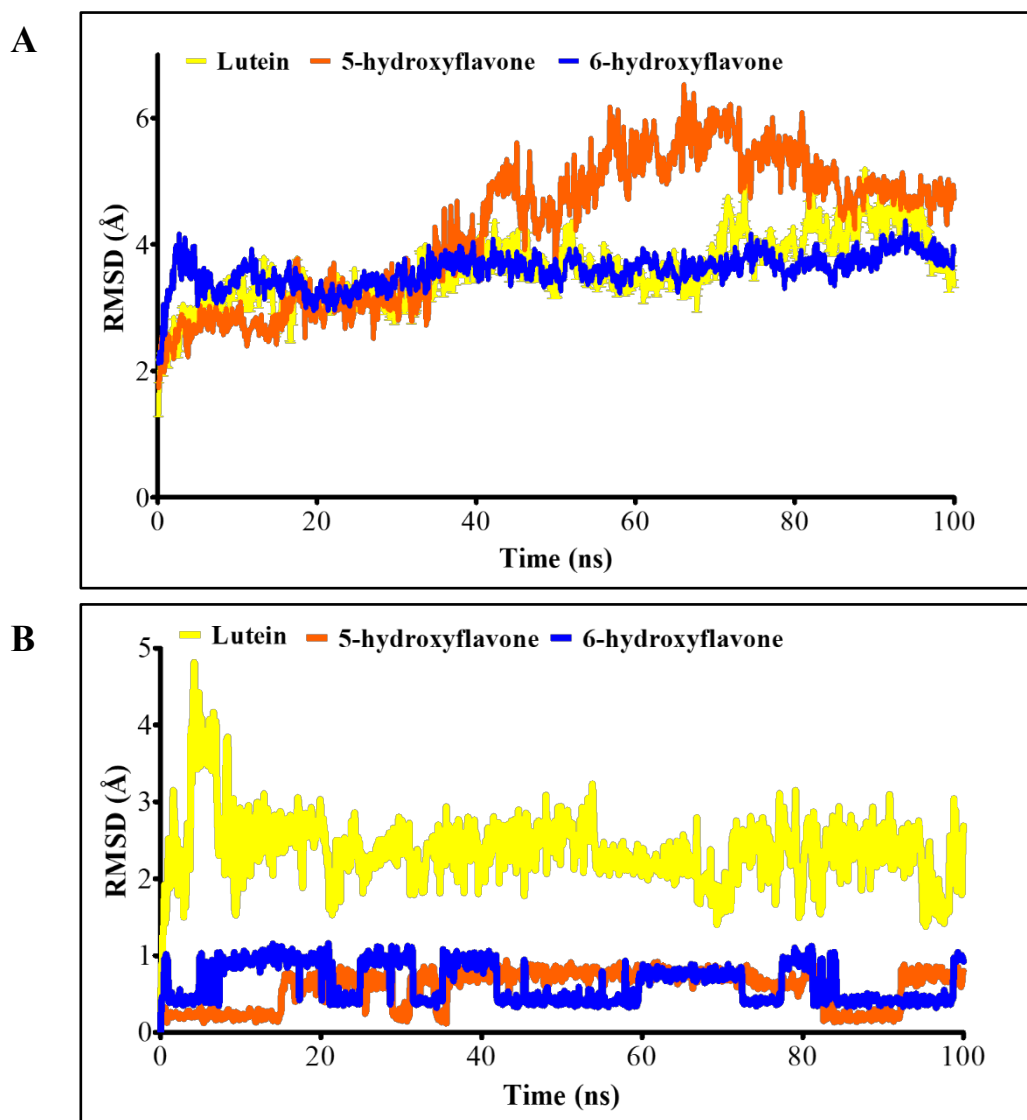


**Figure 2.4** Analysis of RMSD trajectories A) DHHC20 protein trajectories in complex with ligands. B) ligand trajectories in complex with DHHC20 protein throughout 100 ns MD simulation run.

During the MD simulation, we monitored other crucial parameters, including the Rg and SASA, to evaluate the global stability of the complexes. The results indicated that the highest Rg values (up to 29 Å) were observed during the initial frames of the MD simulation for all DHHC20-ligand complexes, suggesting an expansion of the DHHC20-ligand interaction during this period (**Figure 2.5A** and **Table 2.2**). Additionally, SASA was calculated for all protein-ligand complexes, reflecting unfavorable interactions between water molecules and the protein across all complexes (**Figure 2.5B** and **Table 2.2**).

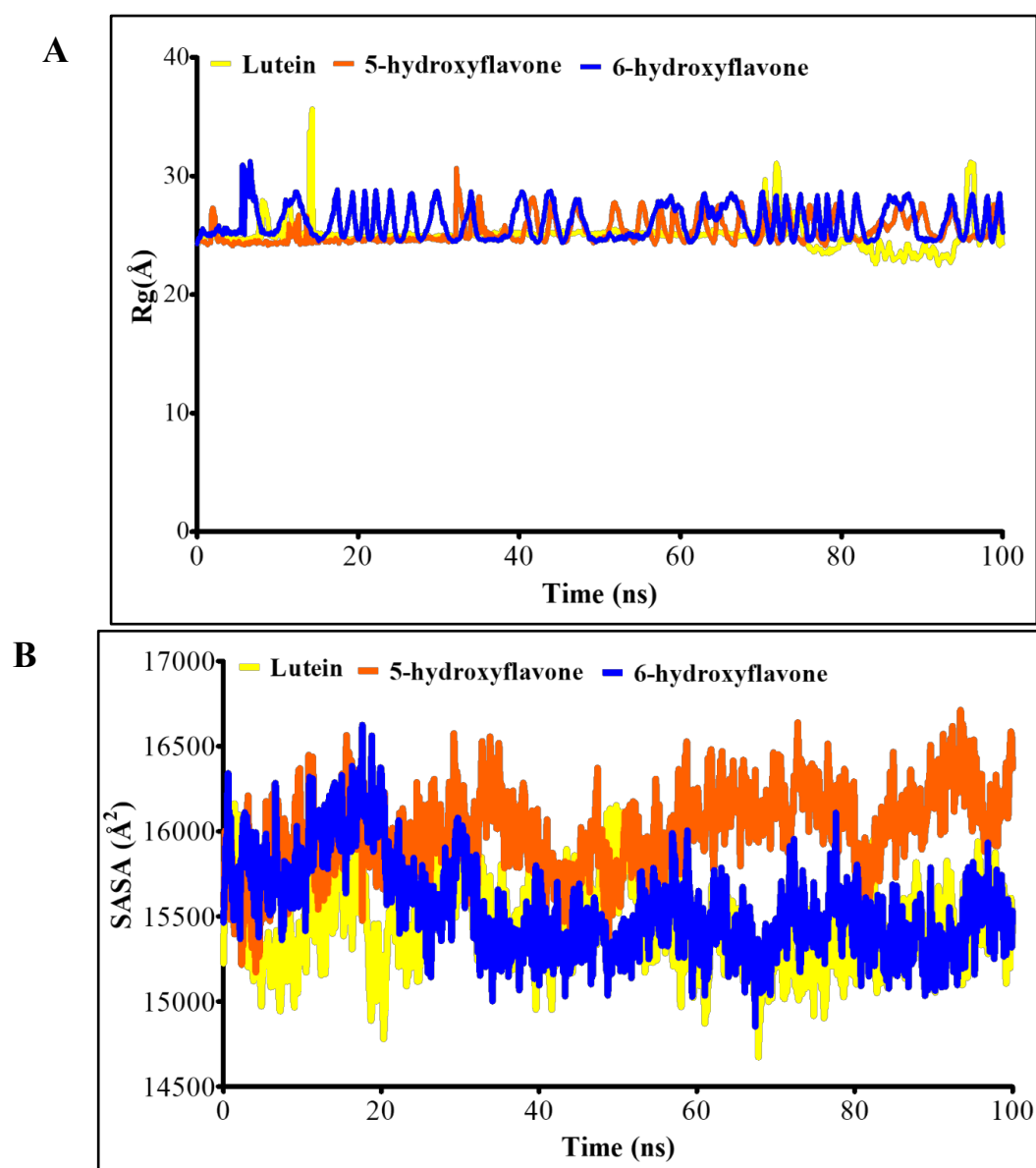


**Figure 2.5** Analysis of A) Rg and B) SASA trajectories of DHHC20 in complex with ligands (lutein, 5-hydroxyflavone, and 6-hydroxyflavone) throughout the 100 ns MD simulation run.

The RMSF evaluates the specific regions of structure (e.g., protein residue) that deviate the most (or least) from their reference structure during the entire production run [325]. We calculated the C $\alpha$ -RMSF for the entire MD simulation trajectories, identifying that only four core residues exhibited the highest RMSF values. These residues, located within the tunnel area of the DHHC20 receptor, were 39, 93, 194, and 282 (**Figure 2.6**).

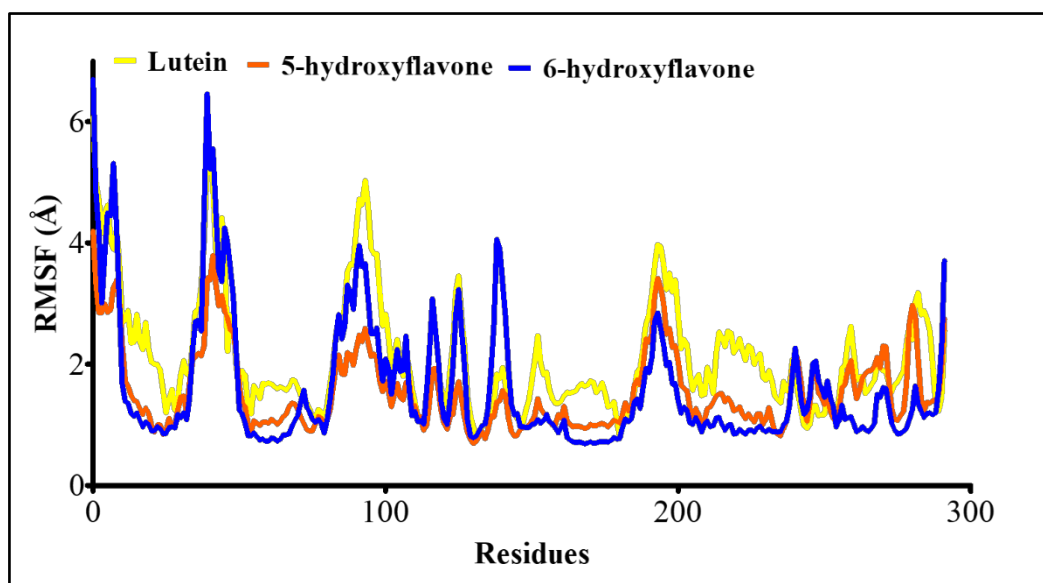


**Figure 2.6** Graphical representation of RMSF plot of DHHC20 in complex with ligands (lutein, 5-hydroxyflavone, and 6-hydroxyflavone) throughout the 100 ns MD simulation run.

We then calculated the  $\Delta G_{\text{bind}}$  using the MM-GBSA method to eradicate inaccurate predictions. The  $\Delta G_{\text{bind}}$  calculations confirmed our docking results, revealing that lutein had highest binding free energy for the DHHC20 receptor compared to 5-hydroxyflavone and 6-hydroxyflavone (**Table 2.3**). The  $\Delta G_{\text{bind}}$  values were -133.80, -81.75, and -75.34 kcal/mol for lutein, 5-hydroxyflavone, and 6-hydroxyflavone, respectively (**Figure 2.7**).

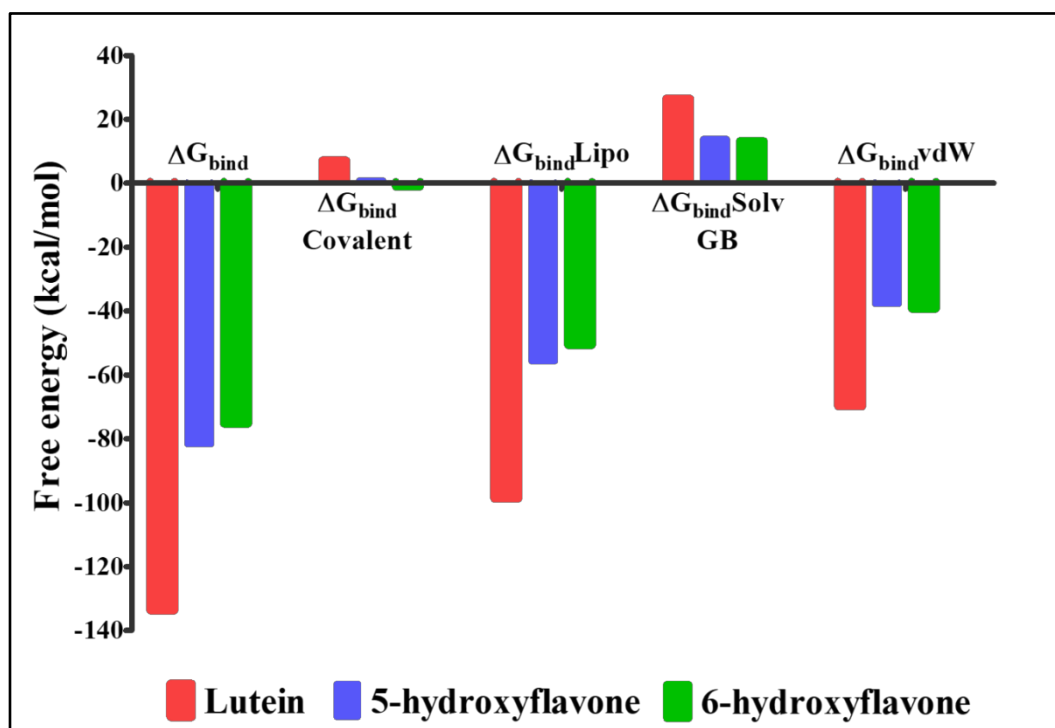


**Figure 2.7** Binding free energies and the corresponding energy components (lipophilic, covalent, and generalized Born electrostatic solvation, and van der Waals) obtained *via* MM-GBSA analysis of DHHC20 in complex with ligands (lutein, 5-hydroxyflavone, and 6-hydroxyflavone) throughout the 100 ns MD simulation run. All values are in kcal/mol.

**Table 2.2** Lists the mean RMSD, Rg, and SASA scores of DHHC20 protein in complex with ligands.

Molecules	RMSD (Å)	Rg (Å)	SASA (Å <sup>2</sup> )
Lutein	3.60	25.00	15443.48
5-hydroxyflavone	4.28	25.35	16004.10
6-hydroxyflavone	3.59	26.10	15550.07

**Table 2.3** Lists the energy components obtained for protein-ligand complexes.

<b>Molecules</b>	$\Delta G_{\text{bind}}$ (kcal/mol)	$\Delta G_{\text{bind}}^{\text{C}}$ <b>ovalent</b> (kcal/mol)	$\Delta G_{\text{bin}}$ <b>dLipo</b> (kcal/mol)	$\Delta G_{\text{bind}}^{\text{SolvGB}}$ (kcal/mol)	$\Delta G_{\text{bind}}^{\text{vdW}}$ (kcal/mol)
Lutein	-133.80	7.17	-98.73	26.57	-69.92
5-hydroxyflavone	-81.75	0.93	-55.73	13.89	-37.88
6-hydroxyflavone	-75.34	-1.15	-50.67	13.24	-39.32

Subsequently, we investigated numerous interactions to evaluate the structural and dynamic characteristics of all ligands within the DHHC20 binding pocket. A time-based illustration of potential interactions and contacts (including hydrophobic interactions, hydrogen bonds, ionic interactions, and water bridges) between the ligands and the DHHC20 binding groove is presented in **Figure 2.8**. The top section shows the total number of identified contacts, while the bottom panel indicates which residues interact with each ligand in every trajectory frame. The color intensity, with darker shades of orange, signifies residues having multiple contacts with the ligands. The most frequent interactions within the DHHC20 groove involved residues Trp158, Cys182, Val216, Phe220, Ser223, and Tyr230 (**Figure 2.8**).

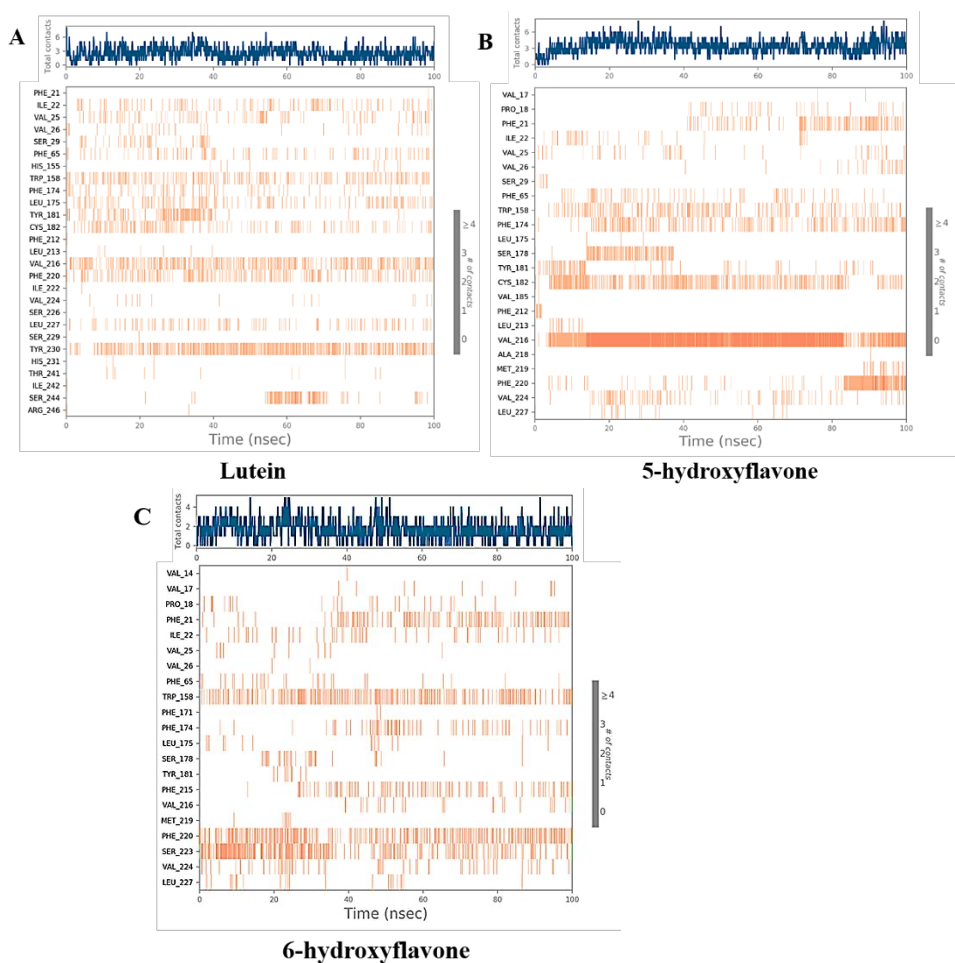


**Figure 2.8** Protein-ligand contact maps were generated between DHHC20 and ligands (lutein, 5-hydroxyflavone, and 6-hydroxyflavone) throughout 100 ns MD simulation run.

The most prominent H-bond interactions included Cys182, Ser244, and Val216 for the lutein, 5-hydroxyflavone, and 6-hydroxyflavone, which occurred more than 30.0% of the time throughout the simulation (**Figure 2.9**). Most of the

identified interactions remained consistently preserved throughout the MD simulation.

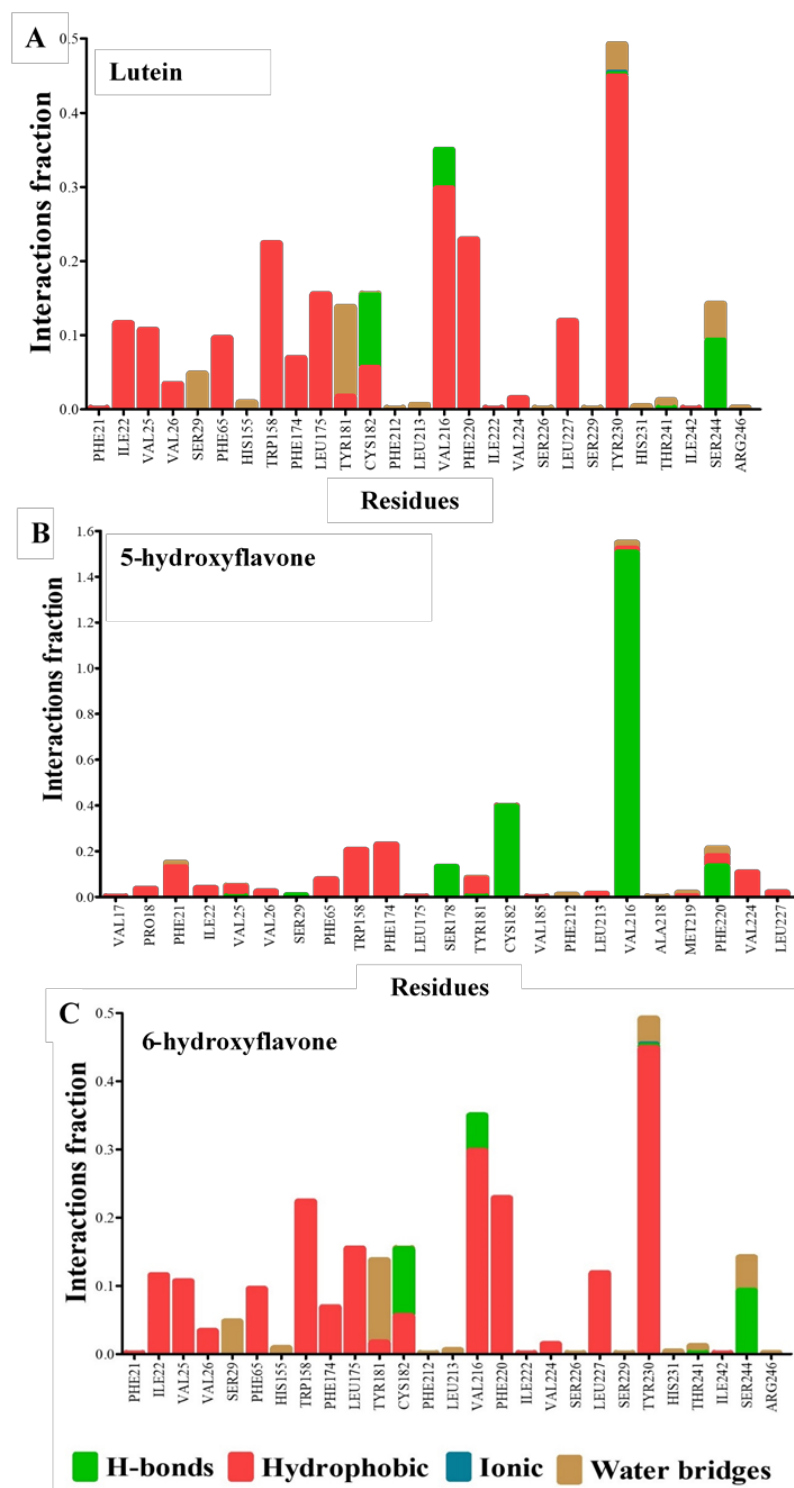


**Figure 2.9** Protein-ligand interactions were monitored between DHHC20 and ligands (lutein, 5-hydroxyflavone, and 6-hydroxyflavone) throughout 100 ns MD simulation run. These interactions are classified into four types: Hydrophobic, H-bonds, Ionic, and Water bridges.

### 2.3.3 The physiochemical and ADMET properties of the selected molecules:

Before classifying any molecule as an effective drug, it is essential to determine whether it meets the criteria for an acceptable drug, which can be ascertained by Lipinski's rule of five (Ro5) [326]. According to this rule, a typical pharmacological molecule must have no more than 10 HBA, no more than 5 HBD, a consensus Log Po/w (cLog P) of less than 5, and a M.W. of less than 500 Da. Compounds that meet these criteria are likely to have better absorption or penetration [326]. Notably, 5-hydroxyflavone and 6-hydroxyflavone satisfied these drug-likeness criteria. All the compounds also had a topological polar surface area (TPSA) below  $140\text{\AA}^2$  (**Table 2.4**). However, strict adherence to the Ro5 has limited the discovery of new drug candidates for targets with flat, groove, or tunnel-shaped binding sites that are challenging to drug with Ro5-compliant compounds. To address this, the concept of beyond the rule of five (bRo5) was proposed. According to this rule, compounds with at least one of the following characteristics M.W. > 700 Da, PSA >  $200\text{\AA}^2$ , HBD > 5, HBA > 10, cLogP < 0 or > 7.5, and more than 20 rotatable bonds—could be considered effective drug candidates [327]. The bRo5 classification includes cyclic peptides, macrocycles, and natural products [327]. By 2018, the U.S. FDA had approved twelve new drugs that followed bRo5 and significantly impacted the treatment of various pathological conditions, including cancer (venetoclax: M.W. = 868.44 g/mol, cLogP = 10.4), hepatitis C virus infection (HCV, velpatasvir: M.W. = 883.02 g/mol, cLogP = 2.5), and cardiovascular diseases (edoxaban: M.W. = 548.06 g/mol, cLogP = -0.9) [328]. Notably, our molecule lutein (M.W. = 568.9 g/mol, cLogP = 9.21) met the bRo5 criteria and could be a suitable candidate for therapeutics (**Table 2.4**).

Another crucial parameter was to investigate the ADMET properties, including absorption, distribution, metabolism, excretion, and toxicity of the three chosen molecules. The ADMET database includes HIA, skin permeability, total drug clearance rate, a substrate/inhibitor of the metabolizing enzyme CYP450, and median lethal dose (LD<sub>50</sub>) toxicity. The ADMET database includes HIA, skin permeability, total drug clearance rate, substrate/inhibitor status for the metabolizing enzyme CYP450, and median lethal dose (LD<sub>50</sub>) toxicity [329]. According to the results, all three selected compounds could be absorbed in the



human intestine ( $Abs > 30\%$ ) (**Table 2.5**). According to research on skin permeability, the higher the negative log  $K_p$  (with  $K_p$  in cm/s), the less permeable the substance is [330]. All three chosen molecules exhibited lower skin permeability (value  $< -3$ ). P-gp is a crucial drug efflux transporter that significantly affects its substrates' gastrointestinal absorption, distribution, metabolism, excretion, and toxicity [331]. Our results showed that 5-hydroxyflavone and 6-hydroxyflavone could be P-gp substrates, while lutein is predicted to be both a P-gp II inhibitor and a substrate (**Table 2.5**).

The next step was to map out the distribution of drugs throughout the body, starting with the volume of distribution at steady state ( $VD_{ss}$ ). Drugs that bind to tissues typically exhibit a greater apparent volume of distribution, while those that bind to plasma proteins tend to have a reduced apparent volume of distribution [332]. Our results revealed that the  $VD_{ss}$  for all three molecules ranged from -0.23 to 0.214 logL/kg (**Table 2.5**). Secondly, we assessed the ability of molecules to cross the BBB. Studies indicate that molecules with a log BB value greater than 0.3 can easily penetrate the BBB. In contrast, molecules with a log BB value less than -1 have limited ability to traverse the BBB [333]. Except for lutein, the other two molecules had log BB  $> 0.3$ . The remaining significant parameters, such as human unbound fraction and central nervous system (CNS) permeability of the selected molecules, are listed in **Table 2.5**.

Next, we evaluated how the body metabolizes these drugs. Cytochrome P450 enzymes (CYPs) are hemoproteins that often serve as monooxygenases and are involved in the metabolism of medicines, fatty acids, steroids, bile acids, and carcinogens [334]. Our data revealed that all three molecules could be CYP3A4 substrates. The excretion profile indicated that all three molecules had an overall excretion rate between 0.317 and 0.924 log ml/min/kg (**Table 2.5**).

Lastly, we assessed the toxicity profile of the identified molecules. Interestingly, none of the compounds were predicted to be skin-sensitive or hepatotoxic. All the molecules examined for acute toxicity in rats had  $LD_{50}$  values between 1.89 and 3.50 mol/kg. Notably, except for lutein, the other two molecules were favorable for the Ames test, which detects whether a molecule is mutagenic (**Table 2.5**). A positive Ames test indicates that the molecule may act as a carcinogen [335]. Quite apart from the obtained results, 5-hydroxyflavone, and

6-hydroxyflavone are ineffective for treating cancer. It has been shown that 5-hydroxyflavone and 6-hydroxyflavone augment the recombinant human soluble-tumor necrosis factor-related apoptosis-inducing ligand 1 (rhSTRAIL), mediated cancer cell apoptosis [336]. Thus, *in vitro* determination of the effects of 5-hydroxyflavone, and 6-hydroxyflavone on the DHHC20-mediated cancer cell growth needs to be clarified.

**Table 2.4** Lists the physicochemical characteristics of lutein, 5- hydroxyflavone, and 6-hydroxyflavone.

Descriptor	Lutein	5-hydroxyflavone	6-hydroxyflavone
M.W. (g/mol)	568.886	238.242	238.242
Consensus Log P <sub>o/w</sub>	9.21	3.05	2.85
Rotatable bonds	10	1	1
H-bond acceptors	2	3	3
H-bond donors	2	1	1
MR	186.76	69.94	69.94
TPSA	40.46	50.44	50.44
Fraction Csp <sup>3</sup>	0.45	0	0
Lipinski #violations	2	0	0
Ghose #violations	4	0	0
Veber #violations	0	0	0
Egan #violations	1	0	0
Muegge #violations	1	0	0
Bioavailability Score	0.17	0.55	0.55
PAINS #alerts	0	0	0

<b>Descriptor</b>	<b>Lutein</b>	<b>5-hydroxyflavone</b>	<b>6-hydroxyflavone</b>
Brenk #alerts	2	0	0
Lead likeness #violations	3	2	2

**Table 2.5** Lists the ADMET characteristics of lutein, 5-hydroxyflavone, and 6-hydroxyflavone.

<b>Descriptor</b>	<b>Properties</b>	<b>Lutein</b>	<b>5-hydroxyflavone</b>	<b>6-hydroxyflavone</b>
Absorption	Water Solubility (log mol/L)	-6.822	-3.683	-3.77
Absorption	CaCo2 permeability (log papp in 10 <sup>-6</sup> cm/s)	1.251	1.263	1.277
Absorption	Human intestinal absorption (% Absorbed)	89.781	94.776	95.237
Absorption	Skin permeability (log Kp)	-2.741	-2.775	-2.736
Absorption	p-glycoprotein substrate	Yes	Yes	Yes
Absorption	p-glycoprotein inhibitor I	No	No	No
Absorption	p-glycoprotein inhibitor II	Yes	No	No
Distribution	VDss (log l/kg)	-0.23	0.214	-0.031
Distribution	Human fraction unbound (Fu)	0	0.151	0.165

<b>Descriptor</b>	<b>Properties</b>	<b>Lutein</b>	<b>5-hydroxyflavone</b>	<b>6-hydroxyflavone</b>
Distribution	BBB permeability (log BB)	-0.215	0.462	0.418
Distribution	CNS permeability (log PS)	-1.144	-1.733	-1.749
Metabolism	CYP2D6 substrate	No	No	No
Metabolism	CYP3A4 substrate	Yes	Yes	Yes
Metabolism	CYP1A2 inhibitor	No	Yes	Yes
Metabolism	CYP2C19 inhibitor	No	Yes	Yes
Metabolism	CYP2C9 inhibitor	No	No	Yes
Metabolism	CYP2D6 inhibitor	No	No	No
Metabolism	CYP3A4 inhibitor	No	No	No
Excretion	Total Clearance (log ml/min/kg)	0.924	0.325	0.317
Excretion	Renal OCT2 substrate	No	No	No
Toxicity	AMES toxicity	No	Yes	Yes
Toxicity	Maximum tolerated dose (human)	-1.068	-0.09	0.015
Toxicity	hERG I inhibitor	No	No	No
Toxicity	hERG II inhibitor	Yes	No	No
Toxicity	Oral rat acute toxicity (LD <sub>50</sub> ) (mol/kg)	3.491	1.991	1.893

Descriptor	Properties	Lutein	5-hydroxyflavone	6-hydroxyflavone
Toxicity	Oral rat chronic toxicity (LOAEL) (log mg/kg_bw/day)	2.572	1.582	1.613
Toxicity	Hepatotoxicity	No	No	No
Toxicity	Skin sensitization	No	No	No
Toxicity	<i>T.Pyriformis</i> toxicity (log µg/L)	0.335	0.699	0.793
Toxicity	Minnow toxicity (log mM)	-2.213	1.205	0.637

#### 2.3.4 Identification of molecular targets:

Globally, the use of small natural and synthetic molecules as acceptable drug candidate have grown dramatically in recent years [337]. Identifying their disease-related molecular targets is one method of assessing their potential for therapeutic uses. To do this, we also evaluated the molecular targets of lutein, 5-hydroxyflavone, and 6-hydroxyflavone. The results revealed that nuclear receptors (NR), kinases, and GPCR, (Family A) were the primary targets of the selected molecules (**Figure 2.10**). These *in silico*-predicted targets (NR, GPCR, and kinases) are among the most common DHHC substrates [298]. For example, estrogen receptor (which belongs to the NR-superfamily) is reported to be *S*-palmitoylated by DHHC7 and DHHC21 to boost breast cancer proliferation [338]. Similarly, palmitoylation is critical in regulating GPCR signaling [298]. Additionally, several *S*-palmitoylated kinases, including AKT, JNK, JAK1, and p38- MAPK, are connected to severe disease outcomes [339]. Therefore, the *S*-palmitoylation status of the identified targets enabled us to further evaluate the three selected candidates as potential DHHC-mediated *S*-palmitoylation inhibitors. A more precise description has been given in **Appendix Table A3**.

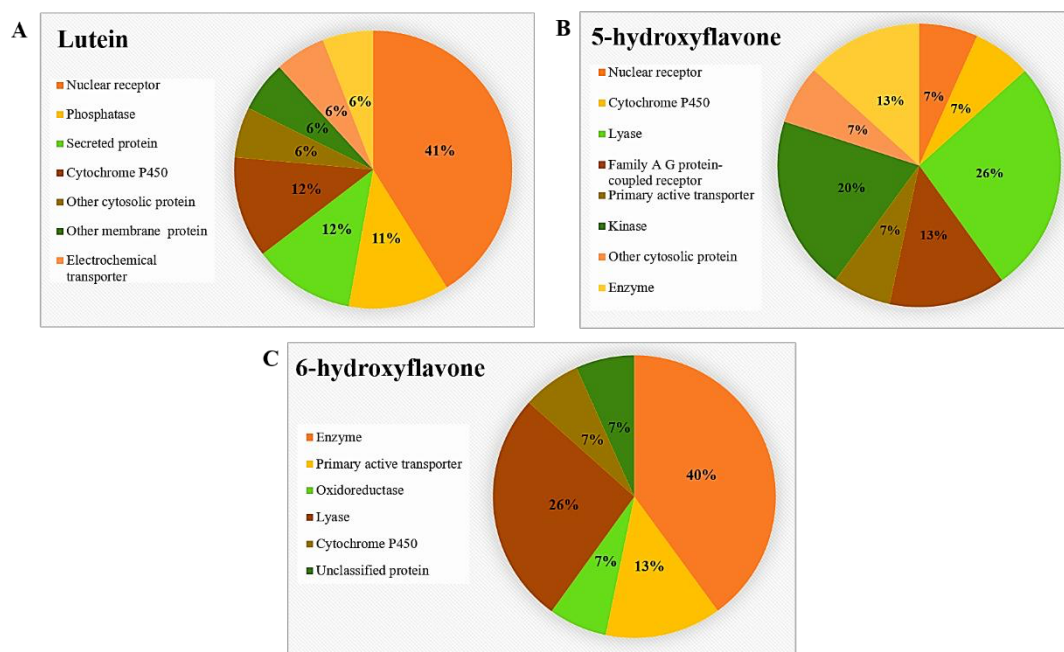


**Figure 2.10** The pie chart depicting the molecular targets of the selected compounds: A) lutein, B) 5-hydroxyflavone, and C) 6-hydroxyflavone.

### 2.3.5 PASS analysis: Predictions of biological activity:

The PASS analysis was utilized to evaluate the biological activities of the selected compounds. This study disclosed that lutein, 5-hydroxyflavone, and 6-hydroxyflavone could be a potent anti-neoplastic, antioxidant, and effective apoptotic agonists (**Table 2.6**). It is well established that DHHC20 fosters the capacity of cells to transform into cancerous; limiting DHHC20 with compounds such as carotenoids and flavonoids could prove a potential strategy to combat cancer.

**Table 2.6** Lists the biological activities associated with lutein, 5-hydroxyflavone, and 6-hydroxyflavone.

Descriptor	Lutein		5-hydroxyflavone		6-hydroxyflavone	
	Pa	Pi	Pa	Pi	Pa	Pi
Anti-oxidant	0.609	0.004	0.631	0.004	0.521	0.017
Anti-neoplastic	0.913	0.005	0.703	0.026	0.619	0.041

Descriptor	Lutein		5-hydroxyflavone		6-hydroxyflavone	
	Pa	Pi	Pa	Pi	Pa	Pi
Descriptor	Lutein		5-hydroxyflavone		6-hydroxyflavone	
	Pa	Pi	Pa	Pi	Pa	Pi
Anti-hypercholesterolemia	-	-	-	-	0.558	0.016
Anti-parasites	0.187	0.102	0.428	0.025	-	-
Anti-carcinogenic	0.623	0.004	0.539	0.016	0.532	0.017
Lipid metabolism regulator	0.805	0.005	0.578	0.025	0.511	0.042
Anti-acne	0.674	0.003	-	-	-	-
Apoptosis agonist	0.889	0.004	0.808	0.008	0.704	0.014
Reductant	0.943	0.002	0.502	0.024	0.479	0.025
Fatty-acyl-CoA synthase inhibitor	0.272	0.134	0.640	0.002	0.604	0.025
Anti-allergic	-	-	0.402	0.052	0.398	0.053
Anti-viral (Rhinovirus)	0.366	0.135	0.381	0.118	0.362	0.141
Anti-inflammatory, intestinal	0.463	0.028	0.623	0.027	0.546	0.044
Anti-bacterial	0.531	0.014	0.371	0.038	0.358	0.058
Anti-fungal	0.584	0.020	0.489	0.032	0.420	0.046
Chemo-preventive	0.877	0.003	0.523	0.013	0.533	0.008

## **2.4 Conclusion:**

The association between various DHHC isoforms and cellular disruptions has been extensively studied. However, the lack of effective inhibitors is a major problem in the in-depth investigation of DHHC-related disorders. In light of this, we selected 115 well-known plant-based bioactive compounds that could serve as potential inhibitors of DHHCs and conducted molecular docking with them. Notably, 24 molecules interacted with the Cys156 residue with a higher negative B.E. than 2-BP. After that, we subjected the top three molecules for further validation through MD simulations. From the results, we concluded that lutein (a carotenoid molecule) stabilized more in the DHHC20 groove than two flavonoid molecules (5-hydroxyflavone and 6-hydroxyflavone). The long aliphatic chain of lutein (mimicking palmitic acid) might be the reason why it stabilized more in the DHHC20 binding pocket. We further evaluated the drug-likeness and ADMET profiles of the three molecules. The findings obtained strongly imply that the compounds had acceptable pharmacokinetic characteristics. In addition, we conducted a PASS-analysis, which indicated that all these molecules are strongly associated with health-beneficial activities, such as apoptosis-agonist or antioxidant. The results showed that these compounds can be used as DHHC-targeting inhibitors and effectively reduce DHHCs-mediated perturbations. The obtained results can be a good starting point for further research using these natural molecules as DHHC inhibitors.







## Chapter 3: Unraveling the potential contribution of DHHC2 in cancer biology *via* untargeted metabolomics

---

---

### 3.1 Introduction:

The heightened hydrophobicity resulting from palmitoylation is a critical biochemical characteristic that impacts various aspects of proteins and introduces variability to the roles of DHHCs in different cases [191]. For example, DHHC2-mediated *S*-palmitoylation of AGK enables its translocation to the plasma membrane and activates the PI3K-AKT-mTOR signaling pathway in ccRCC [340]. Conversely, the palmitoylation of CKAP4 through DHHC2 is required for its translocation from the endoplasmic reticulum to the plasma membrane, where palmitoylated CKAP4 acts as a receptor for APF, and inhibiting the CKAP4 palmitoylation prevents the APF-induced alterations in the expression of genes like vimentin and E-cadherin, hindering its ability to regulate cell proliferation [115, 116, 341]. Similarly, it was shown that reduced expression of DHHC2 is associated with gastric tumor tissues by qRT-PCR and immunostaining. Low DHHC2 expression was observed in 44.7% (211/472) of gastric adenocarcinoma patients, significantly correlating with lymph node metastasis ( $P$  value < 0.001) and histological grade ( $P$  value < 0.001) [342]. Again, increased DHHC2 expression hindered the proliferation, migration, and invasion of the HCC cell line Bel-7402 *in vitro* [114]. Conclusively, from the above studies, we found that the hydrophobicity introduced by DHHC2 to different proteins varied its role in different cancers.

Cancer cells also modify their cellular metabolism and associated pathways to inappropriately proliferate and maintain the energy fuel. For example, The Warburg effect, initially observed by Otto Warburg in the 1920s, delineated that cancer cells predominantly rely on glycolysis as their primary energy source, even in the presence of oxygen [293]. Cancer cells also depend on utilizing glutamine, lipids, amino acids, and redox processes to facilitate tumor proliferation and withstand challenging conditions [294]. The roles of several key regulators in cancer metabolism, including EGFR and p53, have been extensively studied [295, 343]. A research study by Yang et al. (2020) revealed

that the EGFR signaling pathway activates phosphorylated ETS like-1 protein Elk-1 (ELK1), leading to the transcription of glutamate dehydrogenase 1 (GDH1) and increased glutamine metabolism [295]. Another, e.g., included mutant p53, which stimulates the Warburg effect. This stimulation occurs by promoting glucose transporter (GLUT1) translocation to the plasma membrane, thereby augmenting tumor metabolism [343].

Furthermore, there is evidence documenting the role of palmitoylated protein substrates and their impact on cellular metabolic changes. Recently, Chen et al. (2024) group identified DHHC9 as a crucial regulator of the Warburg effect by activating LDHA. They proved that DHHC9-mediated palmitoylation of Cys163-LDHA is increased in cancer. Palmitoylation of LDHA enhances lactate production while decreasing ROS generation. Substituting endogenous LDHA with palmitoylation-deficient mutant results in reduced proliferation of pancreatic cancer cells, increased T-cell infiltration, and restricted tumor growth [344]. Another study reported that palmitoylated- prolactin-releasing peptide 31 analog (palm11-PrRP31) improved biochemical parameters, including lowered body weight and glucose tolerance *via* a significant decrease of formate and 1-methyl nicotinamide in spontaneously hypertensive rats (SHR) and alanine, allantoin, dimethylamine, and N-butyryl glycine in WKY rats [345]. The above-mentioned findings showed that palmitoylated protein participates in cellular metabolism. However, the direct effect of DHHCs on the cancer condition and how they regulate cellular metabolism remain inadequately explored in current scientific literature.

As mentioned above, DHHC2 has various roles in cancer progression and prevention through modification of various substrates, but how it acts on cellular metabolism is not known yet. Therefore, we aimed to explore the effect of DHHC2 on the cancer system by quantitatively identifying associated metabolites and metabolic pathways using LC-MS/MS-based untargeted metabolomics. We conducted comprehensive metabolites profiling of the human embryonic kidney-293T (HEK-293T) cell line with DHHC2-Knockdown (DHHC2-KD), DHHC2-Overexpression (DHHC2-OE), and empty vector control (Ctrl) conditions. Our dataset revealed the identification of a total of 73 metabolites encompassing all the conditions, with

only 22 showing significant differences in univariate analysis. Also, we performed pathway analysis with metabolites having  $VIP \geq 0.7$ ,  $P$  value  $\leq 0.05$ , and fold change (FC)  $> 2$  in DHHC2-OE (upregulated) and FC  $< 0.5$  in DHHC2-OE or FC  $> 2$  in DHHC2-KD condition (downregulated). As a result, we revealed significant expression of pyrimidine metabolism, urea cycle, and aspartate metabolism due to the abundance of onco-metabolites such as glutamine, uridine, and glutamic acid in the DHHC2-KD condition. However, DHHC2 overexpression resulted in a higher expression of metabolites previously reported to be associated with anti-cancer activity, such as betaine and 5'-methylthioadenosine (5'-MTA). Overall, this study sheds light on the changes mediated by DHHC2 in a cellular metabolome and suggests avenues for further investigation into other DHHC isoforms and their metabolic aspects

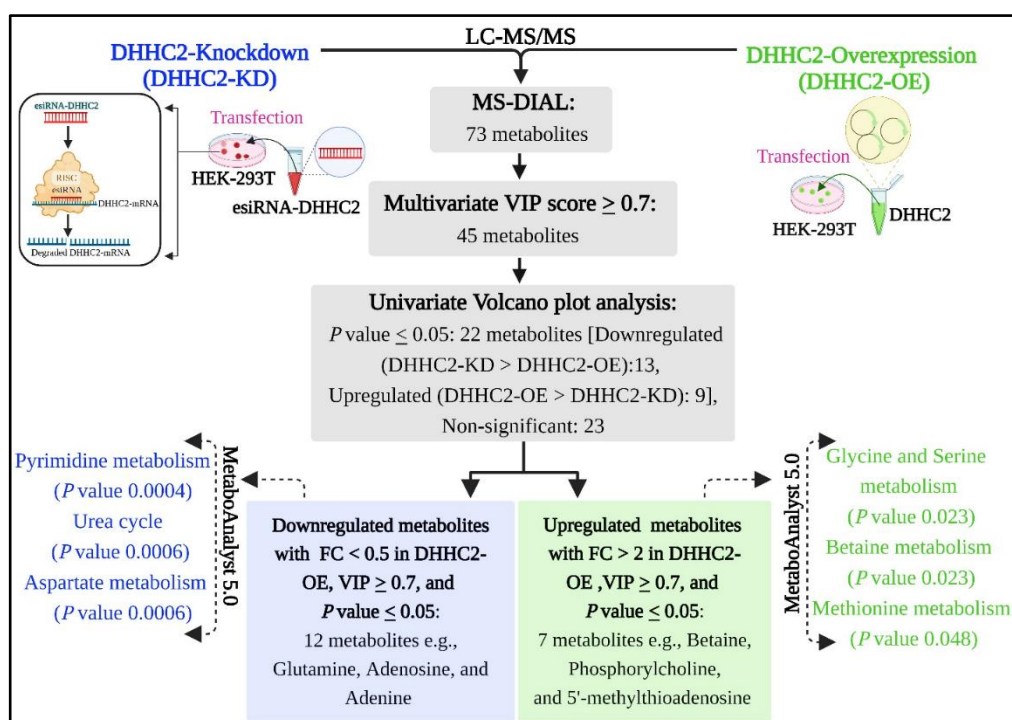


**Figure 3.1** Schematic representation of the workflow (The figure was drawn using [www.biorender.com](http://www.biorender.com)).

(Figure 3.1).

## 3.2. Material and methods:

### 3.2.1 Cell culture and reagents:

The HEK-293T cell line was obtained from the National Centre for Cell Science (NCCS), Pune, India, and cultured in Dulbecco's Modified Eagle's Medium (DMEM; Gibco, Thermo Fisher Scientific, USA) with 10% fetal bovine serum

(FBS; Gibco, Thermo Fisher Scientific, USA). Cultures were maintained in a humidified atmosphere with 5% CO<sub>2</sub> at 37°C [346]. Antibodies, including HA-Tag antibody [(Ab), sc-7392], horseradish peroxidase (HRP)-conjugated IgG secondary mouse-Ab (sc-516102), and secondary rabbit-Ab (sc-2357) were sourced from Santa Cruz (Dallas, TX, United States). Glyceraldehyde-3-phosphate dehydrogenase rabbit monoclonal-Ab (GAPDH mAb; 5174S) and p53-Ab (9284S) were procured from Cell Signaling Technology (Beverly, MA, United States).

### **3.2.2 Cell culture, transfection, and RNA extraction:**

Cells were seeded at  $4 \times 10^5$  cells/well in a six-well cluster plate and cultured for 24 hours (hrs). The media was then replaced with serum-free DMEM. 2 hr after adding serum-free media, cells at 40-50% confluence were transiently transfected with 0.8 µg of DHHC2-HA-tag plasmid DNA/well and an empty vector plasmid (gifts from Professor Hening Lin, Department of Chemistry and Chemical Biology at Cornell University, Ithaca, New York) using the calcium phosphate transfection method for the next 6-7 hrs [347]. For endoribonuclease prepared small interfering RNA (esiRNA)-mediated knockdown, cells were transfected with 0.8µg of DHHC2-esiRNA/well (Sigma-Aldrich, St. Louis, MO, USA) and siRNA universal negative control #1/well (Sigma-Aldrich, St. Louis, MO, USA) in serum-free DMEM for 6-7 hrs using siRNA transfection reagent (Santa Cruz, Dallas, TX, United States). Subsequently, the media was replaced with 10% serum-containing DMEM for both transfection methods. Lastly, after 48 hrs of transfection, the cells were collected and utilized for qRT-PCR, western blot, and LC-MS/MS analysis [348, 349]. For qRT-PCR, RNA extraction was performed using Trizol™ reagent (Invitrogen; Thermo Fisher Scientific, USA) following the manufacturer's protocols. All the independent experiments were conducted in biological triplicate.

### **3.2.3 Parameters for qRT-PCR:**

cDNA was synthesized from 1 µg of total RNA using the cDNA synthesis kit (Thermo Fisher Scientific, USA). The mRNA expression of the synthesized cDNA was quantified by SYBR Green master mix (Applied biosystems; Thermo Fisher Scientific, USA) in a 10µl total volume [350, 351]. Cycling conditions included initial denaturation at 50°C for 2 minutes (mins) and 95°C

for 2 mins, followed by 40 cycles of 95°C for 15 seconds and 60°C for 1 min. To calculate the relative FC observed in the qRT-PCR analysis, the comparative Ct ( $2^{-\Delta\Delta C_t}$ ) method was utilized [352]. GAPDH was used as endogenous control. Notably, the list of primers used for DHHC2, GAPDH, MDM2, p53, and CAD are included in **Table 3.1**.

**Table 3.1** List of primers used in mRNA expression analysis using qRT-PCR.

Gene	Forward primer (5'-3')	Reverse primer (5'-3')
GAPDH	ACCCACTCCTCCACCTTTGAC	TGTTGCTGTAGCCAAATTC GTT
DHHC2	ATGGCTGCTCCTTTCCAACCTT	GTAAGAAGGTGGCTCTGG GAC
MDM2	GCCCTTCGTGAGAATTGGCT	AAGCCCTCTTCAGCTTGTG TT
p53	GCTGCTCAGATAGCGATGGT	CTCATAGGGCACCACCAC AC
CAD	AGCACCTGGGAATTGTTGGG	CAGTGGATAACCTGTGGC CT

### 3.2.4. Western blot analysis:

After 48 hrs of transfection, cells were collected and washed twice with 1x PBS (10 mM Na<sub>2</sub>HPO<sub>4</sub>, 1.8 mM KH<sub>2</sub>PO<sub>4</sub>, 2.7 mM KCl, 137 mM NaCl). Then, the cells were lysed in lysis buffer containing 150 mM NaCl, 50 mM Tris-Cl, 1% NP-40, 1 mM EDTA, pH 8.0, and 1% protease inhibitor cocktail). After this, the Bradford assay was used for protein quantification. An equal amount of protein samples (25 µg) were separated by 10% SDS-PAGE [90 volts, 120 mins, room temperature (RT)] and transferred to a nitrocellulose membrane (100 volts, 120 min, and 4°C). Following this, the membrane was blocked with 5% bovine serum albumin (BSA) in 1xPBST (10 mM Na<sub>2</sub>HPO<sub>4</sub>, 1.8 mM KH<sub>2</sub>PO<sub>4</sub>, 2.7 mM KCl, 137 mM NaCl, and 0.1% Tween-20) for 1 hr. The membrane was incubated overnight at 4°C with primary rabbit/mouse IgG antibodies (1:1000), followed by washing with 1x PBST (thrice, 5 min). Afterward, the membrane

was incubated with HRP-conjugated anti-rabbit/anti-mouse IgG secondary antibodies (1:2000) for 2 hrs at RT, followed by washing with 1x PBST (thrice, 5 min). The membrane was developed using a standard chemiluminescent substrate (BioRad), and images were captured on the Fusion Solo S chemidoc system (Vilber). GAPDH was used as loading control, and protein band intensities were quantified using Image J software (NIH) relative to their respective loading controls [353].

### **3.2.5 Metabolites extraction:**

After transfection, the cells were collected and stored at -80°C. For extraction, the falcon tubes containing the cells were initially thawed in an ice bath. Afterwards 3ml of chilled MilliQ was added and subjected the cells to three cycles of rapid freezing in liquid nitrogen followed by slow thawing in an ice bath. Cells were lysed through five cycles of ultrasonic extraction, each consisting of 1 min at 100% pulse. A mixture of methanol and chloroform (1:1) was added to the lysed cells to extract intracellular metabolites. The mixtures were incubated at 4°C for 1 hr with intermittent vortexing every 10 mins. Subsequently, the samples were centrifuged at 5000 rpm (or 2400 xg) and 4°C for 30 mins. The upper aqueous phase (polar and semi-polar metabolites) was lyophilized, and the lower organic phase (non-polar metabolites) was dried in SpeedVac and stored at -80°C. On the day of analysis, the upper phase samples were reconstituted in HPLC-grade methanol, and the lower phase in a methanol-acetonitrile (2:3) mixture (Sigma-Aldrich, St. Louis, MO, USA) to a final concentration of 1 mg/ml, and 10 µL of each sample was used for LC-MS/MS analysis [292, 354, 355].

### **3.2.6 Metabolomics data analysis:**

To assess the metabolic perturbations post-DHHC2 silencing and overexpression, a total of 12 samples [9 samples (three biological triplicates of three conditions), and three pool quality control (QC)] were subjected to LC-MS/MS-based metabolite identification. ThermoFisher Scientific Vanquish HPLC system coupled to a ThermoFisher Scientific Q-Exactive Orbitrap mass spectrometer (Thermo Scientific, UK) was utilized for metabolomics data acquisition. Electrospray ionization was employed to enhance the coverage and identification of metabolites. Two chromatographic runs were performed using



hydrophilic interaction chromatography (HILIC) and reverse-phase (C18) column. For HILIC column compound separation, the mobile phase consisted of 20 mM ammonium acetate in water (solvent A) and acetonitrile (solvent B). The elution gradient was set as 0 min, 95% B; 15 min, 50% B; 23 min, 5% B; 25 min, 5% B; 26 min, 95% B; 40 min, 95% B. The flow rate was 0.3 mL/min. In the reverse phase, water with 0.1% formic acid (solvent A) and acetonitrile with 0.1% formic acid (solvent B) were used. The elution gradient was set as 0 min, 1% B; 20 min, 99% B; 25 min, 99% B; 28 min, 1% B; 40 min, 1% B. The flow rate was 0.3 mL/min [356]. Each sample had an injection volume of 10  $\mu$ L, and the column temperature was maintained at 35°C. The mass scan range was spanned from 100 to 1,000 Da, with a resolution of 60,000 for MS and 15,000 for MS/MS. The flow rates for Auxiliary and Sweep gas were set at 15 and 1 arb, respectively. The vaporizer temperature was 200°C. Pooled quality control samples were analyzed periodically (every 3 samples) throughout the analytical run. This approach aimed to assess analytical variability and ensure the reliability of the data obtained through LC-MS/MS [357, 358]. The samples were normalized *via* QC sample: average peak intensity of metabolite/ intensity in pool QC sample.

### **3.2.7 Identification of the metabolites through MS-DIAL:**

The raw spectral data files (.raw) were analyzed using MS-DIAL version 4.9 <http://prime.psc.riken.jp/compms/msdial/main.html> [359]. The retention time was 40 minutes, and mass collection occurred within the 100-1000 Da scan range. Peak detection utilized a linear-weighted moving average, with minimum peak width and height parameters set at 5 Da and 500 amplitude, respectively. Three levels of smoothing scans were implemented. Following this, spectral centroiding was carried out by integrating mass spectra within a range of  $\pm 0.01$  Da in MS1 and  $\pm 0.025$  Da in MS2. The acquired spectra were compared against the various .MSP metabolite libraries such as GNPS, North mass bank, HMDB, and MoNA database, allowing a tolerance of 0.01 Da for MS1 and 0.05 Da for MS2, respectively. Common adducts  $[(M+H)^+]$ ,  $[(M+NH_4)^+]$ ,  $[(M+Na)^+]$ ,  $[(M-H_2O-H)^-]$ , and  $[(M-H)^-]$ , etc.] were annotated before the identification process. For further validation, metabolites were chosen based on their matched MS/MS spectra and charge-to-mass ratio ( $m/z$ ) [359, 360].

### 3.2.8 Statistical analysis:

MetaboAnalyst 5.0 <https://www.metaboanalyst.ca>, a web-based analytical pipeline designed for high-throughput metabolomics studies, was utilized. A range of multivariate and univariate statistical approaches were utilized for metabolomics analysis. Multivariate approaches included principle component analysis (PCA), partial least squares-discriminant analysis (PLS-DA), and correlation using variable importance in projection (VIP). *P* value and FC-based volcano plot was utilized as univariate analysis. To gain insights into the biologically altered pathways, a functional enrichment analysis of the experimental data was carried out using MetaboAnalyst 5.0 [361]. The statistical data were plotted through GraphPad Prism 8.0 <https://graphpad-prism.software.informer.com/8.0>, ChemDraw Ultra 12.0 <https://chemistrydocs.com/chemdraw-ultra-12-0>, and BioRender software <https://www.biorender.com>.

## 3.3 Results:

### 3.3.1 Silencing of *DHHC2* gene post-esiRNA mediated knockdown in HEK-293T cell line:

Metabolomics provides an unbiased perspective to understand how physiological processes are interconnected with external factors and conditions, and it enables the measurement of responses to disturbances, particularly those associated with diseases [362]. In this context, the pivotal contribution of *DHHC2* in tumor biology has captured our interest for extensive exploration of its role in cancer metabolism using an untargeted metabolomics-based approach. Our primary focus was unraveling the metabolic consequences in cancer cells with silenced *DHHC2* (*DHHC2*-KD) compared to those with overexpressed *DHHC2* (*DHHC2*-OE). We transfected *DHHC2* into the HEK-293T cell line through the calcium phosphate transfection. The successful uptake of *DHHC2*-HA tag plasmids into cells was confirmed by western blot analysis, where *DHHC2* (42 kDa) was detected, with GAPDH (37 kDa) serving as a loading control (**Figure 3.2A**). Conversely, to inhibit *DHHC2* activity in the HEK-293T cell line, we employed esiRNA-mediated transient knockdown. We assessed the knockdown efficiency through qRT-PCR, revealing a 60-70% reduction in *DHHC2* mRNA expression post-transient knockdown compared to

KD-negative control and Ctrl samples with a  $P$  value  $< 0.001$  (**Figure 3.2B**). However, a significant increase has been observed in the DHHC2 mRNA expression compared to both the control conditions post-DHHC2 overexpression ( $P$  value  $< 0.01$ ) (**Figure 3.2B**). From here, we have continued our study with Ctrl, DHHC2-KD, and DHHC2-OE conditions.

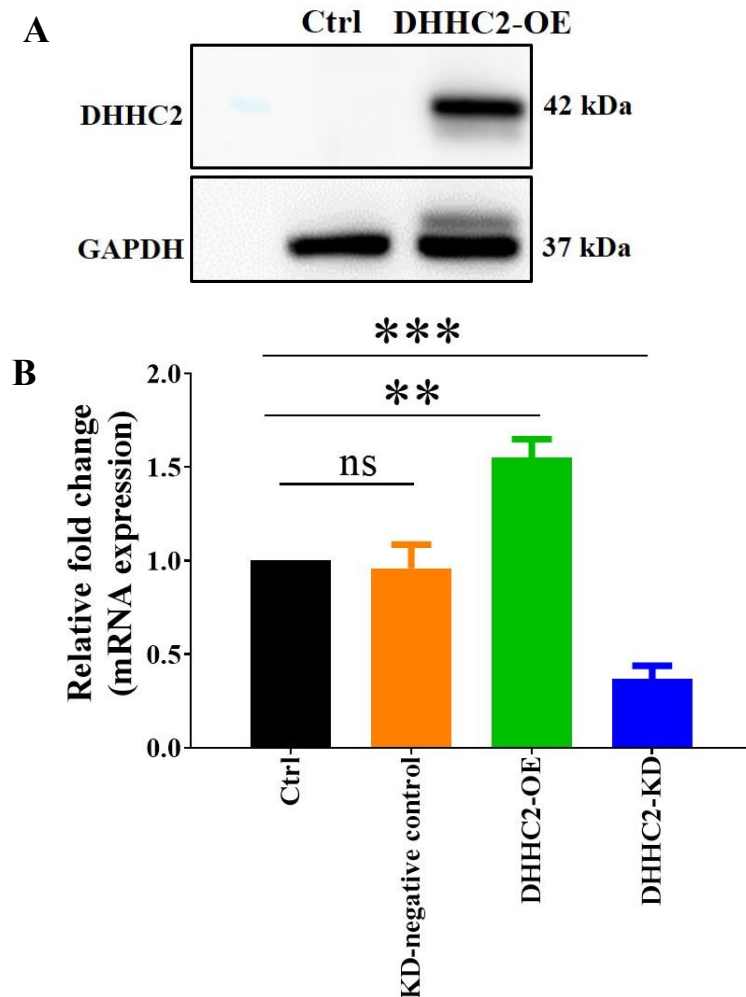
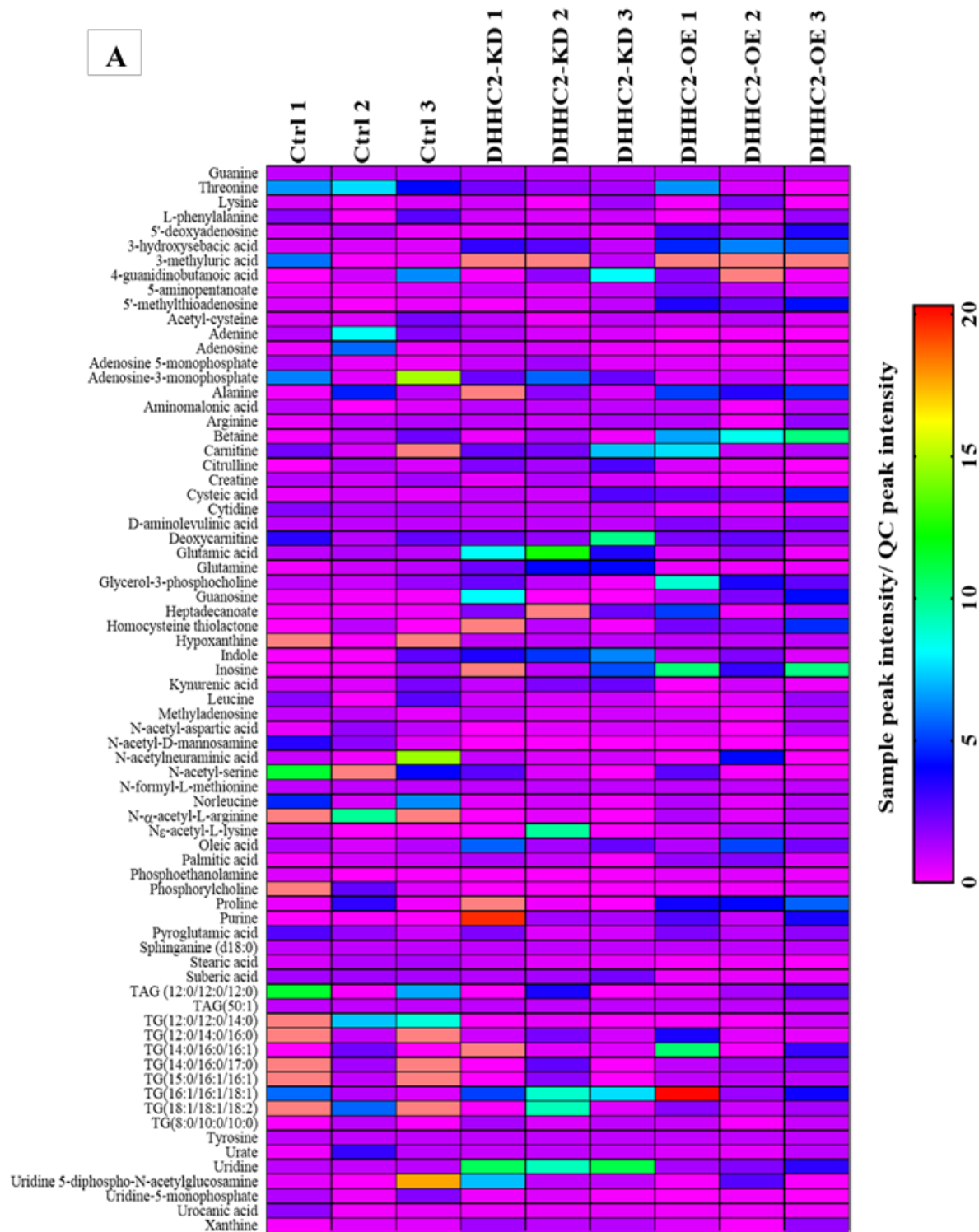


**Figure 3.2** A) Western blot analysis of DHHC2 and Ctrl post-transfection. B) Relative fold change of mRNA expression post-DHHC2 overexpression and knockdown compared to the control conditions. Samples were normalized with the endogenous control GAPDH (n=3).

### 3.3.2 Identification of metabolites:

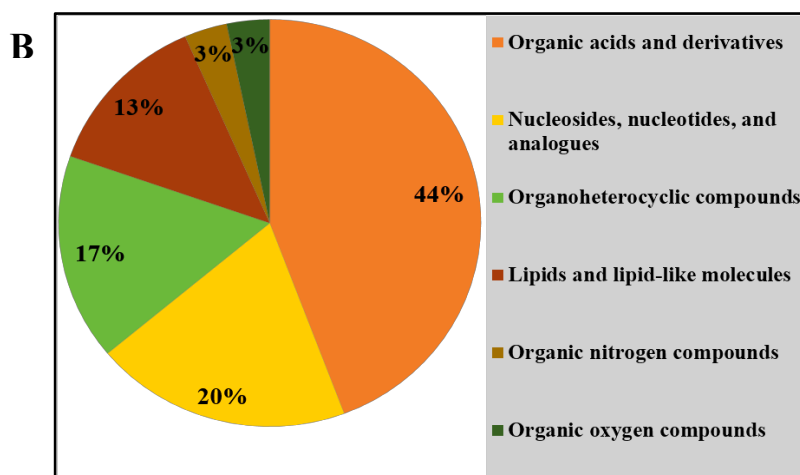
Tumor cells undergo metabolic changes to drive cancer growth and spread, resulting in a unique metabolite profile with potential applications in biomarker discovery and cancer diagnosis [363, 364]. Hence, to investigate the impact of DHHC2 overexpression and knockdown on the HEK-293T cell metabolome, we performed LC-MS/MS analysis. Raw spectral files were processed and

matched with reference libraries using the MS-DIAL tool, revealing 73 metabolites across DHHC2-OE, DHHC2-KD, and Ctrl conditions ( **Appendix Table A4**). These metabolites post-normalization with pool QC samples are represented through the heatmap, highlighting their correlations with the respective conditions (**Figure 3.3A**). The majority of the identified metabolites mainly fell into three major classes. The primary class comprised organic acids and their derivatives ( $P$  value 0.001), encompassing betaine, arginine, glutamine, glutamic acid, tyrosine, and proline. The second major class included nucleosides, nucleotides, and analogues ( $P$  value 0.004), like adenosine, cytidine, guanosine, inosine, uridine-5-monophosphate, along with various nucleotide metabolism intermediates. The third class involved organoheterocyclic compounds ( $P$  value 0.001), such as 3-methyluric acid, uric acid, xanthine, urocanic acid, kynurenic acid, and indole. The remaining metabolites are categorized into lipids and lipid-like molecules, organic nitrogen and oxygen-containing compounds. This comprehensive classification was performed using MetaboAnalyst 5.0, as shown in **Figure 3.3B** and **Table 3.2**.



**Table 3.2** Lists the classification of metabolites into the 6 super-compound classes through MetaboAnalyst 5.0.

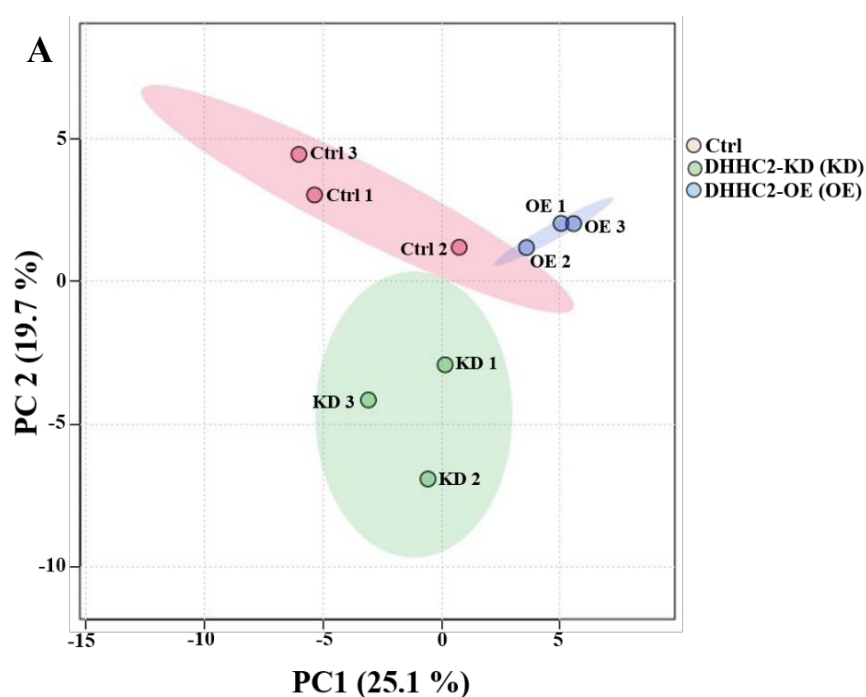
S. no.	Super class	Total compound	Hits	Statistic Q	Expected Q	Raw P	FDR
1	Organic acids and derivatives	4605	27	38.21	20	0.001	0.004
2	Nucleosides, nucleotides, and analogues	560	12	51.95	20	0.004	0.009
3	Organoheterocyclic compounds	6558	10	47.33	20	0.001	0.004
4	Lipids and lipid-like molecules	94103	8	28.03	20	0.167	0.201
5	Organic nitrogen compounds	632	2	10.85	20	0.684	0.684
6	Organic oxygen compounds	3244	2	35.95	20	0.153	0.201



**Figure 3.3** A) The heatmap depicting the correlation of identified 73 metabolites with their respective conditions (DHHC2-OE, DHHC2-KD and Ctrl). B) The pie chart representing the classification of metabolites into the 6 super compound classes.

### 3.3.3 Classification of differentially expressed metabolites *via* multivariate and univariate analysis:

Subsequently, we used pattern recognition techniques such as PLS-DA and PCA on the dataset to directly evaluate the metabolic changes and ascertain potential differences in metabolic profiles among groups. The results are visualized as score plots, wherein samples with akin metabolic profiles (e.g., control samples) tend to aggregate in distinct regions of the plot and are visualized by three different colors [365, 366]. The PCA plot (PC1 vs. PC2) accounted for 44.8% of the total variance (**Figure 3.4A**), revealing differences in the metabolite profiles of the DHHC2-OE, DHHC2-KD, and Ctrl groups. Similarly, the identified metabolites underwent another multivariate statistical analysis PLS-DA. Notably, the PLS-DA plot captured 39.1% of the total variance (**Figure 3.4B**). This statistically supervised distinction among the groups confirms the presence of discriminative metabolites identified in the DHHC2-OE, DHHC2-KD, and Ctrl conditions. Subsequently, the VIP scores highlighted that a total of 45 metabolites ( $VIP \geq 0.7$ ) contributed more towards the separation of DHHC2-OE, DHHC2-KD, and Ctrl conditions (**Table 3.3**). The top 10 metabolites are displayed in **Figure 3.4C**. Based on this multivariate analysis, we have concluded that DHHC2-overexpression and knockdown resulted in distinct metabolite profiling, which might be associated with its role in cancer biology.



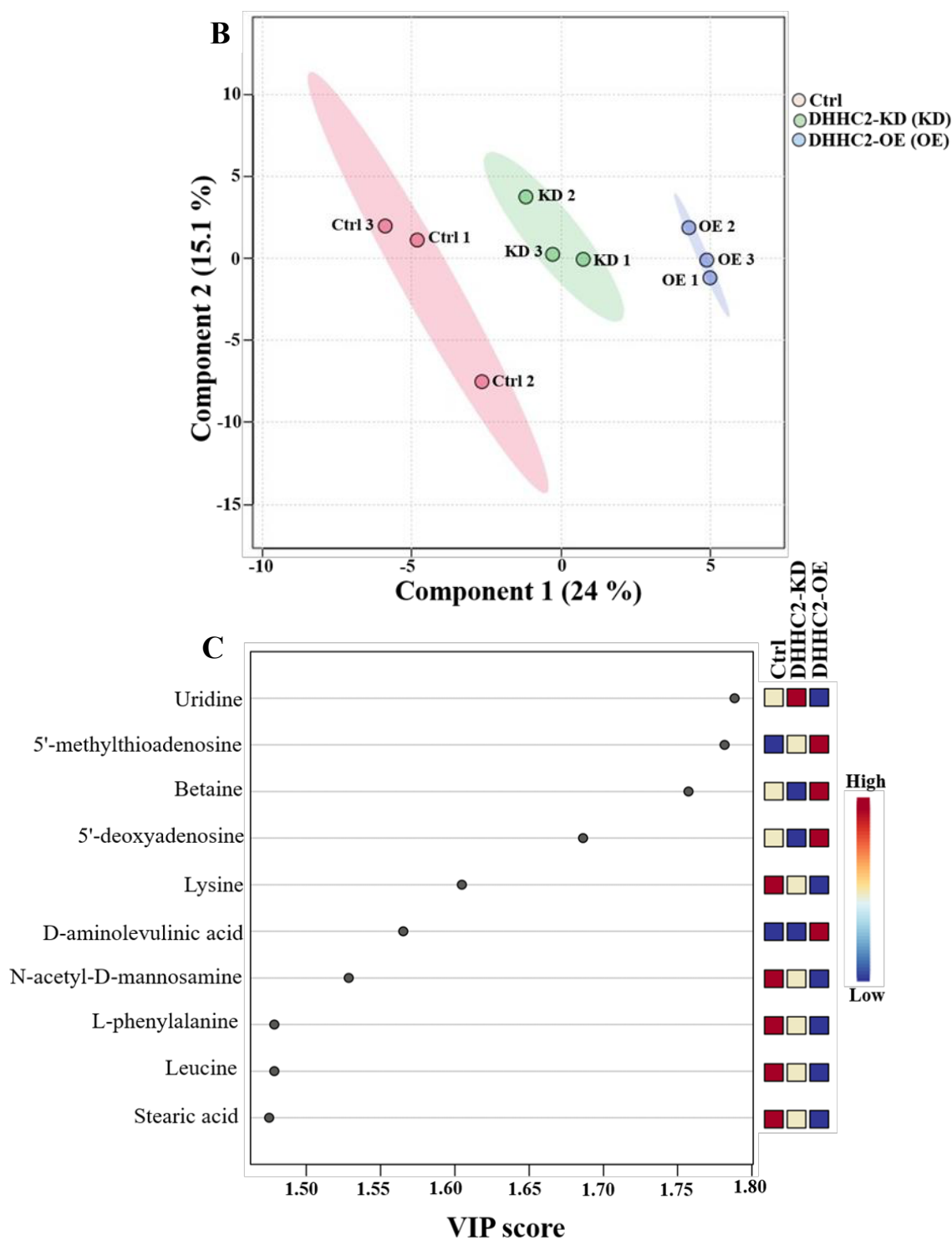
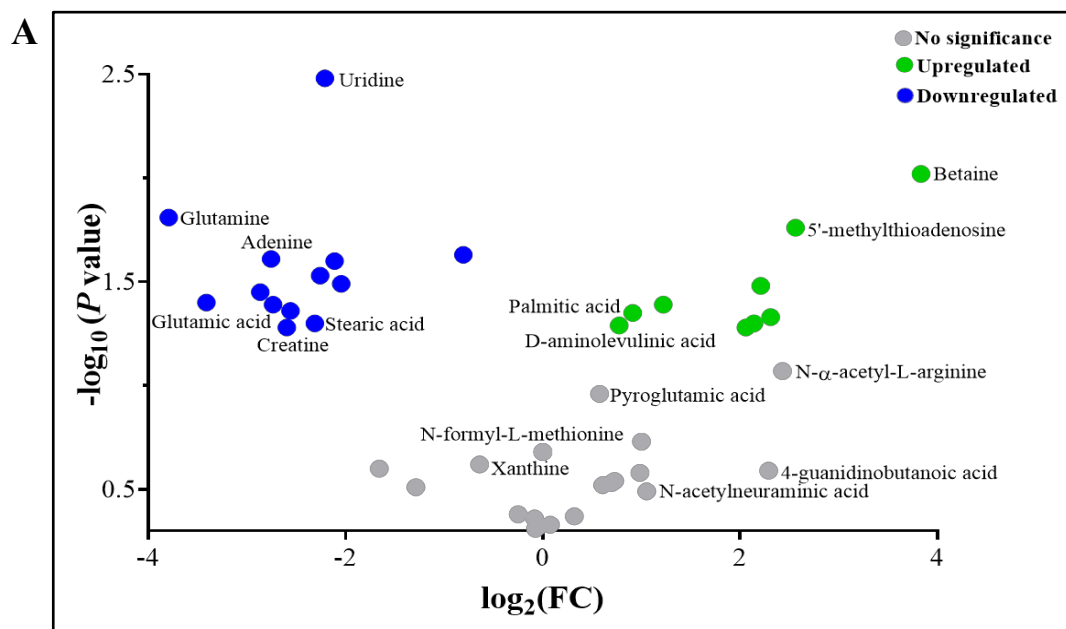


**Figure 3.4** A) PCA score plot: The X and Y axes were labeled with the first and second principal components, accounting for 25.1% and 19.7% of the total variation, respectively. B) PLS-DA score plot: The X and Y axes were labeled with the first and second components, accounting for 24 % and 15.1 % of the total variation, respectively. Colors in PCA and PLS-DA score plots indicated three different groups. C) The top 10 features responsible for the segregation of OE, KD, and Ctrl groups having VIP > 1.

Metabolites are described as proximal reporters of disease because their abundance in biological specimens is often directly related to pathogenic



mechanisms [367]. In order to identify the signature altered metabolites post-DHHC2 induction and silencing, a univariate t-test ( $P$  value) and FC-based volcano plot analysis was performed with the 45 metabolites having  $VIP \geq 0.7$  identified through the multivariate analysis, post-comparison with the Ctrl groups. Metabolites having FC: DHHC2-OE > DHHC2-KD were considered upregulated, while those with DHHC2-KD > DHHC2-OE were considered downregulated, as shown in **Figure 3.5A**. In total, 22 metabolites displayed significant differential expression ( $P$  value  $\leq 0.05$ ) between silenced and overexpressed conditions (**Table 3.3** and **Figure 3.5B**), and the matched spectra of these metabolites with the *in silico* libraries are given in **Appendix Figure A1**. Among these, 9 metabolites were upregulated in DHHC2-OE conditions, with 7 of them showing a relative FC > 2, including betaine, 5'-deoxyadenosine, and 5'-MTA compared to DHHC2-KD groups (**Figure 3.5B**). Conversely, 13 metabolites exhibited significantly higher expression in DHHC2-KD conditions, with 12 showing a relative FC > 2 in DHHC2-KD or < 0.5 in DHHC2-OE conditions. Notably, key metabolites like glutamine, glutamic acid, adenine, and uridine were among this group (**Figure 3.5B**).



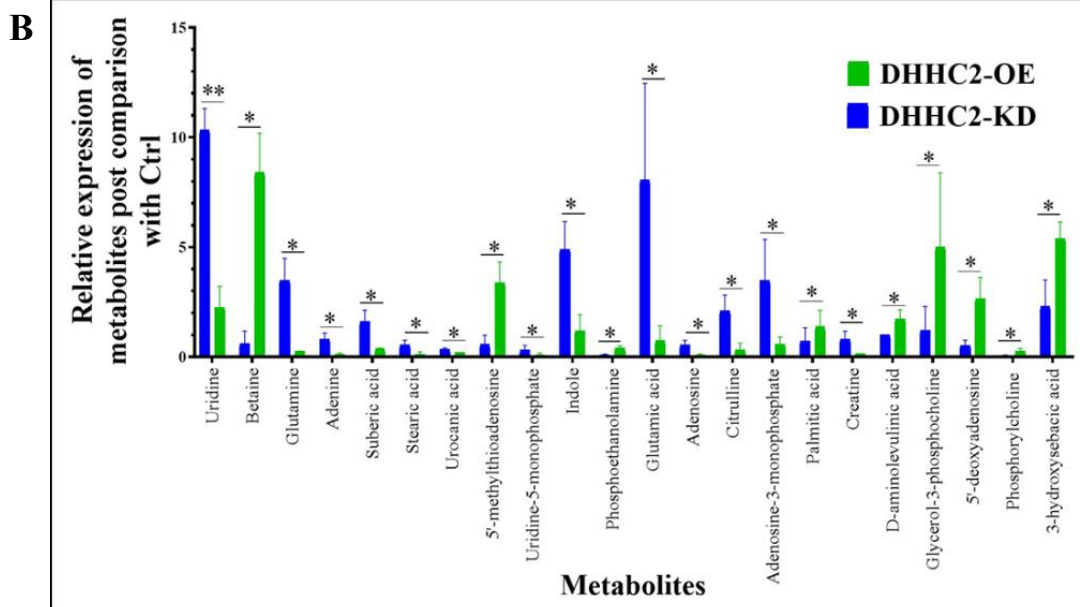


**Figure 3.5** A) Volcano plots of differentially expressed metabolites. The graph was plotted in the  $[\log_2(\text{FC})]$  vs. t-test  $P$  values  $[-\log_{10}(P \text{ value})]$ . In this figure, down refers to the FC: DHHC2-KD > DHHC2-OE, while up refers to FC: DHHC2-OE > DHHC2-KD. B) The bar graph representing significantly altered 22 metabolites in DHHC2-KD and DHHC2-OE groups post comparison with Ctrl in the HEK-293T cell line.

**Table 3.3** List of 45 metabolites having VIP score  $\geq 0.7$  identified through VIP-multivariate analysis.

S. no.	Metabolites	Fold Change <sup>*1</sup>	VIP Score	$P$ value	Express ion <sup>*2</sup>	Used for pathway analysis <sup>*3</sup>
1	Uridine	0.22	1.78	0.003	Down	DHHC2-KD
2	5'-MAT	5.91	1.78	0.02	Up	DHHC2-OE
3	Betaine	14.26	1.75	0.01	Up	DHHC2-OE
4	5'-deoxyadenosine	4.95	1.68	0.05	Up	DHHC2-OE
5	Lysine	0.95	1.60	0.49	Down	
6	D-aminolevulinic acid	1.71	1.56	0.05	Up	

S. no.	Metabolites	Fold Change *1	VIP Score	P value	Express ion*2	Used for pathway analysis *3
7	N-acetyl-D-mannosamine	0.84	1.529	0.42	Down	
8	Leucine	0.97	1.478	0.48	Down	
9	L-Phenylalanine	0.97	1.478	0.48	Down	
10	Stearic acid	0.20	1.475	0.05	Down	DHHC2-KD
11	Xanthine	0.64	1.42	0.24	Down	
12	Hypoxanthine	1.00	1.39	0.21	NC	
13	Palmitic acid	1.88	1.38	0.04	Up	
14	TG(12:0/14:0/16:0)	1.25	1.36	0.42	Up	
15	N- $\alpha$ -acetyl-L-arginine	5.39	1.34	0.08	Up	
16	Glycero-3-phosphocholine	4.17	1.31	0.05	Up	DHHC2-OE
17	Adenosine-3-monophosphate	0.17	1.30	0.04	Down	DHHC2-KD
18	N-acetyl-aspartic acid	1.52	1.27	0.30	Up	
19	Adenine	0.15	1.26	0.02	Down	DHHC2-KD
20	TG(18:1/18:1/18:2)	0.41	1.23	0.31	Down	
21	Arginine	0.94	1.23	0.44	Down	

S. no.	Metabolites	Fold Change *1	VIP Score	P value	Express ion*2	Used for pathway analysis *3
22	Creatine	0.17	1.22	0.05	Down	DHHC2-KD
23	TG(15:0/16:1/16:1)	1.62	1.18	0.30	Up	
24	3-methyluric acid	1.98	1.17	0.26	Up	
25	Norleucine	2.00	1.17	0.19	Up	
26	Uridine-5-monophosphate	0.21	1.12	0.03	Down	DHHC2-KD
27	Acetyl-cysteine	1.05	1.10	0.46	Up	
28	Urocanic acid	0.57	1.10	0.02	Down	
29	Adenosine	0.14	1.03	0.04	Down	DHHC2-KD
30	Pyroglutamic acid	1.49	1.02	0.11	Up	
31	TG(14:0/16:0/17:0)	1.66	0.99	0.29	Up	
32	Glutamine	0.07	0.97	0.02	Down	DHHC2-KD
33	N-acetylneuraminic acid	2.07	0.94	0.32	Up	
34	Glutamic acid	0.09	0.93	0.04	Down	DHHC2-KD
35	Phosphorylcholine	4.41	0.92	0.05	Up	DHHC2-OE
36	N-formyl-L-methionine	1.00	0.92	0.21	NC	

S. no.	Metabolites	Fold Change *1	VIP Score	P value	Express ion*2	Used for pathway analysis *3
37	Sphinganine (d18:0)	1.00	0.92	0.21	NC	
38	TAG(50:1)	1.00	0.92	0.21	NC	
39	Phosphoethanolamine	4.62	0.92	0.03	Up	DHHC2-OE
40	3-hydroxysebacic acid	2.33	0.79	0.04	Up	DHHC2-OE
41	Citrulline	0.15	0.90	0.04	Down	DHHC2-KD
42	Uridine 5-diphospho-N-acetylglucosamine	0.32	0.84	0.25	Down	
43	4-guanidinobutanoinic acid	4.89	0.87	0.26	Up	
44	Suberic acid	0.23	0.73	0.02	Down	DHHC2-KD
45	Indole	0.24	0.70	0.03	Down	DHHC2-KD

**Notes:**

\*1Fold Change: Peak intensity of DHHC2-OE vs. DHHC2-KD.

\*2Metabolites having FC: DHHC2-OE > DHHC2-KD considered as up. While metabolites having FC: DHHC2-OE < DHHC2-KD are down. NC refers to No change.

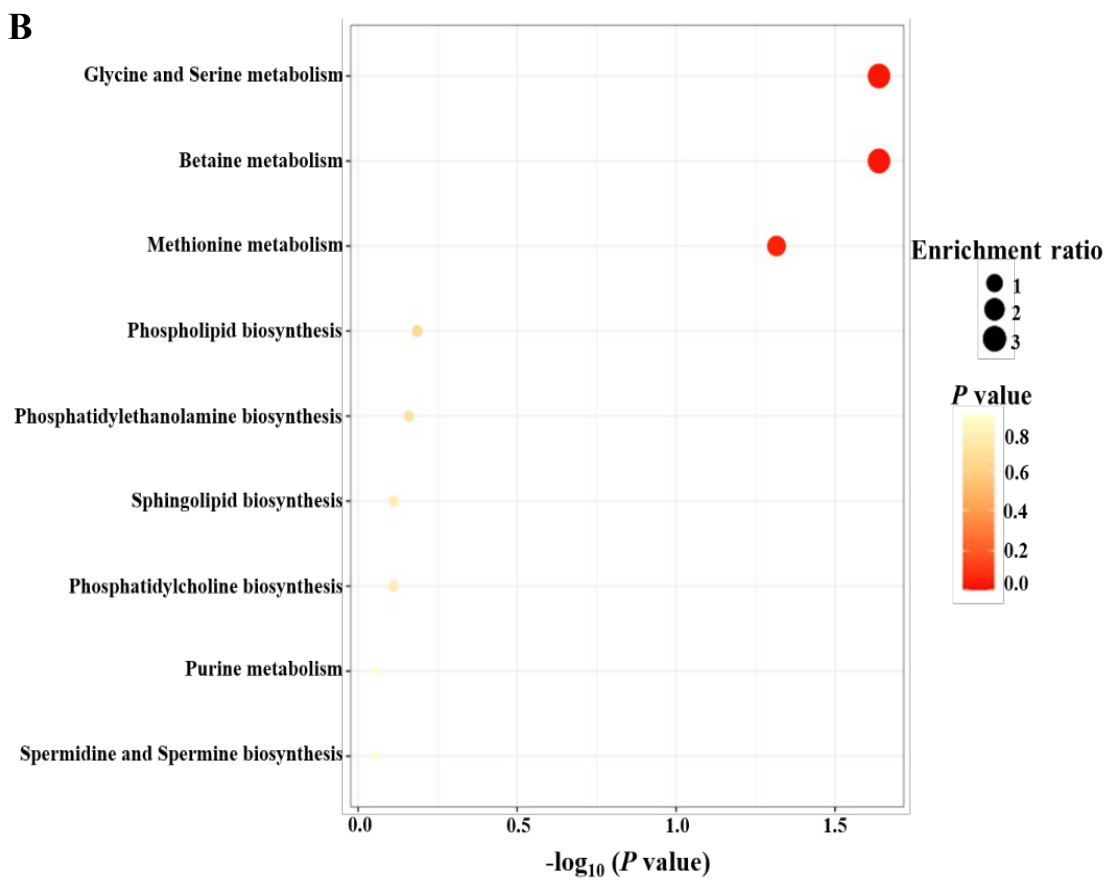
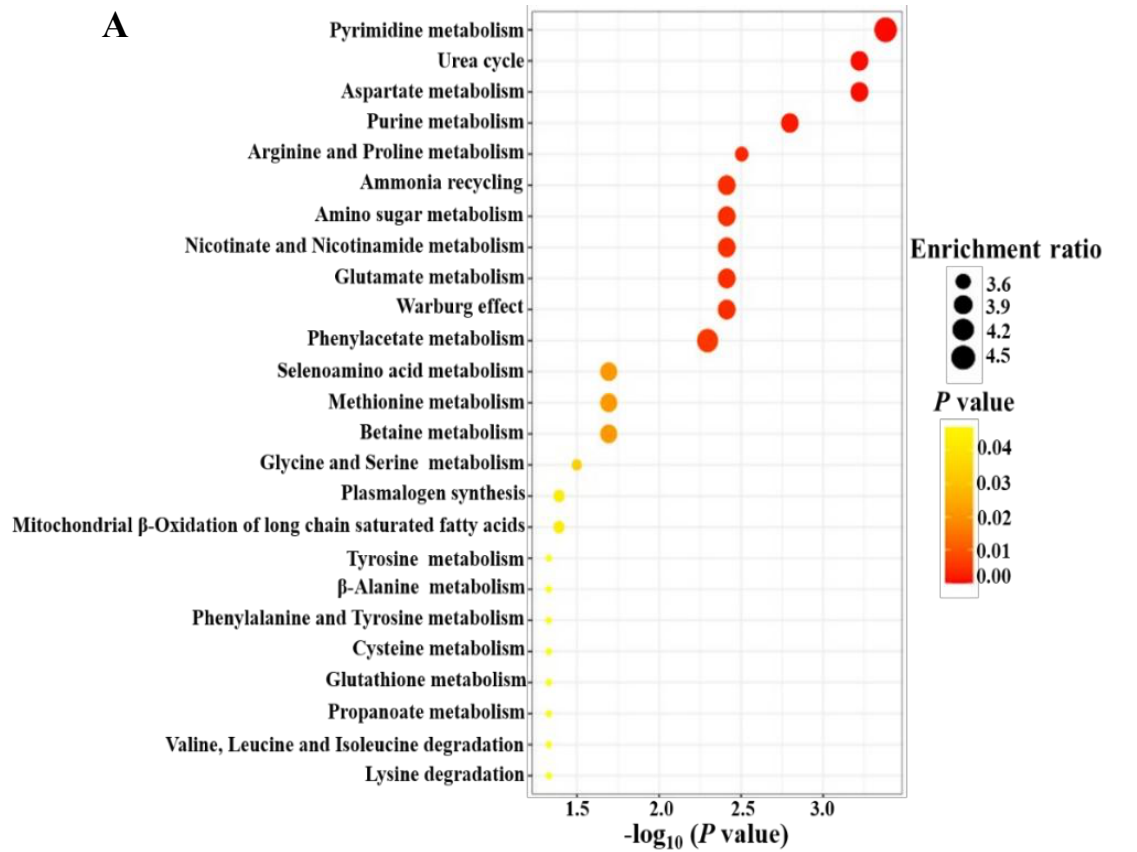
\*3Metabolites having FC > 2, VIP  $\geq$  0.7 and P value  $\leq$  0.05 utilized for the pathway analysis in DHHC2-OE group, on the other hand metabolites having FC < 0.5 in DHHC2-OE (or FC > 2 in DHHC2-KD), VIP  $\geq$  0.7, and P value  $\leq$  0.05 utilized for pathway analysis in DHHC2-KD group.

### 3.3.4 Pathway enrichment analysis: Investigating the impact of metabolites on the biological pathways:

The existing knowledge of molecular entities such as genes, proteins, and metabolites is associated with curated biological pathways, offering insight into how these entities collectively function and interact within a biological context [368]. To delve deeper into the interaction of metabolites with the biological pathways, we conducted pathway enrichment analysis using MetaboAnalyst 5.0, focusing on metabolites with an FC > 2,  $P$  value  $\leq 0.05$ , and VIP score  $\geq 0.7$ . We identified 12 metabolites in the DHHC2- KD group and 7 in the DHHC2-OE group, meeting these criteria from both univariate and multivariate analysis. Our analysis revealed 32 disrupted canonical pathways (downregulated) post-DHHC2 silencing. The top three downregulated pathways are pyrimidine metabolism, urea cycle, and aspartate metabolism, each with a  $P$  value < 0.001 (**Figure 3.6A** and **Table 3.4**).

Usually, cells meet their pyrimidine nucleotide requirements through recycling from cell turnover or dietary intake, but this is insufficient to meet the increased demands of proliferating cancer cells[369]. Wang et al. (2019) found that glioblastoma stem cells upregulates the *de novo* pyrimidine synthesis pathway, contributing to poorer outcomes in glioblastoma patients [370]. Inhibiting this pathway decreased cancer cell viability and self-renewal [371]. Proliferating cells primarily rely on the *de novo* pathway to maintain their nucleotide pools, utilizing amino acids like glutamine and aspartic acid as precursors[372]. This pathway involves several steps catalyzed by critical enzymes such as CAD, DHODH, and UMPS [369]. CAD, a multifunctional enzyme, consists of three domains: carbamoyl-phosphate synthetase II, aspartate transcarbamylase, and dihydroorotase. The initial three steps of the *de novo* pyrimidine synthesis pathway, converting cytosolic glutamine to dihydroorotate, are catalyzed by CAD [373]. Of the three enzymes involved in *de novo* UMP synthesis, CAD is most often overexpressed in tumors, according to data from the FireBrowse database [374]. Studies have shown that inhibiting CAD disrupts cancer cell survival [375-377]. Additionally, deregulation of the urea cycle in cancer can increase pyrimidine synthesis by redirecting nitrogen toward CAD [376]. In our study, we identified pyrimidine synthesis as the most affected pathway following DHHC2-KD, with elevated levels of glutamine and uridine observed.

However, the potential connection between DHHC-mediated *S*-palmitoylation and pyrimidine metabolism has yet to be explored. Therefore, we examined the mRNA expression of CAD under DHHC2-OE, DHHC2-KD, and Ctrl conditions to investigate a possible link between DHHC2 and CAD. Our results revealed that overexpressing DHHC2 in HEK-293T cells led to a 0.5-0.6 fold reduction in CAD mRNA level compared to the control ( $P$  value  $< 0.05$ ). On the other hand, knocking down DHHC2 resulted in a 70-80% increase in CAD mRNA level ( $P$  value  $< 0.01$ ) compared to the Ctrl (**Figure 3.6C**). These results suggest that DHHC2 might regulate the pyrimidine synthesis pathway by modulating CAD mRNA expression, although further research is necessary to confirm this regulatory mechanism. In the DHHC2-OE group, we identified 9 canonical pathways, considered upregulated. The top three are glycine-serine metabolism, betaine-metabolism, and methionine metabolism, each with a  $P$  value  $< 0.05$ . These pathways were affected by the substantial expression of betaine and 5'-MTA (**Figure 3.6B** and **Table 3.5**). Nevertheless, it is crucial to emphasize that further *in vitro* validation is essential to thoroughly explore the association between DHHC2 and these biologically altered pathways.





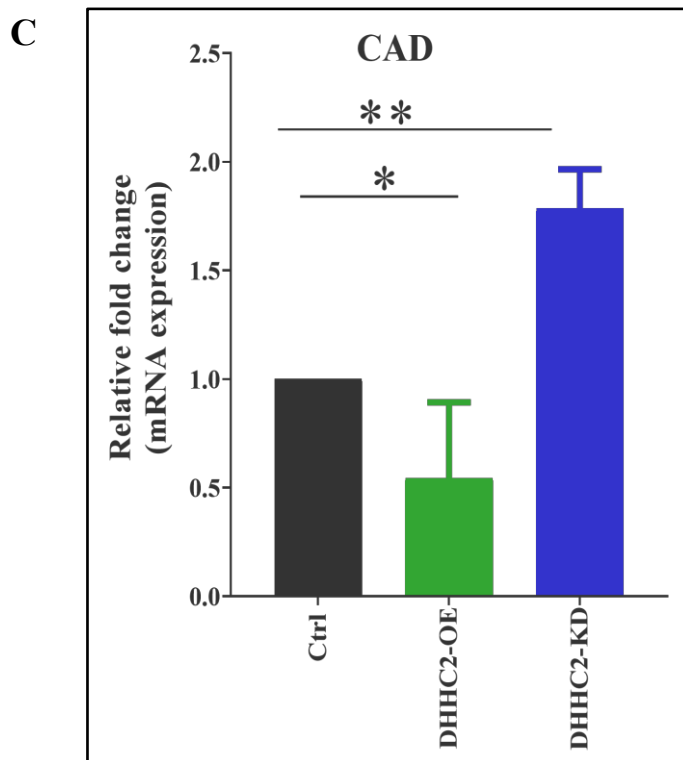


**Figure 3.6** The graphs representing the pathways obtained through MetaboAnalyst 5.0. A) DHHC2-KD and B) DHHC2-OE. The pathways were identified based on the enrichment ratio of the metabolites in the particular pathway vs. the t-test based  $P$  value [ $-\log_{10}(P \text{ value})$ ]. C) Relative CAD-mRNA fold change expression post-DHHC2 overexpression and knockdown compared with Ctrl in HEK-293T cell line. Samples were normalized with the endogenous control GAPDH (n=3).

**Table 3.4** List of the significantly altered pathway in DHHC2-KD group identified via MetaboAnalyst 5.0.

S.no.	Pathways	Total Compounds	Hits	Statistic Q	Expected Q	Raw $P$	FD R
1	Pyrimidine metabolism	57	2	92.25	20	0.0004	0.006
2	Urea cycle	28	3	79.52	20	0.0006	0.006
3	Aspartate metabolism	35	3	79.52	20	0.0006	0.006

<b>S.no.</b>	<b>Pathways</b>	<b>Total Compounds</b>	<b>Hits</b>	<b>Statistic Q</b>	<b>Expected Q</b>	<b>Raw P</b>	<b>FD R</b>
4	Purine Metabolism	73	4	79.25	20	0.002	0.012
5	Arginine and Proline metabolism	52	3	71.49	20	0.003	0.012
6	Ammonia recycling	31	2	79.76	20	0.004	0.012
7	Amino Sugar metabolism	33	2	79.76	20	0.004	0.012
8	Nicotinate and Nicotinamide metabolism	35	2	79.76	20	0.004	0.012
9	Glutamate metabolism	48	2	79.76	20	0.004	0.012
10	Warburg effect	57	2	79.76	20	0.004	0.012
11	Phenylacetate metabolism	9	1	88.60	20	0.005	0.015
12	Selenoamino acid metabolism	27	1	77.69	20	0.020	0.046
13	Methionine metabolism	42	1	77.69	20	0.020	0.046

S.no.	Pathways	Total Compounds	Hits	Statistic Q	Expected Q	Raw P	FD R
14	Betaine metabolism	21	1	77.69	20	0.020	0.046
15	Glycine and Serine metabolism	59	2	68.07	20	0.032	0.047
16	Plasmalogen synthesis	26	1	68.94	20	0.041	0.047
17	Mitochondrial Beta-Oxidation of long chain saturated fatty acids	28	1	68.94	20	0.041	0.047
18	Tyrosine metabolism	70	1	66.79	20	0.047	0.047
19	$\beta$ -Alanine metabolism	34	1	66.79	20	0.047	0.047
20	Phenylalanine and Tyrosine metabolism	27	1	66.79	20	0.047	0.047
21	Cysteine metabolism	26	1	66.79	20	0.047	0.047
22	Glutathione metabolism	20	1	66.79	20	0.047	0.047

<b>S.n o.</b>	<b>Pathways</b>	<b>Total Compounds</b>	<b>Hit s</b>	<b>Statistic Q</b>	<b>Expected Q</b>	<b>Raw P</b>	<b>FD R</b>
23	Propanoate metabolism	42	1	66.79	20	0.047	0.047
24	Valine, Leucine and Isoleucine degradation	59	1	66.79	20	0.047	0.047
25	Lysine degradation	30	1	66.79	20	0.047	0.047
26	Histidine metabolism	42	1	66.79	20	0.047	0.047
27	Folate metabolism	29	1	66.79	20	0.047	0.047
28	Alanine metabolism	17	1	66.79	20	0.047	0.047
29	Tryptophan metabolism	59	1	66.79	20	0.047	0.047
30	Arachidonic Acid metabolism	67	1	66.79	20	0.047	0.047
31	Glucose-Alanine cycle	13	1	66.79	20	0.047	0.047
32	Malate-Aspartate shuttle	10	1	66.79	20	0.047	0.047

**Table 3.5** List of the significantly altered pathway in DHHC2-OE group identified via MetaboAnalyst 5.0.

S.no.	Pathways	Total Compounds	Hits	Statistic Q	Expected Q	Raw P	FDR
1	Glycine and Serine metabolism	59	1	76.29	20	0.023	0.104
2	Betaine metabolism	21	1	76.29	20	0.023	0.104
3	Methionine metabolism	42	2	44.83	20	0.048	0.145
4	Phospholipid biosynthesis	29	1	5.576	20	0.652	0.883
5	Phosphatidylethanolamine biosynthesis	12	1	4.310	20	0.693	0.883
6	Sphingolipid metabolism	40	2	4.805	20	0.775	0.883
7	Phosphatidylcholine biosynthesis	14	2	4.805	20	0.775	0.883
8	Purine metabolism	73	1	0.697	20	0.875	0.883
9	Spermidine and Spermine biosynthesis	18	1	0.615	20	0.883	0.883

### 3.3.5 p53 can be a potential marker behind DHHC2-mediated tumor suppressive activity:

The three crucial findings from the literature sparked our interest in investigating the interplay between p53, MDM2, and DHHC2: Firstly, HEK-

293T cells express a temperature-sensitive variant of the SV40 large T antigen, which bind and inhibit the tumor suppressor activity of p53 and enhances the tumorigenic potential of cells [378, 379]. The second study showed a significant increase in p53 expression in the presence of betaine [380], a lead metabolite identified in DHHC2-OE groups in our study. The third research study focuses on the p53-MDM2 axis, where MDM2, a crucial protein in cancer, acts as an E3 ubiquitin ligase binding to p53 and promoting its degradation, thus hindering p53's ability to activate genes responsible for controlling the cell cycle, senescence, or apoptosis in cancer cells [381]. Remarkably, we observed a two-fold increase in p53 protein expression post-DHHC2 transfection compared to the Ctrl ( $P$  value  $< 0.01$ ) in the HEK-293T cell line (**Appendix Figure A2A and A2B**). On the other hand, our study uncovered a significant reduction in MDM2 mRNA levels post-DHHC2 transfection compared to the Ctrl in the HEK-293T cell line ( $P$  value  $< 0.01$ ) (**Appendix Figure A2C**). In continuation, we also examine the relationship between DHHC2 and p53 expression at the mRNA level, and the obtained results revealed that overexpression of DHHC2 in HEK-293T cells led to a 30-40% increase in p53 mRNA levels compared to the control ( $P$  value  $< 0.05$ ). Conversely, the knockdown of DHHC2 caused a 0.3-0.4 fold reduction in p53 mRNA levels ( $P$  value  $< 0.05$ ) (**Figure 3.7**). These

results underscore the pivotal role of DHHC2 in regulating p53 expression, presenting a new perspective for further investigation.

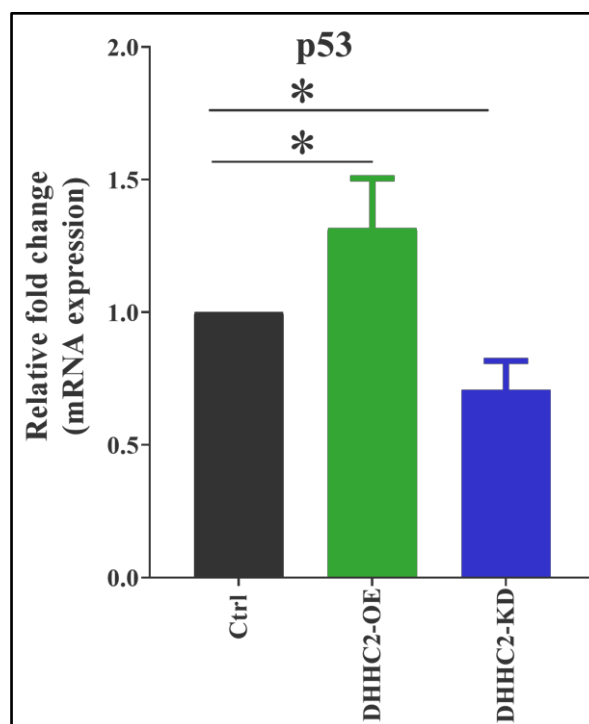


**Figure 3.7** Relative p53-mRNA fold change expression post-DHHC2 overexpression and knockdown compared with Ctrl in HEK-293T cell line. Samples were normalized with the endogenous control GAPDH (n=3).

### **3.4 Discussion and conclusion:**

This study was initiated due to the current recognition of cellular metabolism deregulation as a core hallmark of cancer and the noteworthy role of DHHC2 as a prominent marker in tumor biology, as revealed through previous studies [114, 115]. To better understand the relationship between DHHC2 and cancer, particularly its impact on the metabolome, we conducted metabolite identification using LC-MS/MS under DHHC2-modified conditions. We noted that inhibiting DHHC2 expression resulted in the accumulation of significant intermediates of pyrimidine metabolism, including glutamine, uridine-5'-monophosphate (UMP), and uridine (**Figure 3.9**). From the above data, we found that p53 is positive and CAD is negatively associated with DHHC2 mRNA expression. Additionally, few crucial previous studies have reported an inverse relationship between p53 and CAD. One study showed that mutant p53 promotes the expression of CAD in lung adenocarcinoma, correlating with

poorer patient survival [382]. Additionally, the oncogene MYC has been found to bypass p53-mediated cell cycle arrest in N-(phosphonacetyl)-L-aspartate (PALA)-treated cells through CAD gene amplification [383]. Considering these studies and our current results, it can be concluded that knockdown of DHHC2 may lead to decreased p53 levels, which could result in an upregulation of CAD and promotes the utilization of glutamine to activate the *de novo* pyrimidine synthesis pathway in cancer cells (**Figure 3.8**). Conclusively, our study provides novel insights into the interaction between DHHC2, p53, and CAD, underscoring the importance of our research in laying the groundwork for further investigation and potential therapeutic strategies targeting the nucleotide metabolism of cancer cells.

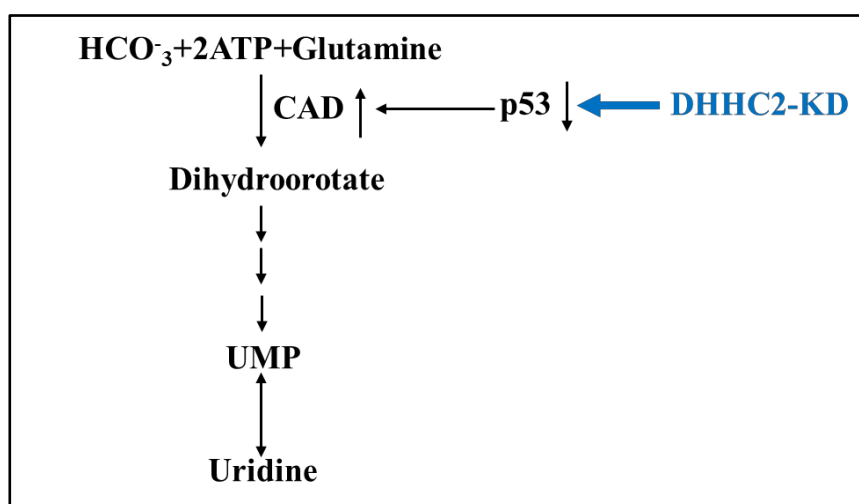


**Figure 3.8** The above figure depicts how DHHC2 negatively regulates the pyrimidine pathway through CAD.

The second most abundant pathway in DHHC2-KD groups was the urea cycle. The plausible explanation could be that alanine underwent transamination within the glucose-alanine cycle with free  $\alpha$ -ketoglutarate, producing glutamate, which was then deaminated to form pyruvate and free ammonium ions. Hepatocytes efficiently metabolize these toxic ammonium through the urea cycle [384]. However, in cases where excess ammonia is not used for urea synthesis, a subset of perivenous hepatocytes absorbs it, detoxifying ammonia by amidating glutamate to produce an elevated level of citrulline (a pivotal component of the urea cycle) in the DHHC2-KD group highlights the prominence of the urea cycle as the second leading pathway. Lastly, the limited uptake of aspartate by tumor cells from the external environment leads to reliance on mitochondrial catabolism of glutamine for their development [385],



highlighting aspartate metabolism as the third leading pathway in the DHHC2-KD condition.

In summary, the depletion of DHHC2 induces a dependence on glutamine and glutamic acid, revealing a specific metabolic vulnerability in cancer cells. Therefore, exploring the relationship between DHHC2 and glutaminolysis holds promising potential for developing effective therapies for glutamine-addicted cancers.

In the DHHC2-OE condition, there was a notable increase in the presence of two essential metabolites: 5'-MTA and betaine. These metabolites play pivotal roles in various metabolic pathways, such as glycine-serine metabolism, betaine metabolism, and methionine metabolism. Betaine, also known as trimethyl-glycine, is synthesized through choline-dependent glycine biosynthesis. This process involves the conversion of betaine into dimethyl-glycine and then sarcosine (N-methylglycine). In healthy individuals, glycine and serine are interchangeable [386, 387]; possibly due to this, the glycine and serine pathways are primarily identified by quantitative enrichment analysis (QEA) in the presence of betaine (trimethyl-glycine). Besides, betaine-homocysteine methyltransferase (BHMT) facilitates the transfer of a methyl group from betaine to the accumulated intermediate homocysteine of methionine metabolism. Adding this methyl group converts homocysteine back into methionine and dimethyl-glycine [388], providing a plausible explanation for the observed interaction between methionine and betaine metabolism.

The second significant metabolite of the DHHC2-OE group is 5'-MTA, which also serves as an intermediary compound or byproduct within the methionine cycle and during the synthesis of polyamines within mammalian tissues. Its methyl group originates from *S*-adenosylmethionine (SAM), a compound synthesized from methionine and adenosine triphosphate (ATP) catalyzed by methionine adenosyltransferases (MAT). During this process, the aminopropyl group from decarboxylated *S*-adenosylmethionine (dASM) is transferred to putrescine, resulting in the formation of spermidine and the release of 5'-MTA as a byproduct [389]. Consequently, due to 5'-MTA and betaine, we noted methionine metabolism as the third most prominent pathway.

Multiple studies have highlighted the cancer-preventive properties of these two metabolites. It has been noted that when choline and betaine are used together, there is an 11% reduction in cancer burden based on dose-response analysis [390, 391]. Similarly, elevated betaine concentrations have been reported to impede cell growth and facilitate p53-mediated cell apoptosis in Hela cells [380, 392]. Notably, we observed an increase in the p53 expression in the presence of DHHC2. Hence, we infer another potential relationship where DHHC2 may amplify p53 expression, leading to the upregulation of betaine in cells. For the second crucial metabolite, 5'-MTA; it has been reported that higher endogenous or exogenous 5'-MTA levels disrupted preneoplastic liver lesions and DNA synthesis in a chemically induced hepatocarcinogenesis rat model [393]. 5'-MTA has also shown inhibitory effects in various cancer cell lines, including human colon cancer cells, cervical cancer cells, lymphoma cells, and leukemia cells [394-396].

In addition to the betaine and 5'-MTA, D-aminolevulinic acid (ALA) is also significantly expressed in DHHC2-OE conditions and reported to be associated with anti-cancer activity. It is reported that ALA suppresses glycolysis-mediated acidosis and enhances the production of superoxide anion radical ( $O_2^{\bullet-}$ ) and active caspase-3 expression. These effects ultimately lead to caspase-dependent apoptosis, inhibiting the Warburg effect in cancer cells [397]. Along with this, ALA induces the generation of ROS upon exposure to light, resulting in apoptotic cell death and necrosis in cancer cells [398].

Conclusively, our investigation has identified a few crucial metabolites in the DHHC2-OE group, like betaine, 5'-MTA, and ALA [393, 398, 399], which are already well-known for their tumor-suppressive roles or therapeutic potential. By activating these metabolites, DHHC2 may act as a tumor suppressor across different cancer types (**Figure 3.9**). Also, our study provided novel insights into the interaction between DHHC2, p53, and CAD, underscoring the importance of this intercome in cancer therapeutics *via* pyrimidine metabolism. However, understanding the metabolic changes in cancer cells remains challenging due to their complexity and dynamic nature. Moreover, the role of DHHCs seems varied in different cancer contexts. Therefore, our study could serve as a

valuable reference for bridging the knowledge gap between DHHCs-mediated cancer and the complex cancer metabolome.

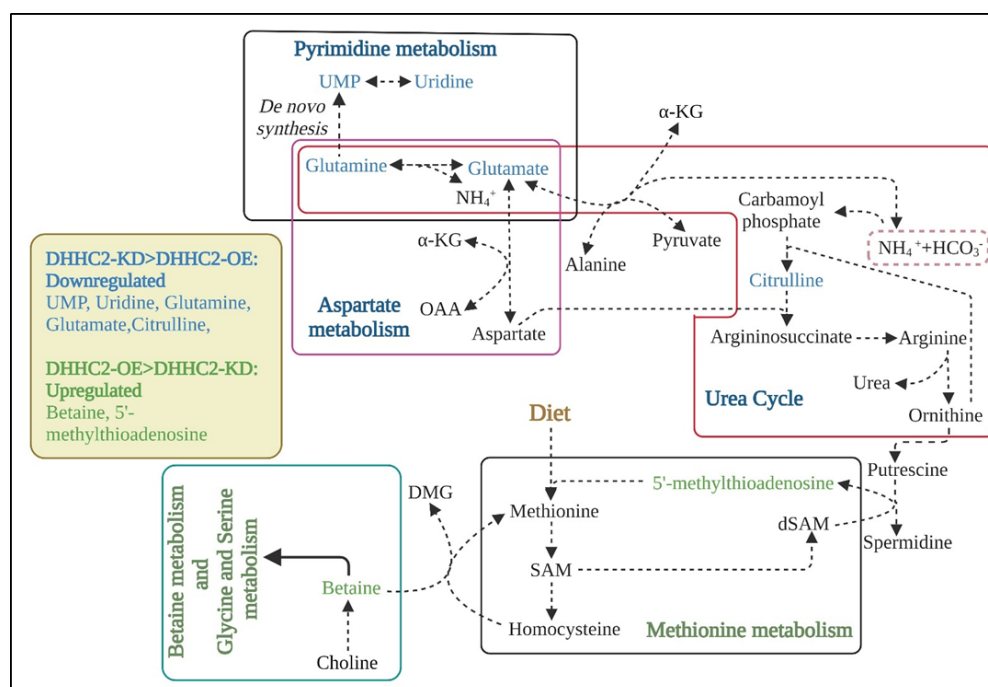


**Figure 3.9** The schematic representation of the identified metabolites and their associated pathways. The metabolites and pathways highlighted in green are significantly expressed in the DHHC2-OE condition and considered upregulated (glycine and serine metabolism, betaine metabolism, and methionine metabolism). Conversely, the blue color indicates the presence of the metabolites and pathways in DHHC2-KD that were considered downregulated (pyrimidine metabolism, urea cycle, and aspartate metabolism). KG: ketoglutarate, OAA: oxaloacetate, DMG: dimethylglycine, SAM: *S*-adenosyl methionine, UMP: uridine-monophosphate, dSAM: decarboxylated *S*-adenosyl methionine. This figure was created using [www.BioRender.com](http://www.BioRender.com).



## Chapter 4: Exploring the potential cross-talk between EGFR and DHHCs through *in silico* methodologies

---

### **4.1 Introduction:**

Studies in genetics and animal models provided strong evidence that DHHC isoforms play a role in a wide range of pathological conditions, including neurological and pathogenic disorders, as well as various cancers [1, 290]. Data analysis from nearly 150 cancer studies has identified genomic alterations in different DHHC enzymes, suggesting that these changes may contribute to cancer pathology by impacting specific proteins and their associated cellular functions [110]. For example, Shan et al. (2024) showed that DHHC6 mediates *S*-palmitoylation of PPAR $\gamma$  within its DNA-binding domain. This modification increases PPAR $\gamma$  stability and reduces its susceptibility to degradation, aiding its nuclear transport and enhancing its activity, ultimately supporting colon cancer progression [131]. Further, multiple studies indicated that DHHC-mediated palmitoylation of the EGFR is linked to its abnormal expression in cancer, with one study explicitly showing that EGFR activation is increased in NSCLC by DHHC20. The palmitate attachment to the intracellular domain of EGFR effectively "pins" its unstructured C-terminal tail to the plasma membrane, thereby boosting EGFR activation [22]. The second study by Bollu et al. (2015) showed that FASN-mediated EGFR palmitoylation leads to its ligand-independent activation in cancer cells [6]. Lastly, a study highlighted that DHHC13-mediated palmitoylation of EGFR is essential for its localization to the plasma membrane, with ARF6 identified as a critical player in this process [72]. When palmitoylated EGFR is recognized by N-myristoylated ARF6, a lipid-lipid contact is formed that recruits the exocyst complex, allowing EGFR to emerge from the Golgi and be transported to the plasma membrane in a GTP-bound form in cancer cell, therefore, disrupting this sorting system can be a suitable cancer-mitigating strategy. [152]. From the above studies, we concluded that much attention had been given to targeting the intracellular domain of EGFR, which drives its signaling post-ligand binding at the ECD. However, the role of *S*-palmitoylation in ECD-EGFR has been relatively

overlooked. Therefore, our study aims to fill this research gap by identifying potential DHHC isoforms interacting with ECD-EGFR using *in silico* tools, providing new avenues to target these isoforms and reduce the EGFR-associated cancer burden. The docking studies revealed that DHHC1 and DHHC4 exhibit the strongest binding affinity with wild type-EGFR (WT-EGFR). Further, the MM-GBSA-based  $\Delta G_{\text{bind}}$  score of -178.83 kcal/mol and -274.48 kcal/mol were obtained for DHHC1 and DHHC4 in complex with EGFR, respectively. Using the CSS-Palm tool, we identified Cys7 of EGFR as a critical residue likely to undergo *S*-palmitoylation. Subsequently, MD simulations showed that the EGFR-Cys7 to Ser (EGFRC7S) mutation impaired the binding of DHHC1 and DHHC4 with EGFR ( $\Delta G_{\text{bind}}$  score of -102.07 kcal/mol and -177.47 kcal/mol for the mutant protein complexes) (**Figure 4.1**). This finding suggests that the DHHC1 and DHHC4-mediated *S*-palmitoylation of ECD-EGFR at Cys7 may facilitate its aberrant activation in cancer cells. However, *in vitro* validation is critically needed to understand this interaction fully.

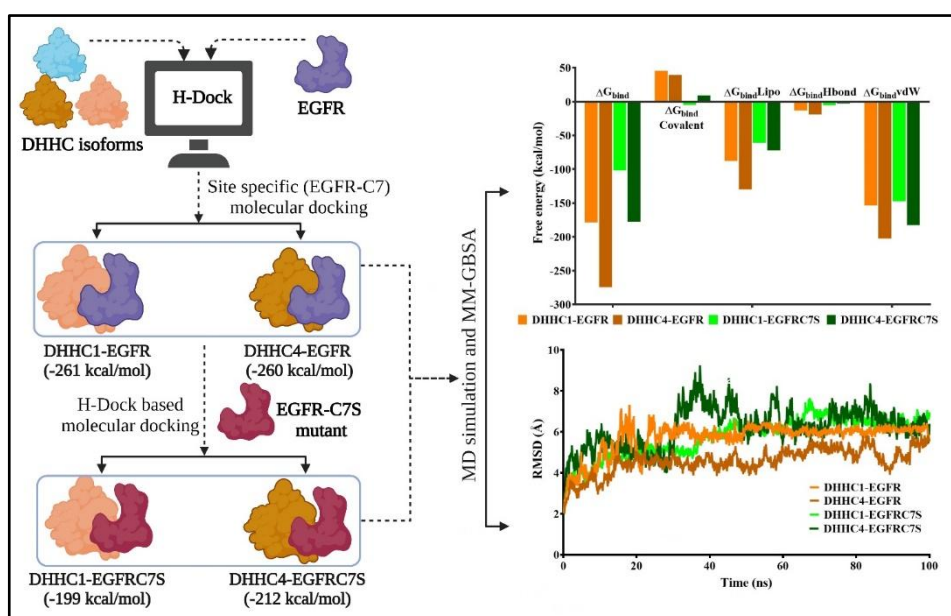


**Figure 4.1** Schematic representation of the workflow. The above figure denotes the cysteine and serine as C and S (This figure was created using [www.biorender.com](http://www.biorender.com)).

## 4.2. Methods:

### 4.2.1 Retrieval of protein structures:

The protein structure of 23 DHHC isoforms were sourced from the Alpha Fold protein structure database <https://alphafold.ebi.ac.uk>. The EGFR-EGF complex

(PDB ID: 7SYD) was sourced from the RCSB protein repository [www.rcsb.org](http://www.rcsb.org) [307].

#### **4.2.2 Prediction of palmitoylation sites and point mutation residue:**

The web-based tool CSS-Palm <https://css-palm.software.informer.com/3.0> was utilized to identify putative *S*-palmitoylation sites within EGFR. This software provides predictions about the positions of Cys residues' potential to undergo palmitoylation, accompanied by corresponding scores (higher scores increased the probability of palmitoylation occurring at the same residue) [400, 401].

The DD-mut <https://biosig.lab.uq.edu.au/ddmut> tool was utilized to identify alternative residues for Cys substitution in the protein. This tool evaluates how point mutations affect protein stability by measuring changes in Gibbs free energy. Positive  $\Delta\Delta G$  values stabilize, while negative  $\Delta\Delta G$  values destabilize protein structure, thus assisting in the selection of suitable replacement residues[402].

#### **4.2.3 Mutant generation:**

C7S point mutation was introduced into the EGFR protein using UCSF Chimera (version 1.17.3) <https://www.cgl.ucsf.edu/chimera> [403]. For this, the crystal structure of the protein was loaded into Chimera, and the residues of interest were selected *via* the sequence viewer and command line interface. Mutations were introduced using the Rotamers tool. The mutated structure underwent energy minimization using the Minimize Structure tool to ensure proper geometric configuration and reduce steric clashes. The minimized and mutated structure was saved in PDB format for subsequent analysis [403].

#### **4.2.4 Validation of the mutant EGFR C7S 3D model:**

The 3D mutant EGFR model was validated using the ERRAT, PROCHECK, and VERIFY 3D programs, accessible *via* the Structural Analysis and Verification Server (SAVES) at <http://nihserver.mbi.ucla.edu/SAVES> [404]. PROCHECK was employed to evaluate the stereochemical quality of the protein structures through Ramachandran plots. VERIFY 3D assessed the compatibility between the atomic 3D model and its amino acid sequence (1D) to ensure the accuracy of the protein's 3D structure. ERRAT was used to verify the crystallographic structure of the proteins [405].

#### 4.2.5 Parameters for molecular docking:

Before the docking study, the EGFR chain B was utilized. The crystal structure was prepared by removing the standard EGF molecule, adding hydrogen atoms and Gasteiger charges *via* AutoDock Vina 1.0 [Downloads – AutoDock Vina \(scripps.edu\)](https://autodock.scripps.edu). Protein-protein docking was conducted using the H-DOCK webserver <http://hdock.phys.hust.edu>, with DHHCs-chain A (receptor) and EGFR chain B (ligand) focusing on the specific residues Cys7 and Ser7 of the EGFR binding site. The docking process utilized default parameters, including a grid spacing of 1.200 (x, y, z coordinates) and angular steps of 15. The docked complex with the highest docking score and interacting with Cys7 residue was chosen for further analysis. Various interactions, such as H-bonds, hydrophobic interactions (including amide- $\pi$  stacking,  $\pi$ - $\pi$  stacking, and  $\pi$ -sigma interactions), electrostatic interactions, van der Waals forces, and unfavorable donor-donor and acceptor-acceptor interactions, were visualized using PDBsum <https://www.ebi.ac.uk/thornton-srv/databases/pdbsum> [406]. The final docked conformations were examined with Discovery Studio Client 2021 <https://discover.3ds.com/discovery-studio-visualizer-download>.

#### 4.2.6 Parameters for MD simulation:

The receptor-ligand docking offers a fixed perspective of a ligand binding at the active site of a receptor protein; in addition, computational MD simulations attempt to determine atom movements over a period using Newton's classical equations of motion [312, 325, 407]. We ran a 100 ns MD simulation to assess the EGFR binding status in the physiological parameter, using Desmond, a Package of Schrödinger LLC ([Desmond | Schrödinger \(Schrodinger. com\)](https://www.schrodinger.com)) [313]. The results yielded from the docking were considered as the basis for the MD simulation. EGFR-DHHC complexes were prepared beforehand using Protein Preparation Wizard of the Maestro Schrodinger Suite 2017, which displayed complex optimization and reduction <https://www.schrodinger.com/protein-preparation-wizard> [314]. The System Builder tool was used to prepare all the systems. TIP3P were selected for the solvent model with an orthorhombic box. The OPLS\_2005 force field was utilized throughout the simulation. Counter ions were added to the models where needed to neutralize them. The system received 0.15 M salt (NaCl) to induce a



physiological state. Seven equilibration stages of the NPT, (N: constant particle numbers, P: pressure, T: temperature)] at 1 atm pressure and 300 K temperature were carried out during the simulation [314]. The protonation of the amino acids was brought to pH 7.0. Before the simulation began, the models were relaxed. The trajectory tracks were stored every ten ps for the above assessment. The stability of the simulation was assessed by computing the RMSD and RMSF of the protein-protein complexes over time.

#### **Free energy calculation through MM-GBSA approach:**

The molecular mechanical energies paired with the MM-GBSA or MM-PBSA are essential methods for determining the  $\Delta G_{\text{bind}}$  of protein-protein (ligand) complexes [315]. For the MM-GBSA analysis, the steepest descent minimization method was used. The binding free energy was calculated using the Prime MM-GBSA approach, and a docked pose was obtained *via* the Glide algorithm [Schrödinger \(schrodinger.com\)](http://schrodinger.com).

The following equation is the formula for the ( $\Delta G_{\text{bind}}$ ):

$$\Delta G_{\text{bind}} = \Delta G (\text{solv}) + \Delta E (\text{MM}) + \Delta G (\text{SA})$$

$\Delta G (\text{solv})$  represents the difference between the sum of solvation energies of unbound receptor-ligand molecules and bound complexes computed with the GB SA.  $\Delta E (\text{MM})$  is the difference between the aggregate of the unbound receptor-ligand molecules energies and minimized energies of the receptor-ligand complex.  $\Delta G (\text{SA})$  is the difference between the complex's surface area energy and the total of the unbound receptor and ligand surface area energies [315, 316]. In addition, the data interpretation for the various RMSD, RMSF, Rg, the SASA, and B.E. were made through GraphPad Prism version 5.0 [GraphPad Prism 5.0 Download - prism.exe \(informer.com\)](http://prism.exe.informer.com) [317].

### **4.3 Results and discussion:**

#### **4.3.1. Identification of the best DHHCs that are potentially interacting with Cys7 residue of EGFR:**

Our study aimed to investigate the role of DHHC enzymes in cancer progression by modifying EGFR substrate at a Cys residue. One significant challenge we observed was identifying which Cys residue in ECD-EGFR is susceptible to palmitoylation. Using the CSS-Palm prediction tool, we determined that Cys7 of EGFR (Cys7-EGFR) was a highly probable site for palmitoylation, with a score of 37.973 using a stringent cut-off of 4.22. This site is also part of cluster C, which aligns with features of other known palmitoylation sites (**Figure 4.2**).

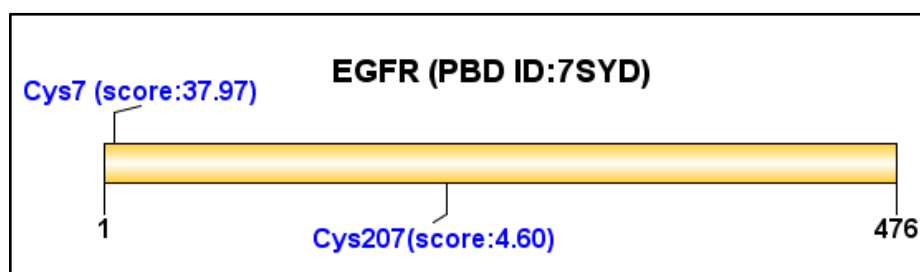


**Figure 4.2** Identification of the significant *S*-palmitoylation site in the ECD domain of EGFR (PDBID: 7SYD) through CSS palm.

We then conducted molecular docking studies using 23 DHHC isoforms and EGFR protein. We found six DHHC isoforms interacted with the Cys7- EGFR through residue-specific docking, with DHHC4 and DHHC1 exhibiting the highest docking score (**Table 4.1**). Detailed analysis revealed that Cys7-EGFR formed a conventional H-bond with Arg390 of DHHC1 at a distance of 1.68 Å, with a docking score of -261 kcal/mol and a confidence score of 0.90 (**Figure 4.3A** and **Figure 4.4A**). Additionally, Pro307 of DHHC4 interacted with Cys7-EGFR by forming a  $\pi$ -alkyl bond at a distance of 4.58 Å, yielding a docking score of -260 kcal/mol and a confidence score of 0.90 (**Figure 4.3B** and **Figure 4.4B**). From these results, we concluded that the interaction between DHHC1 and DHHC4-mediated palmitoylation of Cys7-EGFR is likely critical for its activity in cancer cells. Therefore, we selected DHHC1 and DHHC4 for further study based on their highest docking score.

**Table 4.1** The 6 DHHC isoforms interacting with Cys7-EGFR identified through H-Dock-based molecular docking.

S. no.	DHHC isoforms	Docking score (kcal/mol)	Confidence score	DHHC Chain A-EGFR Chain B interacting interface residue pairs
1	DHHC1	-261	0.9	Arg390:A - Cys7:B
2	DHHC4	-260	0.9	Pro307:A-Cys7:B
3	DHHC8	-244.35	0.86	Pro362:A-Cys7:B, Thr363:A-Cys7:B
4	DHHC9	-209.6	0.76	Pro349:A-Cys7:B
5	DHHC17	-248.06	0.88	Trp 518:A-Cys7:B
6	DHHC19	-219	0.8	Leu185:A-Cys7:B, Pro186:A-Cys7:B

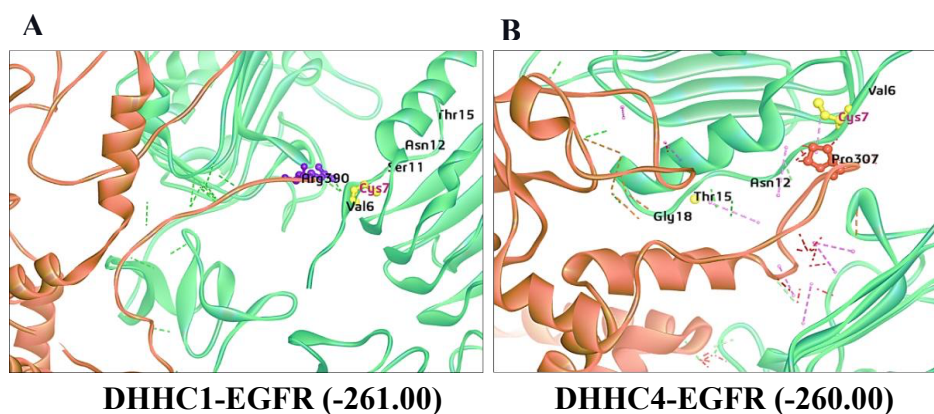
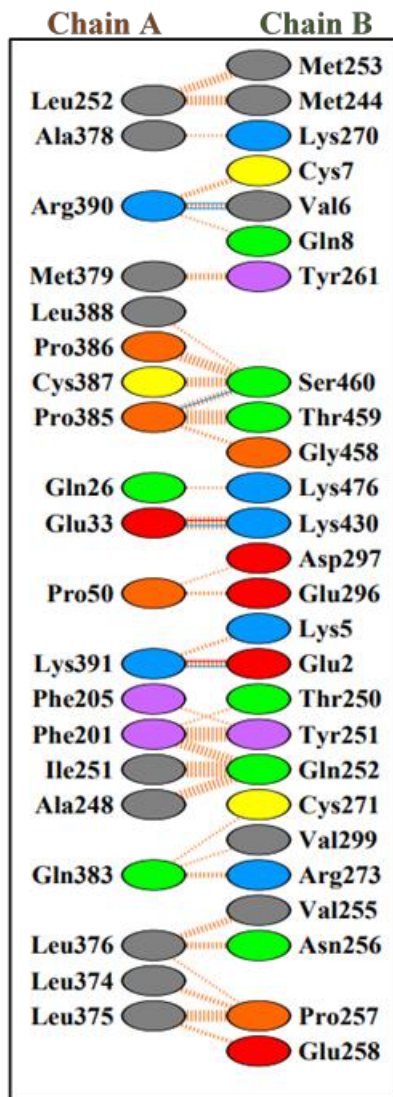


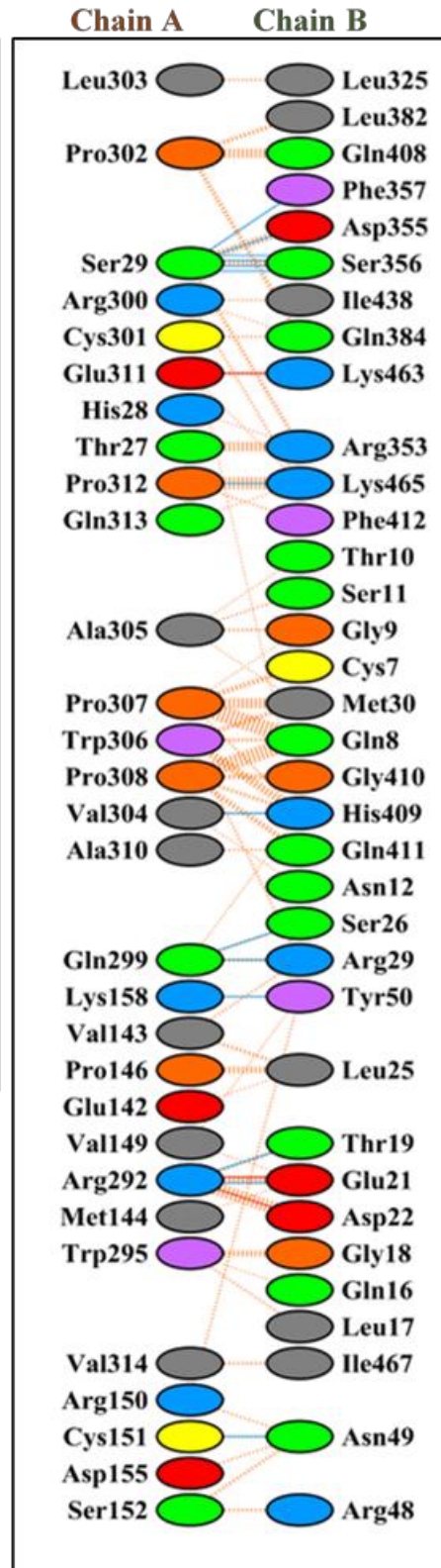
**Figure 4.3** 3D models of protein-protein complexes where Chain A of DHHCs is considered receptor (brown) and Chain B of EGFR as ligand (green) during molecular docking. A) DHHC1-EGFR and B) DHHC4-EGFR. The docking scores are represented in kcal/mol.

A



DHHC1-EGFR

B



DHHC4-EGFR

**Figure 4.4** Details of the individual residue-residue interactions that occurred across the protein-protein complexes are obtained through PDBsum A) DHHC1-EGFR and B) DHHC4-EGFR. Chain A of DHHCs and Chain B of EGFR were utilized.

#### **4.3.2 Validation of EGFR C7S mutant followed by molecular docking with the identified crucial isoforms:**

The above result showed that Cys7 of EGFR is susceptible to DHHC1 and DHHC4-mediated palmitoylation. Therefore, *via* DDMut, we identified Ser as a suitable substitute for Cys7, exhibiting a  $\Delta\Delta G$  score of -4.23 kcal/mol. The notable  $\Delta\Delta G$  score indicates that the C7S mutation of EGFR results in a functional loss relevant to a specific disease context.

We utilized three SAVES server-based tools to validate the stability and quality of the mutated 3D models. The first one was the Ramachandran plot, which revealed that the mutant EGFR C7S model possesses a favorable conformation, with 78.1% of residues in the most preferred areas and 21.1% in allowed regions, indicating robust stability (**Figure 4.5**). The second Verify 3D analysis showed that 72.69% of the residues in the mutant EGFR C7S exhibit a good three-dimensional structure consistent with their respective one-dimensional sequence (**Appendix Figure A3**). Lastly, the ERRAT server, which assesses non-bonded atomic interactions, gave an overall quality factor of 84.4706, well above the threshold of 50 for high-quality models (**Appendix Figure A4**). These results indicated that the mutant EGFR C7S 3D model is structurally reliable.



The molecular docking studies of the EGFR<sup>C7S</sup> mutant with DHHC1 and DHHC4 showed a significant decrease in docking scores compared to WT-EGFR. The docking scores were -199.46 kcal/mol and -212 kcal/mol for DHHC1 and DHHC4, with confidence scores of 0.9 and 0.8, respectively (**Figure 4.6A**, **Figure 4.7A**, **Figure 4.6B** and **Figure 4.7B**). Prior studies indicated that DHHC-mediated palmitoylation enhances protein hydrophobicity and stabilizes it in pathological situations. These results highlight the essential function of DHHC1 and DHHC4 in promoting EGFR stability and maintaining its activity in oncogenic environments.

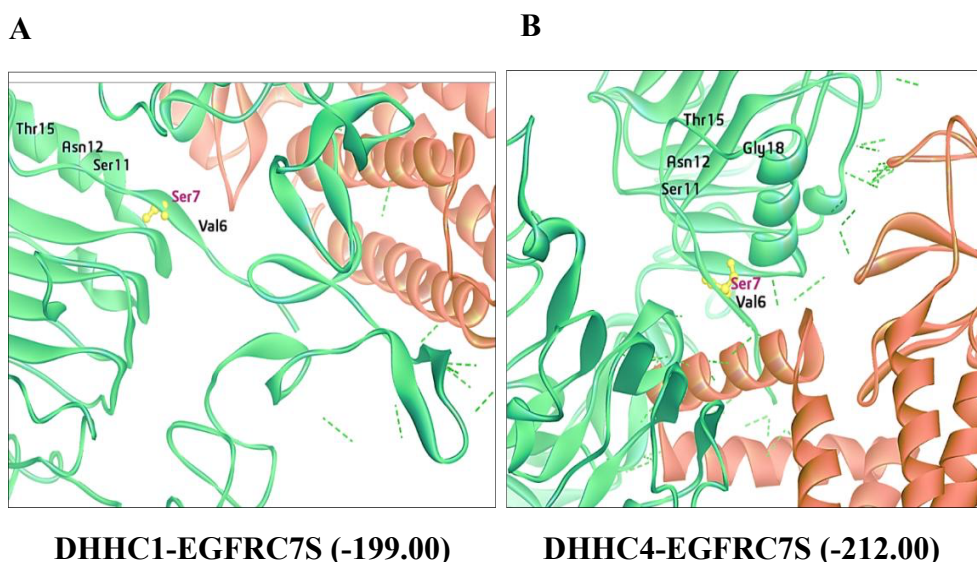


**Figure 4.6** 3D models of protein-protein complexes where Chain A of DHHCs is considered receptor (brown) and Chain B of EGFRC7S as ligand (green) during molecular docking. A) DHHC1-EGFRC7S and B) DHHC4-EGFRC7S. The docking scores are represented in kcal/mol.



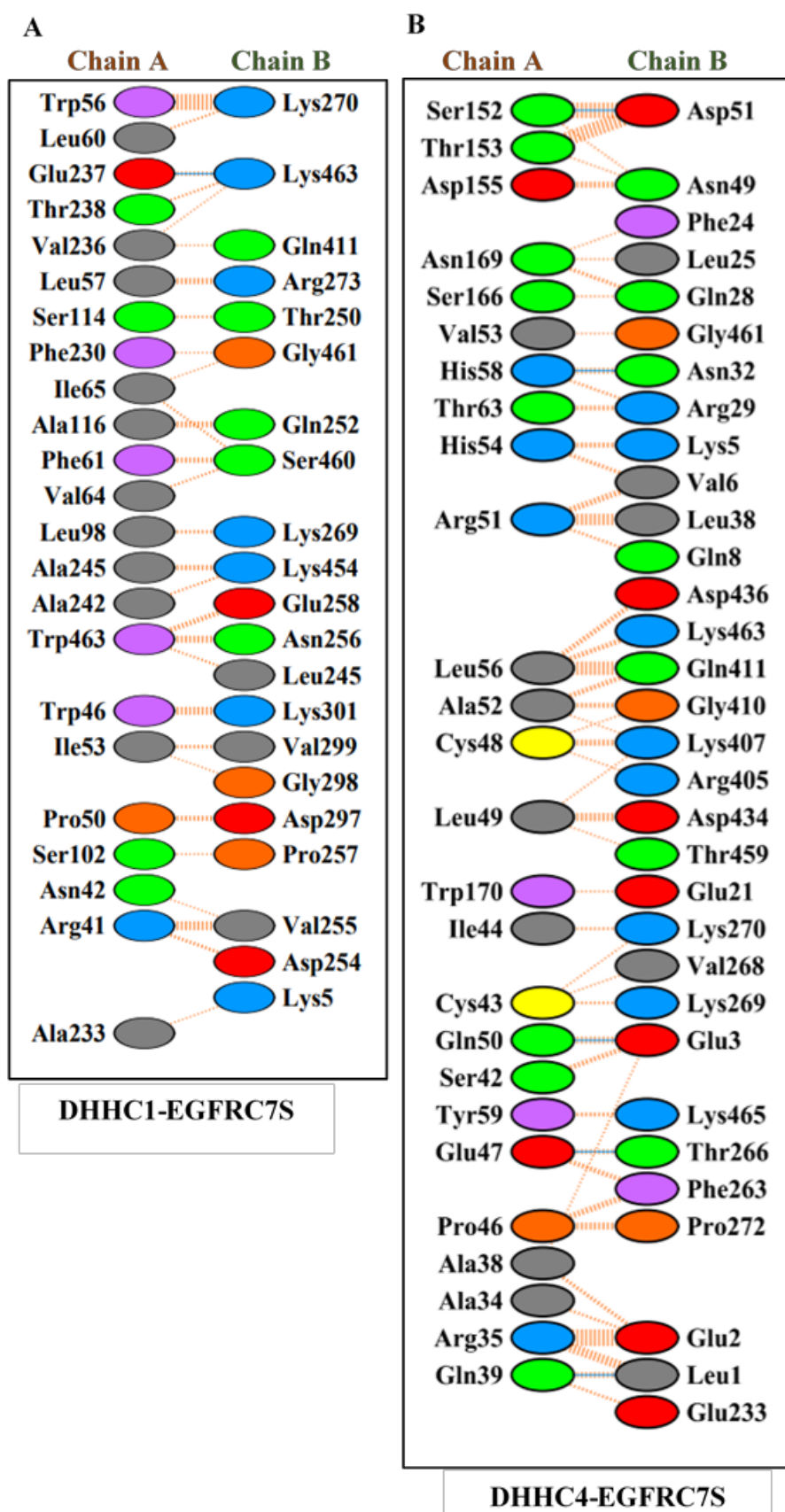


**Figure 4.7** Details of the individual residue-residue interactions that occurred across the protein-protein complexes are obtained through PDBsum A) DHHC1-EGFRC7S and B) DHHC4-EGFR.C7S Chain A of DHHCs and Chain B of EGFR were utilized.



### 4.3.3 MD simulation and binding free energy calculation:

The initial docking studies revealed that DHHC1 and DHHC4 isoforms have strong binding affinities with the EGFR protein. To further explore the stability of these protein-protein complexes, a 100 ns MD simulation was performed. The RMSD plot was utilized to assess the conformational changes in the protein backbone from its initial to final structure during the simulation. Notably, after the first 30 ns, the RMSD trajectory for the EGFR protein in complex with DHHC1 and DHHC4 was stabilized and consistent for the remaining simulation period (>20 ns). These frames were recorded until the completion of the MD simulation. The average RMSD values for EGFR, in complex with DHHC1 and DHHC4 were 5.70 Å and 4.57 Å, respectively. Nevertheless, notable variations in RMSD trajectories were noted upon introducing the EGFR C7S mutation. The EGFR C7S mutant in complex with DHHC1 and DHHC4 showed average RMSD values of 5.77 Å and 6.19 Å, respectively (**Figure 4.8** and **Table 4.2**). These findings suggest that eliminating the Cys7 residue is probably a cause for instability of the interactions between the DHHC1, DHHC4, and EGFR proteins. This loss causes significant conformational changes in protein-protein interaction throughout the simulation and reduces stability.

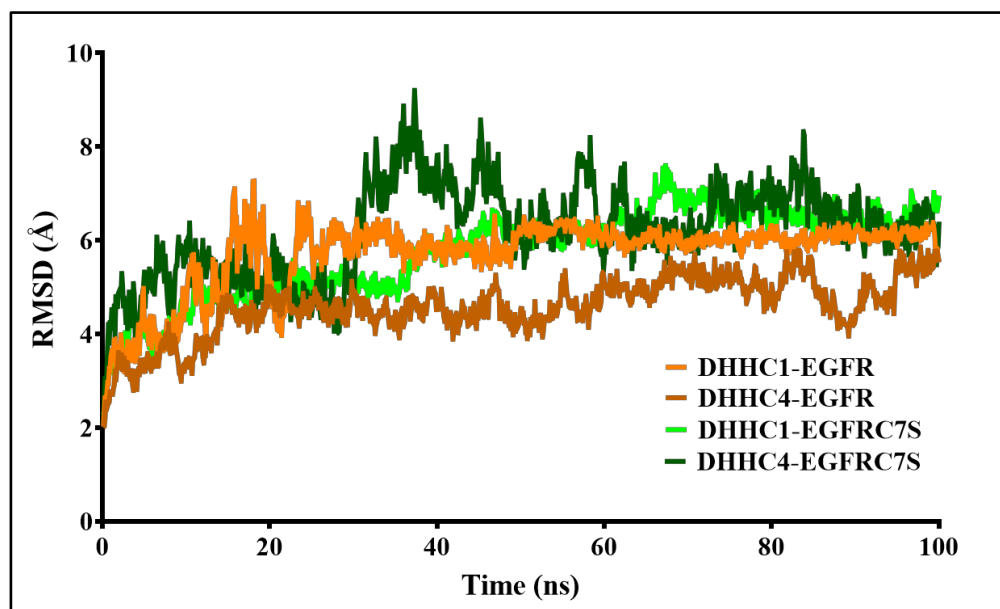


**Figure 4.8** Analysis of RMSD trajectories of EGFR and EGFR C7S in complex with DHHC1 and DHHC4 throughout 100 ns MD simulation run.

To evaluate the global stability of the complexes, we monitored other critical parameters during our MD simulations, including the Rg and SASA. The results showed that the few frames of the DHHC1-EGFRC7S and DHHC4-EGFRC7S complexes exhibited the highest Rg values, up to 35 Å. The mean Rg values for the mutant complexes were 25.60 Å and 29.46 Å, respectively. However, The DHHC1-EGFR and DHHC4-EGFR complexes displayed lower Rg values of 25.03 Å and 26.40 Å, respectively (**Figure 4.9** and **Table 4.2**). The disruption of stabilizing interactions within the protein-protein complex resulted in less stable and expanded structures. It increased Rg in the mutants than in the wild-type complexes, suggesting that they are less compact and more flexible.

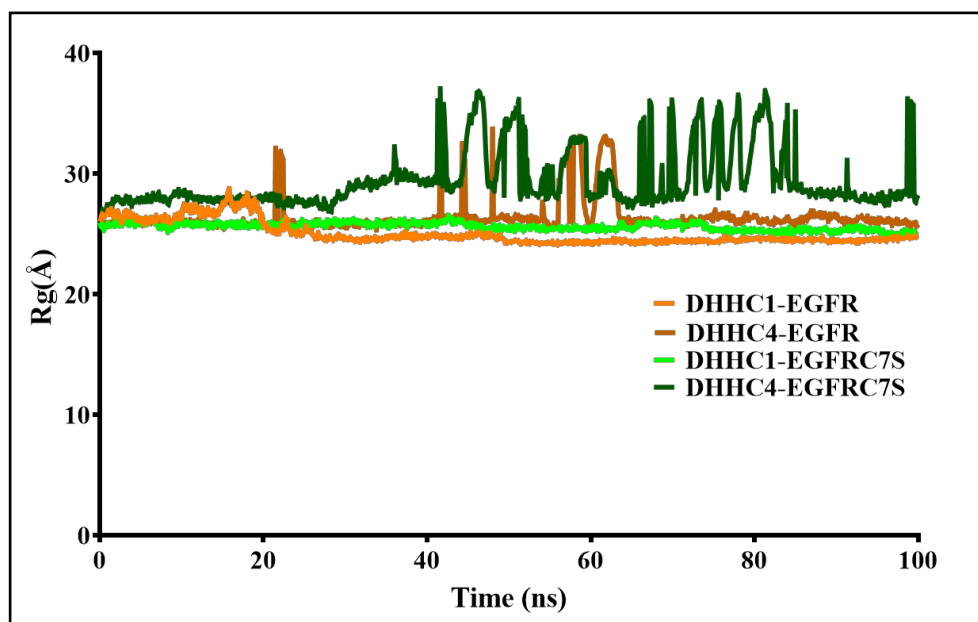


**Figure 4.9** Analysis of Rg trajectories of EGFR and EGFRC7S in complex with DHHC1 and DHHC4 throughout 100 ns MD simulation run.

Following this, the SASA was calculated for all protein-protein complexes. This calculation reflected the unfavorable interactions between water molecules and the protein across all complexes [408]. The average SASA values for the mutant complexes (DHHC1-EGFRC7S and DHHC4-EGFRC7S) were 42301 Å<sup>2</sup> and 41357 Å<sup>2</sup>. However, values for the wild-type complexes (DHHC1-EGFR and DHHC4-EGFR) are 41683 Å<sup>2</sup> and 41084 Å<sup>2</sup> (**Figure 4.10** and **Table 4.2**). The observed increase in SASA for the mutant complexes indicates that the mutation

has induced structural changes in the EGFR protein, making a greater portion of its surface accessible to the solvent.

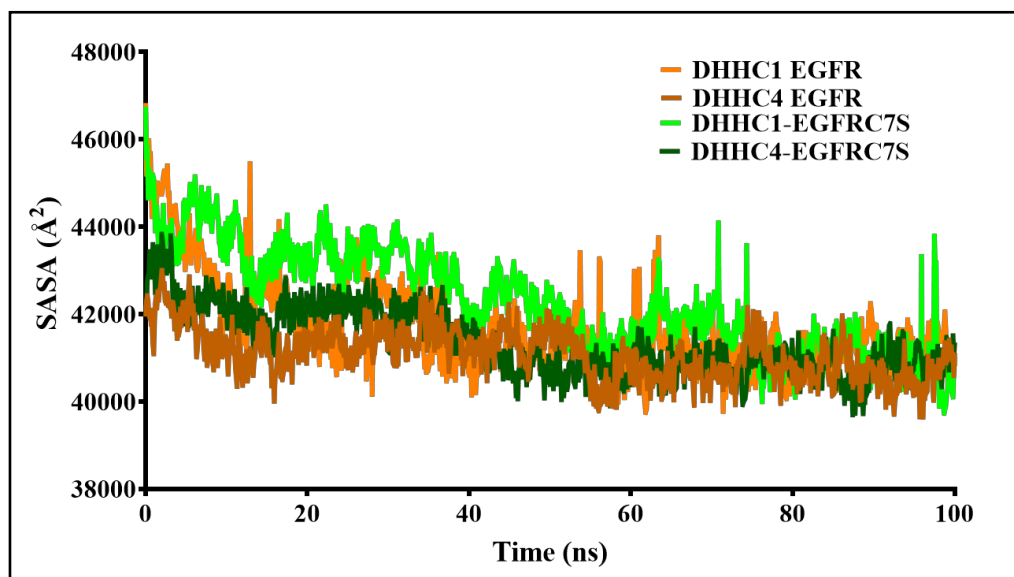


**Figure 4.10** Analysis of SASA trajectories of EGFR and EGFRC7S in complex with DHHC1 and DHHC4 throughout 100 ns MD simulation run.

**Table 4.2** Lists the average RMSD, Rg, and SASA scores obtained for EGFR and EGFRC7S in complex with DHHC isoforms.

Complex	RMSD (Å)	Rg (Å)	SASA (Å <sup>2</sup> )
DHHC1-EGFR	5.70	25.03	41683
DHHC4-EGFR	4.57	26.40	41084
DHHC1-EGFRC7S	5.77	25.60	42301
DHHC4-EGFRC7S	6.19	29.46	41357

Lastly, we performed the MM-GBSA based  $\Delta G_{\text{bind}}$  energy calculations, which provide valuable insights into the stability and affinity of protein-protein complexes [409]. Higher the binding energies more stable and favorable the interactions [410]. The MM-GBSA results showed that the original complexes (DHHC1-EGFR and DHHC4-EGFR) exhibit stronger  $\Delta G_{\text{bind}}$  energies (-178.83 kcal/mol and -274.48 kcal/mol) and better stability than the mutant complexes [DHHC1-EGFRC7S (-102.07 kcal/mol), and DHHC4-EGFRC7S (-177.47 kcal/mol)] (**Figure 4.11** and **Table 4.3**). The result suggests that the C7S

mutations adversely affect the binding interactions between DHHC1, DHHC4, and EGFR, likely disrupting critical stabilizing interactions.

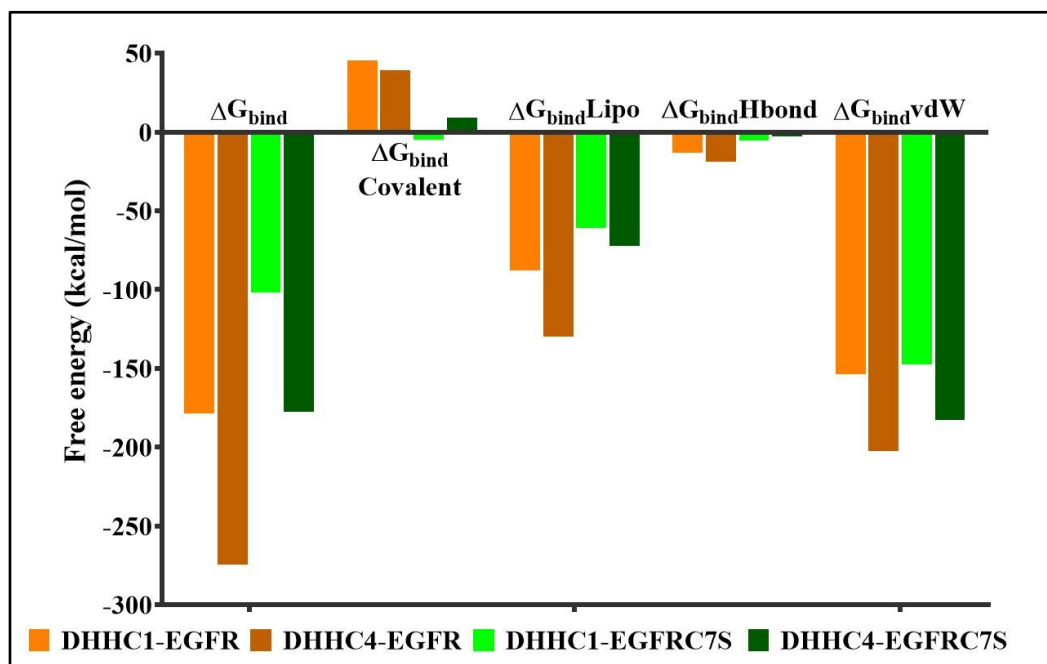


**Figure 4.11** Binding free energies and the corresponding energy components (covalent, lipophilic, Hbond, and van der Waal) obtained from MM-GBSA analysis for EGFR and EGFRC7S in complex with DHHC1 and DHHC4 throughout 100 ns MD simulation run.

**Table 4.3** Lists the energy components obtained for DHHC isoforms in complex with EGFR and EGFRC7S.

Complex	$\Delta G_{\text{bind}}$ (kcal/mol)	$\Delta G_{\text{bind Covalent}}$ (kcal/mol)	$\Delta G_{\text{bind Lipo}}$ (kcal/mol)	$\Delta G_{\text{bind Hbond}}$ (kcal/mol)	$\Delta G_{\text{bind vdW}}$ (kcal/mol)
DHHC1-EGFR	-178.83	45.59	-87.99	-13.16	-153.76
DHHC4-EGFR	-274.48	39.37	-129.80	-19.00	-202.43
DHHC1-EGFRC7S	-102.07	-4.96	-61.06	-5.52	-147.57
DHHC4-EGFRC7S	-177.47	9.3	-72.17	-3.00	-182.93

#### **4.4 Conclusion:**

The role of DHHC-mediated *S*-palmitoylation in cancer progression has been extensively studied, especially its impact on several vital oncogenes, including EGFR. Numerous studies have shown that DHHC-mediated palmitoylation of intracellular Cys residues of EGFR is crucial for its proper localization and function in oncogenic environments [6, 22]. However, these studies have primarily concentrated on intracellular Cys residue's palmitoylation, and no research study has addressed the palmitoylation of the ECD-EGFR. Our study used molecular docking and MD simulations to identify the critical isoforms interacting with ECD-EGFR. Our results indicated that DHHC1 and DHHC4 interacted with the ECD-EGFR domain. Additionally, we found that a mutation at C7S of ECD-EGFR disrupts the interaction between DHHCs and EGFR.

In summary, our research suggests that DHHCs-mediated *S*-palmitoylation at the Cys7-ECD-EGFR site may be responsible for the abnormal expression of EGFR in cancer cells. The possible mechanism could be that palmitoylation at ECD-EGFR causes conformational changes that mimic a ligand-bound state or stabilize an active ECD conformation, resulting in receptor dimerization and activation without ligand binding, thereby promoting continuous signaling. However, an *in vitro* investigation is needed to unravel this mechanism.



## Chapter 5: Conclusion and future perspective

---

### **5.1 Summary of the thesis:**

Protein *S*-palmitoylation is a reversible form of protein lipidation in which the formation of a thioester bond occurs between a Cys residue of a protein and a 16-carbon fatty acid chain. This modification is catalyzed by a family of PAT enzymes, known as DHHCs, so called because of their Asp-His-His-Cys (DHHC) catalytic motif[1]. Dynamic regulation of *S*-palmitoylation is also governed by protein depalmitoylases. These enzymes balance the cycling of palmitoylation and regulate cellular signaling, cell growth, and organization[8]. The *S*-palmitoylation has been recognized as one of the most enigmatic modifications compared to other forms of protein lipidation. This complexity arises due to the 23 distinct DHHC isoforms, each with a wide cellular distribution and a diverse range of substrates[134]. Many of these substrates participate in various cellular processes, ultimately contributing to the development of diseases.

A significant challenge in this field is the lack of suitable and less toxic inhibitors for the cellular system. The most widely used inhibitor, 2-BP, is associated with several limitations, including toxicity and off-target effects [183]. These issues complicate the study of palmitoylation and highlight the need for more effective and safer inhibitors to advance research in this area.

It is well-reported that tumor cells are known for their remarkable flexibility in reprogramming metabolism to support tumor initiation and resistance to therapies. This metabolic reprogramming involves extensive rewiring of bioenergetics, biosynthesis, and redox balance to meet the increased energy demands of cancer cells [411, 412]. Metabolites, the crucial carrier of metabolism, represent the direct signature of the molecular phenotype, making their profiling highly relevant for clinical applications in oncology [413]. Over the past decades, the field of cancer metabolism has benefited from an explosion of advanced biochemical technologies, providing researchers with unprecedented tools to navigate this complexity, including metabolomics.

Notably, all the DHHC isoforms are implicated in various pathological conditions, most commonly in cancer, but how they regulate cancer's cellular metabolism is still understudied. Characterizing DHHC-specific metabolism can help to identify novel metabolite targets for cancer treatment. The significance of *S*-palmitoylation in tumorigenesis has only begun to be elucidated in the past decade. Therefore, these unexplored and enigmatic challenges sparked our curiosity to address them and provide valuable new insights into *S*-palmitoylation and its implications for cancer research. Below is a detailed summary of each chapter.

**Chapter 2:** As discussed earlier, protein *S*-palmitoylation mediated by DHHC enzymes is linked to various health conditions such as neurodegenerative disorders, cancer, and autoimmune diseases[414]. However, the current pan-DHHC inhibitors have pharmacological limitations, including toxicity and off-target effects, which restrict their thorough investigation at the cellular level [87]. Therefore, this chapter explored the therapeutic potential of natural compounds known for their minimal side effects, as DHHC-inhibitors [87, 415]. We conducted an *in silico* screening of 115 phytochemicals to evaluate their interactions with the binding site of DHHC20. Among these compounds, lutein, 5-hydroxyflavone, and 6-hydroxyflavone exhibited highest binding energies (-9.2, -8.5, and -8.5 kcal/mol, respectively) in the DHHC20 groove compared to the pan-DHHC inhibitor 2-BP (-7.0 kcal/mol).

The MD simulation results indicated that DHHC20 formed a more stable conformation with lutein than with 5-hydroxyflavone and 6-hydroxyflavone, involving hydrophobic interactions and H-bonds. The long aliphatic chain of lutein (mimicking palmitic acid) is why it stabilized more in the DHHC20 binding pocket. We further conducted a PASS-analysis, which indicated that all these molecules are strongly associated with health-beneficial activities, such as apoptosis-agonist or antioxidant. In conclusion, this finding represents a promising starting point for further exploration of these natural molecules as potential inhibitors of DHHC20, highlighting their suitability for future therapeutic development in targeting *S*-palmitoylation pathways.

**Chapter 3:** Over the past decade, increasing evidence has highlighted the crucial role of protein DHHC2 in controlling tumorigenesis through the



palmitoylation of diverse protein substrates[114, 116]. However, a thorough understanding of how these proteins mainly affect the metabolic environment of cancer cells remains unclear. Therefore, in this chapter, we conducted a study to examine cellular metabolic changes that occurred by DHHC2 on the HEK-293T cell line under DHHC2-KD, DHHC2-OE, and Ctrl conditions utilizing LC-MS/MS-based untargeted metabolomics analysis. Our dataset identified 73 metabolites across all conditions, with only 22 showing significant differences in univariate analysis. After that, we conducted pathway analysis focusing on metabolites meeting specific criteria ( $VIP \geq 0.7$ ,  $P$  value  $\leq 0.05$ ,  $FC > 2$  (upregulated) and  $< 0.5$  in DHHC2-OE (downregulated)). This analysis showed significant alterations in pathways such as pyrimidine metabolism, urea cycle, and aspartate metabolism in DHHC2-KD groups due to the abundance of onco-metabolites such as glutamine, uridine, and glutamic. Contrarily, we identified a few crucial metabolites in the DHHC2-OE group, like betaine, 5'-MTA, and ALA [393, 398, 399], which are already well-known for their tumor-suppressive roles or therapeutic potential. By activating these metabolites, DHHC2 may act as a tumor suppressor across different cancer types. Additionally, our work shed new light on the interaction of DHHC2, p53, and CAD, highlighting its significance in cancer therapies. Nevertheless, cancer cells are complex and dynamic; it can be challenging to understand the metabolic changes that occur within them. The function of DHHCs also seems to change based on the cancer environment. Thus, our study offers insightful information that may serve as a fundamental resource for a deeper comprehension of the connection between the intricate cancer metabolome and DHHC-mediated *S*-palmitoylation..

**Chapter 4:** Till now, more than 5000 substrates have been identified for DHHC isoforms, including well-known tumor suppressors and promoters, e.g., PD-L1 and EGFR. However, the available research studies regarding DHHC and EGFR have elucidated the involvement of intracellular palmitoylated Cys residue in cancer progression [6]. Notably, no research has addressed the role of palmitoylation of the ECD-EGFR. Our study aims to fill this research gap by identifying potential DHHC isoforms interacting with ECD-EGFR using computational methods. The MD simulation study revealed that DHHC1 and DHHC4 exhibit the strongest binding affinity with WT-EGFR, with the  $\Delta G_{\text{bind}}$

score of -178.83 kcal/mol and -274.48 kcal/mol. Using the CSS-Palm database, we identified Cys7 of EGFR as a critical residue likely to undergo S-palmitoylation. Subsequently, MD simulations showed that the EGFR C7S mutation substantially impaired the binding of DHHC1 and DHHC4 with EGFR ( $\Delta G_{\text{bind}}$  score of -102.07 kcal/mol and -177.47 kcal/mol for the mutant complex). This finding suggests that the DHHC1 and DHHC4-mediated S-palmitoylation of ECD-EGFR at Cys7 may facilitate its aberrant activation in cancer cells. However, *in vitro* validation is critically needed to understand this interaction fully.

## **5.2 Future perspective:**

S-palmitoylation is an emerging field that targets pathological implications, specifically cancer[49]. Therefore, this thesis aims to address some of the critical gaps in the field, such as identifying suitable inhibitors and understanding the role of DHHCs at the metabolomic level, specifically DHHC2, to improve the therapeutic advantages. However, this work serves as a preliminary foundation, and several important aspects need further exploration to achieve conclusive results.

In the second chapter, lutein was identified as an effective inhibitor for the DHHC20 binding groove, likely due to its long aliphatic chain, offering a potential solution to the challenges posed by 2-BP. However, this conclusion is based on computational analysis and needs validation through *in vitro* and *in vivo* studies to overcome the limitations associated with 2-BP.

In the third chapter, we demonstrated that DHHC2 might act as a tumor suppressor at the metabolomic level by upregulating p53 and downregulating CAD (a pyrimidine regulator) in HEK-293T cell lines. However, additional studies should be performed using other cancer cell lines, such as HEP-G2, MDA-MB-231, and U87. Subsequently, this work focuses on the metabolomic aspects of DHHC2; it is essential to investigate how other DHHCs affect the metabolomic environment of cancer cells and validate these effects *in vivo*.

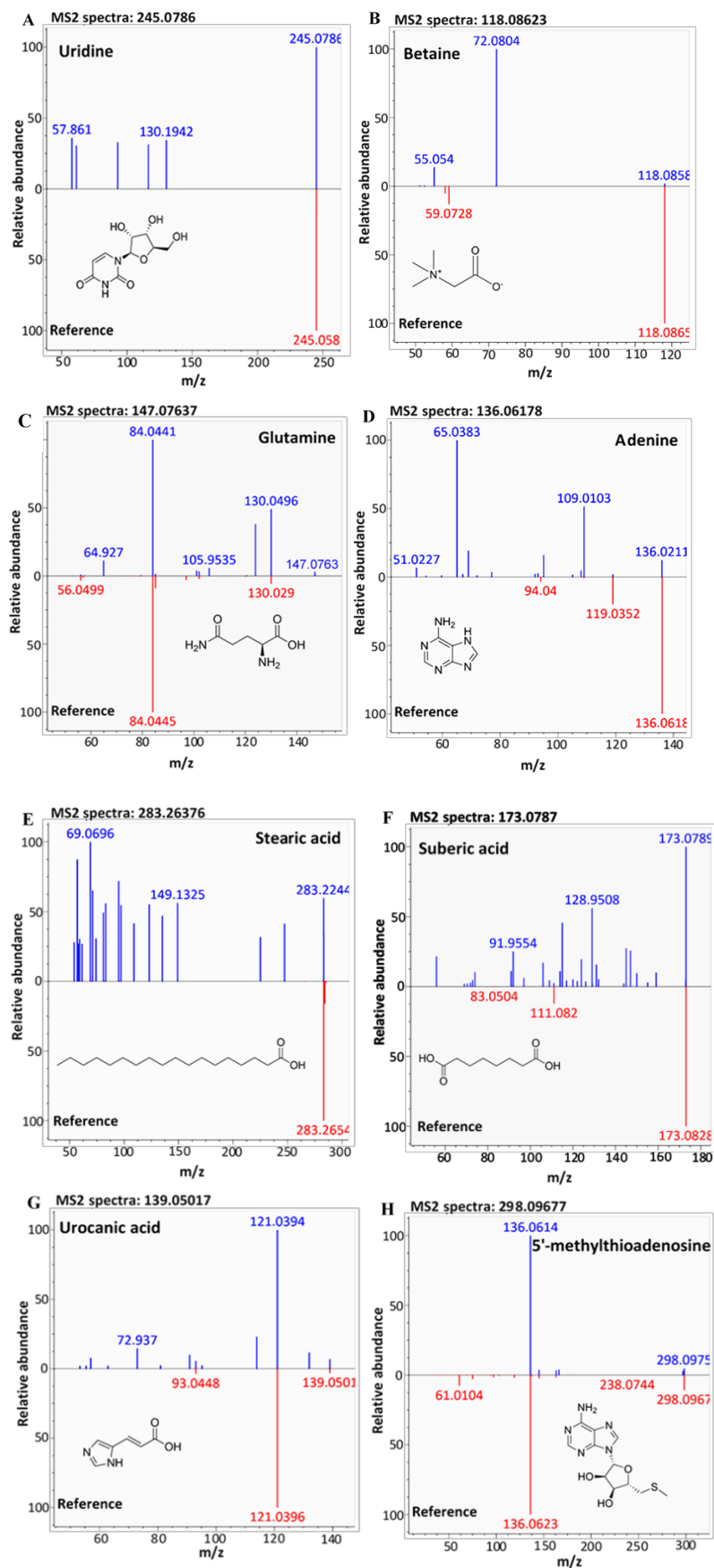
Finally, we showed that DHHC1 and DHHC4 could interact with the ECD-EGFR domain using computational methods. However, this finding also requires *in vitro* and *in vivo* validation, as it may be instrumental in targeting the

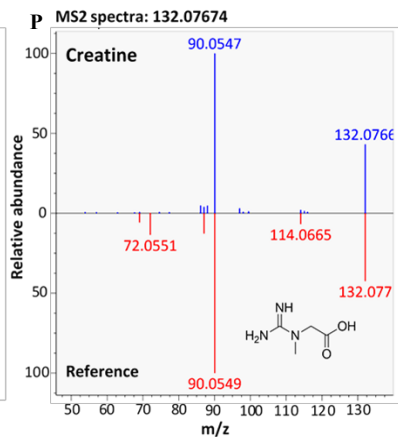
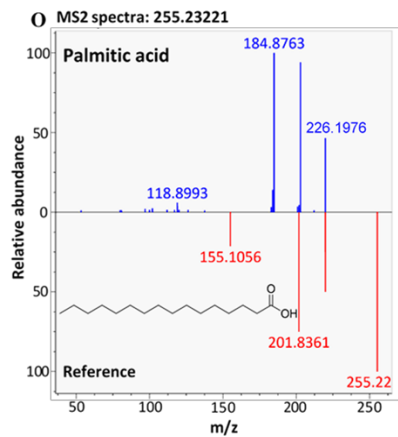
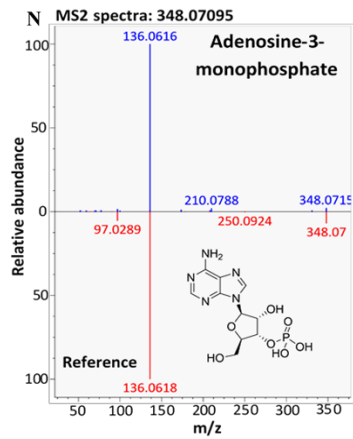
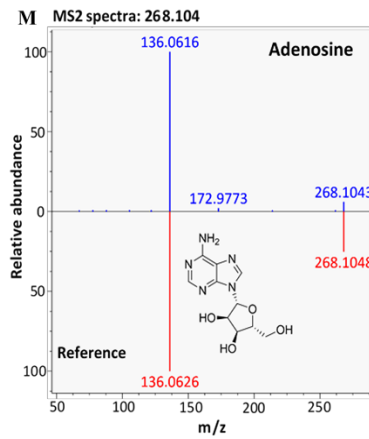
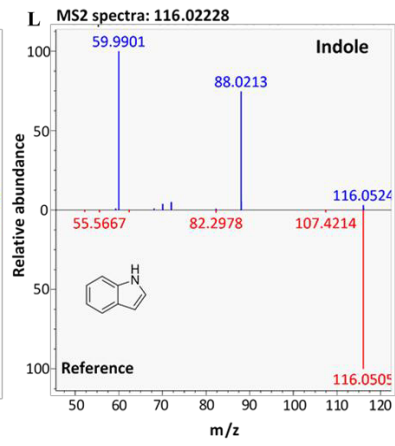
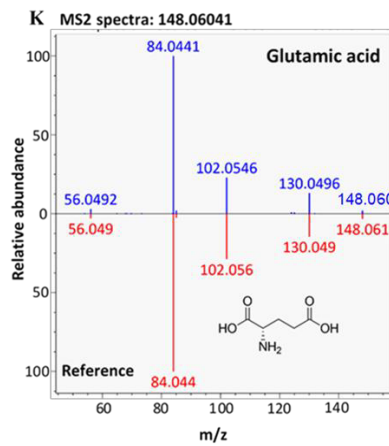
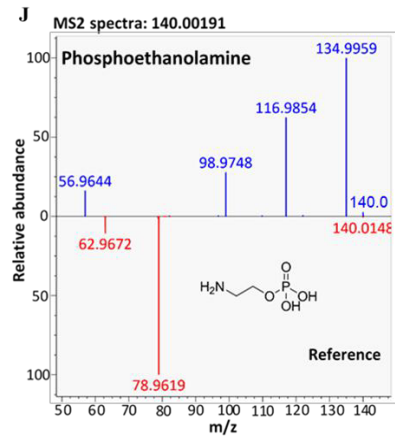
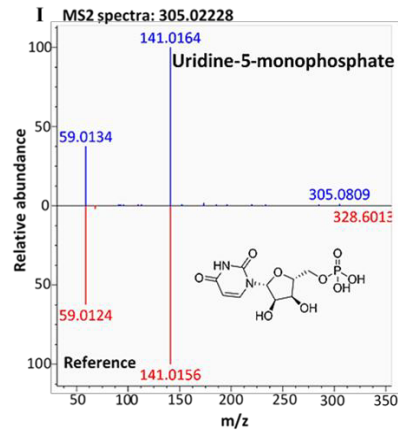
ligand-independent activation of EGFR and addressing cancer relapse, which often occurs even after treatment with EGFR monoclonal antibodies.

In summary, this thesis provides an initial exploration into critical aspects of *S*-palmitoylation, and further in-depth studies are necessary to draw definitive conclusions and contribute to human health.



# Appendix





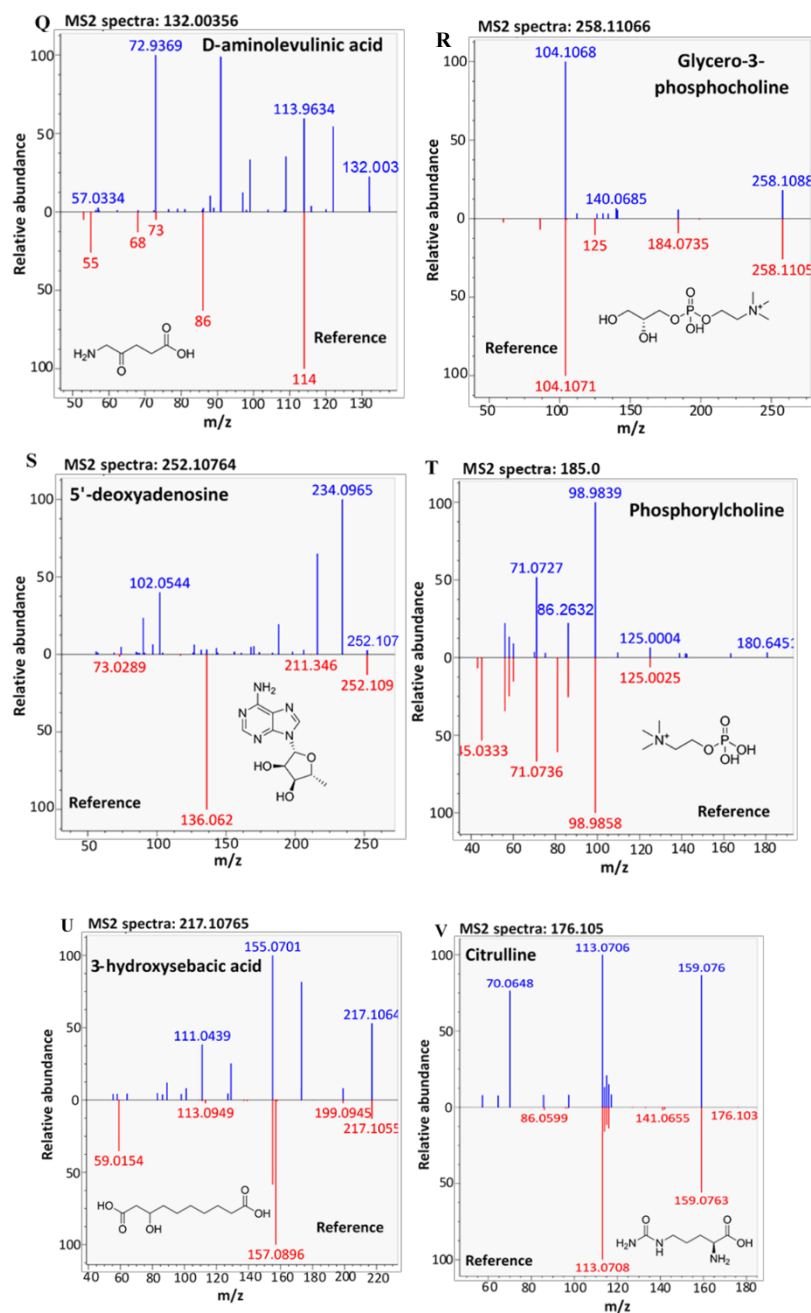


**Figure A1** Metabolites characterization using *in silico* spectral libraries. The MS/MS spectra for the 22 significantly ( $P$  value  $\leq 0.05$ ) altered metabolites are showcased. The upper spectra represents the experimental (blue) peaks of selected metabolite, and the lower spectra shows the reference (red) peaks from the *in silico* spectral libraries, respectively.

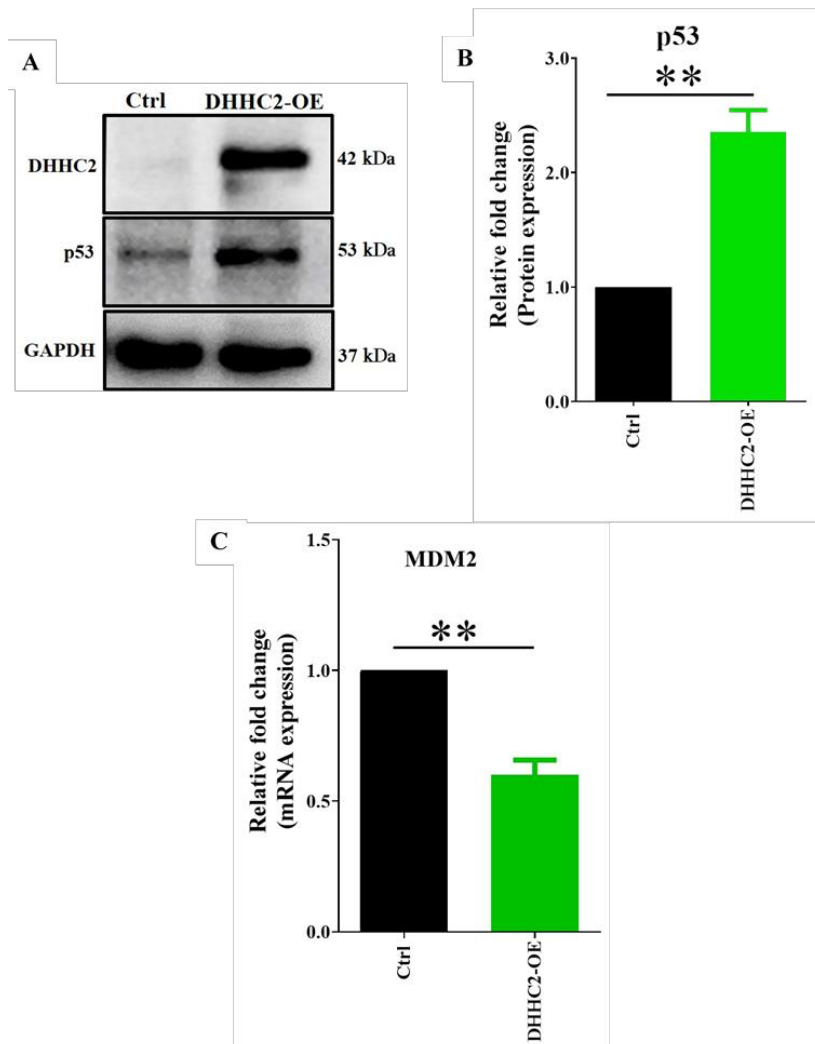


**Figure A2** A) Western blot analysis of p53 protein post-DHHC2 transfection compared with a Ctrl in HEK-293T cell line. B) Statistical representation of relative fold change expression of p53 protein post-DHHC2 transfection compared to Ctrl. C) Relative MDM2-mRNA fold change expression post-DHHC2 overexpression compared with Ctrl in HEK-293T cell line. Samples were normalized with the endogenous control GAPDH (n=3).



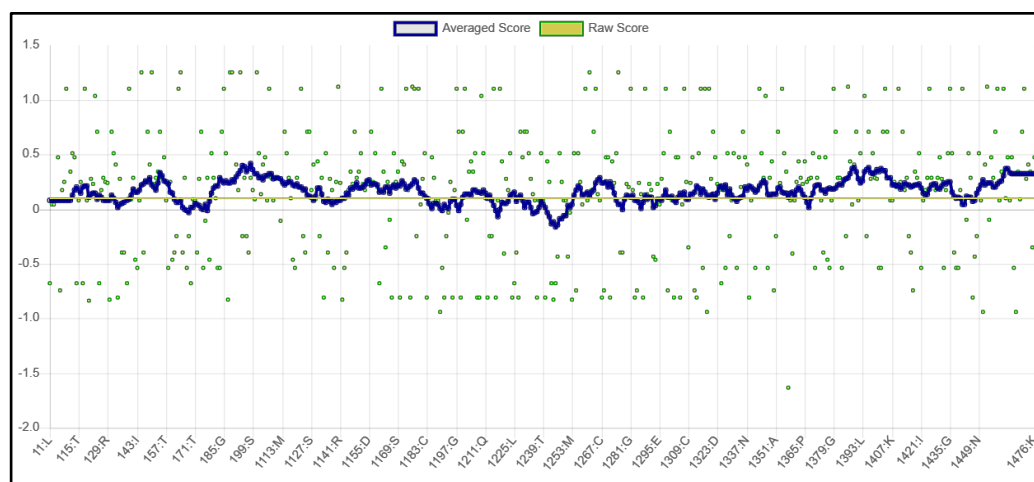


**Figure A3** Verify 3D plot: The plot predicts 72.69% of the residues in mutant EGFR C7S have an averaged 3D-1D score > 0.1.

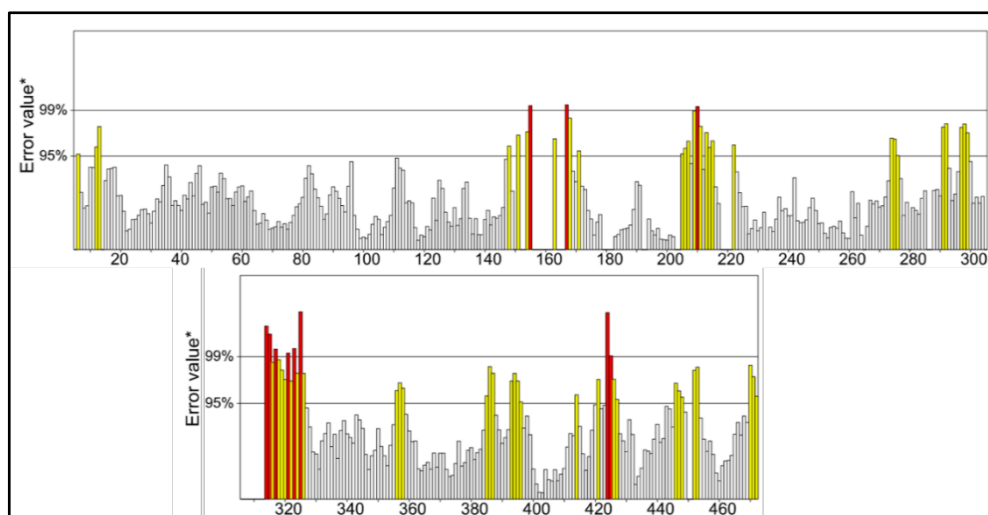


**Figure A4** ERRAT server analysis. Graphics show the overall quality factor of the mutant EGFR C7S protein.

\*On the error value, two lines are drawn to indicate the confidence with which it is possible to reject regions that exceed that error value. Overall quality factor, is expressed as the percentage of the EGFR C7S protein for which the calculated error value falls.



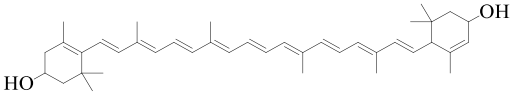
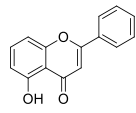
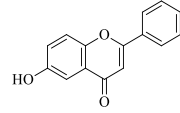
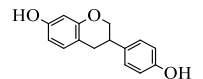
Table A1 Summarizing the role of 23 DHHC isoforms in cancer progression and prevention.

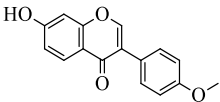
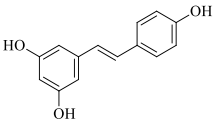
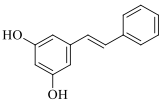
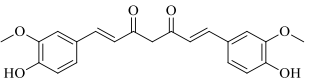
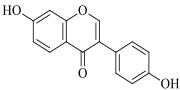
S.No.	DHHC isoforms	M.W. (KDa)	Location	Role in cancer		References
				Tumor suppressor	Tumor promoter	
1	DHHC1	54.81	ER	Breast cancer, Prostate cancer	Not available	[111]
2	DHHC2	42.02	ER, Golgi	Colorectal cancer, Ovarian cancer, Hepatocellular carcinoma, Lymph node metastasis	Clear cell renal cell carcinoma	[14, 114]
3	DHHC3	34.17	Golgi	Not available	Breast cancer, Prostate cancer	[123]
4	DHHC4	39.79	ER	Not available	Glioblastoma, Lung adenocarcinoma	[126, 127]
5	DHHC5	77.55	Cytoplasm	Not available	Glioblastoma, Lung adenocarcinoma	[129]
6	DHHC6	47.66	ER	Not available	Colonl cancer	[131]
7	DHHC7	35.14	Golgi	Prostate cancer	Hepatocellular carcinoma, Breast cancer	[133, 135]
8	DHHC8	81.44	Golgi	Not available	Glioblastoma	[136]

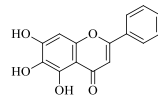
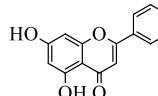
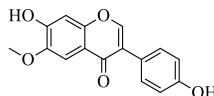
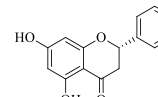
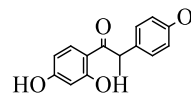
S.No.	DHHC isoforms	M.W. (KDa)	Location	Role in cancer		References
				Tumor suppressor	Tumor promoter	
9	DHHC9	40.91	ER, Golgi, Cytosol	Not available	Colon cancer, Pancreatic cancer	[137]
10	DHHC11	45.98	ER	Lung adenocarcinoma	Burkett lymphoma	[145, 146]
11	DHHC12	30.81	ER, Golgi	Not available	Glioblastoma, Ovarian cancer	[148, 149]
12	DHHC13	70.86	ER, Golgi	Not available	Oral squamous cell carcinoma, Melanoma	[72, 286]
13	DHHC14	53.38	ER	Prostate cancer	Gastric cancer	[154]
14	DHHC15	39.33	Golgi	Not available	Glioma	[155]
15	DHHC16	43.63	ER	Not available	Hepatocellular carcinoma	[156]
16	DHHC17	72.64	Cytosol	Not available	Glioblastoma, Liver tumorigenesis	[11, 160]
17	DHHC18	42.03	Golgi	Not available	Glioblastoma	[161]
18	DHHC19	34.35	ER	Not available	Osteosarcoma, Clear cell renal cell carcinoma	[162, 163]

S.No.	DHHC isoforms	M.W. (KDa)	Location	Role in cancer		References
				Tumor suppressor	Tumor promoter	
19	DHHC20	42.27	Plasma membrane	Not available	Pancreatic ductal adenocarcinoma, Lung cancer	[21, 22, 165]
20	DHHC21	31.38	Golgi, Plasma membrane	Diffuse large B-cell lymphoma	Leukemia	[169, 170]
21	DHHC22	29.10	ER, Golgi	Breast cancer	Not available	[171]
22	DHHC23	45.98	Not reported yet	Not available	Esophageal cancer, Glioma	[172]
23	DHHC24	30.17	Not reported yet	Not available	Lung adenocarcinoma	[127]

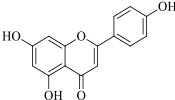
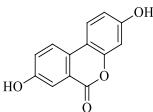
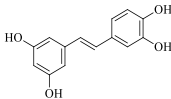
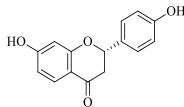
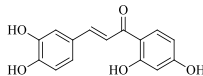
**Table A2** Binding energy of natural molecules docked with DHHC20 (6BML) generated via PyRx based molecular docking.

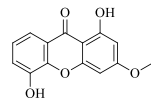
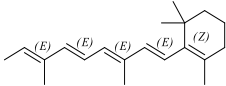
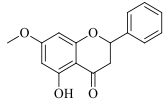
S.no.	PubChem ID	Binding energy (kcal/mol)	Ligands	Sources	Chemical structure
1	5281243	-9.2	Lutein	<i>Spinacia oleracea</i> , <i>Brassica oleracea</i> var. <i>italica</i>	
2	68112	-8.5	5-hydroxyflavone	<i>Conchocarpus heterophyllous</i> , <i>Primula denticulata</i>	
3	72279	-8.5	6-hydroxyflavone	<i>Barleria prionitis</i>	
4	6950272	-8.1	R-Equol	<i>Pueraria mirifica</i>	

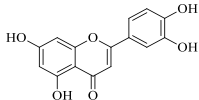
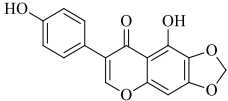
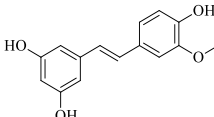
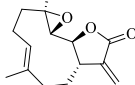
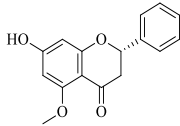
S.no.	PubChem ID	Binding energy (kcal/mol)	Ligands	Sources	Chemical structure
5	5280378	-8	Formononetin	<i>Pterocarpus indicus, Ardisia paniculata</i>	
6	445154	-7.9	Resveratrol	<i>High concentrations in red grapes</i>	
7	5280457	-7.9	Pinosylvin	<i>Alnus pendula, Calligonum leucocladum</i>	
8	969516	-7.9	Curcumin	<i>Curcuma longa</i>	
9	5281708	-7.8	Daidzein	<i>Pueraria mirifica</i>	

S.no.	PubChem ID	Binding energy (kcal/mol)	Ligands	Sources	Chemical structure
10	5281605	-7.7	Baicalein	<i>Scutellaria baicalensis</i> and <i>Scutellaria lateriflora</i>	
11	5281607	-7.7	Chrysin	<i>Oroxylum indicum</i> or Indian trumpet flower	
12	5317750	-7.7	Glycitein	<i>Psidium guajava</i> , <i>Ammopiptanthus mongolicus</i>	
13	68071	-7.7	Pinocembrin	<i>Pinus heartwood</i> , <i>Eucalyptus</i> , <i>Populus</i> , <i>Euphorbia</i> , and <i>Sparattosperma leucanthum</i> ,	
14	3584988	-7.6	Angolensin	<i>Pterocarpus indicus</i> , <i>Pterocarpus erinaceus</i>	

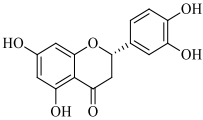
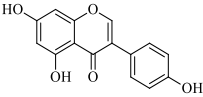
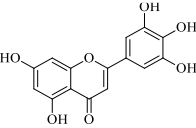
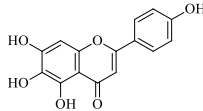


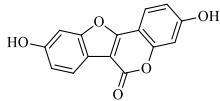
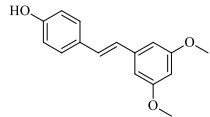
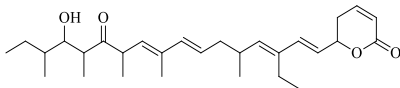
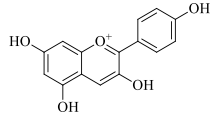
S.no.	PubChem ID	Binding energy (kcal/mol)	Ligands	Sources	Chemical structure
15	5280443	-7.6	Apigenin	<i>Verbascum lychnitis, Carex fraseriana</i>	
16	5488186	-7.6	Urolithin A	<i>Punica granatum and Trogopterus xanthipes</i>	
17	667639	-7.6	Piceatannol	<i>Vitis amurensis, Smilax bracteata</i>	
18	114829	-7.5	Liquiritigenin	<i>Dracaena draco, Pterocarpus marsupium</i>	
19	5281222	-7.5	Butein	<i>Dahlia pinnata, Calanticaria bicolor</i>	

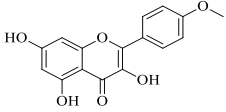
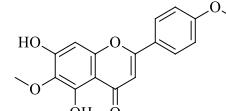
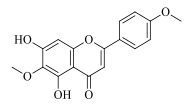
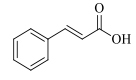
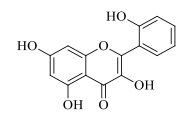
S.no.	PubChem ID	Binding energy (kcal/mol)	Ligands	Sources	Chemical structure
20	5281651	-7.4	Mesuxanthone A	<i>Calophyllum inophyllum, Hypericum chinense</i>	
21	5287722	-7.4	Axerophthene	<i>Senecio algens</i>	
22	5320954	-7.4	Rhapontigenin	<i>Rheum undulatum, Gnetum hainanense</i>	
23	73201	-7.4	Pinostrobin	<i>Taxandria spathulata, Onychium siliculosum</i>	
24	5280373	-7.3	Biochanin A	<i>Trifolium pratense</i>	

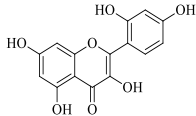
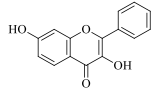
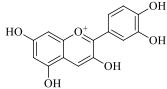
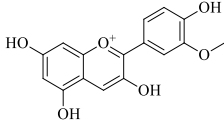
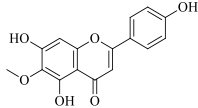
S.n o.	PubChem ID	Binding energy (kcal/mol)	Ligands	Sources	Chemical structure
25	5280445	-7.3	Luteolin	<i>Verbascum lychnitis</i> , <i>Carex fraseriana</i>	
26	5281779	-7.3	Iriline	<i>Iris sofarana</i> , <i>Iris leptophylla</i>	
27	5318650	-7.3	Isorhapontigenin	<i>Smilax corbularia</i> , <i>Aiphanes horrida</i>	
28	7251185	-7.3	Parthenolide	<i>Cyathocline purpurea</i> , <i>Tanacetum parthenium</i>	
29	154279	-7.2	Alpinetin	<i>Alpinia blepharocalyx</i> , <i>Alnus firma</i>	

S.no.	PubChem ID	Binding energy (kcal/mol)	Ligands	Sources	Chemical structure
30	442768	-7.2	Dalbergin	<i>Dalbergia cochinchinensis</i> , <i>Pterocarpus santalinus</i>	
31	4788	-7.2	Phloretin	<i>Malus doumeri</i> , <i>Populus candicans</i>	
32	5280537	-7.2	Moupinamide	<i>Zanthoxylum beecheyanum</i> , <i>Polyalthia suberosa</i>	
33	5281804	-7.2	Prunetin	<i>Iris milesii</i> , <i>Prunus leveilleana</i>	

S.no.	PubChem ID	Binding energy (kcal/mol)	Ligands	Sources	Chemical structure
34	440735	-7.1	Eriodictiol	<i>Eupatorium album, Eupatorium hyssopifolium, and</i>	
35	5280961	-7.1	Genistein	<i>Alchornea cordifolia</i>	
36	5281701	-7.1	Tricetin	<i>Punica granatum, Lathyrus pratensis</i>	
37	5281697	-7	6-Hydroxyapigenin	<i>Scoparia dulcis, Artemisia douglasiana</i>	

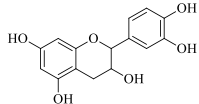
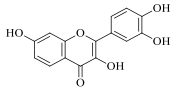
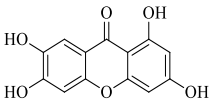
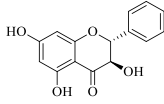
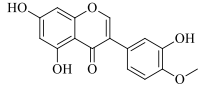
S.no.	PubChem ID	Binding energy (kcal/mol)	Ligands	Sources	Chemical structure
38	5281707	-7	Coumestrol	<i>Campylotropis hirtella</i> , <i>Melilotus messanensis</i>	
39	5281727	-7	Pterostilbene	<i>Vitis rupestris</i> , <i>Pterocarpus marsupium</i>	
40	5471086	-7	Callystatin A	<i>Callyspongia truncata</i>	
41	440832	-6.9	Pelargonidin	<i>Eleocharis dulcis</i> , <i>Eleocharis pallens</i>	

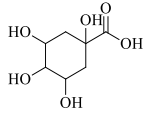
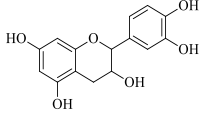
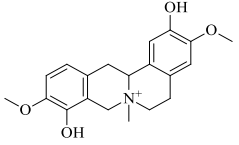
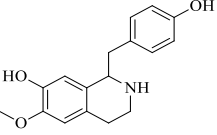
S.no.	PubChem ID	Binding energy (kcal/mol)	Ligands	Sources	Chemical structure
42	5281666	-6.9	Kaempferide	<i>Ageratina altissima, Chromolaena odorata</i>	
43	5320438	-6.9	Pectolinarigenin	<i>Eupatorium cannabinum, Chromolaena odorata</i>	
44	85318818	-6.9	Thymoquinone	<i>Nigella sativa, Monarda fistulosa</i>	
45	444539	-6.8	Cinnamic acid	<i>Marsypopetalum crassum, Aiouea brenesii</i>	
46	5281610	-6.8	Datisctetin	<i>Dianthus caryophyllus</i>	

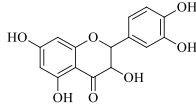
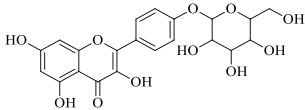
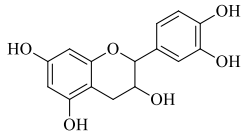
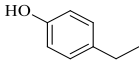
S.no.	PubChem ID	Binding energy (kcal/mol)	Ligands	Sources	Chemical structure
47	5281670	-6.8	Morin	<i>Lotus ucrainicus, Psidium guajava</i>	
48	5393152	-6.8	3,7-Dihydroxyflavone	<i>Zuccagnia punctata</i>	
49	128861	-6.7	Cyanidin	<i>Salix candida, Eleocharis dulcis</i>	
50	441773	-6.7	Peonidin	<i>Vaccinium macrocarpon, Mangifera indica</i>	
51	5281628	-6.7	Hispidulin	<i>Eupatorium cannabinum, Eupatorium perfoliatum</i>	

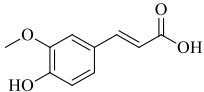
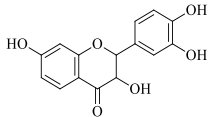
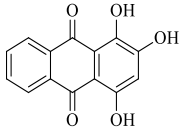
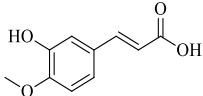


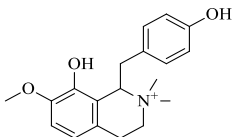
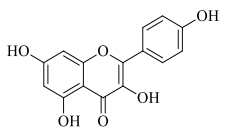
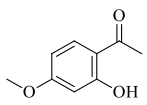
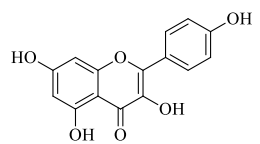
S.n o.	PubChem ID	Binding energy (kcal/mol)	Ligands	Sources	Chemical structure
52	5280343	-6.6	Quercetin	<i>Azadirachta indica</i>	
53	5281616	-6.6	Galangin	<i>Alpinia conchigera</i> , <i>Populus koreana</i>	
54	5281654	-6.6	Isorhamnetin	<i>Lotus ucrainicus</i> , <i>Strychnos pseudoquina</i>	
55	5281703	-6.6	Wogonin	<i>Scutellaria likiangensis</i> , <i>Scutellaria amoena</i>	
56	9064	-6.6	Cianidanol	<i>Visnea mocanera</i> , <i>Salacia chinensis</i>	

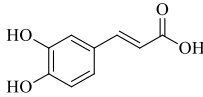
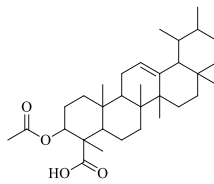
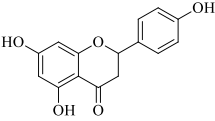
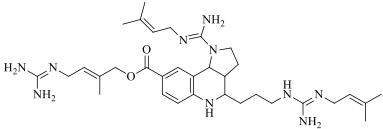
S.no.	PubChem ID	Binding energy (kcal/mol)	Ligands	Sources	Chemical structure
57	10189	-6.5	Eugenin	<i>Crossosoma bigelovii</i> , <i>Pogostemon stellatus</i>	
58	5281614	-6.5	Fisetin	<i>Acacia carneorum</i> , <i>Acacia buxifolia</i>	
59	5281656	-6.5	Norathyriol	<i>Hypericum aucheri</i> , <i>Hypericum elegans</i>	
60	73202	-6.5	Pinobanksin	<i>Populus koreana</i> , <i>Ozothamnus stirlingii</i>	
61	5281803	-6.4	Pratensein	<i>Dalbergia sissoo</i> , <i>Cicer chorassanicum</i>	

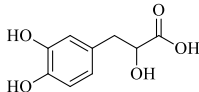
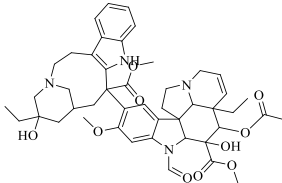
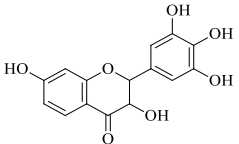
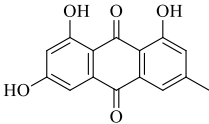
S.no.	PubChem ID	Binding energy (kcal/mol)	Ligands	Sources	Chemical structure
62	65084	-6.4	Galocatechin	<i>Saxifraga cuneifolia</i> , <i>Quercus dentata</i>	
63	73160	-6.4	(-)-Catechin	<i>Smilax corbularia</i> , <i>Cinnamomum kotoense</i> ,	
64	3082134	-6.3	Cyclanoline	<i>Cissampelos pareira</i> , <i>Stephania elegans</i>	
65	440989	-6.3	(R)-coclaurine	<i>Mezilaurus synandra</i> , <i>Stephania excentrica</i>	

S.no.	PubChem ID	Binding energy (kcal/mol)	Ligands	Sources	Chemical structure
66	439533	-6.2	(+)-taxifolin	<i>Austrocedrus chilensis</i> , <i>Smilax corbularia</i>	
67	5491693	-6.2	Kaempferol 4'-glucoside	<i>Urena lobata</i>	
68	72276	-6.2	(-)-Epicatechin	<i>Visnea mocanera</i> , <i>Litsea rotundifolia</i>	
69	31242	-6.1	4-Ethylphenol	<i>Aloe africana</i> , <i>Podocarpus fasciculus</i>	

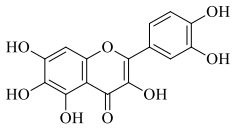
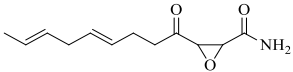
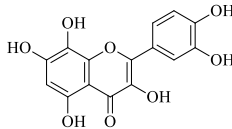
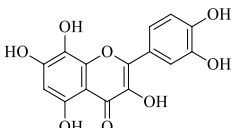
S.no.	PubChem ID	Binding energy (kcal/mol)	Ligands	Sources	Chemical structure
70	445858	-6.1	Ferulic acid	<i>Haplophyllum griffithianum</i> , <i>Visnea mocanera</i>	
71	5317435	-6.1	Fustin	<i>Acacia vestita</i> , <i>Acacia carneorum</i>	
72	6683	-6.1	Purpurin	<i>Rubia argyi</i> , <i>Cinchona calisaya</i>	
73	736186	-6.1	Isoferulic acid	<i>Sibiraea angustata</i> , <i>Astragalus onobrychis</i>	

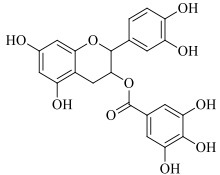
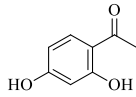
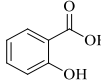
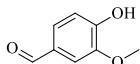
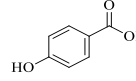
S.no.	PubChem ID	Binding energy (kcal/mol)	Ligands	Sources	Chemical structure
74	157129	-6	Oblongine	<i>Stephania cephalantha</i> , <i>Stephania tetrandra</i>	
75	5280863	-6	Kaempferol	<i>Lotus ucrainicus</i> , <i>Visnea mocanera</i>	
76	11092	-5.9	Paeonol	<i>Vincetoxicum paniculatum</i> , <i>Vincetoxicum glaucescens</i>	
77	15847196	-5.9	Dihydro-caffeic acid	<i>Isatis tinctoria</i> , <i>Ursinia nana</i>	

S.no.	PubChem ID	Binding energy (kcal/mol)	Ligands	Sources	Chemical structure
78	689043	-5.9	Caffeic acid	<i>Pavetta indica, Eupatorium cannabinum</i>	
79	11386458	-5.9	3-Acetyl-beta-boswellic acid	<i>Boswellia sacra</i>	
80	932	-5.9	(-)-Naringenin	<i>Prunus mume, Helichrysum cephaloideum,</i>	
81	10438867	-5.8	(-)-Martinelline	<i>Martinella iquitosensis</i>	

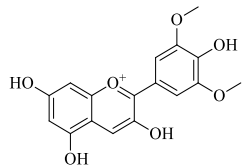
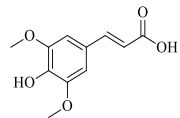
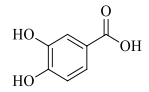
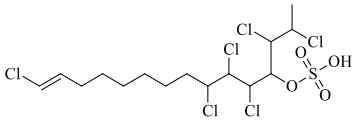
S.no.	PubChem ID	Binding energy (kcal/mol)	Ligands	Sources	Chemical structure
82	11600642	-5.8	Danshensu/Salvianic acid A	<i>Salvia miltiorrhiza</i> , <i>Melissa officinalis</i>	
83	5978	-5.7	Vincristine	<i>Ophioparma ventosa</i> , <i>Cunila</i> ,	
84	20399	-5.8	Dihydrorobinetin	<i>Robinia pseudoacacia</i> and <i>Adenanthera pavonina</i>	
85	3220	-5.8	Emodin	<i>Rumex dentatus</i> , <i>Rhamnus davurica</i>	

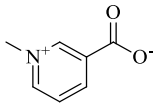
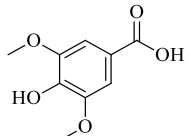
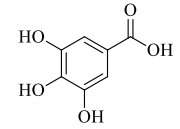


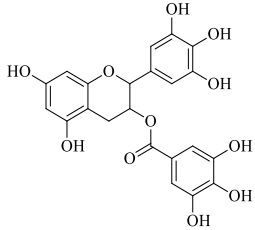
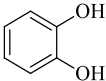
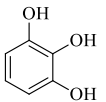
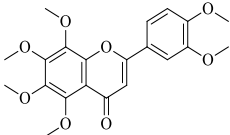
S.no.	PubChem ID	Binding energy (kcal/mol)	Ligands	Sources	Chemical structure
86	5281680	-5.8	Quercetagetin	<i>Calanticaria bicolor, Tagetes subulata</i>	
87	5282054	-5.8	Cerulenin	<i>Cephalosporium caerulens and Euglena gracilis</i>	
88	689095	-5.8	3,5-di-t-butyl-4-hydroxycinnamic acid	<i>Artemisia vulgaris</i>	
89	5280647	-5.7	Gossypetin	<i>Sedum brevifolium, Rhododendron stenophyllum</i>	

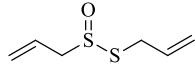
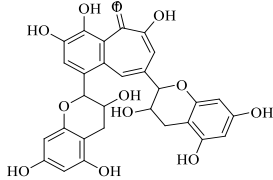
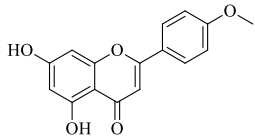
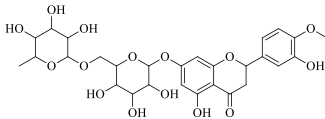
S.no.	PubChem ID	Binding energy (kcal/mol)	Ligands	Sources	Chemical structure
90	6419835	-5.7	(-)-catechin-3-O-gallate	<i>Rheum palmatum, Vitis vinifera</i>	
91	6990	-5.7	2',4'-dihydroxyacetophenone	<i>Vincetoxicum paniculatum, Vincetoxicum atratum</i>	
92	338	-5.6	Salicylic Acid	<i>Catharanthus roseus</i>	
93	1183	-5.5	Vanillin	<i>Vanillia planifolia</i>	
94	135	-5.5	p-Salicylic acid	<i>Escherichia coli (strain K12, MG1655).</i>	

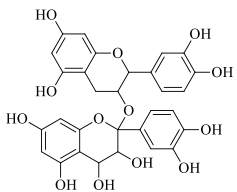
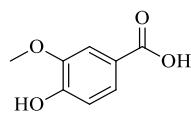
S.n o.	PubChem ID	Binding energy (kcal/mol)	Ligands	Sources	Chemical structure
95	3469	-5.5	2,5-dihydroxybenzoic acid	<i>Persicaria mitis</i> , <i>Tilia tomentosa</i>	
96	68077	-5.5	Tangeretin	<i>Citrus tankan</i> , <i>Citrus keraji</i>	
97	10393	-5.4	2-(4-hydroxyphenyl)ethanol	<i>Thalictrum petaloideum</i> , <i>Casearia sylvestris</i>	
98	5281672	-5.4	Myricetin	<i>Ficus auriculata</i> , <i>Visnea mocanera</i>	

S.no.	PubChem ID	Binding energy (kcal/mol)	Ligands	Sources	Chemical structure
99	159287	-5.3	Malvidin	<i>Lathyrus latifolius, Vaccinium myrtillus</i>	
100	637775	-5.3	Sinapic acid	<i>Sida acuta, Limoniastrum guyonianum</i>	
101	72	-5.3	3,4-dihydroxybenzoic acid	<i>Visnea mocanera, Amomum subulatum</i>	
102	10369173	-5.2	Mytilipin A	<i>Mytilus galloprovincialis</i>	

S.no.	PubChem ID	Binding energy (kcal/mol)	Ligands	Sources	Chemical structure
103	5570	-5.1	Trigonelline	<i>Hypoestes phyllostachya</i> , <i>Schumanniohyton magnificum</i>	
104	10742	-5	Syringic acid	<i>Visnea mocanera</i> , <i>Pittosporum illicioides</i>	
105	370	-5	Gallic acid	<i>Visnea mocanera</i> , <i>Ardisia paniculata</i>	

S.no.	PubChem ID	Binding energy (kcal/mol)	Ligands	Sources	Chemical structure
106	65064	-5	(-)-Epigallocatechin gallate	<i>Limoniastrum guyonianum, Scurrula atropurpurea</i>	
107	289	-4.9	Catechol	<i>Senegalia catechu</i>	
108	1057	-4.7	Pyrogallol	<i>Gunnera perpensa, Nigella glandulifera</i>	
109	72344	-4.7	Nobiletin	<i>Citrus tankan, Citrus keraji</i>	

S.no.	PubChem ID	Binding energy (kcal/mol)	Ligands	Sources	Chemical structure
110	65036	-4.2	Allicin	<i>Allium chinense, Allium nutans</i>	
111	135403798	-3.9	Theaflavine	<i>Vicia faba, Camellia</i>	
112	5280442	-3.4	Acacetin	<i>Verbascum lychnitis, Odontites viscosus</i>	
113	10621	-3.2	Hesperidin	<i>Ficus erecta var. beecheyana, Citrus tankan</i>	

S.no.	PubChem ID	Binding energy (kcal/mol)	Ligands	Sources	Chemical structure
114	107876	-1.8	Procyanidin	<i>Vitis amurens</i> , <i>Syzygium grande</i>	
115	8468	-5.4	Vanillic acid	<i>Ficus septica</i> , <i>Haplophyllum cappadocicum</i> ,	



**Table A3 (A)** Predicated molecular targets of Lutein via Swiss Target Prediction.

Target	Common name	Uniprot ID	ChEMBL ID	Target Class	Probability*	Known actives (3D/2D)
Leukocyte adhesion glycoprotein LFA-1 alpha	ITGAL	P20701	CHEMBL1803	Adhesion	0	0 / 2
Cytochrome P450 19A1	CYP19A1	P11511	CHEMBL1978	Cytochrome P450	0	0 / 44
Cytochrome P450 17A1	CYP17A1	P05093	CHEMBL3522	Cytochrome P450	0	0 / 23
Cytochrome P450 51 (by homology)	CYP51A1	Q16850	CHEMBL3849	Cytochrome P450	0	0 / 1
Norepinephrine transporter	SLC6A2	P23975	CHEMBL222	Electrochemical transporter	0	0 / 2
Dopamine transporter	SLC6A3	Q01959	CHEMBL238	Electrochemical transporter	0	1 / 0
Solute carrier family 22 member 6 (by homology)	SLC22A6	Q4U2R8	CHEMBL1641347	Electrochemical transporter	0	0 / 1
Glutaminase kidney isoform, mitochondrial	GLS	O94925	CHEMBL2146302	Enzyme	0	9 / 0

Target	Common name	Uniprot ID	ChEMBL ID	Target Class	Probability*	Known actives (3D/2D)
Acyl coenzyme A:cholesterol acyltransferase 1 (by homology)	SOAT1	P35610	CHEMBL278 2	Enzyme	0	1 / 0
Arachidonate 12-lipoxygenase	ALOX12	P18054	CHEMBL368 7	Enzyme	0	0 / 2
PI3-kinase p110-gamma subunit	PIK3CG	P48736	CHEMBL326 7	Enzyme	0	1 / 0
PI3-kinase p110-alpha subunit	PIK3CA	P42336	CHEMBL400 5	Enzyme	0	1 / 0
Aldose reductase (by homology)	AKR1B1	P15121	CHEMBL190 0	Enzyme	0	0 / 1
DNA polymerase beta (by homology)	POLB	P06746	CHEMBL239 2	Enzyme	0	0 / 4
Autotaxin	ENPP2	Q13822	CHEMBL369 1	Enzyme	0	1 / 0
Telomerase reverse transcriptase	TERT	O14746	CHEMBL291 6	Enzyme	0	0 / 1
Arachidonate 15-lipoxygenase	ALOX15	P16050	CHEMBL290 3	Enzyme	0	0 / 1

Target	Common name	Uniprot ID	ChEMBL ID	Target Class	Probability*	Known actives (3D/2D)
Carboxylesterase 2	CES2	O00748	CHEMBL3180	Enzyme	0	0 / 3
Lanosterol synthase	LSS	P48449	CHEMBL3593	Enzyme	0	0 / 3
Glucose-6-phosphate 1-dehydrogenase	G6PD	P11413	CHEMBL5347	Enzyme	0	0 / 2
11-beta-hydroxysteroid dehydrogenase 1	HSD11B1	P28845	CHEMBL4235	Enzyme	0	0 / 1
Gonadotropin-releasing hormone receptor	GNRHR	P30968	CHEMBL1855	Family A G protein-coupled receptor	0	1 / 0
Muscarinic acetylcholine receptor M3	CHRM3	P20309	CHEMBL245	Family A G protein-coupled receptor	0	9 / 0
Mu opioid receptor	OPRM1	P35372	CHEMBL233	Family A G protein-coupled receptor	0	1 / 0
Delta opioid receptor	OPRD1	P41143	CHEMBL236	Family A G protein-coupled receptor	0	1 / 0
Kappa Opioid receptor	OPRK1	P41145	CHEMBL237	Family A G protein-coupled receptor	0	1 / 0

Target	Common name	Uniprot ID	ChEMBL ID	Target Class	Probability*	Known actives (3D/2D)
Leukotriene B4 receptor 1	LTB4R	Q15722	CHEMBL3911	Family A G protein-coupled receptor	0	0 / 4
Adenosine A2a receptor	ADORA2A	P29274	CHEMBL251	Family A G protein-coupled receptor	0	0 / 1
Adrenergic receptor beta	ADRB2	P07550	CHEMBL210	Family A G protein-coupled receptor	0	5 / 0
C-X-C chemokine receptor type 3	CXCR3	P49682	CHEMBL4441	Family A G protein-coupled receptor	0	1 / 0
Alpha-2a adrenergic receptor	ADRA2A	P08913	CHEMBL1867	Family A G protein-coupled receptor	0	2 / 0
Prostanoid EP1 receptor	PTGER1	P34995	CHEMBL1811	Family A G protein-coupled receptor	0	0 / 5
Prostanoid EP4 receptor	PTGER4	P35408	CHEMBL1836	Family A G protein-coupled receptor	0	0 / 4
Prostanoid FP receptor	PTGFR	P43088	CHEMBL1987	Family A G protein-coupled receptor	0	0 / 5
Prostanoid EP3 receptor	PTGER3	P43115	CHEMBL3710	Family A G protein-coupled receptor	0	0 / 2

Target	Common name	Uniprot ID	ChEMBL ID	Target Class	Probability*	Known actives (3D/2D)
Prostanoid DP receptor	PTGDR	Q13258	CHEMBL4427	Family A G protein-coupled receptor	0	0 / 1
Serotonin 1d (5-HT1d) receptor	HTR1D	P28221	CHEMBL1983	Family A G protein-coupled receptor	0	1 / 0
Serotonin 2b (5-HT2b) receptor	HTR2B	P41595	CHEMBL1833	Family A G protein-coupled receptor	0	0 / 2
Adenosine A1 receptor	ADORA1	P30542	CHEMBL226	Family A G protein-coupled receptor	0	2 / 1
Adenosine A3 receptor	ADORA3	P0DMS8	CHEMBL256	Family A G protein-coupled receptor	0	1 / 3
Prostanoid EP2 receptor	PTGER2	P43116	CHEMBL1881	Family A G protein-coupled receptor	0	0 / 4
Prostanoid IP receptor	PTGIR	P43119	CHEMBL1995	Family A G protein-coupled receptor	0	0 / 2
Free fatty acid receptor 1	FFAR1	O14842	CHEMBL4422	Family A G protein-coupled receptor	0	0 / 2
Fatty acid binding protein adipocyte	FABP4	P15090	CHEMBL2083	Fatty acid binding protein family	0	0 / 2

Target	Common name	Uniprot ID	ChEMBL ID	Target Class	Probability*	Known actives (3D/2D)
Fatty acid binding protein muscle	FABP3	P05413	CHEMBL3344	Fatty acid binding protein family	0	0 / 3
Butyrylcholinesterase	BCHE	P06276	CHEMBL1914	Hydrolase	0	0 / 1
DNA topoisomerase II alpha	TOP2A	P11388	CHEMBL1806	Isomerase	0	0 / 1
Protein kinase C delta (by homology)	PRKCD	Q05655	CHEMBL2996	Kinase	0	2 / 0
Protein kinase C alpha	PRKCA	P17252	CHEMBL299	Kinase	0	1 / 2
Serine/threonine-protein kinase Chk1	CHEK1	O14757	CHEMBL4630	Kinase	0	2 / 0
Tyrosine-protein kinase receptor FLT3	FLT3	P36888	CHEMBL1974	Kinase	0	3 / 0
Vascular endothelial growth factor receptor 2	KDR	P35968	CHEMBL279	Kinase	0	4 / 0
Serine/threonine-protein kinase mTOR	MTOR	P42345	CHEMBL2842	Kinase	0	1 / 0

Target	Common name	Uniprot ID	ChEMBL ID	Target Class	Probability*	Known actives (3D/2D)
Serine/threonine-protein kinase Aurora-A	AURKA	O14965	CHEMBL472 2	Kinase	0	2 / 0
MAP kinase p38 alpha	MAPK14	Q16539	CHEMBL260	Kinase	0	0 / 1
MAP kinase ERK2	MAPK1	P28482	CHEMBL404 0	Kinase	0	0 / 2
Glycine receptor subunit alpha-1	GLRA1	P23415	CHEMBL584 5	Ligand-gated ion channel	0.082221 517	0 / 1
Serotonin 3a (5-HT3a) receptor (by homology)	HTR3A	P46098	CHEMBL189 9	Ligand-gated ion channel	0	1 / 0
Vitamin D receptor	VDR	P11473	CHEMBL197 7	Nuclear receptor	0.082221 517	0 / 57
Androgen Receptor	AR	P10275	CHEMBL187 1	Nuclear receptor	0.082221 517	0 / 52
LXR-alpha	NR1H3	Q13133	CHEMBL280 8	Nuclear receptor	0.082221 517	0 / 15
Estrogen receptor alpha	ESR1	P03372	CHEMBL206	Nuclear receptor	0	0 / 36
Estrogen receptor beta	ESR2	Q92731	CHEMBL242	Nuclear receptor	0	0 / 42

Target	Common name	Uniprot ID	ChEMBL ID	Target Class	Probability*	Known actives (3D/2D)
Nuclear receptor ROR-gamma	RORC	P51449	CHEMBL1741186	Nuclear receptor	0	0 / 9
Nuclear receptor ROR-alpha	RORA	P35398	CHEMBL5868	Nuclear receptor	0	0 / 4
Retinoic acid receptor gamma (by homology)	RARG	P13631	CHEMBL2003	Nuclear receptor	0	0 / 10
Retinoid X receptor gamma (by homology)	RXRG	P48443	CHEMBL2004	Nuclear receptor	0	0 / 5
Retinoic acid receptor beta (by homology)	RARB	P10826	CHEMBL2008	Nuclear receptor	0	0 / 9
Retinoic acid receptor alpha (by homology)	RARA	P10276	CHEMBL2055	Nuclear receptor	0	0 / 12
Retinoid X receptor alpha	RXRA	P19793	CHEMBL2061	Nuclear receptor	0	0 / 13
Mineralocorticoid receptor	NR3C2	P08235	CHEMBL1994	Nuclear receptor	0	0 / 3
Glucocorticoid receptor	NR3C1	P04150	CHEMBL2034	Nuclear receptor	0	0 / 8



Target	Common name	Uniprot ID	ChEMBL ID	Target Class	Probability*	Known actives (3D/2D)
Progesterone receptor	PGR	P06401	CHEMBL208	Nuclear receptor	0	0 / 2
Peroxisome proliferator-activated receptor gamma	PPARG	P37231	CHEMBL235	Nuclear receptor	0	0 / 10
Peroxisome proliferator-activated receptor alpha	PPARA	Q07869	CHEMBL239	Nuclear receptor	0	0 / 7
Peroxisome proliferator-activated receptor delta	PPARD	Q03181	CHEMBL397 9	Nuclear receptor	0	0 / 5
Retinoid X receptor beta	RXRB	P28702	CHEMBL187 0	Nuclear receptor	0	0 / 2
Nuclear receptor ROR-beta	RORB	Q92753	CHEMBL309 1268	Nuclear receptor	0	0 / 1
RAS guanyl releasing protein 3	RASGRP3	Q8IV61	CHEMBL363 8	Other cytosolic protein	0.082221 517	0 / 1
Heat shock factor protein 1	HSF1	Q00613	CHEMBL586 9	Other cytosolic protein	0	0 / 1
Apoptosis regulator Bcl-2	BCL2	P10415	CHEMBL486 0	Other ion channel	0	10 / 0

Target	Common name	Uniprot ID	ChEMBL ID	Target Class	Probability*	Known actives (3D/2D)
Apoptosis regulator Bcl-X	BCL2L1	Q07817	CHEMBL4625	Other ion channel	0	1 / 0
Niemann-Pick C1-like protein 1	NPC1L1	Q9UHC9	CHEMBL2027	Other membrane protein	0	0 / 7
HMG-CoA reductase	HMGCR	P04035	CHEMBL402	Oxidoreductase	0	0 / 16
Arachidonate 5-lipoxygenase	ALOX5	P09917	CHEMBL215	Oxidoreductase	0	1 / 10
Steroid 5-alpha-reductase 2	SRD5A2	P31213	CHEMBL1856	Oxidoreductase	0	0 / 5
Cyclooxygenase-1	PTGS1	P23219	CHEMBL221	Oxidoreductase	0	0 / 1
Protein-tyrosine phosphatase 1B	PTPN1	P18031	CHEMBL335	Phosphatase	0.082221517	0 / 16
Dual specificity phosphatase Cdc25A	CDC25A	P30304	CHEMBL3775	Phosphatase	0.082221517	0 / 1
Protein-tyrosine phosphatase 2C	PTPN11	Q06124	CHEMBL3864	Phosphatase	0	0 / 1
Vitamin D-binding protein	GC	P02774	CHEMBL2259	Secreted protein	0.082221517	0 / 1

Target	Common name	Uniprot ID	ChEMBL ID	Target Class	Probability*	Known actives (3D/2D)
Plasma retinol-binding protein	RBP4	P02753	CHEMBL3100	Secreted protein	0	0 / 1
Testis-specific androgen-binding protein	SHBG	P04278	CHEMBL3305	Secreted protein	0	0 / 19
TNF-alpha	TNF	P01375	CHEMBL1825	Secreted protein	0	0 / 4
Corticosteroid binding globulin	SERPINA6	P08185	CHEMBL2421	Secreted protein	0	0 / 2
Toll-like receptor (TLR7/TLR9)	TLR9	Q9NR96	CHEMBL5804	Toll-like and Il-1 receptors	0	0 / 1
Hypoxia-inducible factor 1 alpha	HIF1A	Q16665	CHEMBL4261	Transcription factor	0	0 / 2
Sterol regulatory element-binding protein 2	SREBF2	Q12772	CHEMBL1795166	Unclassified protein	0	0 / 1
Transient receptor potential cation channel subfamily A member 1	TRPA1	O75762	CHEMBL6007	Voltage-gated ion channel	0	0 / 1
N-lysine methyltransferase SETD8	ITGAL	P20701	CHEMBL1803	Adhesion	0	0 / 2

**Table A3 (B)** Predicated molecular targets of 5-hydroxyflavone via Swiss Target Prediction.

Target	Common name	Uniprot ID	ChEMBL ID	Target Class	Probability*	Known actives (3D/2D)
Androgen Receptor	AR	P10275	CHEMBL1871	Nuclear receptor	0.982960776	58 / 16
Adenosine A1 receptor (by homology)	ADORA1	P30542	CHEMBL226	Family A G protein-coupled receptor	0.982960776	144 / 23
Adenosine A2a receptor (by homology)	ADORA2A	P29274	CHEMBL251	Family A G protein-coupled receptor	0.982960776	140 / 11
Aldose reductase	AKR1B1	P15121	CHEMBL1900	Enzyme	0.316824689	50 / 63
Cytochrome P450 19A1	CYP19A1	P11511	CHEMBL1978	Cytochrome P450	0.307625406	128 / 19
ATP-binding cassette sub-family G member 2	ABCG2	Q9UNQ0	CHEMBL5393	Primary active transporter	0.262324136	16 / 47
Cyclin-dependent kinase 5/CDK5 activator 1	CDK5R1 CDK5	Q15078 Q00535	CHEMBL1907600	Kinase	0.244186029	77 / 18

Target	Common name	Uniprot ID	ChEMBL ID	Target Class	Probability*	Known actives (3D/2D)
Cyclin-dependent kinase 6	CDK6	Q00534	CHEMBL2508	Kinase	0.244186029	0 / 4
Carbonyl reductase [NADPH] 1	CBR1	P16152	CHEMBL5586	Enzyme	0.244186029	0 / 2
Carbonic anhydrase II	CA2	P00918	CHEMBL205	Lyase	0.235117287	316 / 12
Carbonic anhydrase I	CA1	P00915	CHEMBL261	Lyase	0.235117287	261 / 8
Carbonic anhydrase XII	CA12	O43570	CHEMBL3242	Lyase	0.235117287	176 / 17
Carbonic anhydrase IX	CA9	Q16790	CHEMBL3594	Lyase	0.235117287	210 / 12
Glycogen synthase kinase-3 beta	GSK3B	P49841	CHEMBL262	Kinase	0.235117287	210 / 9
Cyclin-dependent kinase 1/cyclin B	CCNB3 CDK1 CCNB1 CCNB2	Q8WWL7 P06493 P14635 O95067	CHEMBL2094127	Other cytosolic protein	0.226036325	40 / 9
Tankyrase-2	TNKS2	Q9H2K2	CHEMBL6154	Enzyme	0.207865842	13 / 12

Target	Common name	Uniprot ID	ChEMBL ID	Target Class	Probability*	Known actives (3D/2D)
Tankyrase-1	TNKS	O95271	CHEMBL6164	Enzyme	0.207865842	15 / 28
Estrogen receptor alpha	ESR1	P03372	CHEMBL206	Nuclear receptor	0.198808518	21 / 54
Carbonic anhydrase VII	CA7	P43166	CHEMBL2326	Lyase	0.198808518	82 / 8
Poly [ADP-ribose] polymerase-1	PARP1	P09874	CHEMBL3105	Enzyme	0.180616481	135 / 9
Estradiol 17-beta-dehydrogenase 1	HSD17B1	P14061	CHEMBL3181	Enzyme	0.180616481	13 / 4
Xanthine dehydrogenase	XDH	P47989	CHEMBL1929	Oxidoreductase	0.171518552	12 / 21
Transthyretin	TTR	P02766	CHEMBL3194	Secreted protein	0.171518552	10 / 2
Arachidonate 15-lipoxygenase	ALOX15	P16050	CHEMBL2903	Enzyme	0.171518552	22 / 8
Estrogen receptor beta	ESR2	Q92731	CHEMBL242	Nuclear receptor	0.171518552	33 / 57

Target	Common name	Uniprot ID	ChEMBL ID	Target Class	Probability*	Known actives (3D/2D)
Cyclin-dependent kinase 1	CDK1	P06493	CHEMBL308	Kinase	0.171518552	56 / 10
Cystic fibrosis transmembrane conductance regulator	CFTR	P13569	CHEMBL4051	Other ion channel	0.162404208	0 / 1
Cyclooxygenase-2	PTGS2	P35354	CHEMBL230	Oxidoreductase	0.162404208	46 / 13
Monoamine oxidase A	MAOA	P21397	CHEMBL1951	Oxidoreductase	0.153377072	149 / 36
Cytochrome P450 1B1	CYP1B1	Q16678	CHEMBL4878	Cytochrome P450	0.153377072	2 / 47
Carbonic anhydrase IV	CA4	P22748	CHEMBL3729	Lyase	0.144331367	22 / 9
Tyrosine-protein kinase receptor FLT3	FLT3	P36888	CHEMBL1974	Kinase	0.12615425	59 / 7
Arachidonate 12-lipoxygenase	ALOX12	P18054	CHEMBL3687	Enzyme	0.12615425	12 / 11
Tyrosine-protein kinase SYK	SYK	P43405	CHEMBL2599	Kinase	0.117056358	28 / 3

Target	Common name	Uniprot ID	ChEMBL ID	Target Class	Probability*	Known actives (3D/2D)
Aldo-keto reductase family 1 member B10	AKR1B10	O60218	CHEMBL5 983	Enzyme	0.11705 6358	5 / 3
Receptor-type tyrosine-protein phosphatase S	PTPRS	Q13332	CHEMBL2 396508	Phosphatase	0.11705 6358	0 / 8
AMY1C	AMY1A	P04745	CHEMBL2 478	Enzyme	0.11705 6358	0 / 1
Acetylcholinesterase	ACHE	P22303	CHEMBL2 20	Hydrolase	0.11705 6358	28 / 23
NADPH oxidase 4	NOX4	Q9NPH5	CHEMBL1 250375	Enzyme	0.11705 6358	3 / 7
Arachidonate 5-lipoxygenase	ALOX5	P09917	CHEMBL2 15	Oxidoreductase	0.11705 6358	90 / 46
P-glycoprotein 1	ABCB1	P08183	CHEMBL4 302	Primary active transporter	0.10801 8051	3 / 44
Lysine-specific demethylase 4D-like	KDM4E	B2RXH2	CHEMBL1 293226	Eraser	0.10801 8051	5 / 2
Casein kinase II alpha	CSNK2A1	P68400	CHEMBL3 629	Kinase	0.10801 8051	14 / 2



Target	Common name	Uniprot ID	ChEMBL ID	Target Class	Probability*	Known actives (3D/2D)
Monoamine oxidase B	MAOB	P27338	CHEMBL2039	Oxidoreductase	0.098947479	256 / 38
G protein-coupled receptor kinase 6	GRK6	P43250	CHEMBL6144	Kinase	0.098947479	1 / 4
Tyrosine-protein kinase LCK	LCK	P06239	CHEMBL258	Kinase	0.089872067	52 / 3
Adenosine A3 receptor	ADORA3	P0DMS8	CHEMBL256	Family A G protein-coupled receptor	0.089872067	44 / 23
Glyoxalase I	GLO1	Q04760	CHEMBL2424	Enzyme	0.089872067	0 / 4
DNA topoisomerase I (by homology)	TOP1	P11387	CHEMBL1781	Isomerase	0.089872067	0 / 1
Arginase-1 (by homology)	ARG1	P05089	CHEMBL1075097	Enzyme	0.089872067	0 / 2
Multidrug resistance-associated protein 1	ABCC1	P33527	CHEMBL3004	Primary active transporter	0.080792387	1 / 11
Calmodulin	CALM1	P62158	CHEMBL6093	Unclassified protein	0.080792387	1 / 1

Target	Common name	Uniprot ID	ChEMBL ID	Target Class	Probability*	Known actives (3D/2D)
Matrix metalloproteinase 9	MMP9	P14780	CHEMBL321	Protease	0.080792387	95 / 2
Matrix metalloproteinase 2	MMP2	P08253	CHEMBL333	Protease	0.080792387	65 / 2
Inhibitor of nuclear factor kappa B kinase beta subunit	IKBKB	O14920	CHEMBL1991	Kinase	0.071715932	32 / 1
Neurokinin 2 receptor	TACR2	P21452	CHEMBL2327	Family A G protein-coupled receptor	0.071715932	0 / 1
DNA-dependent protein kinase	PRKDC	P78527	CHEMBL3142	Kinase	0.071715932	52 / 15
NEDD8-activating enzyme E1 regulatory subunit	NAE1	Q13564	CHEMBL2016431	Unclassified protein	0.071715932	0 / 1
Neurotrophic tyrosine kinase receptor type 2	NTRK2	Q16620	CHEMBL4898	Kinase	0.071715932	3 / 1
Thromboxane-A synthase	TBXAS1	P24557	CHEMBL1835	Cytochrome P450	0.071715932	12 / 2
Tyrosinase	TYR	P14679	CHEMBL1973	Oxidoreductase	0.062621967	0 / 3

Target	Common name	Uniprot ID	ChEMBL ID	Target Class	Probability*	Known actives (3D/2D)
Estrogen-related receptor alpha	ESRRA	P11474	CHEMBL3429	Nuclear receptor	0.062621967	0 / 2
Beta amyloid A4 protein	APP	P05067	CHEMBL2487	Membrane receptor	0.062621967	10 / 13
Butyrylcholinesterase	BCHE	P06276	CHEMBL1914	Hydrolase	0.062621967	14 / 4
Phosphodiesterase 5A	PDE5A	O76074	CHEMBL1827	Phosphodiesterase	0.062621967	60 / 5
Serine/threonine-protein kinase PIM1	PIM1	P11309	CHEMBL2147	Kinase	0.062621967	75 / 7
Cytosolic phospholipase A2	PLA2G4A	P47712	CHEMBL3816	Enzyme	0.062621967	0 / 2
Lymphocyte differentiation antigen CD38	CD38	P28907	CHEMBL4660	Enzyme	0.062621967	9 / 2
Cytochrome P450 1A1	CYP1A1	P04798	CHEMBL2231	Cytochrome P450	0.062621967	1 / 7
Cytochrome P450 1A2	CYP1A2	P05177	CHEMBL3356	Cytochrome P450	0.062621967	1 / 10

Target	Common name	Uniprot ID	ChEMBL ID	Target Class	Probability*	Known actives (3D/2D)
Matrix metalloproteinase 12	MMP12	P39900	CHEMBL4393	Protease	0.062621967	4 / 2
Telomerase reverse transcriptase	TERT	O14746	CHEMBL2916	Enzyme	0.062621967	16 / 20
MAP kinase ERK1	MAPK3	P27361	CHEMBL3385	Kinase	0.062621967	7 / 1
6-phosphofructo-2-kinase/fructose-2,6-bisphosphatase 3	PFKFB3	Q16875	CHEMBL2331053	Enzyme	0.062621967	53 / 2
Plasminogen	PLG	P00747	CHEMBL1801	Protease	0.062621967	0 / 3
Estradiol 17-beta-dehydrogenase 2	HSD17B2	P37059	CHEMBL2789	Enzyme	0.062621967	22 / 3
Epidermal growth factor receptor erbB1	EGFR	P00533	CHEMBL203	Kinase	0.062621967	268 / 29
Phospholipase A2 group IIA	PLA2G2A	P14555	CHEMBL3474	Enzyme	0.062621967	10 / 2
Tyrosine-protein kinase FYN	FYN	P06241	CHEMBL1841	Kinase	0.062621967	7 / 1

Target	Common name	Uniprot ID	ChEMBL ID	Target Class	Probability*	Known actives (3D/2D)
DNA-3-methyladenine glycosylase	MPG	P29372	CHEMBL3 396943	Enzyme	0.05355 6076	0 / 1
Cyclin-dependent kinase 2	CDK2	P24941	CHEMBL3 01	Kinase	0.05355 6076	107 / 10
Stem cell growth factor receptor	KIT	P10721	CHEMBL1 936	Kinase	0.05355 6076	17 / 3
Beta-secretase 1	BACE1	P56817	CHEMBL4 822	Protease	0.05355 6076	148 / 13
Serine/threonine-protein kinase PLK1	PLK1	P53350	CHEMBL3 024	Kinase	0.05355 6076	29 / 3
PI3-kinase p85-alpha subunit	PIK3R1	P27986	CHEMBL2 506	Enzyme	0.05355 6076	0 / 1
Protein kinase N1	PKN1	Q16512	CHEMBL3 384	Kinase	0.05355 6076	0 / 3
Serine/threonine-protein kinase NEK6	NEK6	Q9HC98	CHEMBL4 309	Kinase	0.05355 6076	0 / 2
Phospholipase A2 group 1B	PLA2G1B	P04054	CHEMBL4 426	Enzyme	0.05355 6076	0 / 1

Target	Common name	Uniprot ID	ChEMBL ID	Target Class	Probability*	Known actives (3D/2D)
Tyrosine-protein kinase receptor UFO	AXL	P30530	CHEMBL4895	Kinase	0.053556076	0 / 4
DNA-(apurinic or apyrimidinic site) lyase	APEX1	P27695	CHEMBL5619	Enzyme	0.053556076	0 / 1
Aldo-keto reductase family 1 member C2 (by homology)	AKR1C2	P52895	CHEMBL5847	Enzyme	0.053556076	0 / 1
Aldo-keto reductase family 1 member C1 (by homology)	AKR1C1	Q04828	CHEMBL5905	Enzyme	0.053556076	0 / 1
Aldo-keto reductase family 1 member C4 (by homology)	AKR1C4	P17516	CHEMBL4999	Enzyme	0.053556076	0 / 1
Tyrosine-protein kinase SRC	SRC	P12931	CHEMBL267	Kinase	0.053556076	115 / 4
PI3-kinase p110-gamma subunit	PIK3CG	P48736	CHEMBL3267	Enzyme	0.053556076	105 / 1
Delta opioid receptor	OPRD1	P41143	CHEMBL236	Family A G protein-coupled receptor	0.053556076	8 / 5
Vascular endothelial growth factor receptor 2	KDR	P35968	CHEMBL279	Kinase	0.053556076	202 / 3

Target	Common name	Uniprot ID	ChEMBL ID	Target Class	Probability*	Known actives (3D/2D)
Hepatocyte growth factor receptor	MET	P08581	CHEMBL3717	Kinase	0.053556076	133 / 4
Nitric oxide synthase, inducible	NOS2	P35228	CHEMBL4481	Enzyme	0.053556076	46 / 3
ALK tyrosine kinase receptor	ALK	Q9UM73	CHEMBL4247	Kinase	0.053556076	25 / 4

**Table A3 (C)** Predicated molecular targets of 6-hydroxyflavone via Swiss Target Prediction.

Target	Common name	Uniprot ID	ChEMBL ID	Target Class	Probability*	Known actives (3D/2D)
Calmodulin	CALM1	P62158	CHEMBL6093	Unclassified protein	0.982960776	1 / 1

Target	Common name	Uniprot ID	ChEMBL ID	Target Class	Probability*	Known actives (3D/2D)
Aldose reductase (by homology)	AKR1B1	P15121	CHEMBL1900	Enzyme	0.516533431	65 / 59
Tankyrase-1	TNKS	O95271	CHEMBL6164	Enzyme	0.480131243	19 / 28
Cytochrome P450 19A1	CYP19A1	P11511	CHEMBL1978	Cytochrome P450	0.443750811	104 / 20
Poly [ADP-ribose] polymerase-1	PARP1	P09874	CHEMBL3105	Enzyme	0.262324136	123 / 9
Tankyrase-2	TNKS2	Q9H2K2	CHEMBL6154	Enzyme	0.262324136	12 / 12
ATP-binding cassette sub-family G member 2	ABCG2	Q9UNQ0	CHEMBL5393	Primary active transporter	0.244186029	17 / 47
Monoamine oxidase B	MAOB	P27338	CHEMBL2039	Oxidoreductase	0.171518552	188 / 42
Carbonic anhydrase II	CA2	P00918	CHEMBL205	Lyase	0.153377072	239 / 11



Target	Common name	Uniprot ID	ChEMBL ID	Target Class	Probability*	Known actives (3D/2D)
Carbonic anhydrase I	CA1	P00915	CHEMBL261	Lyase	0.153377072	204 / 6
Carbonic anhydrase XII	CA12	O43570	CHEMBL3242	Lyase	0.153377072	109 / 15
Carbonic anhydrase IX	CA9	Q16790	CHEMBL3594	Lyase	0.153377072	131 / 10
Aldo-keto reductase family 1 member B10	AKR1B10	O60218	CHEMBL5983	Enzyme	0.153377072	16 / 3
Cytochrome P450 1B1	CYP1B1	Q16678	CHEMBL4878	Cytochrome P450	0.144331367	4 / 46
Estradiol 17-beta-dehydrogenase 1	HSD17B1	P14061	CHEMBL3181	Enzyme	0.135226129	39 / 4
Arachidonate 15-lipoxygenase	ALOX15	P16050	CHEMBL2903	Enzyme	0.135226129	14 / 7
Tyrosine-protein kinase LCK	LCK	P06239	CHEMBL258	Kinase	0.12615425	63 / 3

Target	Common name	Uniprot ID	ChEMBL ID	Target Class	Probability*	Known actives (3D/2D)
Androgen Receptor	AR	P10275	CHEMBL1871	Nuclear receptor	0.117056358	82 / 16
DNA-dependent protein kinase	PRKDC	P78527	CHEMBL3142	Kinase	0.108018051	39 / 17
Adenosine A1 receptor	ADORA1	P30542	CHEMBL226	Family A G protein-coupled receptor	0.108018051	72 / 22
Adenosine A2a receptor	ADORA2A	P29274	CHEMBL251	Family A G protein-coupled receptor	0.108018051	70 / 11
Cytochrome P450 1A1	CYP1A1	P04798	CHEMBL2231	Cytochrome P450	0.108018051	0 / 7
Neurokinin 2 receptor	TACR2	P21452	CHEMBL2327	Family A G protein-coupled receptor	0.108018051	0 / 1
Cytochrome P450 1A2	CYP1A2	P05177	CHEMBL3356	Cytochrome P450	0.108018051	0 / 9
Cyclin-dependent kinase 5/CDK5 activator 1	CDK5R1 CDK5	Q15078 Q00535	CHEMBL1907600	Kinase	0.108018051	56 / 18

Target	Common name	Uniprot ID	ChEMBL ID	Target Class	Probability*	Known actives (3D/2D)
Arachidonate 5-lipoxygenase	ALOX5	P09917	CHEMBL215	Oxidoreductase	0.108018051	106 / 46
Phosphodiesterase 5A	PDE5A	O76074	CHEMBL1827	Phosphodiesterase	0.098947479	42 / 4
Carbonic anhydrase VII	CA7	P43166	CHEMBL2326	Lyase	0.098947479	62 / 8
Tyrosine-protein kinase FYN	FYN	P06241	CHEMBL1841	Kinase	0.098947479	2 / 1
Cyclin-dependent kinase 1	CDK1	P06493	CHEMBL308	Kinase	0.098947479	35 / 10
Cyclin-dependent kinase 1/cyclin B	CCNB3 CDK1 CCNB1 CCNB2	Q8WWL7 P06493 P14635 O95067	CHEMBL2094127	Other cytosolic protein	0.098947479	27 / 6
Monoamine oxidase A	MAOA	P21397	CHEMBL1951	Oxidoreductase	0.098947479	94 / 33
Thromboxane-A synthase	TBXAS1	P24557	CHEMBL1835	Cytochrome P450	0.089872067	7 / 2

Target	Common name	Uniprot ID	ChEMBL ID	Target Class	Probability*	Known actives (3D/2D)
Beta-galactoside alpha-2,6-sialyltransferase 1	ST6GAL1	P15907	CHEMBL3 596075	Transferase	0.08987 2067	1 / 2
Xanthine dehydrogenase	XDH	P47989	CHEMBL1 929	Oxidoreductase	0.08987 2067	17 / 18
MAP kinase ERK1	MAPK3	P27361	CHEMBL3 385	Kinase	0.08079 2387	10 / 1
Cyclin-dependent kinase 6	CDK6	Q00534	CHEMBL2 508	Kinase	0.08079 2387	0 / 4
Carbonic anhydrase IV	CA4	P22748	CHEMBL3 729	Lyase	0.08079 2387	7 / 9
Phospholipase A2 group IIA	PLA2G2A	P14555	CHEMBL3 474	Enzyme	0.08079 2387	14 / 2
Epidermal growth factor receptor erbB1	EGFR	P00533	CHEMBL2 03	Kinase	0.08079 2387	172 / 28
Glycogen synthase kinase-3 beta	GSK3B	P49841	CHEMBL2 62	Kinase	0.08079 2387	158 / 13

Target	Common name	Uniprot ID	ChEMBL ID	Target Class	Probability*	Known actives (3D/2D)
Cyclooxygenase-2	PTGS2	P35354	CHEMBL230	Oxidoreductase	0.071715932	53 / 21
Estrogen receptor beta	ESR2	Q92731	CHEMBL242	Nuclear receptor	0.071715932	47 / 44
Estrogen receptor alpha	ESR1	P03372	CHEMBL206	Nuclear receptor	0.071715932	56 / 45
Receptor-type tyrosine-protein phosphatase S	PTPRS	Q13332	CHEMBL2396508	Phosphatase	0.071715932	0 / 8
AMY1C	AMY1A	P04745	CHEMBL2478	Enzyme	0.071715932	0 / 1
Arachidonate 12-lipoxygenase	ALOX12	P18054	CHEMBL3687	Enzyme	0.071715932	7 / 9
Beta amyloid A4 protein	APP	P05067	CHEMBL2487	Membrane receptor	0.071715932	14 / 12
Carbonyl reductase [NADPH] 1	CBR1	P16152	CHEMBL5586	Enzyme	0.071715932	1 / 2

Target	Common name	Uniprot ID	ChEMBL ID	Target Class	Probability*	Known actives (3D/2D)
Transthyretin	TTR	P02766	CHEMBL3194	Secreted protein	0.071715932	11 / 2
Tyrosine-protein kinase receptor FLT3	FLT3	P36888	CHEMBL1974	Kinase	0.071715932	53 / 7
NADPH oxidase 4	NOX4	Q9NPH5	CHEMBL1250375	Enzyme	0.062621967	5 / 6
Tyrosine-protein kinase SYK	SYK	P43405	CHEMBL2599	Kinase	0.062621967	29 / 3
Sigma opioid receptor	SIGMAR1	Q99720	CHEMBL287	Membrane receptor	0.062621967	7 / 66
G protein-coupled receptor kinase 6	GRK6	P43250	CHEMBL6144	Kinase	0.062621967	1 / 4
Acetylcholinesterase	ACHE	P22303	CHEMBL220	Hydrolase	0.062621967	34 / 23
Inhibitor of nuclear factor kappa B kinase beta subunit	IKBKB	O14920	CHEMBL1991	Kinase	0.062621967	28 / 1

Target	Common name	Uniprot ID	ChEMBL ID	Target Class	Probability*	Known actives (3D/2D)
Dopamine D2 receptor	DRD2	P14416	CHEMBL217	Family A G protein-coupled receptor	0.062621967	25 / 60
Cyclin-dependent kinase 2	CDK2	P24941	CHEMBL301	Kinase	0.053556076	64 / 11
Lysine-specific demethylase 4D-like	KDM4E	B2RXH2	CHEMBL1293226	Eraser	0.053556076	1 / 2
Casein kinase II alpha	CSNK2A1	P68400	CHEMBL3629	Kinase	0.053556076	7 / 2
Matrix metalloproteinase 9	MMP9	P14780	CHEMBL321	Protease	0.053556076	165 / 2
Matrix metalloproteinase 2	MMP2	P08253	CHEMBL333	Protease	0.053556076	140 / 2
Cytosolic phospholipase A2	PLA2G4A	P47712	CHEMBL3816	Enzyme	0.053556076	1 / 2
Adenosine A3 receptor	ADORA3	P0DMS8	CHEMBL256	Family A G protein-coupled receptor	0.053556076	21 / 19

Target	Common name	Uniprot ID	ChEMBL ID	Target Class	Probability*	Known actives (3D/2D)
Serine/threonine-protein kinase PIM1	PIM1	P11309	CHEMBL2147	Kinase	0.053556076	69 / 7
Cystic fibrosis transmembrane conductance regulator	CFTR	P13569	CHEMBL4051	Other ion channel	0.053556076	3 / 1
Multidrug resistance-associated protein 1	ABCC1	P33527	CHEMBL3004	Primary active transporter	0.053556076	1 / 10
Glyoxalase I	GLO1	Q04760	CHEMBL2424	Enzyme	0.053556076	0 / 4
Arginase-1 (by homology)	ARG1	P05089	CHEMBL1075097	Enzyme	0.053556076	0 / 2
Steryl-sulfatase	STS	P08842	CHEMBL3559	Enzyme	0.053556076	31 / 18
Tyrosinase	TYR	P14679	CHEMBL1973	Oxidoreductase	0.053556076	1 / 3
Telomerase reverse transcriptase	TERT	O14746	CHEMBL2916	Enzyme	0.053556076	5 / 18



Target	Common name	Uniprot ID	ChEMBL ID	Target Class	Probability*	Known actives (3D/2D)
Estradiol 17-beta-dehydrogenase 2	HSD17B2	P37059	CHEMBL2789	Enzyme	0.053556076	39 / 3
P-glycoprotein 1	ABCB1	P08183	CHEMBL4302	Primary active transporter	0.053556076	3 / 42
6-phosphofructo-2-kinase/fructose-2,6-bisphosphatase 3	PFKFB3	Q16875	CHEMBL2331053	Enzyme	0.053556076	57 / 2
Beta-secretase 1	BACE1	P56817	CHEMBL4822	Protease	0.053556076	62 / 12
Aryl hydrocarbon receptor	AHR	P35869	CHEMBL3201	Transcription factor	0.053556076	0 / 1
Estrogen-related receptor alpha	ESRRA	P11474	CHEMBL3429	Nuclear receptor	0.053556076	0 / 2
Neurotrophic tyrosine kinase receptor type 2	NTRK2	Q16620	CHEMBL4898	Kinase	0.053556076	1 / 1
NEDD8-activating enzyme E1 regulatory subunit	NAE1	Q13564	CHEMBL2016431	Unclassified protein	0.053556076	0 / 1

Target	Common name	Uniprot ID	ChEMBL ID	Target Class	Probability*	Known actives (3D/2D)
ALK tyrosine kinase receptor	ALK	Q9UM73	CHEMBL4247	Kinase	0.053556076	15 / 4
Butyrylcholinesterase	BCHE	P06276	CHEMBL1914	Hydrolase	0.053556076	7 / 6
Vascular endothelial growth factor receptor 1 (by homology)	FLT1	P17948	CHEMBL1868	Kinase	0.053556076	18 / 0
Platelet-derived growth factor receptor beta	PDGFRB	P09619	CHEMBL1913	Kinase	0.053556076	12 / 0
Delta opioid receptor	OPRD1	P41143	CHEMBL236	Family A G protein-coupled receptor	0.053556076	9 / 5
Carbonic anhydrase XIV	CA14	Q9ULX7	CHEMBL3510	Lyase	0.053556076	46 / 3
Matrix metalloproteinase 12	MMP12	P39900	CHEMBL4393	Protease	0.053556076	7 / 2
Phospholipase A-2-activating protein	PLAA	Q9Y263	CHEMBL6114	Unclassified protein	0.053556076	12 / 0

Target	Common name	Uniprot ID	ChEMBL ID	Target Class	Probability*	Known actives (3D/2D)
DNA-3-methyladenine glycosylase	MPG	P29372	CHEMBL3 396943	Enzyme	0.05355 6076	0 / 1
Catechol O-methyltransferase	COMT	P21964	CHEMBL2 023	Transferase	0.05355 6076	14 / 0
DNA topoisomerase I	TOP1	P11387	CHEMBL1 781	Isomerase	0.05355 6076	1 / 1
Plasminogen	PLG	P00747	CHEMBL1 801	Protease	0.05355 6076	0 / 3
Serine/threonine-protein kinase Aurora-B	AURKB	Q96GD4	CHEMBL2 185	Kinase	0.05355 6076	68 / 4
Vascular endothelial growth factor receptor 2	KDR	P35968	CHEMBL2 79	Kinase	0.05355 6076	159 / 3
PI3-kinase p110-gamma subunit	PIK3CG	P48736	CHEMBL3 267	Enzyme	0.05355 6076	109 / 1
Matrix metalloproteinase 3	MMP3	P08254	CHEMBL2 83	Protease	0.05355 6076	69 / 1

Target	Common name	Uniprot ID	ChEMBL ID	Target Class	Probability*	Known actives (3D/2D)
Stem cell growth factor receptor	KIT	P10721	CHEMBL1936	Kinase	0.053556076	31 / 3
Microtubule-associated protein tau	MAPT	P10636	CHEMBL1293224	Unclassified protein	0.053556076	9 / 1
SUMO-activating enzyme	SAE1 UBA2	Q9UBE0 Q9UBT2	CHEMBL2095174	Enzyme	0.053556076	1 / 0

**Table A4** List of total 73 metabolites identified across DHHC2 overexpression, knockdown and Ctrl conditions via MS-DIAL based spectral matching from the reference libraries.

S.no.	Metabolite name	Average RT (min)	Precursor m/z	Adduct type	Molecular formula
1	Guanine	3.06	152.06	[M+H] <sup>+</sup>	C <sub>5</sub> H <sub>5</sub> N <sub>5</sub> O
2	Threonine	12.45	120.07	[M+H] <sup>+</sup>	C <sub>4</sub> H <sub>9</sub> NO <sub>3</sub>
3	Lysine	16.172	147.11	[M+H] <sup>+</sup>	C <sub>6</sub> H <sub>14</sub> N <sub>2</sub> O <sub>2</sub>

S.no.	Metabolite name	Average RT (min)	Precursor m/z	Adduct type	Molecular formula
4	L-Phenylalanine	11.55	166.09	[M+H] <sup>+</sup>	C <sub>9</sub> H <sub>11</sub> NO <sub>2</sub>
5	5'-deoxyadenosine	3.12	252.11	[M+H] <sup>+</sup>	C <sub>10</sub> H <sub>13</sub> N <sub>5</sub> O <sub>3</sub>
6	3-hydroxysebacic acid	11.92	217.11	[M-H] <sup>-</sup>	C <sub>10</sub> H <sub>18</sub> O <sub>5</sub>
7	3-methyluric acid	11.52	181.03	[M-H] <sup>-</sup>	C <sub>6</sub> H <sub>6</sub> N <sub>4</sub> O <sub>3</sub>
8	4-guanidinobutanoic acid	11.4	146.09	[M+H] <sup>+</sup>	C <sub>5</sub> H <sub>11</sub> N <sub>3</sub> O <sub>2</sub>
9	5-aminopentanoate	14.32	118.09	[M+H] <sup>+</sup>	C <sub>5</sub> H <sub>11</sub> NO <sub>2</sub>
10	5'-methylthioadenosine	8.58	298.1	[M+H] <sup>+</sup>	C <sub>11</sub> H <sub>15</sub> N <sub>5</sub> O <sub>3</sub> S
11	Acetyl-cysteine	12.41	164.03	[M+H] <sup>+</sup>	C <sub>5</sub> H <sub>9</sub> NO <sub>3</sub> S
12	Adenine	9.27	136.06	[M+H] <sup>+</sup>	C <sub>5</sub> H <sub>5</sub> N <sub>5</sub>
13	Adenosine	9.25	268.1	[M+H] <sup>+</sup>	C <sub>10</sub> H <sub>13</sub> N <sub>5</sub> O <sub>4</sub>
14	Adenosine 5-monophosphate	2.44	348.07	[M+H] <sup>+</sup>	C <sub>10</sub> H <sub>14</sub> N <sub>5</sub> O <sub>7</sub> P
15	Adenosine-3-monophosphate	2.47	348.07	[M+H] <sup>+</sup>	C <sub>10</sub> H <sub>14</sub> N <sub>5</sub> O <sub>7</sub> P
16	Alanine	12.26	134.02	[M+2Na-H]	C <sub>3</sub> H <sub>7</sub> NO <sub>2</sub>
17	Aminomalonic acid	26.1	120.02	[M+H] <sup>+</sup>	C <sub>3</sub> H <sub>5</sub> NO <sub>4</sub>

S.no.	Metabolite name	Average RT (min)	Precursor m/z	Adduct type	Molecular formula
18	Arginine	15.78	175.12	[M+H] <sup>+</sup>	C <sub>6</sub> H <sub>14</sub> N <sub>4</sub> O <sub>2</sub>
19	Betaine	11.54	118.08	[M+H] <sup>+</sup>	C <sub>5</sub> H <sub>11</sub> NO <sub>2</sub>
20	Carnitine	2.33	162.11	[M+H] <sup>+</sup>	C <sub>7</sub> H <sub>15</sub> NO <sub>3</sub>
21	Citrulline	13.78	176.1	[M+H] <sup>+</sup>	C <sub>6</sub> H <sub>13</sub> N <sub>3</sub> O <sub>3</sub>
22	Creatine	12.00	132.08	[M+H] <sup>+</sup>	C <sub>4</sub> H <sub>9</sub> N <sub>3</sub> O <sub>2</sub>
23	Cysteic acid	15.35	167.99	[M-H] <sup>-</sup>	C <sub>3</sub> H <sub>7</sub> NO <sub>5</sub> S
24	Cytidine	11.74	266.07	[M+Na] <sup>+</sup>	C <sub>9</sub> H <sub>13</sub> N <sub>3</sub> O <sub>5</sub>
25	D-aminolevulinic acid	25.41	132	[M+H] <sup>+</sup>	C <sub>5</sub> H <sub>9</sub> NO <sub>3</sub>
26	Deoxycarnitine	12.78	146.12	[M+H] <sup>+</sup>	C <sub>7</sub> H <sub>15</sub> NO <sub>2</sub>
27	Glutamic acid	11.95	148.06	[M+H] <sup>+</sup>	C <sub>5</sub> H <sub>9</sub> NO <sub>4</sub>
28	Glutamine	13.22	147.08	[M+H] <sup>+</sup>	C <sub>5</sub> H <sub>10</sub> N <sub>2</sub> O <sub>3</sub>
29	Glycero-3-phosphocholine	2.20	258.11	[M+H] <sup>+</sup>	C <sub>8</sub> H <sub>21</sub> NO <sub>6</sub> P <sup>+</sup>
30	Guanosine	8.51	284.1	[M+H] <sup>+</sup>	C <sub>10</sub> H <sub>13</sub> N <sub>5</sub> O <sub>5</sub>
31	Heptadecanoate	31.03	269.25	[M-H] <sup>-</sup>	C <sub>17</sub> H <sub>34</sub> O <sub>2</sub>

S.no.	Metabolite name	Average RT (min)	Precursor m/z	Adduct type	Molecular formula
32	Homocysteine thiolactone	15.34	118.01	[M+H] <sup>+</sup>	C <sub>4</sub> H <sub>7</sub> NOS
33	Hypoxanthine	7.38	137.05	[M+H] <sup>+</sup>	C <sub>5</sub> H <sub>4</sub> N <sub>4</sub> O
34	Indole	21.21	116.05	[M-H] <sup>-</sup>	C <sub>8</sub> H <sub>7</sub> N
35	Inosine	7.15	291.07	[M+Na] <sup>+</sup>	C <sub>10</sub> H <sub>12</sub> N <sub>4</sub> O <sub>5</sub>
36	Kynurenic acid	2.27	188.03	[M-H] <sup>-</sup>	C <sub>10</sub> H <sub>7</sub> NO <sub>3</sub>
37	Leucine	11.369	132.1019	[M+H] <sup>+</sup>	C <sub>6</sub> H <sub>13</sub> NO <sub>2</sub>
38	Methyladenosine	12.96	282.12	[M+H] <sup>+</sup>	C <sub>11</sub> H <sub>15</sub> N <sub>5</sub> O <sub>4</sub>
39	N-acetyl-aspartic acid	9.94	174.04	[M-H] <sup>-</sup>	C <sub>6</sub> H <sub>9</sub> NO <sub>5</sub>
40	N-acetyl-D-mannosamine	2.02	222.10	[M+H] <sup>+</sup>	C <sub>8</sub> H <sub>15</sub> NO <sub>6</sub>
41	N-acetylneuraminic acid	2.39	308.1	[M-H] <sup>-</sup>	C <sub>11</sub> H <sub>19</sub> NO <sub>9</sub>
42	N-acetyl-serine	10.7	146.05	[M-H] <sup>-</sup>	C <sub>5</sub> H <sub>9</sub> NO <sub>4</sub>
43	N-formyl-L-methionine	12.11	176.04	[M-H] <sup>-</sup>	C <sub>6</sub> H <sub>11</sub> NO <sub>3</sub> S
44	Norleucine	3.11	132.1	[M+H] <sup>+</sup>	C <sub>6</sub> H <sub>13</sub> NO <sub>2</sub>
45	N- $\alpha$ -acetyl-L-arginine	32.52	217.13	[M+H] <sup>+</sup>	C <sub>8</sub> H <sub>16</sub> N <sub>4</sub> O <sub>3</sub>

S.no.	Metabolite name	Average RT (min)	Precursor m/z	Adduct type	Molecular formula
46	Nε-acetyl-L-lysine	32.62	189.12	[M+H] <sup>+</sup>	C <sub>8</sub> H <sub>16</sub> N <sub>2</sub> O <sub>3</sub>
47	Oleic acid	30.93	281.25	[M-H] <sup>-</sup>	C <sub>18</sub> H <sub>34</sub> O <sub>2</sub>
48	Palmitic acid	2.87	255.23	[M-H] <sup>-</sup>	C <sub>16</sub> H <sub>32</sub> O <sub>2</sub>
49	Phosphoethanolamine	31.99	140	[M-H] <sup>-</sup>	C <sub>2</sub> H <sub>8</sub> NO <sub>4</sub> P
50	Phosphorylcholine	2.15	184.07	[M+H] <sup>+</sup>	C <sub>5</sub> H <sub>15</sub> NO <sub>4</sub> P <sup>+</sup>
51	Proline	13.02	116.07	[M+H] <sup>+</sup>	C <sub>5</sub> H <sub>9</sub> NO <sub>2</sub>
52	Purine	30.35	143.04	[M+Na] <sup>+</sup>	C <sub>5</sub> H <sub>4</sub> N <sub>4</sub>
53	Pyroglutamic acid	3.14	130.05	[M+H] <sup>+</sup>	C <sub>5</sub> H <sub>7</sub> NO <sub>3</sub>
54	Sphinganine (d18:0)	3.45	324.29	[M+Na] <sup>+</sup>	C <sub>18</sub> H <sub>39</sub> NO <sub>2</sub>
55	Stearic acid	23.25	283.26	[M-H] <sup>-</sup>	C <sub>18</sub> H <sub>36</sub> O <sub>2</sub>
56	Suberic acid	3.00	173.08	[M-H] <sup>-</sup>	C <sub>8</sub> H <sub>14</sub> O <sub>4</sub>
57	TAG (12:0/12:0/12:0)	24.04	657.00	[M+NH <sub>4</sub> ] <sup>+</sup>	C <sub>39</sub> H <sub>74</sub> O <sub>6</sub>
58	TAG(50:1)	3.32	850.79	[M+NH <sub>4</sub> ] <sup>+</sup>	C <sub>53</sub> H <sub>100</sub> O <sub>6</sub>
59	TG(12:0/12:0/14:0)	24.82	684.61	[M+NH <sub>4</sub> ] <sup>+</sup>	C <sub>41</sub> H <sub>78</sub> O <sub>6</sub>



S.no.	Metabolite name	Average RT (min)	Precursor m/z	Adduct type	Molecular formula
60	TG(12:0/14:0/16:0)	25.97	740.68	[M+NH <sub>4</sub> ] <sup>+</sup>	C <sub>45</sub> H <sub>86</sub> O <sub>6</sub>
61	TG(14:0/16:0/16:1)	3.21	794.72	[M+NH <sub>4</sub> ] <sup>+</sup>	C <sub>49</sub> H <sub>92</sub> O <sub>6</sub>
62	TG(14:0/16:0/17:0)	28.08	810.75	[M+NH <sub>4</sub> ] <sup>+</sup>	C <sub>50</sub> H <sub>96</sub> O <sub>6</sub>
63	TG(15:0/16:1/16:1)	26.38	806.72	[M+NH <sub>4</sub> ] <sup>+</sup>	C <sub>50</sub> H <sub>92</sub> O <sub>6</sub>
64	TG(16:1/16:1/18:1)	26.85	846.75	[M+NH <sub>4</sub> ] <sup>+</sup>	C <sub>53</sub> H <sub>93</sub> O <sub>6</sub>
65	TG(18:1/18:1/18:2)	27.61	900.8	[M+NH <sub>4</sub> ] <sup>+</sup>	C <sub>57</sub> H <sub>102</sub> O <sub>6</sub>
66	TG(8:0/10:0/10:0)	34.72	544.46	[M+H] <sup>+</sup>	C <sub>31</sub> H <sub>58</sub> O <sub>6</sub>
67	Tyrosine	11.36	182.08	[M+H] <sup>+</sup>	C <sub>9</sub> H <sub>11</sub> NO <sub>3</sub>
68	Urate	22.31	169.04	[M+H] <sup>+</sup>	C <sub>5</sub> H <sub>4</sub> N <sub>4</sub> O <sub>3</sub>
69	Uridine	17.91	245.08	[M+H] <sup>+</sup>	C <sub>9</sub> H <sub>12</sub> N <sub>2</sub> O <sub>6</sub>
70	Uridine 5-diphospho-N-acetylglucosamine	1.98	606.07	[M-H] <sup>-</sup>	C <sub>17</sub> H <sub>27</sub> N <sub>3</sub> O <sub>17</sub> P <sub>2</sub>
71	Uridine-5-monophosphate	4.92	305.02	[M-H <sub>2</sub> O-H] <sup>-</sup>	C <sub>9</sub> H <sub>13</sub> N <sub>2</sub> O <sub>9</sub> P
72	Urocanic acid	9.2	139.05	[M+H] <sup>+</sup>	C <sub>6</sub> H <sub>6</sub> N <sub>2</sub> O <sub>2</sub>
73	Xanthine	4.83	153.04	[M+H] <sup>+</sup>	C <sub>5</sub> H <sub>4</sub> N <sub>4</sub> O <sub>2</sub>



## References

1. De, I. and S. Sadhukhan, Emerging Roles of DHHC-mediated Protein S-palmitoylation in Physiological and Pathophysiological Context. *Eur J Cell Biol*, 2018. **97**(5): pp. 319-338.
2. Greaves, J. and L.H. Chamberlain, DHHC palmitoyl transferases: substrate interactions and (patho)physiology. *Trends Biochem Sci*, 2011. **36**(5): pp. 245-253.
3. Zhong, Q., et al., Protein posttranslational modifications in health and diseases: Functions, regulatory mechanisms, and therapeutic implications. *MedComm* (2020), 2023. **4**(3): p. e261.
4. Hanahan, D. and R.A. Weinberg, The Hallmarks of Cancer. *Cell*, 2000. **100**(1): pp. 57-70.
5. Blaustein, M., et al., Akt Is S-Palmitoylated: A New Layer of Regulation for Akt. *Front Cell Dev Biol*, 2021. **9**: p. 626404.
6. Bollu, L.R., et al., Intracellular activation of EGFR by fatty acid synthase dependent palmitoylation. *Oncotarget*, 2015. **6**(33): p. 34992.
7. Liao, D., et al., The role of s-palmitoylation in neurological diseases: implication for zDHHC family. *Front Pharmacol*, 2024. **14**: p. 1342830.
8. Hu, X., et al., A mini review of small-molecule inhibitors targeting palmitoyltransferases. *Eur J Med Chem Rep*, 2022. **5**: p. 100041.
9. Davda, D., et al., Profiling Targets of the Irreversible Palmitoylation Inhibitor 2-Bromopalmitate. *ACS Chem Biol*, 2013. **8**.
10. Atanasov, A.G., et al., Discovery and resupply of pharmacologically active plant-derived natural products: A review. *Biotechnol Adv*, 2015. **33**(8): pp. 1582-1614.
11. Chen, X., et al., Activation of JNK and p38 MAPK Mediated by ZDHHC17 Drives Glioblastoma Multiforme Development and Malignant Progression. *Theranostics*, 2020. **10**(3): pp. 998-1015.
12. Binoy, A., et al., Protein S-palmitoylation is markedly inhibited by 4"-alkyl ether lipophilic derivatives of EGCG, the major green tea polyphenol: In vitro and in silico studies. *BBA - Biomembrane*, 2024. **1866**(3): p. 184264.
13. Anderson, A.M. and M.A. Ragan, Palmitoylation: a protein S-acylation with implications for breast cancer. *npj Breast Cancer*, 2016. **2**(1): p. 16028.
14. Sun, Y., et al., ZDHHC2-Mediated AGK Palmitoylation Activates AKT-mTOR Signaling to Reduce Sunitinib Sensitivity in Renal Cell Carcinoma. *Cancer Res*, 2023. **83**(12): pp. 2034-2051.
15. Yan, S.M., et al., Reduced expression of ZDHHC2 is associated with lymph node metastasis and poor prognosis in gastric adenocarcinoma. *PLoS One*, 2013. **8**(2): p. e56366.
16. Ju, Z., et al., Transcriptomic and metabolomic profiling reveal the p53-dependent benzeneacetic acid attenuation of silica-induced epithelial-mesenchymal transition in human bronchial epithelial cells. *Cell Biosci*, 2021. **11**(1): p. 30.
17. Yao, Y., et al., Metabolomic differentiation of benign vs malignant pulmonary nodules with high specificity via high-resolution mass spectrometry analysis of patient sera. *Nat Commun*, 2023. **14**(1): p. 2339.
18. Čermáková, M., et al., Metabolomic study of obesity and its treatment with palmitoylated prolactin-releasing peptide analog in spontaneously hypertensive and normotensive rats. *J Proteome Res*, 2019. **18**(4): pp. 1735-1750.
19. Dai, M.-Y., et al., High-potency PD-1/PD-L1 degradation induced by Peptide-PROTAC in human cancer cells. *Cell Death Dis*, 2022. **13**(11): p. 924.
20. Sanders, S.S., F.I. De Simone, and G.M. Thomas, mTORC1 Signaling Is Palmitoylation-Dependent in Hippocampal Neurons and Non-neuronal Cells and Involves Dynamic Palmitoylation of LAMTOR1 and mTOR. *Front Cell Neurosci*, 2019. **13**: p. 115.
21. Runkle, K.B., et al., Inhibition of DHHC20-Mediated EGFR Palmitoylation Creates a Dependence on EGFR Signaling. *Mol Cell*, 2016. **62**(3): pp. 385-396.
22. Kharbanda, A., et al., Blocking EGFR palmitoylation suppresses PI3K signaling and mutant KRAS lung tumorigenesis. *Sci Signal*, 2020. **13**(621): p. eaax2364.

23. Ramazi, S. and J. Zahiri, Posttranslational modifications in proteins: resources, tools and prediction methods. Database (Oxford), 2021. **2021**.
24. Chen, L. and A. Kashina, Post-translational Modifications of the Protein Termini. Front Cell Dev Biol, 2021. **9**: p. 719590.
25. Wang, H., et al., Protein post-translational modifications in the regulation of cancer hallmarks. Cancer Gene Ther, 2022. **30**.
26. Wang, R. and Y.Q. Chen, Protein Lipidation Types: Current Strategies for Enrichment and Characterization. Int J Mol Sci, 2022. **23**(4).
27. Prendeville, H. and L. Lynch, Diet, lipids, and antitumor immunity. Cell Mol Immunol, 2022. **19**(3): pp. 432-444.
28. Horn, A. and J.K. Jaiswal, Structural and signaling role of lipids in plasma membrane repair. Curr Top Membr, 2019. **84**: pp. 67-98.
29. Jiang, H., et al., Protein Lipidation: Occurrence, Mechanisms, Biological Functions, and Enabling Technologies. Chem Rev, 2018. **118**(3): pp. 919-988.
30. Bogdanov, M., E. Mileykovskaya, and W. Dowhan, Lipids in the assembly of membrane proteins and organization of protein supercomplexes: implications for lipid-linked disorders. Subcell Biochem, 2008. **49**: pp. 197-239.
31. Corradi, V., et al., Emerging Diversity in Lipid-Protein Interactions. Chem Rev, 2019. **119**(9): p. 5775-5848.
32. Cournia, Z., et al., Membrane Protein Structure, Function, and Dynamics: a Perspective from Experiments and Theory. J Membr Biol, 2015. **248**(4): pp. 611-40.
33. Žak, A., et al., Deciphering Lipid Arrangement in Phosphatidylserine/Phosphatidylcholine Mixed Membranes: Simulations and Experiments. Langmuir, 2023. **39**(51): pp. 18995-19007.
34. Kastelowitz, N., et al., Peptides derived from MARCKS block coagulation complex assembly on phosphatidylserine. Sci Rep, 2017. **7**(1): p. 4275.
35. Lemmon, M.A., Pleckstrin homology (PH) domains and phosphoinositides. Biochem Soc Symp, 2007.(74): pp. 81-93.
36. Singh, N., et al., Redefining the specificity of phosphoinositide-binding by human PH domain-containing proteins. Nat Commun, 2021. **12**(1): p. 4339.
37. Resh, M.D., Covalent lipid modifications of proteins. Curr Biol, 2013. **23**(10): pp. R431-R435.
38. Brunsvel, L., H. Waldmann, and D. Huster, Membrane binding of lipidated Ras peptides and proteins — The structural point of view. BBA - Biomembranes, 2009. **1788**(1): pp. 273-288.
39. Santiago-Tirado, F.H. and T.L. Doering, All about that fat: Lipid modification of proteins in *Cryptococcus neoformans*. J Microbiol, 2016. **54**(3): pp. 212-222.
40. Guan, X. and C.A. Fierke, Understanding Protein Palmitoylation: Biological Significance and Enzymology. Sci China Chem, 2011. **54**(12): pp. 1888-1897.
41. Yuan, Y., et al., Protein lipidation in health and disease: molecular basis, physiological function and pathological implication. Signal Transduct Target Ther, 2024. **9**(1): p. 60.
42. Spinelli, M., Nutrient-Dependent Changes of Protein Palmitoylation: Impact on Nuclear Enzymes and Regulation of Gene Expression. Int J Mol Sci, 2018. **19**.
43. Hanna, C.C., et al., Chemical Synthesis and Semisynthesis of Lipidated Proteins. Angew Chem Int Ed Engl, 2022. **61**(15): p. e202111266.
44. Nůšková, H., et al., Competition for cysteine acylation by C16:0 and C18:0 derived lipids is a global phenomenon in the proteome. J Biol Chem, 2023. **299**(9): p. 105088.
45. Chen, J.J., Y. Fan, and D. Boehning, Regulation of Dynamic Protein S-Acylation. Front Mol Biosci, 2021. **8**: p. 656440.
46. Putilina, T., P. Wong, and S. Gentleman, The DHHC domain: a new highly conserved cysteine-rich motif. Mol Cell Biochem, 1999. **195**(1-2): pp. 219-226.
47. Fukata, Y., D.S. Bredt, and M. Fukata, Protein palmitoylation by DHHC protein family. The dynamic synapse: molecular methods in ionotropic receptor biology, 2006: pp. 83-88.
48. Chaturvedi, S., et al., Role of EGFR and FASN in breast cancer progression. J Cell Commun Signal, 2023. **17**(4): pp. 1249-1282.
49. Linder, M.E. and R.J. Deschenes, Palmitoylation: policing protein stability and traffic. Nat Rev Mol Cell Biol, 2007. **8**(1): pp. 74-84.
50. Ramzan, F., et al., Lost in traffic: consequences of altered palmitoylation in neurodegeneration. Front Physiol, 2023. **14**: p. 1166125.

51. Cervilla-Martínez, J.F., et al., Altered Cortical Palmitoylation Induces Widespread Molecular Disturbances in Parkinson's Disease. *Int J Mol Sci*, 2022. **23**(22).
52. Li, W., et al., Aberrant palmitoylation caused by a ZDHHC21 mutation contributes to pathophysiology of Alzheimer's disease. *BMC Med*, 2023. **21**(1): p. 223.
53. Zhang, H., et al., Fine-mapping of ZDHHC2 identifies risk variants for schizophrenia in the Han Chinese population. *Mol Genet Genomic Med*, 2020. **8**(7): p. e1190.
54. Casellas-Vidal, D., et al., ZDHHC15 as a candidate gene for autism spectrum disorder. *Am J Med Genet A*, 2023. **191**(4): pp. 941-947.
55. Schmidt, M.F., M. Bracha, and M.J. Schlesinger, Evidence for covalent attachment of fatty acids to Sindbis virus glycoproteins. *PNAS*, 1979. **76**(4): pp. 1687-1691.
56. Ramadan, A.A., et al., Identification of SARS-CoV-2 Spike Palmitoylation Inhibitors That Results in Release of Attenuated Virus with Reduced Infectivity. *Viruses*, 2022. **14**(3).
57. Sobocińska, J., P. Roszczenko-Jasińska, and K. Kwiatkowska, Protein palmitoylation and its role in bacterial and viral infections. *Front Immunol*, 2018. **8**: p. 323924.
58. Schroeder, C., et al., The influenza virus ion channel and maturation cofactor M2 is a cholesterol-binding protein. *Eur Biophys J*, 2005. **34**(1): pp. 52-66.
59. Kordyukova, L.V., et al., S acylation of the hemagglutinin of influenza viruses: mass spectrometry reveals site-specific attachment of stearic acid to a transmembrane cysteine. *J Virol*, 2008. **82**(18): pp. 9288-9292.
60. Veit, M., et al., The hemagglutinating glycoproteins of influenza B and C viruses are acylated with different fatty acids. *Virology*, 1990. **177**(2): pp. 807-811.
61. Kordyukova, L.V., et al., Site-specific attachment of palmitate or stearate to cytoplasmic versus transmembrane cysteines is a common feature of viral spike proteins. *Virology*, 2010. **398**(1): pp. 49-56.
62. Li, X., et al., Protein Palmitoylation Modification During Viral Infection and Detection Methods of Palmitoylated Proteins. *Front Cell Infect Microbiol*, 2022. **12**: p. 821596.
63. Caballero, M., et al., Measles virus fusion protein is palmitoylated on transmembrane-intracytoplasmic cysteine residues which participate in cell fusion. *J Virol*, 1998. **72**(10): pp. 8198-8204.
64. Huang, Y., et al., Metabolic profiles of fish nodavirus infection in vitro: RGNNV induced and exploited cellular fatty acid synthesis for virus infection. *Cell Microbiol*, 2020. **22**(9): p. e13216.
65. Das, T., J.S. Yount, and H.C. Hang, Protein S-palmitoylation in immunity. *Open Biol*, 2021. **11**(3): p. 200411.
66. Blanc, M., et al., SwissPalm: protein palmitoylation database. *F1000Res*, 2015. **4**:p.261.
67. Dunn, J., It Is Time to Close the Gap in Cancer Care. *JCO Glob Oncol*, 2023. **9**: p. e2200429.
68. Ravi, S., et al., An Update to Hallmarks of Cancer. *Cureus*, 2022. **14**(5): p. e24803.
69. Chen, Y., et al., Prolyl isomerase Pin1: a promoter of cancer and a target for therapy. *Cell Death Dis*, 2018. **9**(9): p. 883.
70. López-Otín, C., et al., Meta-hallmarks of aging and cancer. *Cell Metab*, 2023. **35**(1): pp. 12-35.
71. Zhang, Q., et al., Reprogramming of palmitic acid induced by dephosphorylation of ACOX1 promotes  $\beta$ -catenin palmitoylation to drive colorectal cancer progression. *Cell Discov*, 2023. **9**(1): p. 26.
72. Guo, H., et al., Targeting EGFR-dependent tumors by disrupting an ARF6-mediated sorting system. *Nat Commun*, 2022. **13**(1): p. 6004.
73. Lobo, S., et al., Identification of a Ras Palmitoyltransferase in *Saccharomyces cerevisiae* \*. *J Biol Chem*, 2002. **277**(43): pp. 41268-41273.
74. Babu, P., R.J. Deschenes, and L.C. Robinson, Akr1p-dependent Palmitoylation of Yck2p Yeast Casein Kinase 1 Is Necessary and Sufficient for Plasma Membrane Targeting\*. *J Biol Chem*, 2004. **279**(26): pp. 27138-27147.
75. Roth, A.F., et al., The yeast DHHC cysteine-rich domain protein Akr1p is a palmitoyl transferase. *J Cell Biol*, 2002. **159**(1): pp. 23-28.
76. Ocasio, C.A., et al., A palmitoyl transferase chemical–genetic system to map ZDHHC-specific S-acylation. *Nat Biotechnol*, 2024.
77. Politis, E.G., A.F. Roth, and N.G. Davis, Transmembrane Topology of the Protein Palmitoyl Transferase Akr1\*. *J Biol Chem*, 2005. **280**(11): pp.10156-10163.

78. Hou, H., et al., Analysis of DHHC acyltransferases implies overlapping substrate specificity and a two-step reaction mechanism. *Traffic*, 2009. **10**(8): pp. 1061-1073.
79. Dighe, S.A. and K.G. Kozminski, Swf1p, a member of the DHHC-CRD family of palmitoyltransferases, regulates the actin cytoskeleton and polarized secretion independently of its DHHC motif. *Mol Biol Cell*, 2008. **19**(10): pp. 4454-4468.
80. Smotrys, J.E., et al., The vacuolar DHHC-CRD protein Pfa3p is a protein acyltransferase for Vac8p. *J Cell Biol*, 2005. **170**(7): pp. 1091-1099.
81. Roth, A.F., et al., Global analysis of protein palmitoylation in yeast. *Cell*, 2006. **125**(5): p. 1003-13.
82. Batistic, O., Genomics and localization of the Arabidopsis DHHC-cysteine-rich domain S-acyltransferase protein family. *Plant Physiol*, 2012. **160**(3): pp. 1597-1612.
83. Porcellato, E., et al., The S-palmitoylome and DHHC-PAT interactome of *Drosophila melanogaster* S2R+ cells indicate a high degree of conservation to mammalian palmitoylomes. *PLoS One*, 2022. **17**(8): p. e0261543.
84. González Montoro, A., R. Quiroga, and J. Valdez Taubas, Zinc co-ordination by the DHHC cysteine-rich domain of the palmitoyltransferase Swf1. *Biochem J*, 2013. **454**(3): pp. 427-435.
85. Rana, M.S., et al., Fatty acyl recognition and transfer by an integral membrane S-acyltransferase. *Science*, 2018. **359**(6372).
86. Stix, R., et al., Structure and Mechanism of DHHC Protein Acyltransferases. *J Mol Biol*, 2020. **432**(18): pp. 4983-4998.
87. Lan, T., C. Delalande, and B.C. Dickinson, Inhibitors of DHHC family proteins. *Curr Opin Chem Biol*, 2021. **65**: pp. 118-125.
88. Toyoda, T., H. Sugimoto, and S. Yamashita, Sequence, expression in *Escherichia coli*, and characterization of lysophospholipase II. *Biochim Biophys Acta*, 1999. **1437**(2): pp. 182-193.
89. Camp, L.A. and S.L. Hofmann, Purification and properties of a palmitoyl-protein thioesterase that cleaves palmitate from H-Ras. *J Biol Chem*, 1993. **268**(30): pp. 22566-22574.
90. Soyombo, A.A. and S.L. Hofmann, Molecular cloning and expression of palmitoyl-protein thioesterase 2 (PPT2), a homolog of lysosomal palmitoyl-protein thioesterase with a distinct substrate specificity. *J Biol Chem*, 1997. **272**(43): pp. 27456-27463.
91. Calero, G., et al., The Crystal Structure of Palmitoyl Protein Thioesterase-2 (PPT2) Reveals the Basis for Divergent Substrate Specificities of the Two Lysosomal Thioesterases, PPT1 and PPT2\*. *J Biol Chem*, 2003. **278**(39): pp. 37957-37964.
92. Hirano, T., et al., Thioesterase activity and subcellular localization of acylprotein thioesterase 1/lysophospholipase 1. *BBA-Mol Cell Biol Lipids*, 2009. **1791**(8): pp. 797-805.
93. Kong, E., et al., Dynamic palmitoylation links cytosol-membrane shuttling of acyl-protein thioesterase-1 and acyl-protein thioesterase-2 with that of proto-oncogene H-ras product and growth-associated protein-43. *J Biol Chem*, 2013. **288**(13): pp. 9112-9125.
94. Duncan, J.A. and A.G. Gilman, A cytoplasmic acyl-protein thioesterase that removes palmitate from G protein  $\alpha$  subunits and p21RAS. *J Biol Chem*, 1998. **273**(25): pp. 15830-15837.
95. Tomatis, V.M., et al., Acyl-protein thioesterase 2 catalyzes the deacylation of peripheral membrane-associated GAP-43. *PLoS one*, 2010. **5**(11): p. e15045.
96. Abrami, L., et al., Palmitoylated acyl protein thioesterase APT2 deforms membranes to extract substrate acyl chains. *Nat Chem Biol*, 2021. **17**(4): pp. 438-447.
97. Lin, D.T. and E. Conibear, ABHD17 proteins are novel protein depalmitoylases that regulate N-Ras palmitate turnover and subcellular localization. *Elife*, 2015. **4**: p. e11306.
98. Tortosa, E., et al., Dynamic Palmitoylation Targets MAP6 to the Axon to Promote Microtubule Stabilization during Neuronal Polarization. *Neuron*, 2017. **94**(4): pp. 809-825.e7.
99. Kwon, H., et al., Flotillin-1 palmitoylation turnover by APT-1 and ZDHHC-19 promotes cervical cancer progression by suppressing IGF-1 receptor desensitization and proteostasis. *Cancer Gene Ther*, 2023. **30**(2): pp. 302-312.
100. Remsberg, J.R., et al., ABHD17 regulation of plasma membrane palmitoylation and N-Ras-dependent cancer growth. *Nat Chem Biol*, 2021. **17**(8): pp. 856-864.

101. Gu, M., et al., Palmitoyltransferase DHHC9 and acyl protein thioesterase APT1 modulate renal fibrosis through regulating  $\beta$ -catenin palmitoylation. *Nat Commun*, 2023. **14**(1): p. 6682.
102. Zhang, M., et al., A STAT3 palmitoylation cycle promotes T(H)17 differentiation and colitis. *Nature*, 2020. **586**(7829): pp. 434-439.
103. Zheng, S., et al., ZDHHC5-mediated NLRP3 palmitoylation promotes NLRP3-NEK7 interaction and inflammasome activation. *Mol Cell*, 2023. **83**(24): pp. 4570-4585.
104. Shetty, M., et al., Dopamine transporter membrane mobility is bidirectionally regulated by phosphorylation and palmitoylation. *Curr Res Physiol*, 2023. **6**: p. 100106.
105. Barylko, B., et al., Mimicking Protein Kinase C Phosphorylation Inhibits Arc/Arg3.1 Palmitoylation and Its Interaction with Nucleic Acids. *Int J Mol Sci*, 2024. **25**(2): p. 780.
106. Luse, M.A., et al., Nitrosation of CD36 regulates endothelial function and serum lipids. *bioRxiv*, 2024: **2024** :p. 588733.
107. Shen, Z.-C., et al., Regulation of anxiety-like behaviors by S-palmitoylation and S-nitrosylation in basolateral amygdala. *Biomed Pharmacother*, 2023. **169**: p. 115859.
108. Tien, C.F., et al., Glycosylation and S-palmitoylation regulate SARS-CoV-2 spike protein intracellular trafficking. *iScience*, 2022. **25**(8): p. 104709.
109. Seo, J., et al., Myristoylation-dependent palmitoylation of cyclin Y modulates long-term potentiation and spatial learning. *Prog Neurobiol*, 2022. **218**: p. 102349.
110. Resh, M.D., Palmitoylation of proteins in cancer. *Biochem Soc Trans*, 2017. **45**(2): pp. 409-416.
111. Le, X., et al., DNA methylation downregulated ZDHHC1 suppresses tumor growth by altering cellular metabolism and inducing oxidative/ER stress-mediated apoptosis and pyroptosis. *Theranostics*, 2020. **10**(21): pp. 9495-9511.
112. Jiang, N., et al., Overexpression of zinc finger DHHC-type containing 1 is associated with poor prognosis and cancer cell growth and metastasis in uterine corpus endometrial carcinoma. *Aging*, 2024. **16**(11): pp. 9784-9812.
113. Zhang, Q., et al., ZDHHC1 downregulates LIPG and inhibits colorectal cancer growth via IGF2BP1 Palmitoylation. *Cancer Gene Ther*, 2024.
114. Peng, C., et al., A critical role for ZDHHC2 in metastasis and recurrence in human hepatocellular carcinoma. *Biomed Res Int*, 2014. **2014**: p. 832712.
115. Planey, S.L., et al., Palmitoylation of cytoskeleton associated protein 4 by DHHC2 regulates antiproliferative factor-mediated signaling. *Mol Biol Cell*, 2009. **20**(5): pp. 1454-1463.
116. Conrads, T.P., et al., CKAP4/p63 is a receptor for the frizzled-8 protein-related antiproliferative factor from interstitial cystitis patients. *J Biol Chem*, 2006. **281**(49): pp. 37836-37843.
117. Li, S.-X., et al., Cytoskeleton-Associated Protein 4, a Promising Biomarker for Tumor Diagnosis and Therapy. *Front Mol Biosci*, 2021. **7**.
118. Sada, R., et al., Dynamic palmitoylation controls the microdomain localization of the DKK1 receptors CKAP4 and LRP6. *Sci Signal*, 2019. **12**(608).
119. Sharma, C., X.H. Yang, and M.E. Hemler, DHHC2 affects palmitoylation, stability, and functions of tetraspanins CD9 and CD151. *Mol Biol Cell*, 2008. **19**(8): pp. 3415-3425.
120. Liu, L., et al., Acyltransferase zinc finger DHHC-type containing 2 aggravates gastric carcinoma growth by targeting Nrf2 signaling: A mechanism-based multicomination bionic nano-drug therapy. *Redox Biol*, 2024. **70**: p. 103051.
121. Le Tourneau, C., E. Raymond, and S. Faivre, Sunitinib: a novel tyrosine kinase inhibitor. A brief review of its therapeutic potential in the treatment of renal carcinoma and gastrointestinal stromal tumors (GIST). *Ther Clin Risk Manag*, 2007. **3**(2): pp. 341-348.
122. Sharma, C., et al., Antioxidant functions of DHHC3 suppress anti-cancer drug activities. *Cell Mol Life Sci*, 2021. **78**(5): pp. 2341-2353.
123. Sharma, C., et al., Protein Acyltransferase DHHC3 Regulates Breast Tumor Growth, Oxidative Stress, and Senescence. *Cancer Res*, 2017. **77**(24): pp. 6880-6890.
124. Yao, H., et al., Inhibiting PD-L1 palmitoylation enhances T-cell immune responses against tumours. *Nat Biomed Eng*, 2019. **3**(4): pp. 306-317.
125. von Knethen, A. and B. Brüne, PD-L1 in the palm of your hand: palmitoylation as a target for immuno-oncology. *Signal Transduct Target Ther*, 2019. **4**(1): p. 18.

126. Zhao, C., et al., GSK3 $\beta$  palmitoylation mediated by ZDHHC4 promotes tumorigenicity of glioblastoma stem cells in temozolomide-resistant glioblastoma through the EZH2-STAT3 axis. *Oncogenesis*, 2022. **11**(1): p. 28.
127. Bian, J., et al., Identification and prognostic biomarkers among ZDHHC4/12/18/24, and APT2 in lung adenocarcinoma. *Sci Rep*, 2024. **14**.
128. Zhang, Y., et al., Potential Role of S-Palmitoylation in Cancer Stem Cells of Lung Adenocarcinoma. *Front Cell Dev Biol*, 2021. **9**: p. 734897.
129. Wang, Y., et al., ZDHHC5-mediated S-palmitoylation of FAK promotes its membrane localization and epithelial-mesenchymal transition in glioma. *Cell Commun Signal*, 2024. **22**(1): p. 46.
130. Chen, X., et al., EZH2 Palmitoylation Mediated by ZDHHC5 in p53-Mutant Glioma Drives Malignant Development and Progression. *Cancer Res*, 2017. **77**(18): pp. 4998-5010.
131. Shan, J., et al., Palmitoyltransferase ZDHHC6 promotes colon tumorigenesis by targeting PPAR $\gamma$ -driven lipid biosynthesis via regulating lipidome metabolic reprogramming. *J Exp Clinl Cancer Res*, 2024. **43**(1): p. 227.
132. Pedram, A., et al., DHHC-7 and -21 are palmitoylacyltransferases for sex steroid receptors. *Mol Biol Cell*, 2012. **23**(1): pp. 188-99.
133. Jiang, Y., et al., STAT3 palmitoylation initiates a positive feedback loop that promotes the malignancy of hepatocellular carcinoma cells in mice. *Sci Signal*, 2023. **16**(814): p. eadd2282.
134. Kong, Y., et al., Palmitoylation landscapes across human cancers reveal a role of palmitoylation in tumorigenesis. *J Transl Med*, 2023. **21**(1): p. 826.
135. Lin, Z., et al., Palmitoyl acyltransferase ZDHHC7 inhibits androgen receptor and suppresses prostate cancer. *Oncogene*, 2023. **42**(26): pp. 2126-2138.
136. Wang, Z., et al., AMPK $\alpha$ 1-mediated ZDHHC8 phosphorylation promotes the palmitoylation of SLC7A11 to facilitate ferroptosis resistance in glioblastoma. *Cancer Lett*, 2024. **584**: p. 216619.
137. Chong, X., et al., ZDHHC9 promotes colon tumor growth by inhibiting effector T cells. *Oncol Lett*, 2023. **25**(1): p. 5.
138. Lin, Z., et al., Targeting ZDHHC9 potentiates anti-programmed death-ligand 1 immunotherapy of pancreatic cancer by modifying the tumor microenvironment. *Biomed Pharmacother*, 2023. **161**: p. 114567.
139. Li, W., et al., ZDHHC9-mediated Bip/GRP78 S-palmitoylation inhibits unfolded protein response and promotes bladder cancer progression. *Cancer Lett*, 2024. **598**: p. 217118.
140. Hood, F.E., et al., Ras protein abundance correlates with Ras isoform mutation patterns in cancer. *Oncogene*, 2023. **42**(15): pp. 1224-1232.
141. Yang, A., et al., Regulation of RAS palmitoyltransferases by accessory proteins and palmitoylation. *Nat Struct Mol Biol*, 2024. **31**(3): pp. 436-446.
142. Chen, L., et al., Palmitoylation alters LDHA activity and pancreatic cancer response to chemotherapy. *Cancer Lett*, 2024. **587**: p. 216696.
143. Fan, X., et al., Blocking Palmitoylation of Apelin Receptor Alleviates Morphine Tolerance in Neuropathic Cancer Pain. *Int J Biol Sci*, 2024. **20**(1): pp. 47-60.
144. Ziel-Swier, L., et al., The Role of the MYC/miR-150/MYB/ZDHHC11 Network in Hodgkin Lymphoma and Diffuse Large B-Cell Lymphoma. *Genes (Basel)*, 2022. **13**(2).
145. Dzikiewicz-Krawczyk, A., et al., ZDHHC11 and ZDHHC11B are critical novel components of the oncogenic MYC-miR-150-MYB network in Burkitt lymphoma. *Leukemia*, 2017. **31**(6): pp. 1470-1473.
146. Murakami, Y., et al., Testis-specific hnRNP is expressed in colorectal cancer cells and accelerates cell growth mediating ZDHHC11 mRNA stabilization. *Cancer Med*, 2022. **11**(19): pp. 3643-3656.
147. Dai, H., et al., ZDHHC11B is decreased in lung adenocarcinoma and inhibits tumorigenesis via regulating epithelial-mesenchymal transition. *Cancer Med*, 2023. **12**(16): pp. 17212-17222.
148. Qixiang, Z. and Y. Yongping, ZDHHC12 regulates tumor properties through YAP1 in glioblastoma. *China Oncol*, 2022. **32**: pp. 527-534.



149. Lu, F., et al., Hypomethylation-induced prognostic marker zinc finger DHHC-type palmitoyltransferase 12 contributes to glioblastoma progression. *Ann Transl Med*, 2022. **10**(6): p. 334.
150. Zhang, X., et al., Inhibition of palmitoyltransferase ZDHHC12 sensitizes ovarian cancer cells to cisplatin through ROS-mediated mechanisms. *Cancer Sci*, 2024. **115**(4): p. 1170-1183.
151. Yuan, M., et al., ZDHHC12-mediated claudin-3 S-palmitoylation determines ovarian cancer progression. *Acta Pharmaceutica Sinica B*, 2020. **10**(8): pp. 1426-1439.
152. Sun, Y., et al., AMPK Phosphorylates ZDHHC13 to Increase MC1R Activity and Suppress Melanomagenesis. *Cancer Res*, 2023. **83**(7): pp. 1062-1073.
153. Yeste-Velasco, M., et al., Identification of ZDHHC14 as a novel human tumour suppressor gene. *J Pathol*, 2014. **232**(5): pp. 566-577.
154. Oo, H.Z., et al., Overexpression of ZDHHC14 promotes migration and invasion of scirrhous type gastric cancer. *Oncol Rep*, 2014. **32**(1): pp. 403-410.
155. Liu, Z.Y., et al., ZDHHC15 promotes glioma malignancy and acts as a novel prognostic biomarker for patients with glioma. *BMC Cancer*, 2023. **23**(1): p. 420.
156. Fan, X., et al., Local anesthetics impair the growth and self-renewal of glioblastoma stem cells by inhibiting ZDHHC15-mediated GP130 palmitoylation. *Stem Cell Res Ther*, 2021. **12**(1): p. 107.
157. Sun, Y., et al., S-palmitoylation of PCSK9 induces sorafenib resistance in liver cancer by activating the PI3K/AKT pathway. *Cell Rep*, 2022. **40**(7): p. 111194.
158. Singh, V., et al., Phosphorylation: Implications in Cancer. *Protein J*, 2017. **36**(1): pp. 1-6.
159. Chen, X., et al., Oct4A palmitoylation modulates tumorigenicity and stemness in human glioblastoma cells. *Neuro Oncol*, 2023. **25**(1): pp. 82-96.
160. Bu, L., et al., High-fat diet promotes liver tumorigenesis via palmitoylation and activation of AKT. *Gut*, 2024.
161. Chen, X., et al., DHHC protein family targets different subsets of glioma stem cells in specific niches. *J Exp Clin Cancer Res*, 2019. **38**(1): p. 25.
162. Liang, S., X. Zhang, and J. Li, Zinc finger Asp-His-His-Cys palmitoyl -acyltransferase 19 accelerates tumor progression through wnt/ $\beta$ -catenin pathway and is upregulated by miR-940 in osteosarcoma. *Bioengineered*, 2022. **13**(3): pp. 7367-7379.
163. Liu, Z., et al., Bioinformatics Analysis of the Prognostic and Biological Significance of ZDHHC-Protein Acyltransferases in Kidney Renal Clear Cell Carcinoma. *Front Oncol*, 2020. **10**: p. 565414.
164. Feng, R., et al., Identification and validation of palmitoylation metabolism-related signature for liver hepatocellular carcinoma. *Biochem Biophys Res Commun*, 2024. **692**: p. 149325.
165. Tomić, G., et al., Palmitoyl transferase ZDHHC20 promotes pancreatic cancer metastasis. 2023, *Res Square*.
166. Zhang, H., et al., ZDHHC20-mediated S-palmitoylation of YTHDF3 stabilizes MYC mRNA to promote pancreatic cancer progression. *Nat Commun*, 2024. **15**(1): p. 4642.
167. Fhu, C.W. and A. Ali, Fatty Acid Synthase: An Emerging Target in Cancer. *Molecules*, 2020. **25**(17).
168. Xiao, Y., et al., The implications of FASN in immune cell biology and related diseases. *Cell Death Dis*, 2024. **15**(1): p. 88.
169. Liu, B., et al., Targeting ZDHHC21/FASN axis for the treatment of diffuse large B-cell lymphoma. *Leukemia*, 2024. **38**(2): pp. 351-364.
170. Shao, X., et al., The palmitoyltransferase ZDHHC21 regulates oxidative phosphorylation to induce differentiation block and stemness in AML. *Blood*, 2023. **142**(4): pp. 365-381.
171. Huang, J., et al., ZDHHC22-mediated mTOR palmitoylation restrains breast cancer growth and endocrine therapy resistance. *Int J Biol Sci*, 2022. **18**(7): pp. 2833-2850.
172. Chen, H., et al., Identification of the miRNA-mRNA regulatory network associated with radiosensitivity in esophageal cancer based on integrative analysis of the TCGA and GEO data. *BMC Med Genomics*, 2022. **15**(1): p. 249.
173. Tang, F., et al., Palmitoyl transferases act as potential regulators of tumor-infiltrating immune cells and glioma progression. *Mol Ther Nucleic Acids*, 2022. **28**: pp. 716-731.

174. Jeong, D.W., et al., Palmitoylation-driven PHF2 ubiquitination remodels lipid metabolism through the SREBP1c axis in hepatocellular carcinoma. *Nat Commun*, 2023. **14**(1): p. 6370.
175. Draper, J.M. and C.D. Smith, Palmitoyl acyltransferase assays and inhibitors (Review). *Mol Membr Biol*, 2009. **26**(1): p. 5-13.
176. Webb, Y., L. Hermida-Matsumoto, and M.D. Resh, Inhibition of protein palmitoylation, raft localization, and T cell signaling by 2-bromopalmitate and polyunsaturated fatty acids. *J Biol Chem*, 2000. **275**(1): pp. 261-70.
177. Chase, J.F. and P.K. Tubbs, Specific inhibition of mitochondrial fatty acid oxidation by 2-bromopalmitate and its coenzyme A and carnitine esters. *Biochem J*, 1972. **129**(1): p. 55-65.
178. Coleman, R.A., et al., 2-Bromopalmitoyl-CoA and 2-bromopalmitate: promiscuous inhibitors of membrane-bound enzymes. *Biochim Biophys Acta*, 1992. **1125**(2): p. 203-209.
179. Zheng, B., S. Zhu, and X. Wu, Clickable analogue of cerulenin as chemical probe to explore protein palmitoylation. *ACS Chem Biol*, 2015. **10**(1): pp. 115-121.
180. Lawrence, D.S., J.T. Zilfou, and C.D. Smith, Structure– Activity Studies of Cerulenin Analogues as Protein Palmitoylation Inhibitors. *J Med Chem*, 1999. **42**(24): pp. 4932-4941.
181. Patterson, S.I. and J. Skene, Novel inhibitory action of tunicamycin homologues suggests a role for dynamic protein fatty acylation in growth cone-mediated neurite extension. *J Cell Biol*, 1994. **124**(4): pp. 521-536.
182. Ducker, C.E., et al., Discovery and characterization of inhibitors of human palmitoyl acyltransferases. *Mol Cancer Thera*, 2006. **5**(7): pp. 1647-1659.
183. Jennings, B.C., et al., 2-Bromopalmitate and 2-(2-hydroxy-5-nitro-benzylidene)-benzo[b]thiophen-3-one inhibit DHHC-mediated palmitoylation in vitro. *J Lipid Res*, 2009. **50**(2): pp. 233-242.
184. Coleman, D.T., et al., Curcumin prevents palmitoylation of integrin  $\beta$ 4 in breast cancer cells. *PLoS One*, 2015. **10**(5): p. e0125399.
185. Yu, W., et al., Design, synthesis and biological activity evaluation of novel covalent S-acylation inhibitors. *Mol Divers*, 2023.
186. Azizi, S.-A., et al. Charting the Chemical Space of Acrylamide-Based Inhibitors of zDHHC20. *ACS Med Chem Lett*, 2022. **13**: pp.1648-1654
187. Azizi, S.A., et al., Development of an Acrylamide-Based Inhibitor of Protein S-Acylation. *ACS Chem Biol*, 2021. **16**(8): pp. 1546-1556.
188. Salaun, C., et al., Development of a novel high-throughput screen for the identification of new inhibitors of protein S-acylation. *J Biol Chem*, 2022. **298**(10).
189. Bai, M., et al., Targeted degradation of zDHHC-PATs decreases substrate S-palmitoylation. *Plos one*, 2024. **19**(3): p. e0299665.
190. Qiu, N., et al., Artemisinin inhibits NRas palmitoylation by targeting the protein acyltransferase ZDHHC6. *Cell Chem Biol*, 2022. **29**(3): pp. 530-537.
191. Chaturvedi, S., et al., Identification of selective plant-derived natural carotenoid and flavonoids as the potential inhibitors of DHHC-mediated protein S-palmitoylation: an in silico study. *J Biomol Struct Dyn*, 2024: pp. 1-14.
192. Zhang, F., et al., Conjugated linoleic acid (CLA) reduces intestinal fatty acid uptake and chylomicron formation in HFD-fed mice associated with the inhibition of DHHC7-mediated CD36 palmitoylation and the downstream ERK pathway. *Food Funct*, 2024. **15**(9): pp. 5000-5011.
193. Wang, Q., et al., Benzocriptin C induces lysosomal degradation of PD-L1 and promotes antitumor immunity by targeting DHHC3. *Cell Rep Med*, 2024. **5**(2): p. 101357.
194. Rudzińska, M., et al., Current Status and Perspectives of Protease Inhibitors and Their Combination with Nanosized Drug Delivery Systems for Targeted Cancer Therapy. *Drug Des Devel Ther*, 2021. **15**: pp. 9-20.
195. Vargason, A.M., A.C. Anselmo, and S. Mitragotri, The evolution of commercial drug delivery technologies. *Nat Biomed Eng*, 2021. **5**(9): pp. 951-967.
196. Nalawansha, D.A. and C.M. Crews, PROTACs: An Emerging Therapeutic Modality in Precision Medicine. *Cell Chem Biol*, 2020. **27**(8): pp. 998-1014.

197. Shi, Y.Y., et al., A cyclic peptide-based PROTAC induces intracellular degradation of palmitoyltransferase and potently decreases PD-L1 expression in human cervical cancer cells. *Front Immunol*, 2023. **14**: p. 1237964.
198. Smyth, L.A. and I. Collins, Measuring and interpreting the selectivity of protein kinase inhibitors. *J Chem Biol*, 2009. **2**(3): pp. 131-51.
199. Jenkinson, S., et al., A practical guide to secondary pharmacology in drug discovery. *J Pharmacol Toxicol Methods*, 2020. **105**: p. 106869.
200. Liu, X., et al., A proteomic platform to identify off-target proteins associated with therapeutic modalities that induce protein degradation or gene silencing. *Sci Rep*, 2021. **11**(1): p. 15856.
201. Dekker, F.J., et al., Small-molecule inhibition of APT1 affects Ras localization and signaling. *Nat Chem Biol*, 2010. **6**(6): pp. 449-456.
202. Rusch, M., et al., Identification of Acyl Protein Thioesterases 1 and 2 as the Cellular Targets of the Ras-Signaling Modulators Palmostatin B and M. *Angew Chem Int Ed*, 2011. **50**(42): pp. 9838-9842.
203. Hedberg, C., et al., Development of highly potent inhibitors of the Ras-targeting human acyl protein thioesterases based on substrate similarity design. *Angew Chem Int Ed Engl*, 2011. **50**(42): pp. 9832-9837.
204. Siegel, G., et al., A functional screen implicates microRNA-138-dependent regulation of the depalmitoylation enzyme APT1 in dendritic spine morphogenesis. *Nat Cell Biol*, 2009. **11**(6): pp. 705-716.
205. Adibekian, A., et al., Characterization of a Selective, Reversible Inhibitor of Lysophospholipase 2 (LYPLA2), in Probe Reports from the NIH Molecular Libraries Program. 2010, NCBI (US).
206. Won, S.J., et al., Molecular Mechanism for Isoform-Selective Inhibition of Acyl Protein Thioesterases 1 and 2 (APT1 and APT2). *ACS Chem Biol*, 2016. **11**(12): pp. 3374-3382.
207. Hernandez, J.L., et al., APT2 Inhibition Restores Scribble Localization and S-Palmitoylation in Snail-Transformed Cells. *Cell Chem Biol*, 2017. **24**(1): pp. 87-97.
208. Won, S.J. and B.R. Martin, Temporal Profiling Establishes a Dynamic S-Palmitoylation Cycle. *ACS Chem Biol*, 2018. **13**(6): pp. 1560-1568.
209. Martin, B.R., et al., Global profiling of dynamic protein palmitoylation. *Nat Methods*, 2012. **9**(1): pp. 84-89.
210. Zuhl, A.M., et al., Probe Development Efforts to Identify Novel Inhibitors of ABHD10, in Probe Reports from the NIH Molecular Libraries Program. 2010, NCBI (US).
211. Remsberg, J.R., et al., ABHD17 regulation of plasma membrane palmitoylation and N-Ras-dependent cancer growth. *Nat Chem Biol*, 2021. **17**(8): pp. 856-864.
212. Schlesinger, M.J., A.I. Magee, and M.F. Schmidt, Fatty acid acylation of proteins in cultured cells. *J Biol Chem*, 1980. **255**(21): pp. 10021-10024.
213. Schmidt, M.F., M. Bracha, and M.J. Schlesinger, Evidence for covalent attachment of fatty acids to Sindbis virus glycoproteins. *PNAS*, 1979. **76**(4): pp. 1687-1691.
214. Waterborg, J.H. and H.R. Matthews, Fluorography of polyacrylamide gels containing tritium. *Methods Mol Biol*, 1994. **32**: pp. 163-167.
215. O'Brien, P.J. and M. Zatz, Acylation of bovine rhodopsin by [3H]palmitic acid. *J Biol Chem*, 1984. **259**(8): pp. 5054-5057.
216. Drisdel, R.C. and W.N. Green, Labeling and quantifying sites of protein palmitoylation. *Biotechniques*, 2004. **36**(2): pp. 276-285.
217. Bizzozero, O.A., Chemical analysis of acylation sites and species. *Methods Enzymol*, 1995. **250**: pp. 361-379.
218. Kolb, H.C., M.G. Finn, and K.B. Sharpless, Click Chemistry: Diverse Chemical Function from a Few Good Reactions. *Angew Chem Int Ed*, 2001. **40**(11): pp. 2004-2021.
219. Hang, H.C., et al., Chemical Probes for the Rapid Detection of Fatty-Acylated Proteins in Mammalian Cells. *J Am Chem Society*, 2007. **129**(10): pp. 2744-2745.
220. Martin, B.R. and B.F. Cravatt, Large-scale profiling of protein palmitoylation in mammalian cells. *Nat Methods*, 2009. **6**(2): pp. 135-138.
221. Speers, A.E. and B.F. Cravatt, Profiling enzyme activities in vivo using click chemistry methods. *Chem Biol*, 2004. **11**(4): pp. 535-546.
222. Gao, X., et al., Membrane targeting of palmitoylated Wnt and Hedgehog revealed by chemical probes. *FEBS letters*, 2011. **585**(15): pp. 2501-2506.

223. Drisdell, R.C. and W.N. Green, Labeling and quantifying sites of protein palmitoylation. *BioTechniques*, 2004. **36**(2): pp. 276-285.
224. Hurst, C.H., et al., Maleimide scavenging enhances determination of protein S-palmitoylation state in acyl-exchange methods. *Biotechniques*, 2017. **62**(2): pp. 69-75.
225. Forrester, M.T., et al., Site-specific analysis of protein S-acylation by resin-assisted capture. *J Lipid Res*, 2011. **52**(2): pp. 393-398.
226. Morales, J., et al., Plasma membrane localization of G alpha z requires two signals. *Mol Biol Cell*, 1998. **9**(1): pp. 1-14.
227. Zhou, B., et al., Low-Background Acyl-Biotinyl Exchange Largely Eliminates the Coisolation of Non-S-Acylated Proteins and Enables Deep S-Acylproteomic Analysis. *Anal Chem*, 2019. **91**(15): pp. 9858-9866.
228. Edmonds, M.J., et al., Analysis of the brain palmitoyl-proteome using both acyl-biotin exchange and acyl-resin-assisted capture methods. *Sci Rep*, 2017. **7**(1): p. 3299.
229. Percher, A., et al., Mass-tag labeling reveals site-specific and endogenous levels of protein S-fatty acylation. *PNAS*, 2016. **113**(16): pp. 4302-4307.
230. Hong, J.Y., et al., High-Throughput Enzyme Assay for Screening Inhibitors of the ZDHHC3/7/20 Acyltransferases. *ACS Chemical Biology*, 2021. **16**(8): p. 1318-1324.
231. Siegel, R.L., K.D. Miller, and A. Jemal, Cancer statistics, 2016. *CA Can J Clin*, 2016. **66**(1): pp. 7-30.
232. Sung, H., et al., Global cancer statistics 2020: GLOBOCAN estimates of incidence and mortality worldwide for 36 cancers in 185 countries. *CA Can J Clin*, 2021. **71**(3): pp. 209-249.
233. Tao, Z., et al., Breast cancer: epidemiology and etiology. *Cell Biochem Biophys*, 2015. **72**(2): pp. 333-338.
234. Sun, Y.-S., et al., Risk factors and preventions of breast cancer. *Int J Biol Sci*, 2017. **13**(11): p. 1387.
235. Abulkhair, O., et al., Prevalence of BRCA1 and BRCA2 mutations among high-risk Saudi patients with breast cancer. *J Global Oncol*, 2018. **4**: p. 18.
236. Secq, V., et al., Triple negative breast carcinoma EGFR amplification is not associated with EGFR, Kras or ALK mutations. *Br J Cancer*, 2014. **110**(4): pp. 1045-1052.
237. Keeton, A.B., E.A. Salter, and G.A. Piazza, The RAS-Effector Interaction as a Drug Target. *Cancer Res*, 2017. **77**(2): pp. 221-226.
238. Kallergi, G., et al., Phosphorylated EGFR and PI3K/Akt signaling kinases are expressed in circulating tumor cells of breast cancer patients. *Breast Cancer Res*, 2008. **10**(5): p. R80.
239. Andl, C.D., et al., EGFR-induced cell migration is mediated predominantly by the JAK-STAT pathway in primary esophageal keratinocytes. *Am J Physiol Gastrointest Liver Physiol*, 2004. **287**(6): pp. G1227- G1237.
240. Randon, G., et al., EGFR Amplification in Metastatic Colorectal Cancer. *J Natl Cancer Inst*, 2021. **113**(11): pp. 1561-1569.
241. Masuda, H., et al., Role of epidermal growth factor receptor in breast cancer. *Breast Cancer Res Treat*, 2012. **136**(2): pp. 331-345.
242. Yarden, Y., The EGFR family and its ligands in human cancer. signalling mechanisms and therapeutic opportunities. *Eur J Cancer*, 2001. **37**: pp. S3-S8.
243. Cruz-Gordillo, P., et al., ELP-dependent expression of MCL1 promotes resistance to EGFR inhibition in triple-negative breast cancer cells. *Sci Signal*, 2020. **13**(658): p. eabb9820.
244. Ogiso, H., et al., Crystal structure of the complex of human epidermal growth factor and receptor extracellular domains. *Cell*, 2002. **110**(6): pp. 775-787.
245. Wang, Q., X. Chen, and Z. Wang, Dimerization drives EGFR endocytosis through two sets of compatible endocytic codes. *J Cell Sci*, 2015. **128**(5): pp. 935-950.
246. Ogiso, H., et al., Crystal structure of the complex of human epidermal growth factor and receptor extracellular domains. *Cell*, 2002. **110**(6): p. 775-787.
247. Olayioye, M.A., et al., The ErbB signaling network: receptor heterodimerization in development and cancer. *EMBO J*, 2000.
248. Zhan, L., B. Xiang, and S.K. Muthuswamy, Controlled activation of ErbB1/ErbB2 heterodimers promote invasion of three-dimensional organized epithelia in an ErbB1-dependent manner: implications for progression of ErbB2-overexpressing tumors. *Cancer Res*, 2006. **66**(10): pp. 5201-5208.

249. Yarden, Y., The EGFR family and its ligands in human cancer: signalling mechanisms and therapeutic opportunities. *Eur J Cancer*, 2001. **37**: pp. 3-8.
250. Leroy, C., et al., Activation of IGF1R/p110 $\beta$ /AKT/mTOR confers resistance to  $\alpha$ -specific PI3K inhibition. *Breast Cancer Res*, 2016. **18**: pp. 1-13.
251. Jean, S. and A.A. Kiger, Classes of phosphoinositide 3-kinases at a glance. *J Cell Sci*, 2014. **127**(Pt 5): p. 923-928.
252. Huang, C.H., et al., The structure of a human p110 $\alpha$ /p85 $\alpha$  complex elucidates the effects of oncogenic PI3K $\alpha$  mutations. *Science*, 2007. **318**(5857): p. 1744-8.
253. Mukohara, T., PI3K mutations in breast cancer: prognostic and therapeutic implications. *Breast Cancer*, 2015. **7**: pp. 111-123.
254. Fedele, C.G., et al., Inositol polyphosphate 4-phosphatase II regulates PI3K/Akt signaling and is lost in human basal-like breast cancers. *PNAS*, 2010. **107**(51): pp. 22231-22236.
255. Yi, J., et al., Oncogenic activation of PI3K-AKT-mTOR signaling suppresses ferroptosis via SREBP-mediated lipogenesis. *PNAS*, 2020. **117**(49): pp. 31189-31197.
256. Henry, W.S., et al., Aspirin suppresses growth in PI3K-mutant breast cancer by activating AMPK and inhibiting mTORC1 signaling. *Cancer Res*, 2017. **77**(3): pp. 790-801.
257. Downward, J., Mechanisms and consequences of activation of protein kinase B/Akt. *Curr Opin Cell Biol*, 1998. **10**(2): pp. 262-267.
258. Song, G., G. Ouyang, and S. Bao, The activation of Akt/PKB signaling pathway and cell survival. *J Cell Mol Med*, 2005. **9**(1): pp. 59-71.
259. Oshiro, N., et al., The proline-rich Akt substrate of 40 kDa (PRAS40) is a physiological substrate of mammalian target of rapamycin complex 1. *J Biol Chem*, 2007. **282**(28): pp. 20329-20339.
260. Nitulescu, G.M., et al., The Akt pathway in oncology therapy and beyond (Review). *Int J Oncol*, 2018. **53**(6): pp. 2319-2331.
261. Petrocelli, T. and J.M. Slingerland, PTEN deficiency: a role in mammary carcinogenesis. *Breast Cancer Res*, 2001. **3**(6): pp. 356-360.
262. Mirza, A.M., et al., Oncogenic transformation of cells by a conditionally active form of the protein kinase Akt/PKB. *Cell Growth Differ*, 2000. **11**(6): pp. 279-292.
263. Brunet, A., et al., Akt promotes cell survival by phosphorylating and inhibiting a Forkhead transcription factor. *Cell*, 1999. **96**(6): pp. 857-868.
264. Nidai Ozes, O., et al., NF- $\kappa$ B activation by tumour necrosis factor requires the Akt serine-threonine kinase. 1999. *Nature*, **401**(6748): pp. 82-85.
265. Park, B.-K., X. Zeng, and R.I.J.C.r. Glazer, Akt1 induces extracellular matrix invasion and matrix metalloproteinase-2 activity in mouse mammary epithelial cells. *Cancer*, 2001. **61**(20): pp. 7647-7653.
266. Galiè, M., RAS as Supporting Actor in Breast Cancer. *Front Oncol*, 2019. **9**: p. 1199.
267. Denayer, E., T. de Ravel, and E. Legius, Clinical and molecular aspects of RAS related disorders. *J Med Gene*, 2008. **45**(11): pp. 695-703.
268. Janes, P.W., et al., Activation of the Ras signalling pathway in human breast cancer cells overexpressing erbB-2. *Oncogene*, 1994. **9**(12): pp. 3601-3608.
269. Yaeger, R. and R.B. Corcoran, Targeting alterations in the RAF-MEK pathway. *Cancer Discov*, 2019. **9**(3): pp. 329-341.
270. Hu, L., et al.,  $\Delta$ Np63 $\alpha$  is a common inhibitory target in oncogenic PI3K/Ras/Her2-induced cell motility and tumor metastasis. *PNAS*, 2017. **114**(20): pp. e3964-e3973.
271. Jin, W., et al., Roles of the PI-3K and MEK pathways in Ras-mediated chemoresistance in breast cancer cells. *Br J Cancer*, 2003. **89**(1): pp. 185-191.
272. Zoppoli, G., et al., Ras-induced resistance to lapatinib is overcome by MEK inhibition. *Curr Cancer Drug Targets*, 2010. **10**(2): pp. 168-175.
273. Douillard, J.-Y., et al., Panitumumab-FOLFOX4 treatment and RAS mutations in colorectal cancer. *N Engl J Med*, 2013. **369**(11): pp. 1023-1034.
274. Di Simone, D., et al., c-Ha-ras transfection and expression of MDR-related genes in MCF-10A human breast cell line. *Anticancer Res*, 1997. **17**(5A): pp. 3587-3592.
275. Ricoult, S.J., et al., Oncogenic PI3K and K-Ras stimulate de novo lipid synthesis through mTORC1 and SREBP. *Oncogene*, 2016. **35**(10): pp. 1250-1260.
276. Meraz, M.A., et al., Targeted disruption of the Stat1 gene in mice reveals unexpected physiologic specificity in the JAK-STAT signaling pathway. *Cell*, 1996. **84**(3): pp. 431-442.

277. Hu, X., et al., The JAK/STAT signaling pathway: from bench to clinic. *Signal Transduct Target Ther*, 2021. **6**(1): p. 402.
278. Becker, S., B. Groner, and C.W.J.N. Müller, Three-dimensional structure of the Stat3 $\beta$  homodimer bound to DNA. *Nature*, 1998. **394**(6689): pp. 145-151.
279. Igelmann, S., H.A. Neubauer, and G.J.C. Ferbeyre, STAT3 and STAT5 activation in solid cancers. *Cancer (Basel)*, 2019. **11**(10): p. 1428.
280. Yu, H. and R.J.N.R.C. Jove, The STATs of cancer—new molecular targets come of age. *Nat Rev Cancer*, 2004. **4**(2): pp. 97-105.
281. Widschwendter, A., et al., Prognostic significance of signal transducer and activator of transcription 1 activation in breast cancer. *Clin Cancer Res*, 2002. **8**(10): pp. 3065-3074.
282. Ivanov, V.N., et al., Cooperation between STAT3 and c-jun suppresses Fas transcription. *Mol Cell*, 2001. **7**(3): pp. 517-528.
283. Niu, G., et al., Role of Stat3 in regulating p53 expression and function. *Mol Cell Biol*, 2005. **25**(17): pp. 7432-7440.
284. Gyamfi, J., et al., Interleukin-6/STAT3 signalling regulates adipocyte induced epithelial-mesenchymal transition in breast cancer cells. *Sci Rep*, 2018; **8**(1): p.8859.
285. Du, Z., et al., Structure–function analysis of oncogenic EGFR Kinase Domain Duplication reveals insights into activation and a potential approach for therapeutic targeting. *Nat Commun*, 2021. **12**(1): p. 1382.
286. Huang, J., et al., Overexpression of RAB27A in Oral Squamous Cell Carcinoma Promotes Tumor Migration and Invasion via Modulation of EGFR Membrane Stability. *Int J Mol Sci*, 2023. **24**(17).
287. Purba, E.R., E.I. Saita, and I.N. Maruyama, Activation of the EGF Receptor by Ligand Binding and Oncogenic Mutations: The "Rotation Model". *Cells*, 2017. **6**(2).
288. Nair, S., et al., Novel EGFR ectodomain mutations associated with ligand-independent activation and cetuximab resistance in head and neck cancer. *PLoS One*, 2020. **15**(2): p. e0229077.
289. Zheng, B., et al., 2-Bromopalmitate Analogues as Activity-Based Probes To Explore Palmitoyl Acyltransferases. *J Am Chem Society*, 2013. **135**(19): pp. 7082-7085.
290. Chen, Y., Y. Li, and L. Wu, Protein S-palmitoylation modification: implications in tumor and tumor immune microenvironment. *Front Immunol*, 2024. **15**.
291. Li, M., L. Zhang, and C.W. Chen, Diverse Roles of Protein Palmitoylation in Cancer Progression, Immunity, Stemness, and Beyond. *Cells*, 2023. **12**(18).
292. Zhang, A., et al., Cell metabolomics. *Omics*, 2013. **17**(10): pp. 495-501.
293. Thompson, C.B., et al., A century of the Warburg effect. *Nat Metab*, 2023. **5**(11): pp. 1840-1843.
294. Wang, B., et al., A glutamine tug-of-war between cancer and immune cells: recent advances in unraveling the ongoing battle. *J Exp Clin Cancer Res*, 2024. **43**(1): p. 74.
295. Yang, R., et al., EGFR activates GDH1 transcription to promote glutamine metabolism through MEK/ERK/ELK1 pathway in glioblastoma. *Oncogene*, 2020. **39**(14): pp. 2975-2986.
296. Li, Z., et al., Involvement of ZDHHC9 in lung adenocarcinoma: regulation of PD-L1 stability via palmitoylation. *In Vitro Cell Dev Biol Anim*, 2023. **59**(3): pp. 193-203.
297. Fhu, C.W. and A. Ali, Protein Lipidation by Palmitoylation and Myristoylation in Cancer. *Front Cell Dev Biol*, 2021. **9**: p. 673647.
298. Liu, Z., et al., Emerging roles of protein palmitoylation and its modifying enzymes in cancer cell signal transduction and cancer therapy. *Int J Biol Sci*, 2022. **18**(8): pp. 3447-3457.
299. Rana, M.S., et al., Fatty acyl recognition and transfer by an integral membrane S-acyltransferase. *Science*, 2018. **359**(6372): p. eaao6326.
300. Panina, I., et al., Molecular Dynamics of DHHC20 Acyltransferase Suggests Principles of Lipid and Protein Substrate Selectivity. *Int J Mol Sci*, 2022. **23**(9).
301. Davda, D., et al., Profiling targets of the irreversible palmitoylation inhibitor 2-bromopalmitate. *ACS Chem Biol*, 2013. **8**(9): pp. 1912-1917.
302. Azizi, S.A., et al., Charting the Chemical Space of Acrylamide-Based Inhibitors of zDHHC20. *ACS Med Chem Lett*, 2022. **13**(10): pp. 1648-1654.
303. Wang, Z., et al., Small-Molecule Modulation of Protein Lipidation: From Chemical Probes to Therapeutics. *ChemBioChem*, 2023: p. e202300071.

304. Chaturvedi, S., et al., Role of EGFR and FASN in breast cancer progression. *J Cell Commun Signal*, 2023.
305. Buszka, A., et al., S-Palmitoylation of Synaptic Proteins in Neuronal Plasticity in Normal and Pathological Brains. *Cells*, 2023. **12**(3): p. 387.
306. Subbaraj, G.K., Y.S. Kumar, and L. Kulanthaivel, Antiangiogenic role of natural flavonoids and their molecular mechanism: an update. *Egypt J Int Med*, 2021. **33**(1): pp. 1-10.
307. Burley, S.K., et al., RCSB Protein Data Bank: powerful new tools for exploring 3D structures of biological macromolecules for basic and applied research and education in fundamental biology, biomedicine, biotechnology, bioengineering and energy sciences. *Nucleic Acids Res*, 2021. **49**(D1): pp. D437-D451.
308. Pandya, N. and A. Kumar, Immunoinformatics analysis for design of multi-epitope subunit vaccine by using heat shock proteins against *Schistosoma mansoni*. *J Biomol Struct Dyn*, 2023. **41**(5): pp. 1859-1878.
309. Eberhardt, J., et al., AutoDock Vina 1.2.0: New Docking Methods, Expanded Force Field, and Python Bindings. *J Chem Inf Model*, 2021. **61**(8): pp. 3891-3898.
310. Arefin, A., et al., Target specificity of selective bioactive compounds in blocking  $\alpha$ -dystroglycan receptor to suppress Lassa virus infection: an in silico approach. *J Biomed Res*, 2021. **35**(6): p. 459.
311. Morshed, A.K.M.H., et al., Oncoinformatic screening of the gene clusters involved in the HER2-positive breast cancer formation along with the in silico pharmacodynamic profiling of selective long-chain omega-3 fatty acids as the metastatic antagonists. *Mol Diver*, 2022.
312. Ion, B., M. Aboelnga, and J. Gauld, Insights From Molecular Dynamics on Substrate Binding and Effects of Active Site Mutations in  $\Delta$ 1-Pyrroline-5-Carboxylate Dehydrogenase. *Can J Chem*, 2016. **94**.
313. Chen, W., et al., Enhancing Hit Discovery in Virtual Screening through Absolute Protein–Ligand Binding Free-Energy Calculations. *J Chem Inform Model*, 2023. **63**(10): pp. 3171-3185.
314. Ivanova, L., et al., Molecular Dynamics Simulations of the Interactions between Glial Cell Line-Derived Neurotrophic Factor Family Receptor GFR $\alpha$ 1 and Small-Molecule Ligands. *ACS Omega*, 2018. **3**(9): pp. 11407-11414.
315. Forouzes, N. and N. Mishra, An Effective MM/GBSA Protocol for Absolute Binding Free Energy Calculations: A Case Study on SARS-CoV-2 Spike Protein and the Human ACE2 Receptor. *Molecules*, 2021. **26**(8).
316. Aboelnga, M.M., Exploring the structure function relationship of heme peroxidases: Molecular dynamics study on cytochrome c peroxidase variants. *Comput Biol Med*, 2022. **146**: p. 105544.
317. Nipun, T.S., et al., Active site-specific quantum tunneling of hACE2 receptor to assess its complexing poses with selective bioactive compounds in co-suppressing SARS-CoV-2 influx and subsequent cardiac injury. *J Adv Vet Anim Res*, 2021. **8**(4): pp. 540-556.
318. Paul, P.K., et al., Catabolic profiling of selective enzymes in the saccharification of non-food lignocellulose parts of biomass into functional edible sugars and bioenergy: An in silico bioprospecting. *J Adv Vet Anim Res*, 2022. **9**(1): pp. 19-32.
319. Rahman, M.H., et al., WGS-based screening of the co-chaperone protein Dj1A-induced curved DNA binding protein A (CbpA) from a new multidrug-resistant zoonotic mastitis-causing *Klebsiella pneumoniae* strain: a novel molecular target of selective flavonoids. *Mol Divers*, 2023.
320. Anjum, F., et al., Bioactive phytoconstituents as potent inhibitors of casein kinase-2: Dual implications in cancer and COVID-19 therapeutics. *RSC Adv*, 2022. **12**(13): pp. 7872-7882.
321. Daina, A., O. Michielin, and V. Zoete, SwissTargetPrediction: updated data and new features for efficient prediction of protein targets of small molecules. *Nucleic acids Res*, 2019. **47**(W1): pp. W357-W364.
322. Ferdousi, N., et al., Point-specific interactions of isovitexin with the neighboring amino acid residues of the hACE2 receptor as a targeted therapeutic agent in suppressing the SARS-CoV-2 influx mechanism. *J Adv Vet Anim Res*, 2022. **9**(2): pp. 230-240.
323. Jabin, A., et al., Target-specificity of different amylin subunits in impeding HCV influx mechanism inside the human cells considering the quantum tunnel profiles and

- molecular strings of the CD81 receptor: a combined in silico and in vivo study. In *Silico Pharmacol*, 2023. **11**(1): p. 8.
324. Monzon, A.M., et al., Conformational diversity analysis reveals three functional mechanisms in proteins. *PLoS Comput Biol*, 2017. **13**(2): p. e1005398.
  325. Pandya, N. and A. Kumar, An immunoinformatics analysis: design of a multi-epitope vaccine against *Cryptosporidium hominis* by employing heat shock protein triggers the innate and adaptive immune responses. *J Biomol Struct Dyn*, 2023: pp. 1-17.
  326. Karami, T.K., et al., Eyes on Lipinski's Rule of Five: A New "Rule of Thumb" for Physicochemical Design Space of Ophthalmic Drugs. *J Ocul Pharmacol Ther*, 2021. **38**(1): pp. 43-55.
  327. O' Donovan, D.H., et al., Trends in Molecular Properties, Bioavailability, and Permeability across the Bayer Compound Collection. *J Med Chem*, 2023. **66**(4): pp. 2347-2360.
  328. DeGoey, D.A., et al., Beyond the Rule of 5: Lessons Learned from AbbVie's Drugs and Compound Collection. *J Med Chem*, 2018. **61**(7): pp. 2636-2651.
  329. Xiong, G., et al., ADMETlab 2.0: an integrated online platform for accurate and comprehensive predictions of ADMET properties. *Nucleic Acids Res*, 2021. **49**(W1): pp. W5-W14.
  330. Chang, Y.-C., C.-P. Chen, and C.-C. Chen, Predicting Skin Permeability of Chemical Substances using a Quantitative Structure-activity Relationship. *Procedia Eng*, 2012. **45**: pp. 875-879.
  331. Lai, J.-I., et al., Clinical Perspective of FDA Approved Drugs With P-Glycoprotein Inhibition Activities for Potential Cancer Therapeutics. *Front Oncol*, 2020. **10**.
  332. Guan, L., et al., ADMET-score - a comprehensive scoring function for evaluation of chemical drug-likeness. *Med chem comm*, 2019. **10**(1): pp. 148-157.
  333. Sanchez Martinez, J.D., et al., Blood–Brain Barrier Permeability Study of Potential Neuroprotective Compounds Recovered From Plants and Agri-Food by-Products. *Front Nutr*, 2022. **9**: p. 924596.
  334. Guengerich, F.P., C.J. Wilkey, and T.T.N. Phan, Human cytochrome P450 enzymes bind drugs and other substrates mainly through conformational-selection modes. *J Biol Chem*, 2019. **294**(28): pp. 10928-10941.
  335. Zeiger, E., The test that changed the world: The Ames test and the regulation of chemicals. *Mutat Res Genet Toxicol Environ Mutagen*, 2019. **841**: pp. 43-48.
  336. Bronikowska, J., et al., Novel Structurally Related Flavones Augment Cell Death Induced by rhsTRAIL. *Int J Mol Sci*, 2017. **18**(6).
  337. Chopra, B. and A.K. Dhingra, Natural products: A lead for drug discovery and development. *Phytother Res*, 2021. **35**(9): pp. 4660-4702.
  338. Chen, B., et al., Protein Lipidation in Cell Signaling and Diseases: Function, Regulation, and Therapeutic Opportunities. *Cell Chem Biol*, 2018. **25**(7): pp. 817-831.
  339. Hernandez, L.M., et al., Palmitoylation-dependent control of JAK1 kinase signaling governs responses to neuropoietic cytokines and survival in DRG neurons. *J Biol Chem*, 2023. **299**(8): p. 104965.
  340. Sun, Y., et al., ZDHHC2-Mediated AGK Palmitoylation Activates AKT–mTOR Signaling to Reduce Sunitinib Sensitivity in Renal Cell Carcinoma. *Cancer Res*, 2023. **83**(12): pp. 2034-2051.
  341. Zhang, J., et al., Identification of CKAP4/p63 as a major substrate of the palmitoyl acyltransferase DHHC2, a putative tumor suppressor, using a novel proteomics method. *Mol Cell Proteomics*, 2008. **7**(7): pp. 1378-88.
  342. Yan, S.-M., et al., Reduced expression of ZDHHC2 is associated with lymph node metastasis and poor prognosis in gastric adenocarcinoma. *PLoS one*, 2013. **8**(2): p. e56366.
  343. Zhang, C., et al., Tumour-associated mutant p53 drives the Warburg effect. *Nat Commun*, 2013. **4**: p. 2935.
  344. Chen, L., et al., Palmitoylation alters LDHA activity and pancreatic cancer response to chemotherapy. *Cancer Lett*, 2024. **587**: p. 216696.
  345. Čermáková, M., et al., Metabolomic Study of Obesity and Its Treatment with Palmitoylated Prolactin-Releasing Peptide Analog in Spontaneously Hypertensive and Normotensive Rats. *J Proteome Res*, 2019. **18**(4): pp. 1735-1750.
  346. Tan, E., et al., HEK293 Cell Line as a Platform to Produce Recombinant Proteins and Viral Vectors. *Front Bioeng Biotechnol*, 2021. **9**: p. 796991.



347. Kwon, M. and B.L. Firestein, DNA transfection: calcium phosphate method. *Methods Mol Biol*, 2013. **1018**: pp. 107-110.
348. Xu, F., et al., Bromodomain protein 4 is a key molecular driver of TGF $\beta$ 1-induced hepatic stellate cell activation. *Biochim Biophys Acta Mol Cell Res*, 2023. **1870**(8): p. 119569.
349. Guo, J., et al., The short-chain fatty acid butyrate exerts a specific effect on VE-cadherin phosphorylation and alters the integrity of aortic endothelial cells. *Front Cell Dev Biol*, 2023. **11**: p. 1076250.
350. Barbau-Piednoir, E., et al., Development and validation of qualitative SYBR®Green real-time PCR for detection and discrimination of *Listeria* spp. and *Listeria monocytogenes*. *Appl Microbiol Biotechnol*, 2013. **97**(9): pp. 4021-4037.
351. Shanker, S., et al., Evaluation of commercially available RNA amplification kits for RNA sequencing using very low input amounts of total RNA. *J Biomol Tech*, 2015. **26**(1): pp. 4-18.
352. Rao, X., et al., An improvement of the 2<sup>-</sup>(-delta delta CT) method for quantitative real-time polymerase chain reaction data analysis. *Biostat Bioinforma Biomath*, 2013. **3**(3): pp. 71-85.
353. Mahmood, T. and P.C. Yang, Western blot: technique, theory, and trouble shooting. *N Am J Med Sci*, 2012. **4**(9): pp. 429-434.
354. Lauri, I., et al., Development of an Optimized Protocol for NMR Metabolomics Studies of Human Colon Cancer Cell Lines and First Insight from Testing of the Protocol Using DNA G-Quadruplex Ligands as Novel Anti-Cancer Drugs. *Metabolites*, 2016. **6**(1): p. 4.
355. Ser, Z., et al., Extraction parameters for metabolomics from cultured cells. *Anal Biochem*, 2015. **475**: pp. 22-28.
356. Souza, A.L. and G.J. Patti, A Protocol for Untargeted Metabolomic Analysis: From Sample Preparation to Data Processing. *Methods Mol Biol*, 2021. **2276**: pp. 357-382.
357. Xiao, J.F., B. Zhou, and H.W. Ransom, Metabolite identification and quantitation in LC-MS/MS-based metabolomics. *Trends Analyt Chem*, 2012. **32**: pp. 1-14.
358. Naser, F.J., et al., Two complementary reversed-phase separations for comprehensive coverage of the semipolar and nonpolar metabolome. *Anal Bioanal Chem*, 2018. **410**(4): pp. 1287-1297.
359. Tsugawa, H., et al., MS-DIAL: data-independent MS/MS deconvolution for comprehensive metabolome analysis. *Nat Methods*, 2015. **12**(6): pp. 523-526.
360. Lai, Z., et al., Identifying metabolites by integrating metabolome databases with mass spectrometry cheminformatics. *Nat Methods*, 2018. **15**(1): pp. 53-56.
361. Pang, Z., et al., Using MetaboAnalyst 5.0 for LC–HRMS spectra processing, multi-omics integration and covariate adjustment of global metabolomics data. *Nat Protocols*, 2022. **17**(8): pp. 1735-1761.
362. Qiu, S., et al., Small molecule metabolites: discovery of biomarkers and therapeutic targets. *Signal Transduct Target Ther*, 2023. **8**(1): p. 132.
363. Ali, J.S., et al., Biomarker selection and imaging design in cancer: A link with biochemical pathways for imminent engineering. *Heliyon*, 2020. **6**(2): p. e03340.
364. Faubert, B., A. Solmonson, and R.J. DeBerardinis, Metabolic reprogramming and cancer progression. *Science*, 2020. **368**(6487).
365. Worley, B. and R. Powers, Multivariate Analysis in Metabolomics. *Curr Metab*, 2013. **1**(1): pp. 92-107.
366. Gromski, P.S., et al., A tutorial review: Metabolomics and partial least squares-discriminant analysis--a marriage of convenience or a shotgun wedding. *Anal Chim Acta*, 2015. **879**: pp. 10-23.
367. Hashimoto, Y., M. Hamaguchi, and M. Fukui, Microbe-associated metabolites as targets for incident type 2 diabetes. *J Diabetes Investig*, 2021. **12**(4): pp. 476-478.
368. Karnovsky, A. and S. Li, Pathway Analysis for Targeted and Untargeted Metabolomics. 2020. pp. 387-400.
369. Chen, J., et al., De novo nucleotide biosynthetic pathway and cancer. *Genes Dis*, 2023. **10**(6): pp. 2331-2338.
370. Wang, X., et al., Targeting pyrimidine synthesis accentuates molecular therapy response in glioblastoma stem cells. *Sci Transl Med*, 2019. **11**(504).
371. Wang, W., et al., Targeting Pyrimidine Metabolism in the Era of Precision Cancer Medicine. *Front Oncol*, 2021. **11**: p. 684961.

372. Liu, X., et al., The significant role of amino acid metabolic reprogramming in cancer. *Cell Commun Signal*, 2024. **22**(1): p. 380.
373. Li, G., et al., Pyrimidine biosynthetic enzyme CAD: its function, regulation, and diagnostic potential. *Int J Mol Sci*, 2021. **22**(19): p. 10253.
374. Mollick, T. and S. L  n, Modulating pyrimidine ribonucleotide levels for the treatment of cancer. *Cancer Metab*, 2020. **8**(1): p. 12.
375. Breitkopf, S.B., et al., Serial-omics of P53<sup>-/-</sup>, Brca1<sup>-/-</sup> Mouse Breast Tumor and Normal Mammary Gland. *Sci Rep*, 2017. **7**(1): p. 14503.
376. Lee, J.S., et al., Urea Cycle Dysregulation Generates Clinically Relevant Genomic and Biochemical Signatures. *Cell*, 2018. **174**(6): pp. 1559-1570.
377. Pizzorno, G., et al., Homeostatic control of uridine and the role of uridine phosphorylase: a biological and clinical update. *BBA-Mol Basis Dis*, 2002. **1587**(2): pp. 133-144.
378. Lin, Y.-C., et al., Genome dynamics of the human embryonic kidney 293 lineage in response to cell biology manipulations. *Nat Commun*, 2014. **5**(1): p. 4767.
379. Ali, S. and J. DeCaprio, Cellular transformation by SV40 large T antigen: Interaction with host proteins. *Semin Cancer Biol*, 2001. **11**: pp. 15-23.
380. Guo, Y., et al., Betaine Effects on Morphology, Proliferation, and p53-induced Apoptosis of HeLa Cervical Carcinoma Cells in Vitro. *Asian Pac J Cancer Prev*, 2015. **16**(8): pp. 3195-201.
381. Shi, D. and W. Gu, Dual Roles of MDM2 in the Regulation of p53: Ubiquitination Dependent and Ubiquitination Independent Mechanisms of MDM2 Repression of p53 Activity. *Genes Cancer*, 2012. **3**(3-4): pp. 240-248.
382. Wang, H., et al., High expression levels of pyrimidine metabolic rate-limiting enzymes are adverse prognostic factors in lung adenocarcinoma: a study based on The Cancer Genome Atlas and Gene Expression Omnibus datasets. *Purinergic Signal*, 2020. **16**(3): pp. 347-366.
383. Chernova, O.B., et al., MYC abrogates p53-mediated cell cycle arrest in N-(phosphonacetyl)-L-aspartate-treated cells, permitting CAD gene amplification. *Mol Cell Biol*, 1998. **18**(1): pp. 536-545.
384. Keshet, R., et al., Rewiring urea cycle metabolism in cancer to support anabolism. *Nat Rev Cancer*, 2018. **18**(10): pp. 634-645.
385. Gorgoglione, R., et al., Glutamine-Derived Aspartate Biosynthesis in Cancer Cells: Role of Mitochondrial Transporters and New Therapeutic Perspectives. *Cancers (Basel)*, 2022. **14**(1).
386. Craig, S.A.S., Betaine in human nutrition. *Ame J Clin Nutr*, 2004. **80**(3): pp. 539-549.
387. Zhao, G., et al., Betaine in Inflammation: Mechanistic Aspects and Applications. *Front Immunol*, 2018. **9**: p. 1070.
388. Sternbach, S., et al., The BHMT-betaine methylation pathway epigenetically modulates oligodendrocyte maturation. *PLoS One*, 2021. **16**(5): p. e0250486.
389. Mart  nez, Y., et al., The role of methionine on metabolism, oxidative stress, and diseases. *Amino Acids*, 2017. **49**(12): pp. 2091-2098.
390. Abbasi, M.S.P., et al., Dietary choline and betaine intake, cardio-metabolic risk factors and prevalence of metabolic syndrome among overweight and obese adults. *BMC Endocr Disord*, 2023. **23**(1): p. 67.
391. Youn, J., E. Cho, and J.E. Lee, Association of choline and betaine levels with cancer incidence and survival: A meta-analysis. *Clin Nutr*, 2019. **38**(1): pp. 100-109.
392. Hussein, R.M. and S.M. Al-Dalain, Betaine downregulates microRNA 34a expression via a p53-dependent manner in cisplatin-induced nephrotoxicity in rats. *J Biochem Mol Toxicol*, 2021. **35**(9): p. e22856.
393. Li, Y., Y. Wang, and P. Wu, 5'-Methylthioadenosine and Cancer: old molecules, new understanding. *J Cancer*, 2019. **10**(4): pp. 927-936.
394. Ferra, F.d. and C. Baglioni, Correlation between growth inhibition and presence of 5'-methylthioadenosine in cells treated with interferon. *Cancer Res*, 1984. **44**(6): pp. 2297-2301.
395. Tomasi, M.L., et al., S-adenosylmethionine and methylthioadenosine inhibit cancer metastasis by targeting microRNA 34a/b-methionine adenosyltransferase 2A/2B axis. *Oncotarget*, 2017. **8**(45): p. 78851.
396. Barekatin, Y., et al., Methylthioadenosine is Not Dramatically Elevated in MTAP-Homozygous Deleted Primary Glioblastomas. *Nat Commun*, 2019: p. 769885.

397. Sugiyama, Y., et al., The heme precursor 5-aminolevulinic acid disrupts the Warburg effect in tumor cells and induces caspase-dependent apoptosis. *Oncol Rep*, 2014. **31**(3): pp. 1282-1286.
398. Adachi, R., et al., The Effect of Photodynamic Therapy Using 5-Aminolevulinic Acid in Bone and Soft Tissue Sarcoma Cells. *Anticancer Res*, 2024. **44**(3): pp. 963-969.
399. Kar, F., et al., Betaine suppresses cell proliferation by increasing oxidative stress-mediated apoptosis and inflammation in DU-145 human prostate cancer cell line. *Cell Stress Chaperones*, 2019. **24**(5): pp. 871-881.
400. Zhou, F., et al., CSS-Palm: palmitoylation site prediction with a clustering and scoring strategy (CSS). *Bioinformatics*, 2006. **22**(7): pp. 894-896.
401. Ren, J., et al., CSS-Palm 2.0: An updated software for palmitoylation sites prediction. *Protein engineering, design & selection : PEDS*, 2008. **21**: pp. 639-644.
402. Zhou, Y., et al., DDMut: predicting effects of mutations on protein stability using deep learning. *Nucleic Acids Res*, 2023. **51**(W1): pp. W122-W128.
403. Pettersen, E.F., et al., UCSF ChimeraX: Structure visualization for researchers, educators, and developers. *Protein Sci*, 2021. **30**(1): pp. 70-82.
404. Pandya, M., R. Rawal, and A. Daga, "Structural and functional analysis of af9-mll oncogenic fusion protein using homology modeling and simulation based approach.". *International J Pharm Pharm Sci*, 2015. **7**.
405. Eisenberg, D., R. Luethy, and J. Bowie, VERIFY3D: Assessment of Protein Models with Three-Dimensional Profiles. *Methods Enzymol*, 1997. **277**: pp. 396-404.
406. Laskowski, R.A., et al., PDBsum: Structural summaries of PDB entries. *Protein Sci*, 2018. **27**(1): pp. 129-134.
407. Padhi, A.K., M. Janežič, and K.Y.J. Zhang, Chapter 26 - Molecular dynamics simulations: Principles, methods, and applications in protein conformational dynamics, in *Advances in Protein Molecular and Structural Biology Methods*, T. Tripathi and V.K. Dubey, Editors. 2022, Academic Press. pp. 439-454.
408. Ahmed, M.H., et al., Bound water at protein-protein interfaces: partners, roles and hydrophobic bubbles as a conserved motif. *PLoS One*, 2011. **6**(9): p. e24712.
409. Genheden, S. and U. Ryde, The MM/PBSA and MM/GBSA methods to estimate ligand-binding affinities. *Expert Opin Drug Discov*, 2015. **10**(5): pp. 449-61.
410. Forouzesh, N. and A.V. Onufriev, MMGB/SA Consensus Estimate of the Binding Free Energy Between the Novel Coronavirus Spike Protein to the Human ACE2 Receptor. *bioRxiv*, 2020.
411. Danzi, F., et al., To metabolomics and beyond: a technological portfolio to investigate cancer metabolism. *Signal Transduct Target Ther*, 2023. **8**(1): p. 137.
412. Koundouros, N. and G. Poulogiannis, Reprogramming of fatty acid metabolism in cancer. *Br J Cancer*, 2020. **122**(1): pp. 4-22.
413. Wang, W., et al., Cancer metabolites: promising biomarkers for cancer liquid biopsy. *Biomarker Res*, 2023. **11**(1): p. 66.
414. Main, A. and W. Fuller, Protein S-Palmitoylation: advances and challenges in studying a therapeutically important lipid modification. *FEBS J*, 2022. **289**(4): pp. 861-882.
415. Dzobo, K., The Role of Natural Products as Sources of Therapeutic Agents for Innovative Drug Discovery. *Compr Pharmacol*, 2022. pp. 408-422.